
Towards ${}^6\text{Li}$ - ${}^{40}\text{K}$ Ground State Molecules

Johannes Felix Simon Brachmann



München 2012

Towards ${}^6\text{Li}$ - ${}^{40}\text{K}$ Ground State Molecules

Johannes Felix Simon Brachmann

Dissertation
an der Fakultät für Physik
der Ludwig-Maximilians-Universität
München
und am
Max-Planck-Institut für Quantenoptik
Garching

vorgelegt von
Johannes Felix Simon Brachmann
aus Berlin

München, 2012

Erstgutachter: Prof. Dr. Theodor W. Hänsch

Zweitgutachter: Dr. habil. Markus Weber

Tag der mündlichen Prüfung: 08.02.2013

Abstract

The production of a quantum gas with strong long - range dipolar interactions is a major scientific goal in the research field of ultracold gases. In their ro-vibrational ground state Li - K dimers possess a large permanent dipole moment, which could possibly be exploited for the realization of such a quantum gas. A production of these molecules can be achieved by the association of Li and K at a Feshbach resonance, followed by a coherent state transfer. In this thesis, detailed theoretical and experimental preparations to achieve state transfer by means of Stimulated Raman Adiabatic Passage (STIRAP) are described.

The theoretical preparations focus on the selection of an electronically excited molecular state that is suitable for STIRAP transfer. In this context, molecular transition dipole moments for both transitions involved in STIRAP transfer are predicted for the first time. This is achieved by the calculation of Franck - Condon factors and a determination of the state in which the ${}^6\text{Li} - {}^{40}\text{K}$ Feshbach molecules are produced. The calculations show that state transfer by use of a single STIRAP sequence is experimentally very well feasible. Further, the optical wavelengths that are needed to address the selected states are calculated. The high accuracy of the data will allow to carry out the molecular spectroscopy in a fast and efficient manner. Further, only a comparatively narrow wavelength tuneability of the spectroscopy lasers is needed.

The most suitable Feshbach resonance for the production of ${}^6\text{Li} - {}^{40}\text{K}$ molecules at experimentally manageable magnetic field strengths is occurring at 155 G. Experimentally, this resonance is investigated by means of cross - dimensional relaxation. The application of the technique at various magnetic field strengths in the vicinity of the 155 G Feshbach resonance allows a determination of the resonance position and width with so far unreached precision. This reveals the production of molecules on the atomic side of the resonance, thereby establishing the first observation of a many body effect in the crossover regime of a narrow Feshbach resonance. Further, mass dependent factors, with which the equilibration of an induced anisotropic temperature of the trapped particle samples can be described, are experimentally determined for the first time. The type of resonance as well as the measured molecular lifetimes are found to be very well suited for STIRAP transfer.

A Raman laser system is designed based on the transition wavelengths and durations of state transfer which are predicted. As the wavelengths of the Raman lasers differ widely but coherence of the light fields is needed, the technical realization of a laser system is challenging. As a part of the laser system, the construction and characterization of a reference optical resonator are presented. Laser frequency stabilization with a linewidth of approximately 500 Hz and an Allan deviation below 10^{-12} for timespans up to several ten seconds are demonstrated. Further, the stabilization of a frequency comb to this reference laser is demonstrated.

For the laser spectroscopy of electronically excited Li - K states an interferometric laser frequency stabilization will be used. The device is a commercial design, for which a calibration procedure that enhances the precision by several orders of magnitude is worked out within this thesis. The calibration scheme includes the precise measurement of the stabilization's wavelength dependent frequency deviations by means of a frequency comb. By the implementation of several calibration steps a remaining frequency deviation of less than 5.7 MHz (rms 1.6 MHz) in the whole relevant wavelength range 750 - 795 nm is achieved. Only the exceptional precision of the fully calibrated device permits the usage for the Li - K spectroscopy, while the demonstrated wide tuning capability facilitates the completion of the latter in a fast and convenient manner.

Zusammenfassung

Eines der wesentlichen wissenschaftlichen Ziele im Forschungsgebiet ultrakalter Gase ist die Erzeugung eines Quantengases mit langreichweitiger Dipolwechselwirkung. Eine Möglichkeit mit sehr guten Erfolgsaussichten hierfür, besteht darin das große permanente Dipolmoment von Li-K Dimeren im Rotations- und Vibrationsgrundzustand zu nutzen. Solche Grundzustandsmoleküle können erzeugt werden, indem man die atomaren Spezies an einer Feshbach Resonanz assoziiert und danach kohärent in den Grundzustand transferiert. In dieser Dissertation werden die experimentellen und theoretischen Vorbereitungen für einen Ramantransfer (STIRAP) von Li-K Molekülen in den Grundzustand beschrieben.

Die theoretischen Vorbereitungen beschäftigen sich damit, einen elektronisch angeregten Molekülzustand zu finden, der sich für den STIRAP transfer eignet. In diesem Zusammenhang werden die Dipolübergangsmomente für beide Übergänge der STIRAP Sequenz zum ersten Mal vorhergesagt. Dazu werden Franck-Condon Faktoren berechnet und der Zustand, in dem die ${}^6\text{Li}$ - ${}^{40}\text{K}$ Moleküle erzeugt werden, wird bestimmt. Die Berechnungen zeigen, dass der Zustandstransfer mit einer einzigen STIRAP Sequenz experimentell möglich ist. Desweiteren werden die optischen Wellenlängen, die man zum Ansprechen der vorher ausgewählten Molekülzustände benötigt, berechnet. Die hohe Genauigkeit dieser Daten wird eine schnelle und effiziente Durchführung der Molekülspektroskopie ermöglichen. Zusätzlich bestehen geringe Anforderungen an die Durchstimbarkeit der Laser.

Die experimentell am besten geeignete Feshbach Resonanz zur Erzeugung von ${}^6\text{Li}$ - ${}^{40}\text{K}$ Molekülen tritt bei 155 G auf. Diese Resonanz wird mittels "cross-dimensional relaxation" experimentell untersucht. Durch die Anwendung der Methode bei verschiedenen Magnetfeldstärken im Bereich der Resonanz kann deren genaue Position und Breite bestimmt werden. Dadurch wird erkennbar, dass Moleküle auch auf der atomaren Seite der Resonanz erzeugt werden. Dies ist die erste Beobachtung eines Vielteilcheneffekts im Crossover-Bereich einer schmalen Feshbach Resonanz. Desweiteren werden masseabhängige Faktoren, mit denen die Li-K Relaxationsraten quantitativ beschrieben werden können, experimentell bestimmt. Die Untersuchungen zeigen, dass sowohl die Moleküllebensdauern als auch die Art der Feshbach Resonanz sehr gut für den Grundzustandstransfer geeignet sind.

Im Weiteren wird - basierend auf den optischen Wellenlängen und benötigten Zeitdauern, die für die STIRAP Sequenz bestimmt wurden - das Design für ein Raman Lasersystem entwickelt. Da die Raman Wellenlängen sehr unterschiedlich sind, aber die Lichtfelder über den Zeitraum des Transfers kohärent bleiben müssen, ist die technische Realisierung des Lasersystems eine Herausforderung. Die Konstruktion und Charakterisierung eines Referenz Fabry-Pérot Resonators sind Teil der experimentellen Vorbereitungen für den Grundzustandstransfer. Es gelingt die Stabilisierung eines Lasers mit einer Linienbreite von etwa 500 Hz und einer Allan-Varianz $< (10^{-12})^2$ für Zeitdauern von bis zu einigen zehn Sekunden. Desweiteren wird die Stabilisierung eines Frequenzkamms auf diesen Referenzlaser erreicht.

Für die Spektroskopie elektronisch angeregter Li-K Zustände wird eine kommerzielle interferometrische Laserfrequenzstabilisierung zum Einsatz kommen. Durch ein für das Gerät im Rahmen dieser Arbeit entwickeltes Kalibrationsschema, konnte eine Präzisionssteigerung um mehrere Größenordnungen erreicht werden. Dafür werden die Frequenzabweichungen des Geräts, die mittels eines Frequenzkamms mit hoher Genauigkeit gemessen werden können, für die Kompensation systematischer Fehler verwendet. Das vollständig kalibrierte Gerät weist Abweichungen von unter 5.7 MHz (rms 1.6 MHz) im gesamten für die Spektroskopie relevanten Wellenlängenbereich von 750 bis 795 nm auf. Erst die durch die Kalibration erzielte Genauigkeit ermöglicht es, das Gerät für die Spektroskopie der Li-K Moleküle zu verwenden und vom breiten Verstimmbereich der Frequenzstabilisierung zu profitieren.

Contents

1	Introduction	1
1.1	Ultracold quantum gases	1
1.2	The ultracold ${}^6\text{Li}$ - ${}^{40}\text{K}$ - ${}^{87}\text{Rb}$ mixture	5
1.2.1	This thesis	5
1.2.2	Outline of this thesis	6
2	The ultracold Li - K mixture, bound and unbound states	9
2.1	Ideal gases in harmonic trap potentials	10
2.2	Li- K interaction potentials and bound states	13
2.2.1	States of alkali metal dimers	13
2.2.2	Adiabatic Li- K potentials	15
2.2.3	The Franck - Condon principle	16
2.2.4	Eigenstates in the $\mathbf{X}^1\Sigma^+$ and $\mathbf{1}^1\Pi$ potentials	19
2.2.5	Relevant Franck - Condon factors	24
2.3	Scattering in the ultracold Li- K mixture	27
2.3.1	Elastic scattering	28
2.3.2	Inelastic scattering	30
2.4	Feshbach resonances	34
2.4.1	Asymptotic Bound State Model	36
3	Experimental apparatus	41
3.1	The production of an ultracold mixture with up to three species	41
3.2	Optical trapping of atoms and molecules	44
3.3	Imaging of particles in the Li- K mixture	48
3.3.1	Absorption imaging of the atomic species and Feshbach molecules	48
3.3.2	Imaging of deeply bound Li- K molecules	49
4	Experimental investigation of the Feshbach resonance at 155 G	51
4.1	Cross - dimensional relaxation	51
4.2	Experimental generation of kinetic energy anisotropies	53
4.3	Experimental observation of cross - dimensional relaxation	55
4.4	Experimental determination of the position and width of the 155 G resonance	56
4.5	Resonant ${}^6\text{Li}$ - ${}^{40}\text{K}$ scattering cross sections around 155 G	57
4.6	Magnetic field dependent lifetime of ${}^6\text{Li}$ - ${}^{40}\text{K}$ dimers	58

CONTENTS

5	Raman transitions between molecular states of Li-K	61
5.1	Stimulated Raman Adiabatic Passage in a Λ -configuration three level system	61
5.2	Wavelengths and dipole moments of transitions between molecular states in the $X^1\Sigma^+$ and $1^1\Pi$ potentials	64
5.3	Optimization of the STIRAP pulse sequence	69
5.3.1	Selection rules	69
5.3.2	Adiabaticity criterion	69
5.3.3	Cloud temperature and sensitivity the detunings Δ and δ	71
5.3.4	Decay from the electronically excited state	72
5.3.5	STIRAP via multiple excited states	72
5.4	Photon recoil and non-adiabatic change of the dipole trapping potential .	74
6	Molecular spectroscopy	75
6.1	Spectroscopy of the electronically excited states	75
6.2	A tool for molecular spectroscopy	78
6.2.1	Functional principle	78
6.2.2	Calibration steps	78
6.2.3	Accuracy of the calibrated interferometer setup	79
6.2.4	Molecular spectroscopy with the calibrated interferometer setup .	80
6.3	Two-photon spectroscopy of low lying states in the $X^1\Sigma^+$ potential . . .	81
7	Raman laser system	83
7.1	Design of the Raman laser system	83
7.1.1	The laser system	84
7.1.2	Alternative laser system designs	86
7.1.3	Tuneability of the Raman lasers	88
7.2	Zerodur Fabry-Pérot reference resonator	89
7.2.1	Fabry-Pérot resonator design	89
7.2.2	Pound-Drever-Hall frequency stabilization	93
7.2.3	Characterization of the Fabry-Pérot resonator and the stabilized Raman laser	95
8	Conclusion and outlook	103
A	Calibration of an interferometric laser frequency stabilization	109
A.1	Functional principle	109
A.2	Phase-frequency relation	111
A.2.1	Prediction of an interferometer phase	111
A.3	Calibrations	114
A.3.1	Signal correction	114
A.3.2	Etalon drift	114
A.3.3	Compensation for the effect of multiple interference	115
A.3.4	Calibration of the etalon's optical pathlength	115
A.4	Discussion	120
A.4.1	Etalon length calibration	120

CONTENTS

A.4.2 Possible causes for systematic frequency deviations	122
A.5 Stability of the calibration	125
A.6 Comparison of two interferometer setups	126
A.7 Conclusive remarks	126
Bibliography	129
Danksagung	143

Chapter 1

Introduction

1.1 Ultracold quantum gases

Ever since the first experimental realizations of Bose-Einstein condensates [Anderson et al., 1995, Davis et al., 1995a, Bradley et al., 1995], the field of ultracold quantum gases has witnessed a very fast evolution and diversification. Even though experimentally more challenging, a quantum degenerate gas of fermionic particles [DeMarco and Jin, 1999] was produced for the first time around four years after reaching quantum degeneracy of bosons. In a process continuing up to today, increasingly more sophisticated experimental methods and techniques have allowed to enter new regimes and quantum phases, which can be studied in a very direct manner. Quantum gases offer the possibility to control the very pure physical systems with an unprecedented accuracy. Further, it is possible to precisely tune physical parameters, while unwanted interactions with the environment can be kept at a negligible strength. Today, newest imaging techniques allow to observe physical systems at highest resolution and up to the single particle level [Nelson et al., 2007, Gericke et al., 2008, Bakr et al., 2009, Zimmermann et al., 2011], thereby enabling a precise direct investigation of the particle statistics of quantum states.

Apart from more traditional areas of atomic physics like precision measurements and atomic clocks, one of the most exciting aspects of ultracold gases is the possibility to reach regimes in which connections to other areas of physics are made. This allows to use ultracold quantum gases for simulations of certain properties and aspects of solid state systems or systems in particle physics. In future, the controllability and tuneability of quantum gases might allow to gain insight into general physical characteristics and phenomena known from other systems that are experimentally difficult to access and theoretically difficult to treat. Much work is put into the development of tools that allow the interactions between particles of a sample to be tuned on the one hand as well as possibilities to shape the external potentials on the other hand. This allows to engineer Hamiltonians that are tailored for the purpose of studying specific quantum systems. Further, the controllability and protection from external perturbations make quantum gas systems a possible candidate for the realization of a quantum computer.

Optical lattices. A fascinating aspect of the work with ultracold gases is the possibility of shaping external potential landscapes acting on the particles. This can be achieved

1.1 Ultracold quantum gases

by the use of light fields detuned from a transition between internal states of the particles in the sample. Interfering light fields are used to create periodic potentials, which can resemble the potential due to the atomic cores in condensed matter systems. These optical lattices, among other applications, allow to enter the strongly correlated regime and enabled the experimental realization of bosonic and fermionic Hubbard models [Jaksch et al., 1998, Greiner et al., 2002, Jördens et al., 2008]. Exciting new possibilities arise from high resolution optical systems, which allow the detection of single particles with a resolution corresponding to one lattice site. These cannot only be used for detection but also for projection of optical lattices, allowing a more versatile shaping of potentials [Bakr et al., 2010, Sherson et al., 2010, Zimmermann et al., 2011].

Feshbach resonances have proved a valuable tool for controlling the interactions between particles in ultracold samples of atoms [Chin et al., 2010]. The use of these scattering resonances allow to tune interactions from repulsive to attractive values of widely different strength. Feshbach resonances have been found and exploited in systems of fermions and bosons of the same species as well as in mixed systems (heteronuclear Feshbach resonances) of particles (see e.g. [O'Hara et al., 2002, Dieckmann et al., 2002, Donley et al., 2001, Inouye et al., 2004]). The tuning of interactions makes it possible to enter different regimes and physical states.

In the regime of strong interactions, strongly correlated states have been realized. These have drawn much attention and are subject to ongoing theoretical and experimental investigations. A description of the underlying many-body physics is difficult and cannot be achieved by a mean field approach. Quantum gases have for the first time made it experimentally possible to continuously change the physical state of a fermion system between two opposite regimes: In the regime of strong attractive interaction fermions pair in momentum space and are in a superfluid state. If interactions are tuned from large attractive to small repulsive values, the binding length of paired fermions is continuously reduced to a molecular level. Thus, the tuneability of interactions allow for the first time to study physical systems in the whole crossover between Bardeen-Cooper-Schrieffer- and Bose-Einstein Condensate regimes. In this context it is interesting to note that quantum gas systems, even though likely the coldest systems in the universe, are also, in the regime of strong attractive interactions, the superfluids with the highest transition temperature (in respect to the Fermi energy) known today. The fermionic pairing gap as well as other quantities connected to the superfluidity of fermions have been investigated in a number of publications. Some of these are [Bourdel et al., 2003, Regal et al., 2004a, Chin et al., 2004, Zwierlein et al., 2005]. More recently, further insight into the strongly correlated states has been gained by a set of universal relations [Tan, 2008, Braaten et al., 2011]. These allow to connect the strength of correlations to the thermodynamics of a many-body system by use of a quantity called Tan's Contact. Recently, the Contact has been experimentally determined in fermionic and bosonic systems [Kuhnle et al., 2010, Stewart et al., 2010, Wild et al., 2012].

In the contrary case, when the strength of interactions is tuned to values close to zero, states which resemble ideal gases can be realized [O'Hara et al., 2002, Weber et al., 2003].

Feshbach resonances do not only occur in atomic ensembles, but also scattering

resonances of molecules occur [Forrey et al., 1998]. These might prove a useful tool in a new field of ultracold chemistry.

Feshbach- and ground state molecules. Feshbach resonances allow the adiabatic association of atoms to molecules at ultracold temperatures [Jochim et al., 2003a, Cubizolles et al., 2003, Dürr et al., 2004, Ospelkaus et al., 2006]. These molecules, which are produced in a single quantum state, are the coldest molecules available for experiments today. In the case of bosonic dimers consisting of fermionic atoms, long molecular lifetimes allow to reach quantum degeneracy and the generation of molecular Bose-Einstein condensates [Zwierlein et al., 2003, Greiner et al., 2003, Jochim et al., 2003b].

Alkali metal dimers show widely different characteristics (e.g. in respect to stability of samples, interaction) depending on average internuclear distance, or in other words the ro-vibrational excitation. Feshbach molecules are formed in vibrationally highly excited states. It has been a long standing goal to be able to coherently control the internal, ro-vibrational, degrees of freedom of molecules. Recently, coherent state transfer to lower lying vibrational states and even the absolute ro-vibrational ground state has been demonstrated in the case of K-Rb [Ni et al., 2008], Cs₂ [Danzl et al., 2008, 2010], Rb₂ [Lang et al., 2008] and Rb-Cs [Nägerl, 2012b].

Heteronuclear alkali molecules in the ro-vibrational ground state possess a permanent dipole moment. This promises a possibility for the realization of a quantum gas with strong dipolar interactions and is one of the main motivations to produce ultracold heteronuclear alkali metal dimers in the absolute ro-vibrational ground state.

Dipolar dimers. Quantum gases consisting of ultracold dipolar molecules might allow the experimental realization of whole new classes of systems with new quantum phases. The interaction of permanent electric dipoles with a $1/r^3$ dependency on distance allows to reach to farther ranges as compared to the $1/r^6$ dependency of atomic van-der-Waals interactions. Further, the relative orientation of dipoles matters for the interaction, in other words the interaction is anisotropic. This is depicted in Fig. 1.1. Here, V_{int} denotes the interaction potential, d the dipole moment and z, r are cylindrical coordinates. As shown, dipoles aligned parallel repel each other while dipoles which are aligned head-to-tail attract themselves. In the drawing, dipole moment vectors are drawn as arrows, while atoms are depicted as filled circles. The orientation of dipole moments, together with a tight confinement perpendicular to the direction of orientation (red ellipse) suppresses the attractive interaction.

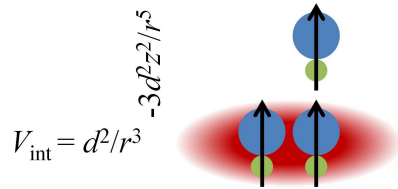


Figure 1.1: Anisotropic dipolar interaction potential V_{int} (cgs units).

Dipolar interactions can not only be realized with molecules, but have also recently been demonstrated in atomic ensembles with Rydberg excitations [Viteau et al., 2011, Schauß et al., 2012]. Further, anisotropic magnetic dipolar interactions have been demonstrated in a Bose-Einstein condensate of Chromium [Griesmaier et al., 2005, Stuhler et al., 2005] and, very recently, Erbium [Aikawa et al., 2012]. In molecules, the

1.1 Ultracold quantum gases

Molecule	[D]	Molecule	[D]	Molecule	[D]
LiNa	0.56	NaK	2.76	KRb	0.61
LiK	3.56	NaRb	3.31	KCs	1.91
LiRb	4.16	NaCs	4.61	RbCs	1.20
LiCs	5.53				

Table 1.1: Permanent dipole moments (in Debye) of heteronuclear alkali metal dimers obtained from an *ab-initio* computation [Aymar and Dulieu, 2005].

vibrational and rotational degrees of freedom allow to tailor the interactions of electric dipoles, which can reach much higher strengths than are realizable in the case of atomic magnetic dipolar interactions [Krems et al., 2009].

The permanent electric dipole moment of a heteronuclear molecule exists due to the different electronegativities of the constituting atoms. For alkali metal dimers, large dipole moments occur only for the shortest equilibrium internuclear distances, that is to say the lowest ro-vibrational excitations in the singlet ground state potentials. In Tab. 1.1 the permanent dipole moments of alkali metal dimers determined from an *ab-initio* computation [Aymar and Dulieu, 2005] are listed.

Without an electric field, however, these permanent dipole moments exist only in the body fixed frame of the molecule. To obtain a dipole moment in the laboratory frame, an electric field needs to be applied. In a quantum mechanical description, the electric field breaks the symmetry of molecular states by mixing states of different parity [Rost et al., 1992, Bohn, 2009]. In this manner, an electric field aligns the dipoles and induces a dipole moment in the laboratory frame. By tuning the electric field strength the induced dipole moment and the dipolar interaction strength can be tuned. In the case of the K-Rb molecule a laboratory frame dipole moment of approximately 0.1 Debye has been reached experimentally [Ni et al., 2008].

Dipolar molecules promise to enable the realization of systems that are of great interest in condensed matter physics. In a quasi two dimensional system and for strongly interacting dipoles oriented in the direction in which excitations are frozen out, a crystalline quantum phase is entered at a sufficiently high phase space density [Li et al., 2008, Petrov et al., 2007, Krems et al., 2009]. Other than in optical lattice systems, phononic excitations could be studied in such a system. Further, in dependence on the dipolar interaction, tuneable by the external DC electric field, a quantum phase transition from a crystalline to a superfluid phase is predicted in 2D geometry. While the superfluid phase is within reach [Pupillo et al., 2008], the phase space densities and dipolar interaction strengths that can be reached with molecular samples today are around two orders of magnitude too low for an experimental observation of the crystalline phase.

Though in itself an interesting subject of study, ultracold chemical reactions can limit the lifetimes of molecular samples severely, especially in the case of bosonic molecules. This constitutes a difficulty in the context of many experiments, which can be overcome by the purely repulsive long-range interactions that can be engineered in two-dimensional systems. Sufficiently strong repulsive interactions prohibit the close encounters of molecules which are needed for chemical reactions to occur, thereby stabilizing molecular samples.

When microwave fields that dress the molecules' rotational energy levels are used in addition, almost arbitrary interaction potential functions can be realized [Büchler et al., 2007a]. Depending on the polarization of the microwave field(s) and the orientation of admixed rotational molecular states, the dipolar interaction can be tailored. In this manner, the experimental realization of a quantum gas system in which three-body interactions dominate over two-body interactions might be within reach [Büchler et al., 2007b, Krems et al., 2009].

Cooling of molecules to ultracold temperatures. One of the greatest experimental challenges is to find and implement appropriate cooling schemes that allow to reach ultracold temperatures with molecular samples. Due to the absence of cycling transitions, it has not proved possible to implement the optical cooling methods, which are used for atomic samples, for the cooling of molecules. Up to today, two possible mechanisms have been demonstrated that allow to obtain molecules at temperatures below the millikelvin regime:

Photoassociation [Krems et al., 2009] occurs when colliding ultracold atoms are excited to an electronically excited molecular state by use of a resonant light field. After the (usually) fast spontaneous decay to states in the ground state potentials, ultracold molecules at a temperature of several ten μK are produced.

At temperatures of several hundred nK, molecules associated at Feshbach resonances are the coldest molecules available and are the only molecules that are produced in a single quantum state. As almost no heating takes place when the molecules are associated, this means that molecules can be produced almost without an increase in entropy. Feshbach molecules are the only molecules for which quantum degeneracy has been reached.

1.2 The ultracold ${}^6\text{Li}$ - ${}^{40}\text{K}$ - ${}^{87}\text{Rb}$ mixture

For the work presented in this thesis a mixture of the three alkali metal species ${}^6\text{Li}$ - ${}^{40}\text{K}$ - ${}^{87}\text{Rb}$ is used. Up to today it is the only three species mixture for which a simultaneous quantum degeneracy of all species has been reached [Taglieber et al., 2008]. While the bosonic species, ${}^{87}\text{Rb}$, is actively cooled by forced evaporation, the fermionic species ${}^6\text{Li}$ and ${}^{40}\text{K}$, which are in thermal contact with each other, are sympathetically cooled [Truscott et al., 2001, Schreck et al., 2001b,a]. From a pure mixture of both fermionic species, which have been cooled to quantum degeneracy by the bosonic species, the first ultracold heteronuclear bosonic Feshbach dimers have been produced [Voigt et al., 2009].

1.2.1 This thesis

This thesis describes experimental as well as theoretical work with an ultracold mixture of ${}^6\text{Li}$ - ${}^{40}\text{K}$. Since the first production of Li-K Feshbach molecules in our group, a major goal has been to achieve coherent transfer from the molecular Feshbach state to the absolute ro-vibrational ground state. In the ro-vibrational ground state of the molecular $X^1\Sigma^+$ potential Li-K molecules are predicted to possess the comparatively strong permanent electric dipole moment of 3.56 D (see Tab. 1.1). A successful coherent ground

1.2 The ultracold ${}^6\text{Li}$ - ${}^{40}\text{K}$ - ${}^{87}\text{Rb}$ mixture

state transfer, together with the high voltage electrodes that have been newly installed in the experimental apparatus, will allow to exploit the molecules' large dipole moment. It is estimated that a laboratory frame dipole moment of approximately 2 Debye can be reached in our experimental setup. This dipole moment is more than one order of magnitude larger than the laboratory frame dipole moment that was achieved with K-Rb [Ni et al., 2008]. The high transfer efficiencies that are predicted will allow the previously reached molecular phase space density to remain unaltered in good approximation. Thus, a molecular quantum gas with unprecedentedly strong dipolar interaction is to be expected. The interaction energy of two Li-K molecules with a laboratory frame dipole moment of 2 Debye in a cubic optical lattice with potential wells separated by 512 nm is approximately 400 nK. This is on the order of the temperature that can be expected for molecules in the ro-vibrational ground state in a three-dimensional bulk gas in our present experimental setup. This thesis describes the detailed experimental and theoretical preparations for the molecular ground state transfer by Stimulated Raman Adiabatic Passage (STIRAP) [Vitanov et al., 2001].

During the time of the experimental work for this thesis, the group and the experimental apparatus moved from LMU Munich to the NUS Singapore. However, the work described in this thesis has been carried out in Munich. The experimental work described in Chap. 4 was finished before the movement and with a fully functional experimental setup here in Munich. The other experimental work described in Chaps. 6, 7 and App. A has been carried out after the movement to Singapore. These chapters describe the experimental preparations made for a laser system for STIRAP and molecular spectroscopy. After completion of these preparations in Munich the finished devices were shipped to Singapore, where they have been integrated into the experimental setup. In order to be able to efficiently approach the Raman transfer the experiment needs to be planned thoroughly. The details of these theoretical preparations are described in Chaps. 2, 3, 5 and 6. As soon as the rebuilding of the experimental setup is complete, Raman ground state transfer of Li-K molecules will be attempted.

1.2.2 Outline of this thesis

The thesis' main part is structured in the following way:

Chapter 2 begins with a brief description of the density and momentum distributions of trapped fermionic and (thermal) bosonic particles in Sec. 2.1. For the Raman transfer of molecules, an accurate knowledge of the Born-Oppenheimer adiabatic potentials of Li-K dimers, the ro-vibronic eigenenergies and the eigenfunctions of bound states within these potentials is very helpful. In Sec. 2.2, publications relating to Li-K molecules are reviewed and the calculations that have been carried out as a part of the work for this thesis are described. These calculations are based on both published and unpublished data of other research groups. Promising electronically excited states via which Raman transfer might be achieved, are selected through an application of the Franck-Condon principle. For these states, existing experimental as well as theoretical data of ${}^7\text{Li}$ - ${}^{39}\text{K}$ as well as ${}^6\text{Li}$ - ${}^{40}\text{K}$ are analyzed. The determination of isotopologue energy shifts allows to gain complete sets of high precision data on the term energies of states in the relevant potentials that were previously selected. Based on these calculations the

wavelengths for Raman transitions between molecular states are predicted in Chap. 5. Ro-vibrational molecular states of the ${}^6\text{Li}$ - ${}^{40}\text{K}$ isotopologue are numerically calculated and the Franck-Condon factors for relevant electronic transitions are determined. In this manner electronically excited molecular states that promise suitable candidates for a STIRAP transfer are found.

Further, scattering properties of atoms and dimers in the Li-K mixture are presented in Sec. 2.3. By comparison with other alkali dimers, a rough estimation for the lifetime of a sample of absolute ground state molecules in a three dimensional bulk gas is made.

In Sec. 2.4, Feshbach resonances are briefly treated and the Asymptotic Bound State Model is introduced. An application of the model allows to determine the spin state in which ${}^6\text{Li}$ - ${}^{40}\text{K}$ molecules are produced at the 155 G resonance. Due to the selection rules of molecular electric dipole transitions, this is important for Raman transfer.

Chapter 3 gives a brief overview over the experimental apparatus used to create a quantum degenerate mixture of the two fermionic, ${}^6\text{Li}$ and ${}^{40}\text{K}$, and the bosonic, ${}^{87}\text{Rb}$, alkali metal species. In Sec. 3.2 the optical trapping of particles by dipole forces is described and applied to estimate the trapping potentials for ${}^6\text{Li}$ and ${}^{40}\text{K}$ atoms as well as ${}^6\text{Li}$ - ${}^{40}\text{K}$ molecules. The change in the trapping potential which the molecules experience when transferred from the highly excited Feshbach state to the absolute ro-vibrational ground state is calculated for typical trap parameters that have previously been used. The imaging of dilute molecule clouds is, except in some special cases, challenging as there exist no closed transitions. Some remarks on this matter are given in Sec. 3.3.

Chapter 4. This chapter describes how the method of cross-dimensional relaxation is used to investigate the scattering properties of ${}^6\text{Li}$ - ${}^{40}\text{K}$ in the vicinity of the Feshbach resonance at 155 G. The measurement allows a precise determination of the position and width of the Feshbach resonance (Sec. 4.4). The magnetic field dependent Li-K scattering cross-sections, which are experimentally determined in Sec. 4.5, follow a Fano resonance function. Further, the dependence of the lifetime on the magnetic field strength, that had previously been determined [Voigt et al., 2009], is discussed for Li-K Feshbach molecules associated at the same resonance.

In chapter 5 the details of a possible STIRAP sequence are described. First, a brief review on STIRAP is given in Sec. 5.1. Then, the wavelengths for the STIRAP lasers are determined based on the calculations presented in Chap. 2. The strengths of relevant electric dipole transitions between molecular states possibly involved in ground state transfer are important for an estimation of laser intensities and coherence times that are needed. Rabi frequencies and an estimate for the duration of STIRAP transfer under realistic experimental conditions is gained. Considerations in respect to the optimization of the STIRAP sequence and the electronically excited levels that are best addressed are mentioned in Sec. 5.3. The photon recoil that is expected from the transfer, as well as the change in the phase space density, that occurs due to an expected change in the optical trapping potential, are briefly estimated in Sec. 5.4.

1.2 The ultracold ${}^6\text{Li}$ - ${}^{40}\text{K}$ - ${}^{87}\text{Rb}$ mixture

Chapter 6 describes how the single photon spectroscopy of electronically excited states (Sec. 6.1) as well as the two-photon spectroscopy of low lying states in the $X^1\Sigma^+$ potential (Sec. 6.3) can be carried out efficiently. Besides being indispensable for the preparation of STIRAP, a precise two-photon spectroscopy allows the determination of the ro-vibrational ground state Stark shift. From this, the molecular dipole moment induced in the laboratory frame in dependency on an applied DC electric field can be determined.

For the use of molecular spectroscopy, the precision of a commercial interferometric laser frequency stabilization is increased to megahertz precision. The stabilization's main advantages are the exceptionally wide in-lock tuning capability together with a high bandwidth frequency stabilization that allows for a fast tuning of lasers. The results of this work, which was done in collaboration with the device's manufacturer¹ are described in Sec. 6.2, while a detailed description of the calibration methods and other technical matters can be found in App. A.

In chapter 7 the preparations for the Raman laser system for ground state transfer are presented. Due to the two very different wavelengths of the Raman lasers needed for ground state STIRAP transfer, the technical realization of a laser system is challenging. Based on the requirements worked out in Chaps. 5 and 6, the design of the Raman laser system is part of this thesis. Two design possibilities are worked out, which are described in Sec. 7.1.

In Sec. 7.2, the construction of the Fabry-Pérot resonator, frequency stabilization of the red Raman laser to the Fabry-Pérot resonator and characterization data is presented. A linewidth of the stabilized Raman laser of approximately 500 Hz and an Allan deviation below 10^{-12} for a duration of > 10 s is demonstrated.

In App. A the details of the (somewhat separate) work carried out in collaboration with TEM Messtechnik is presented. The main focus of this appendix is the calibration procedure that allows to reach frequency deviations as low as 5.7 MHz (rms 1.6 MHz) in the whole wavelength interval 750 – 795 nm. Careful analysis of the calibration data, some of which are gained by means of a frequency comb, and results are presented. This allows to implement several calibration steps that compensate different systematic errors.

¹TEM Messtechnik GmbH, Großer Hillen 38, 30559 Hannover, Germany

Chapter 2

The ultracold Li - K mixture, bound and unbound states

This chapter begins with a brief description of the density and momentum distributions of trapped fermionic and (thermal) bosonic particles in Sec. 2.1. For the Raman transfer of molecules, an accurate knowledge of the Born - Oppenheimer adiabatic potentials of Li - K dimers and the ro - vibronic eigenenergies and the eigenfunctions of bound states within these potentials is very helpful. In Sec. 2.2, publications relating to Li - K molecules are reviewed and calculations based on both published and unpublished data are described. As the labeling of molecular potentials depends on the Hund's coupling cases, the relevant ones for Li - K dimers are described in this context. Promising electronically excited potentials and states via which Raman transfer might be achieved, are selected through an application of the Franck - Condon principle. For these states, existing experimental as well as theoretical data of ${}^7\text{Li} - {}^{39}\text{K}$ as well as ${}^6\text{Li} - {}^{40}\text{K}$ are analyzed. The calculation of isotopologue energy shifts allows to gain complete sets of high precision data on the term energies of states in the relevant potentials that were previously selected. Based on these calculations the wavelengths for Raman transitions between molecular states are predicted in Chap. 5. Further, the data on the vibrational states in the $1^1\Pi$ potential is used to increase the precision of an existing *ab-initio* potential function. Ro - vibrational molecular states of the ${}^6\text{Li} - {}^{40}\text{K}$ isotopologue are numerically calculated and the Franck - Condon factors for relevant electronic transitions are determined. In this manner electronically excited molecular states that promise suitable candidates for a STIRAP transfer are found.

Scattering properties of atoms and dimers in the Li - K mixture are presented in Sec. 2.3. By comparison with other alkali dimers, a rough estimation for the lifetime of a sample of molecules in the absolute ground state is made. Further, possibilities to extend the molecular lifetime are briefly mentioned.

Feshbach resonances are treated in section 2.4. Here, the Asymptotic Bound State Model [Moerdijk et al., 1995, Tiecke et al., 2010] is briefly introduced. The model is applied to the 155 G Li - K Feshbach resonance at which molecules have been associated in our group [Voigt et al., 2009] and their spin state is determined. For the Raman transfer, the spin singlet fraction of the molecular state is a relevant value due to the selection rules for electric dipole transitions between molecular states. The latter are

2.1 Ideal gases in harmonic trap potentials

briefly treated in Chap. 5.

2.1 Ideal gases in harmonic trap potentials

As the particle samples under investigation in typical experimental conditions are dilute and not interacting over long ranges, they often can, to a good approximation, be described as ideal gases. Furthermore, in the case of indistinguishable fermionic particles, the approximation even remains valid in the limit of zero temperature. Bosonic particles condense below a critical temperature, which limits the use of a description as ideal particles because interactions in the condensed fraction cannot be neglected. However, as the bosonic Li-K dimers produced in our group [Voigt et al., 2009] are weakly interacting and dilute, the ideal gas description can be used in good approximation. Further, the experimental trapping potentials can very well be approximated as harmonic. Thus, the treatment of ideal gases in harmonic traps briefly presented here is of importance for the description of the experimental data for both fermionic and bosonic particles, which is mostly gained in the form of absorption images of the gas clouds. For a more detailed description the reader is referred to the review articles [Ketterle et al., 1999, Ketterle and Zwierlein, 2006, Giorgini et al., 2008, Walraven, 2009-2010] and textbooks [Sakurai, 1994, Huang, 1987, Pethick and Smith, 2002].

For the low temperatures that are reached in the experiments, quantum statistics determines the density and momentum distributions of particles. In the grand canonical ensemble, for non-interacting particles, the average occupation $\langle n \rangle$ of the i -th level with energy E_i is

$$\langle n_i \rangle = \frac{1}{e^{\beta(E_i - \mu)} \mp 1} \quad \begin{cases} - \text{ bosons} \\ + \text{ fermions} \end{cases} \quad (2.1)$$

Here, the chemical potential μ is fixed by the particle number $N = \sum_i \langle n_i \rangle$. The inverse of the thermal energy is denoted as $\beta \equiv 1/k_B T$. Here and in the following, the upper sign is for bosons, the lower one for fermions. The assumption that the energy level spacing is much smaller than the thermal energy of the particles $\Delta E_{i+1} - E_i \ll k_B T$ allows a quantum statistical description in phase-space. Continuous variables $\{\mathbf{r}, \mathbf{p}\}$ and a continuous density of states are introduced. With this, the occupation of a phase-space cell is

$$f(\mathbf{r}, \mathbf{p}) = \frac{1}{e^{\beta(E(\mathbf{r}, \mathbf{p}) - \mu)} \mp 1} \quad , \quad (2.2)$$

while each cell has the size of Planck's constant cubed h^3 . Integration of this expression over momentum space yields the density distribution of an ideal gas in an arbitrary trapping potential $V(\mathbf{r})$:

$$n(\mathbf{r}) = \pm \frac{1}{\lambda_{dB}^3} g_{3/2} \left(\pm e^{\beta(\mu - V(\mathbf{r}))} \right) \quad . \quad (2.3)$$

Here, $\lambda_{dB} = \sqrt{\frac{\beta 2\pi\hbar^2}{m}}$ is the thermal de Broglie wavelength with the particle mass m and $g_{3/2}$ is the three-half-order Polylogarithm. A common definition of the n -th order Polylogarithm is

$$g_n(z) = \sum_{k=1}^{\infty} \frac{z^k}{k^n} \quad . \quad (2.4)$$

2. The ultracold Li - K mixture, bound and unbound states

For the specific case of an harmonic trapping potential

$$V(\mathbf{r}) = \frac{1}{2}m(\omega_x^2 x^2 + \omega_y^2 y^2 + \omega_z^2 z^2) \quad (2.5)$$

with oscillator frequencies $\omega_{x,y,z}$, an integration over real space can also be performed. This yields the momentum distribution of the trapped particles:

$$n(\mathbf{p}) = \pm \prod_i \left(\frac{1}{(m\lambda_{dB})^3 w_i} \right) g_{3/2} \left(\pm e^{\beta(\mu - p^2/2m)} \right). \quad (2.6)$$

Here, the oscillator frequencies ω_i of the three spacial dimensions are multiplied yielding a mean trapping frequency cubed $\bar{\omega}^3 = \omega_x \omega_y \omega_z$.

In the classical limit of high temperature, one obtains a Gaussian density distribution of N particles in the harmonic trapping potential

$$n_{cl}(\mathbf{r}) = \prod_i \left(\frac{N}{\pi^{3/2} \sigma_i} \right) e^{-\sum_i r_i^2 / \sigma_i^2} \quad \text{with} \quad \sigma_i^2 = \frac{2}{\beta m \omega_i^2} \quad (2.7)$$

from Eq. 2.3.

In the case of fermionic particles this Gaussian density distribution smoothly changes into a distribution characterized by a sharp edge, when the temperature is lowered towards $T = 0$ K. In the fermionic case of zero temperature all the phase space cells below a fermi surface are occupied by exactly one particle, while above the fermi surface, phase space cells are not occupied:

$$f(\mathbf{r}, \mathbf{p}) = \frac{1}{e^{\beta(E(\mathbf{r}, \mathbf{p}) - \mu)} + 1} \xrightarrow{T \rightarrow 0} \begin{cases} 1, & E(\mathbf{r}, \mathbf{p}) < \mu \\ 0, & E(\mathbf{r}, \mathbf{p}) > \mu. \end{cases} \quad (2.8)$$

In this case, the chemical potential is equal to the highest particle energy in the system, which is also called the Fermi energy E_F . For the harmonic potential (Eq. 2.5), the Fermi energy is

$$E_F = k_B T_F = \hbar \left(6N \prod_i \omega_i \right)^{1/3}, \quad (2.9)$$

which is intuitive. All the particles are ‘‘piled up’’ in the harmonic oscillator energy levels $\hbar\omega$. Thus, the highest energy is fixed by the particle number. The density distribution in the zero temperature limit is an inverted parabola with Fermi radii R_i :

$$n_{T=0}(\mathbf{r}) = \prod_i \left(\frac{8N}{\pi^2 R_i} \right) \left(\max \left[1 - \sum_i \frac{r_i^2}{R_i^2}, 0 \right] \right) \quad \text{with} \quad R_i = \sqrt{\frac{2E_F}{m\omega_i^2}}. \quad (2.10)$$

Thus, in contradiction to a classical gas, the radius of the trapped particle cloud does not approach zero in the limit of $T \rightarrow 0$ and the phase space density is not divergent.

The degeneracy parameter $1/(\beta E_F) = T/T_F$, which is a useful quantity for thermometry and the characterization of gases, can be calculated analytically for harmonic trap potentials. At a degeneracy parameter of around 0.5, the fermi gas changes its

2.1 Ideal gases in harmonic trap potentials

character from a classical gas to a quantum gas. T/T_F is found from an integration of Eq. 2.3 with potential 2.5, which yields the total particle number:

$$N = -\frac{1}{\beta^3 \hbar^3 \prod_i (\omega_i)} g_3(-e^{\beta\mu}) . \quad (2.11)$$

In combination with Eq. 2.9, the expression for the degeneracy parameter is found:

$$\frac{T}{T_F} = \left(\frac{-1}{6 g_3(-e^{\beta\mu})} \right)^{1/3} . \quad (2.12)$$

Bosons form a Bose-Einstein condensate when the temperature is lowered towards zero, which is connected with a phase transition. For the condensed state of typical gas samples of bosonic alkali metal atoms or molecules consisting of these atoms, the interaction cannot be neglected due to the high densities. The ideal gas is in this case of less direct experimental relevance and will not be treated here in more detail. The mean field description of Bose-Einstein condensates by the Gross-Pitaevskii equation is described in detail in [Pethick and Smith, 2002].

Usually, as the cloud size in trap is too small to obtain absorption images with high resolution without using elaborate optical imaging systems, the clouds are expanded prior to imaging (time-of-flight, “tof” imaging [Ketterle et al., 1999]). Furthermore, clouds can be very dense, which prohibits a good signal to noise ratio when imaging without expansion. For tof imaging, the trapping potential is abruptly shut off. In the case of dilute thermal particle clouds, as well as in the case of indistinguishable fermions, the expansion can be approximated as ballistic to a very good approximation. This means that each particle follows the trajectory it is on in the moment the trapping potential is shut off, without an interaction with other particles. In this case the density distribution 2.3 is just scaled by a time dependent factor:

$$b_i(t) = \sqrt{1 + \omega_i^2 t^2} . \quad (2.13)$$

Here, b_i is the scaling factor for the i -th dimension. From this scaling of Eq. 2.3 results the time dependent density distribution during free ballistic expansion:

$$n_{\text{tof}}(\mathbf{r}, t) = \pm \frac{1}{\lambda_{\text{dB}}^3} \prod_i \left(\frac{1}{b_i(t)} \right) g_{3/2} \left(\pm e^{\beta(\mu - m/2 \sum_i (\omega_i r_i / b_i)^2)} \right) \quad (2.14)$$

$$\simeq \pm \frac{1}{\lambda_{\text{dB}}^3} g_{3/2} \left(\pm e^{\beta(\mu - m \mathbf{r}^2 / 2 t^2)} \right) . \quad (2.15)$$

$t \gg 1/\omega_i$

It is to be emphasized here that this treatment describes a system in thermal equilibrium. Thus, for expansion times long compared to the trapping periods, this tof density distribution reflects the intra trap momentum distribution, which is isotropic.

With this the section about trapped quantum gases is concluded. The following section treats some basics on relevant molecular physics, Li-K interaction potentials and bound states in the context of a coherent state transfer of Feshbach molecules.

2.2 Li - K interaction potentials and bound states

When a pair of lithium and potassium atoms closely approach each other they start to interact. At separations large compared to the Bohr radius the interaction is well described by a van der Waals potential. With the interatomic separation getting smaller, the exchange interaction starts to be significant. Thus, for not too small separations, the long range (LR) interaction potential can roughly be described by

$$U_{\text{LR}}(r) = -\frac{C_6}{r^6} - \frac{C_8}{r^8} \pm E_{\text{exch}} \quad (2.16)$$

with $E_{\text{exch}}(r) = A_{\text{exch}} r^\gamma e^{-\beta r}$.

Here, C_6 and C_8 are van der Waals coefficients, while E_{exch} denotes the exchange energy which is parameterized by $A_{\text{exch}}, \gamma, \beta$ [Zemke and Stwalley, 1999, Tiemann et al., 2009]. Values of Li - K C_6 and C_8 coefficients can e.g. be found in [Tang et al., 1976, Movre and Beuc, 1985, Bussery et al., 1987, Derevianko et al., 1999, Ridinger et al., 2011]. The sign of the exchange interaction depends on the spin state of the valence electrons, where the sign is positive for triplet and negative for singlet states. Thus, the interaction of polarized atoms is far weaker at intermediate distances.

At very short distances, the short range (SR) interaction of the positively charged atomic cores dominates. This can be described by a function of the type of Eq.2.17 [Tiemann et al., 2009, Derevianko et al., 1999]:

$$U_{\text{SR}}(r) = A + \frac{B}{r^N} \quad (2.17)$$

with the parameters A, B and N . It is to be emphasized that Eqns.2.16,2.17 allow only a very rough description of the potential curves.

In the following section the potentials of the electronic ground state (K(4s) - Li(2s)), as well as the potentials in which one of the atoms has been electronically excited via a D line transition (K(4p) - Li(2s) and K(4s) - Li(2p)) will be treated. Energies of bound states within these potentials are calculated.

2.2.1 States of alkali metal dimers

In molecules the spherical symmetry of the atom is broken and in the present case of dimers replaced by a cylindrical symmetry. The coupling strengths of a molecule's different angular momenta with each other and to this symmetry axis were first described by Hund [Hund, 1926, Herzberg and Huber, 1950, Carr et al., 2009] and are called Hund's coupling cases. 5 coupling cases (a) - (e) are distinguished, each of which is characterized by a set of different quantum numbers. As molecular states are labeled by good quantum numbers, this means that molecular states are labeled differently for each coupling case. What coupling case a molecule belongs to depends on the separation of the nuclei in the molecule as well as on the types of atoms involved. Hund's coupling cases (a), (b) and (c) are relevant for alkali metal dimers. These are briefly described in the following.

Hund's coupling cases

Hund's case (a) is a good approximation for the coupling of orbital angular momenta at short interatomic separations in the Li - K molecule. A sketch of case (a) is shown in

2.2 Li- K interaction potentials and bound states

Fig. 2.1(a). The total angular momentum of the molecule is denoted by \mathbf{J} . It consists of the angular momentum due to the rotation of the molecule perpendicular to the internuclear axis \mathbf{N} which is coupled to the projection of the total angular momentum of the electron cloud onto the internuclear axis $\mathbf{\Omega}$. \mathbf{S} and \mathbf{L} are the spin and orbital angular momenta of the electron cloud. Both these electronic angular momenta are assumed to be strongly coupled to the internuclear axis, while the coupling to \mathbf{N} is assumed to be weak. Λ is the modulus of the projection of \mathbf{L} onto the internuclear axis, and thus always positive. Σ , the quantum number for the projection of \mathbf{S} onto the internuclear axis, can however be positive or negative. $\Omega = |\Lambda + \Sigma|$ denotes the quantum number of the resulting total angular momentum of the electron cloud in direction of the internuclear axis. Only \mathbf{J} is constant. There is a slow nutation of $\mathbf{\Omega}$ and \mathbf{N} about \mathbf{J} , while \mathbf{L} and \mathbf{S} precess fast about the internuclear axis. In Hund's case (a) there are four good quantum numbers: Λ, S, Σ and Ω . Here, S denotes the quantum number referring to the total spin of the electron cloud.

Hund's case (b) describes states in which $S > 0$ but $\mathbf{L} = \mathbf{0}$ in the case of the Li-K molecule. In this case, no coupling of the spin of the electron cloud \mathbf{S} to the internuclear axis exists. \mathbf{N} and \mathbf{S} are coupled to form a resulting \mathbf{J} .

Specification of molecular states in Hund's cases (a) and (b). In the coupling cases (a) and (b) the molecular states are specified by:

$$i^{2S+1} \Lambda_{g,u}^{\pm} . \quad (2.18)$$

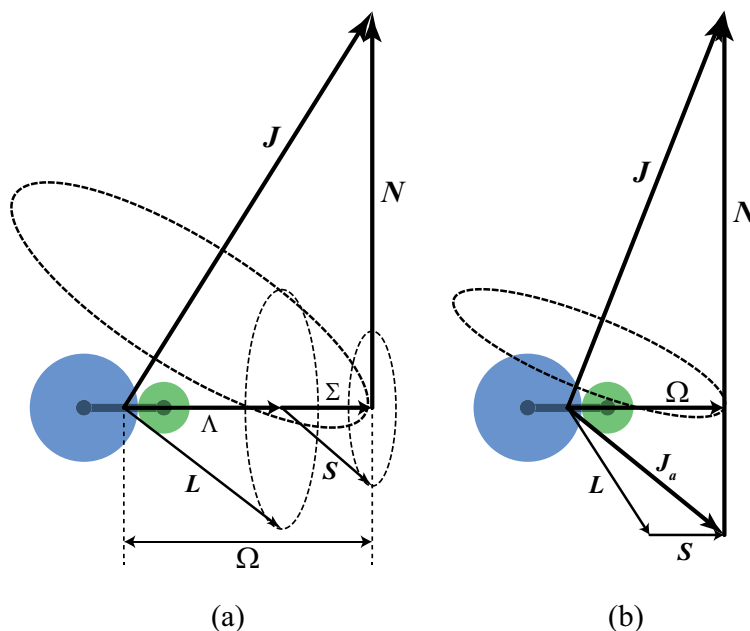


Figure 2.1: Two relevant coupling cases for the Li-K molecule. (a): Hund's case (a) holds well for short internuclear separations and $\Lambda > 0$, (b): Hund's case (c) describes the coupling at large internuclear separations.

2. The ultracold Li - K mixture, bound and unbound states

Here, Λ is defined as above, for which Greek capital letters are used to specify: $\Lambda = 0 \equiv \Sigma$, $\Lambda = 1 \equiv \Pi$, $\Lambda = 2 \equiv \Delta$, and so on. Thus, in the case of alkali metal dimers, coupling case (b) always refers to Σ states. $2S + 1$ is the multiplicity of the electronic state, while \pm denotes the parity with respect to a reflection of the molecule's complete wavefunction at a plane containing the internuclear axis. i labels the electronic excitation of the molecule, on which molecular potentials depend in addition to the electronic angular momentum state. With the exception of the ground state potentials which are commonly labeled "X" (singlet) and "a" (triplet), numbers or letters are commonly given in the order of increasing electronic excitation. Within this thesis, sets of numbers are chosen to label the electronically excited potentials. The specification g, u is only given for completeness here as it is only defined for homonuclear molecules. Thus, it is not specified in the present case of Li-K molecules. It denotes the symmetry with respect to a point reflection of the wavefunction.

Hund's case (c) is a good approximation for the coupling of orbital angular momenta at large interatomic separations in the Li-K molecule. In this case the coupling between \mathbf{L} and \mathbf{S} is stronger than their respective couplings to the internuclear axis. A sketch of case (c) is shown in Fig. 2.1(b). Together, \mathbf{L} and \mathbf{S} are coupled to a vector called \mathbf{J}_a whose projection onto the internuclear axis is again $\mathbf{\Omega}$. These latter vectors are coupled to from a resulting \mathbf{J} . In this case the only good remaining quantum number is $\Omega = |\mathbf{\Omega}|$. Molecular states are labeled by

$$\Omega_{g,u}^{\pm} \tag{2.19}$$

where \pm and g, u are defined as explained in Hund's case (a).

Hund's cases (d) and (e) will not be treated here as they are not of importance for the Li-K molecule. The interested reader may find a description in [Herzberg and Huber, 1950].

2.2.2 Adiabatic Li-K potentials

As the solution of the many particle problem containing the interactions of all electrons and the positively charged cores is not possible for almost all cases, some approximations have to be made. In the Born-Oppenheimer approximation [Sakurai, 1994, Herzberg and Huber, 1950] it is assumed that the electrons adiabatically follow the motion of the much heavier nuclei. With this assumption the wavefunctions of valence electrons and atomic cores separate. The obtained potentials are called adiabatic potentials. For the present case of dimers the relative motion of the atoms is studied by the introduction of a particle with the reduced mass moving in an adiabatic potential. In the treatment described here, as well as in the cited publications, spin orbit interactions are neglected.

Fortunately, there exists rather accurate published data on molecular potentials of Li-K [Busseret et al., 1987, Tiemann et al., 2009, Bednarska et al., 1998, Grochola et al., 2002, 2003, Jastrzebski et al., 2001, Martin et al., 2001, Rousseau et al., 1999, Allouche, 2011, Pashov et al., 1998, Aymar and Dulieu, 2005]. In Fig. 2.2 all singlet and triplet potentials dissociating to K(4s)-Li(2s), K(4p)-Li(2s), K(4s)-Li(2p) are shown. The potential functions are obtained from an *ab-initio* calculation [Allouche, 2011]. While

2.2 Li - K interaction potentials and bound states

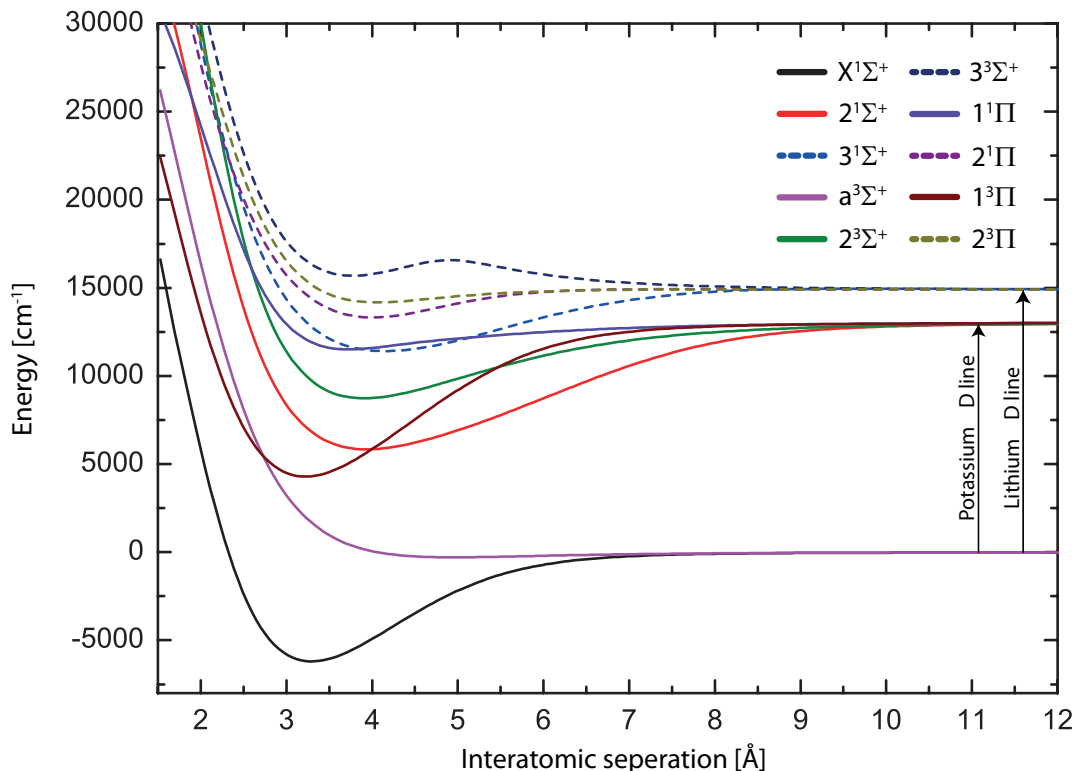


Figure 2.2: Adiabatic Li - K potentials from an *ab-initio* calculation [Rousseau et al., 1999, Allouche, 2011]. Potentials are marked with Hund's case (a) labels. All potentials dissociating to the three lowest asymptotes K(4s)-Li(2s), K(4p)-Li(2s), K(4s)-Li(2p) are shown.

for the ground state there are two, singlet and triplet potential curves dissociating to the same K(4s)-Li(2s) asymptote, there are four potentials dissociating to each of the two electronically excited asymptotes K(4p)-Li(2s) and K(4s)-Li(2p). Of these four potentials there are singlet and triplet states for each $\Lambda = 0$ and $\Lambda = 1$ corresponding to Σ and Π potentials respectively. Almost all of the potentials contain states which are strongly perturbed due to avoided crossings. Further, due to repulsive C_6 coefficients, all potentials dissociating to the K(4s)-Li(2p) asymptote are found to display a local maximum higher than the potentials' asymptotes [Wang and Stwalley, 1998]. In the case of the $3^3\Sigma^+$ potential the very large maximum is obvious, even at this rough energy scale. As a consequence, these states are not suitable for photoassociation [Wang and Stwalley, 1998]. Potentials dissociating to the K(4p)-Li(2s) asymptote do not show this behaviour. For these, the potential functions monotonously decrease from the asymptotes to the potentials' global minima. Typically something on the order of 20-60 vibrational eigenstates exist in each of the shown potentials.

2.2.3 The Franck - Condon principle

Relevant for the strengths of transitions between vibrational energy levels in different potentials is the overlap integral between the wavefunctions of the states that are involved.

2. The ultracold Li - K mixture, bound and unbound states

The modulus squared of such a value is called Franck - Condon factor. As a two-photon Raman transition involves three states, the value of both Franck - Condon factors multiplied is to be optimized in this case. This is however not strictly true in the case of STIRAP, as is described in Chap. 5. In order to maximize the transition strength, an excited potential (see Fig. 2.2) needs to be selected that contains an energy level whose wavefunction has a sufficiently large overlap integral with both the vibrationally highly excited molecular state and the ground state of the $X^1\Sigma^+$ potential.

The Franck - Condon principle states that the electronic transition takes place on a much faster timescale than the vibrational motion of the atomic cores [Herzberg and Huber, 1950]. This means that the cores after the electronic transition have almost

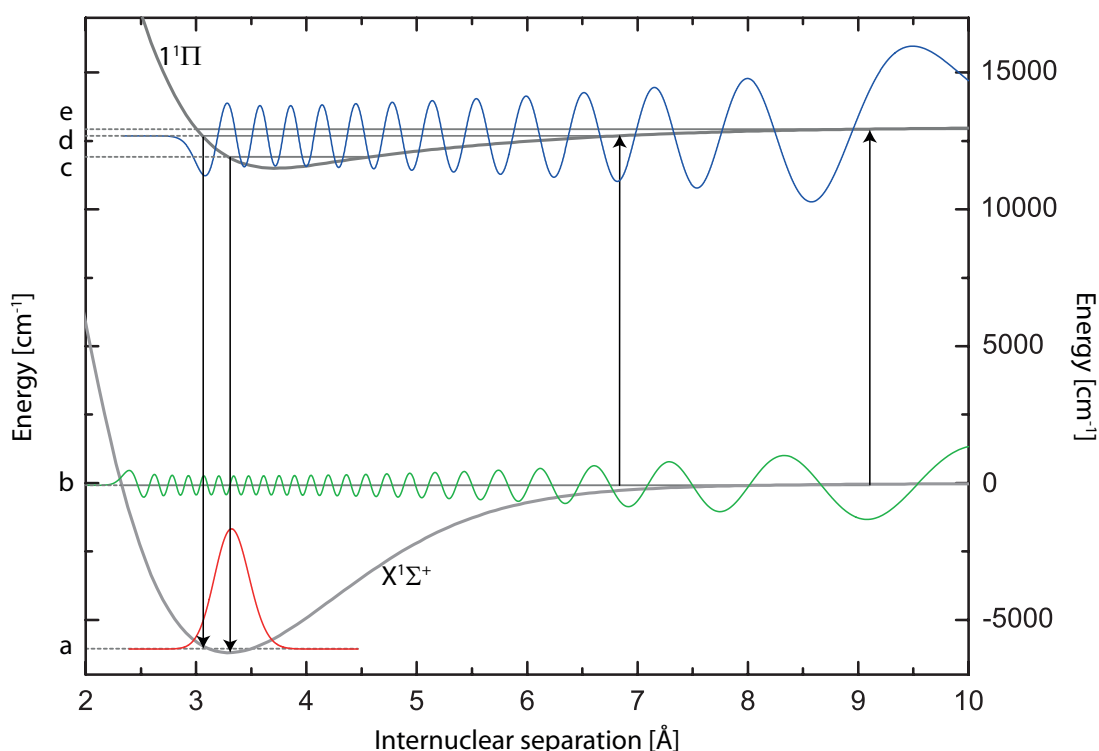


Figure 2.3: Franck - Condon principle applied to the excited potentials shown in Fig. 2.2. The best multiplied Franck - Condon factors are estimated for vibrational energy levels in the $1^1\Pi$ potential. Arrows indicate transitions, while horizontal lines mark energy levels a - e. Wavefunctions were calculated with Robert J. Le Roy's computer program [LeRoy, 2007]. Three wavefunctions are shown: the absolute ground state wavefunction (red), the wavefunction of the vibrationally most highly excited state close to the asymptote in the $X^1\Sigma^+$ potential (green) and a wavefunction in the electronically excited $1^1\Pi$ potential (blue). No attention to wavefunction normalization has been paid. Horizontal lines in the $1^1\Pi$ potential indicate energy levels for which the wavefunction overlap integral with either the excited state wavefunction (green) or the ground state wavefunction (red) in the $X^1\Sigma^+$ potential is optimized. The overall Franck - Condon factor is maximized by the intermediate level d, for which the wavefunction in blue is shown.

2.2 Li- K interaction potentials and bound states

the same locations and velocities. A transition is much more likely, the better the velocities and locations for the initial and final states match. This is illustrated in Fig. 2.3: Classically, a particle with zero kinetic energy in the $X^1\Sigma^+$ potential rests at its bottom. It has a total energy very close to the quantum mechanical ground state energy a . In the $1^1\Pi$ potential a particle with energy c has its left turning point at exactly the same location. Thus, the transition from energy levels c to a has a good chance of occurring when the particle in energy level c is at its inner classical turning point. A more thorough quantum mechanical description still yields the result that the best wavefunction overlap integral will be between vibrational energy levels a and c . It is to be noted that due to the relative displacement of the potential minima the excited state having the best wavefunction overlap integral with the ground state is not the ground state in the $1^1\Pi$ potential.

A particle in the highly excited vibrational state b spends most of the time at large internuclear separations. The missing normalization of the shown wavefunction of level b might be a little misleading here, but was chosen for better visibility. In fact, most of the wavefunction's amplitude is at internuclear separations larger than 10 \AA (see Fig. 2.9). From the Franck-Condon principle applied here follows that the wavefunction of the highly excited level e has the largest overlap integral with the wavefunction of level b .

From the preceding arguments it will be clear that an intermediate level in the $1^1\Pi$ potential with energy d will maximize the multiplied Franck-Condon factor $|\langle a|d\rangle|^2 \cdot |\langle d|b\rangle|^2$. For a two-photon Raman transition from $|b\rangle$ to $|a\rangle$ via $|d\rangle$, this value needs to be optimized.

The choice of an excited potential

The choice of which electronically state in which electronically excited potential is best addressed for STIRAP depends mostly on the strengths of transitions between the initial, intermediate and target states. Due to the selection rules (see Chap. 5), triplet potentials are excluded for transitions to the absolute ro-vibrational singlet ground state, as singlet-triplet electric dipole transitions are prohibited. However, as previously mentioned, states in the electronically excited potentials perturb one another. This leads to a mixing of the perturbed states, that is to say one state inherits properties of the other and vice versa. The perturbation of states with different multiplicity is usually weak, as there exists a "selection rule" that prohibits it [Herzberg and Huber, 1950]. Nevertheless, the mutual perturbation of states in the $1^1\Pi$ and $2^3\Sigma^+$ states of K-Rb was of utter importance for the STIRAP transfer of Feshbach molecules [Ni et al., 2008]. These latter were produced in a pure triplet state and only the admixture due to the perturbation of a singlet state allowed the two-photon transfer into the absolute singlet ro-vibrational ground state. As is shown in Sec. 2.4, the state of the Li-K molecules produced at the 155 G resonance, contains a comparatively large singlet fraction. Thus, for the ground state transfer, no further mixing of singlet and triplet states in the electronically excited state is needed. In the case of Li-K molecules, no extensive data on the perturbation of electronically excited states exists and prior to attempting STIRAP, states will need to be spectroscopically characterized to some extent (see Chap. 6).

In order to select an electronically excited potential out of the remaining four possible choices ($2^1\Sigma^+$, $3^1\Sigma^+$, $1^1\Pi$, $2^1\Pi$ potentials), the Franck-Condon principle can be applied.

2. The ultracold Li - K mixture, bound and unbound states

In order to maximize the overall wavefunction overlap integral, it is clear from Fig. 2.3 that an excited potential is needed for which the difference in energy between levels c and e is as small as possible. This means that the excited potential's minimum needs to be at higher internuclear separations relative to the minimum of the $X^1\Sigma^+$ potential. Further, potentials with longer range have better wavefunction overlap integrals for highly excited states. It follows from a comparison of the potential functions shown in Fig. 2.2 that these last requirements are well met by the $1^1\Pi$ potential. Some of the strongest molecular transitions of Li - K occur between states in the $X^1\Sigma^+$ and $1^1\Pi$ potentials (see Sec. 3.3).

2.2.4 Eigenstates in the $X^1\Sigma^+$ and $1^1\Pi$ potentials

Fortunately, accurate spectroscopic data for ro-vibrational energy levels in both the $X^1\Sigma^+$ and $1^1\Pi$ potentials of ${}^6\text{Li}-{}^{39}\text{K}$ are available. These data cover almost the entire energy range of the potentials. Thus, the transition frequencies between relevant vibrational energy levels have been experimentally determined with high accuracy. While the term energies are listed here, the transition frequencies which are determined based on the term energies are listed in Chap. 5. The $X^1\Sigma^+$ potential is perturbed by the $a^3\Sigma^+$ potential [Tiemann et al., 2009], while the $1^1\Pi$ potential is perturbed by $3^1\Sigma^+$ potential [Jastrzebski et al., 2001]. This makes the experimental data even more valuable for a precise determination of transition frequencies which will allow to experimentally approach the Li - K molecular spectroscopy (see Chap. 6) in a fast and efficient manner. However, in order to be able to predict which energy levels promise the largest Franck - Condon factors, wavefunctions have to be determined. In the following, Robert J. LeRoy's Fortran program [LeRoy, 2007] is used to numerically calculate term energies, wavefunctions and Franck - Condon factors.

As described in Chap. 5, it might be beneficial to address electronically excited states in potentials other than the $1^1\Pi$. This section will however be limited to states with $J = 1$ in the $1^1\Pi$ potential and states with $J = 0$ in the $X^1\Sigma^+$ potential.

The $X^1\Sigma^+$ potential

The most accurate Li - K data available to date exists for the $X^1\Sigma^+$ and $a^3\Sigma^+$ potentials [Tiemann et al., 2009]. Using the ${}^6\text{Li}-{}^{39}\text{K}$ and ${}^7\text{Li}-{}^{39}\text{K}$ $X^1\Sigma^+$ potentials given in [Tiemann et al., 2009], the vibrational term energies and wavefunctions for both isotopologues are determined. The vibrational term energies are given in Tab. 2.1. All level energies given are for the non-rotating case $N = 0$. Only for the highest vibrationally excited state, the experimental value given in [Tiecke et al., 2010] is taken. The value determined from the calculation using the potential function agrees to 300 MHz with the very precisely known experimental value [Tiecke et al., 2010]. A comparison of all these calculated vibrational energy levels to spectroscopic data (supplement of [Tiemann et al., 2009]) shows excellent agreement, with all deviations on the order of the experimental uncertainty of the spectroscopic data. Thus, also the wavefunctions that are calculated in the following section are expected to be of very good accuracy. The difference in reduced masses between that isotopologues ${}^6\text{Li}-{}^{39}\text{K}$ and ${}^6\text{Li}-{}^{40}\text{K}$ is $<1\%$, while the difference between ${}^6\text{Li}-{}^{39}\text{K}$ and ${}^7\text{Li}-{}^{39}\text{K}$ is comparatively large as it differs by 12%. Thus, also the vibrational energies of ${}^6\text{Li}-{}^{39}\text{K}$ and ${}^6\text{Li}-{}^{40}\text{K}$ are expected to be almost the same,

2.2 Li- K interaction potentials and bound states

whereas the term energies of ${}^6\text{Li}-{}^{39}\text{K}$ and ${}^7\text{Li}-{}^{39}\text{K}$ are expected to differ relevantly. In Fig. 2.4 the level energies for both the ${}^6\text{Li}-{}^{39}\text{K}$ and ${}^7\text{Li}-{}^{39}\text{K}$ isotopologues depending on the vibrational excitation is shown. The inset shows the difference between level energies of the isotopologues.

As indicated in Chap. 1, dipole moments of molecular states in the laboratory frame are induced by mixing states of opposite parity. The energy level spacing of the states of opposite parity sets the electric field strengths that must be applied to reach sufficient mixing. In this context, the rotational constants B of states in the $X^1\Sigma^+$ potential are of interest. An approximation with the well known formula for the energy levels of a quantum mechanical rigid rotator [Herzberg and Huber, 1950],

$$F^i(J) = B J(J + 1) \quad (2.20)$$

yields $B = 0.29 \text{ cm}^{-1} = 8.8 \text{ GHz}$ for the first rotational state. Here, F^i are the rotational term energies of the i -th vibrational level.

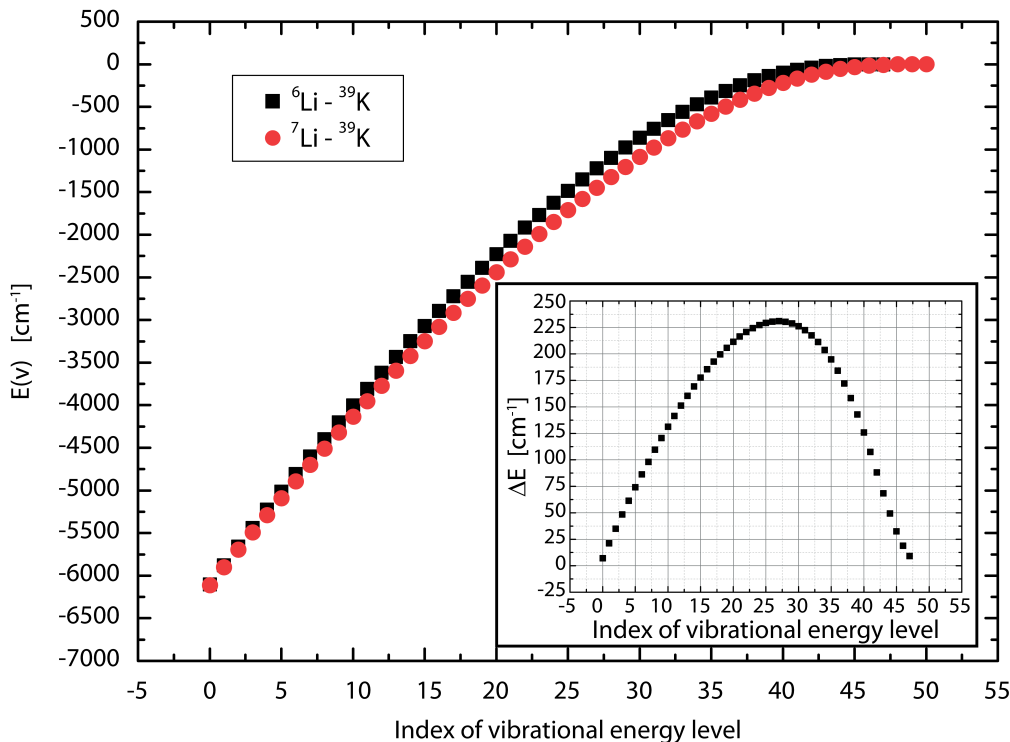


Figure 2.4: Energies of vibrational states in the $X^1\Sigma^+$ potential for ${}^6\text{Li}-{}^{39}\text{K}$ (black squares) and ${}^7\text{Li}-{}^{39}\text{K}$ (red circles). The inset shows the difference in term energies between the two isotopologues. The largest difference of 230.95 cm^{-1} occurs for the energy level with vibrational index $v = 27$. Three more vibrational levels exist for the isotopologue ${}^7\text{Li}-{}^{39}\text{K}$ than for ${}^6\text{Li}-{}^{39}\text{K}$.

2. The ultracold Li - K mixture, bound and unbound states

v	E(v) [cm ⁻¹]						
0	-6104.0393	12	-3619.2217	24	-1624.4067	36	-314.4421
1	-5880.4413	13	-3432.6988	25	-1484.9679	37	-247.8304
2	-5659.7547	14	-3249.5786	26	-1350.3050	38	-189.1456
3	-5441.9980	15	-3069.9311	27	-1220.6022	39	-138.6560
4	-5227.1948	16	-2893.8322	28	-1096.0577	40	-96.5588
5	-5015.3730	17	-2721.3650	29	-976.8854	41	-62.9182
6	-4806.5647	18	-2552.6194	30	-863.3148	42	-37.5639
7	-4600.8050	19	-2387.6935	31	-755.5921	43	-19.9487
8	-4398.1330	20	-2226.6936	32	-653.9802	44	-8.9770
9	-4198.5907	21	-2069.7349	33	-558.7585	45	-3.0831
10	-4002.2242	22	-1916.9422	34	-470.2219	46	-0.6068
11	-3809.0831	23	-1768.4508	35	-388.6778	47	-0.0238

Table 2.1: Non-rotating vibrational energy levels in the $X^1\Sigma^+$ potential of ${}^6\text{Li}-{}^{39}\text{K}$. v denotes the vibrational quantum number. Due to the small difference in reduced mass, these eigenenergies are expected to differ not more than the experimental accuracy of about $\pm 0.02 \text{ cm}^{-1} \simeq 600 \text{ MHz}$ from the eigenenergies of ${}^6\text{Li}-{}^{40}\text{K}$ [Tiemann et al., 2009]. The potential's asymptote is at 0 cm^{-1} . The value for the vibrationally highest excited state is taken from [Tiecke et al., 2010].

The $1^1\Pi$ potential

Even though a precise potential curve up to the asymptote has not been constructed up to date, precise experimental data for the vibrational energy levels in the $1^1\Pi$ potential exists [Pashov et al., 1998, Kowalczyk, 2012, Ridinger et al., 2011]. In Tab. 2.2 a complete set of vibrational energy levels in the $1^1\Pi$ potential of the ${}^6\text{Li}-{}^{40}\text{K}$ isotopologue

v	E(v) [cm ⁻¹]	v	E(v) [cm ⁻¹]	v	E(v) [cm ⁻¹]	v	E(v) [cm ⁻¹]
0	11428.09	9	12348.25	18	12815.26	27	13011.2
1	11567.18	10	12415.12	19	12848.6	28	13020.3
2	11697.20	11	12477.71	20	12879.2	29	13027.7
3	11816.80	12	12536.35	21	12906.5	30	13032.4449
4	11925.95	13	12591.25	22	12930.7	31	13037.6439
5	12025.38	14	12642.61	23	12952.0	32	13041.0752
6	12116.20	15	12690.60	24	12970.5	33	13042.4138
7	12199.58	16	12735.36	25	12986.4	34	13042.8495
8	12276.63	17	12776.97	26	12999.9		

Table 2.2: Complete set of ${}^6\text{Li}-{}^{40}\text{K}$ vibrational energy levels with $J = 1$ in the $1^1\Pi$ potential. Levels 0-18: Mass scaled Dunham expansion (Eq. 2.21). For these levels an accuracy of $\pm 0.7 \text{ cm}^{-1}$ can be estimated. Levels 19-29 are obtained from an interpolation by the fit function shown in Fig. 2.5. For these levels an accuracy of $\pm 5 \text{ cm}^{-1}$ is estimated. Levels 30-34 are taken from [Ridinger et al., 2011]. For these an accuracy of $\pm 0.004 \text{ cm}^{-1}$ is specified. The asymptote of the $1^1\Pi$ potential is at the potassium D2 line transition energy, $13042.8942 \text{ cm}^{-1}$.

2.2 Li- K interaction potentials and bound states

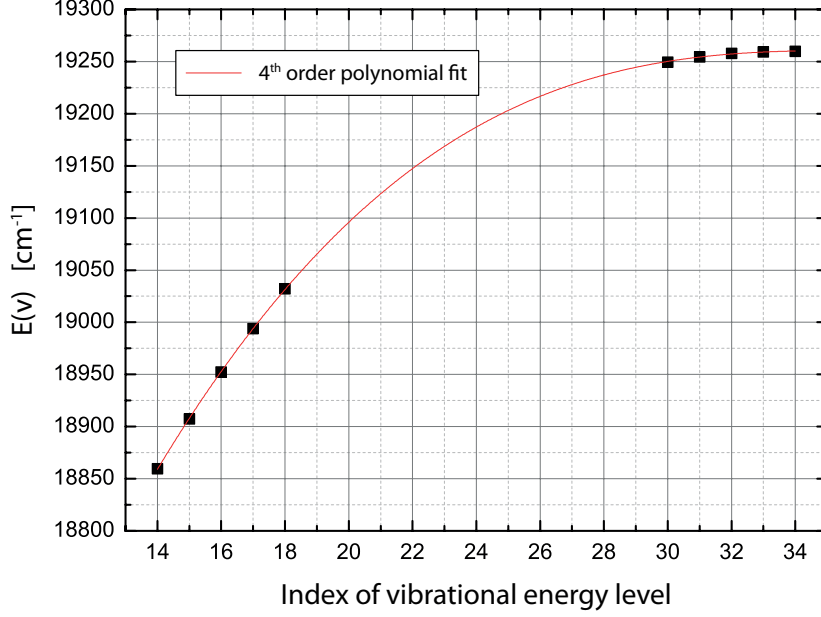


Figure 2.5: Interpolation with which the energies of the vibrational states 19-29 for the ${}^6\text{Li}-{}^{40}\text{K}$ isotopologue are determined. Adjacent data points are fit with a fourth order polynomial.

is listed. The following describes how term energies are obtained. At first the ${}^6\text{Li}-{}^{40}\text{K}$ isotopologue is treated, then ${}^7\text{Li}-{}^{39}\text{K}$.

The vibrational term energies given in Tab. 2.2 are those of the lowest rotational state, $J = 1$, of the ${}^6\text{Li}-{}^{40}\text{K}$ isotopologue. Due to the different sources of the data, different energy levels are known with different precision. While the term energies of the levels 30-34 were directly measured with high precision for the ${}^6\text{Li}-{}^{40}\text{K}$ isotopologue [Ridinger et al., 2011], all other values are obtained from data of the ${}^7\text{Li}-{}^{39}\text{K}$ isotopologue, for which isotopologue shifts are calculated. In [Pashov et al., 1998] Dunham expansion coefficients for levels 0-18 of the ${}^7\text{Li}-{}^{39}\text{K}$ isotopologue are given. These coefficients are mass scaled to obtain the isotopologue shift. The shifted term energies $T(v, J)$ are

$$T(v, J) = T_e + \sum_{k,l} \rho^k \cdot (Y_{kl} + \delta y_{kl}) \left(v + \frac{1}{2}\right)^k (J(J+1) - \Lambda^2)^l \quad (2.21)$$

with $\rho = \sqrt{\frac{\mu}{\mu^i}}$.

Here μ, μ^i are the respective reduced masses of the isotopologues, Y_{kl} and y_{kl} are Dunham coefficients and T_e is the potential's depth. Even though included in Eq. 2.21 for completeness, the parity of the levels in respect to Λ -doubling, set by the parameter δ , is not of importance for the lowest rotational states with $J = 1$ and $\Lambda = 1$ at this level of accuracy. In Eq. 2.21 the isotopologue shift of term energies is obtained up to highest order of the given Dunham expansion. It is to be pointed out that no perturbation of energy levels is contained in the Dunham expansions for both isotopologues. Due to this, it can be estimated that the given term values are accurate to $\pm 0.7 \text{ cm}^{-1}$, with single

2. The ultracold Li - K mixture, bound and unbound states

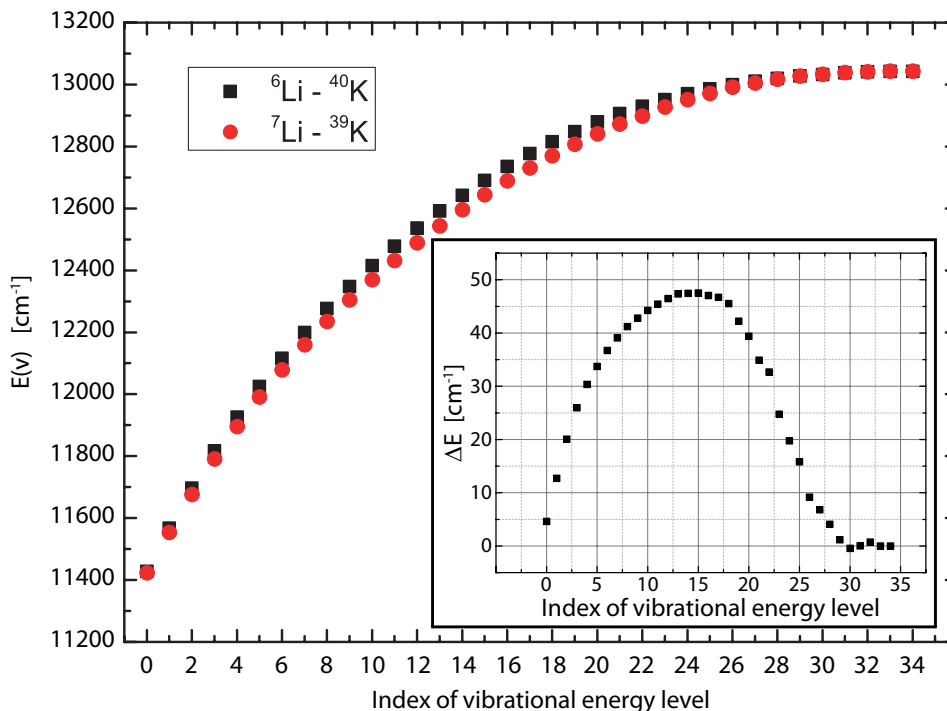


Figure 2.6: Energies of vibrational states for ${}^6\text{Li}-{}^{40}\text{K}$ (black squares) and ${}^7\text{Li}-{}^{39}\text{K}$ (red circles). Due to the small energy spacing of levels close to the asymptote, the two states with highest vibrational excitation are approximated to have the same energies. The inset shows the difference in level energies between the two isotopologues. The largest difference of 47.50 cm^{-1} occurs for the energy level with vibrational index $v=15$. More vibrationally highly excited states might exist for the isotopologue ${}^7\text{Li}-{}^{39}\text{K}$ than are shown.

larger deviations possible. A comparison with spectroscopic data in the case of ${}^7\text{Li}-{}^{39}\text{K}$ shows however that these larger deviations are unlikely. Further, the term energies of vibrational levels 19-29 are estimated from the fourth order polynomial fit shown in Fig. 2.5.

For a test of the accuracy of the data obtained from the fit function, the corresponding term energies of the ${}^7\text{Li}-{}^{39}\text{K}$ isotopologue, for which experimental data exists for the levels 0-32 [Kowalczyk, 2012], are used. A complete set of corresponding term energies for the ${}^7\text{Li}-{}^{39}\text{K}$ isotopologue is obtained in the following way: In order to obtain values for the ro-vibrational levels $v=33-34$, $J=1$ in the case of ${}^7\text{Li}-{}^{39}\text{K}$, the data for ${}^6\text{Li}-{}^{40}\text{K}$ [Ridinger et al., 2011] is used and first order isotopic shifts are calculated. Due to the proximity in energy to the potential's asymptote, the energy spacing is small for these levels. Thus, the absolute error made by only taking first order shifts into account is very small. Further, the vibrational term energies of levels 0-18 are determined from the Dunham expansion without mass scaling [Pashov et al., 1998]. The vibrational term energies, $v=19, \dots, 32$ are determined from experimental data¹. The latter do, however,

¹I thank Prof. P. Kowalczyk a lot for this data.

2.2 Li- K interaction potentials and bound states

not include values for the lowest rotational states. Thus, the term energies of states with the lowest J that are available in the experimental data for the ${}^7\text{Li}$ - ${}^{39}\text{K}$ isotopologue are used to determine rotational constants through an application of Eq. 2.20. Using the determined constants, Eq. 2.20 can again be applied to determine the term energies of the lowest rotational states. As the experimentally determined rotational states are comparatively low lying with J in the range of 2-8, the errors made by approximating the rotational energies with the rigid rotator energies are expected to be of the same order as the experimental uncertainty in the data itself. This is verified by comparisons. Now, a fit function similar to the one shown in Fig. 2.5 can be generated. Like this, the deviation of the data generated by the fit from the experimental data is found. Maximum values of $+4.3, -2.0 \text{ cm}^{-1}$ are found. Most of this deviation is likely to be caused by the perturbation of the vibrational energy levels from levels in the $3^1\Sigma^+$ potential, as well as the measurement uncertainty in the experimental data. A conservative estimate for the accuracy of the vibrational levels 19-29 is $\pm 5 \text{ cm}^{-1}$.

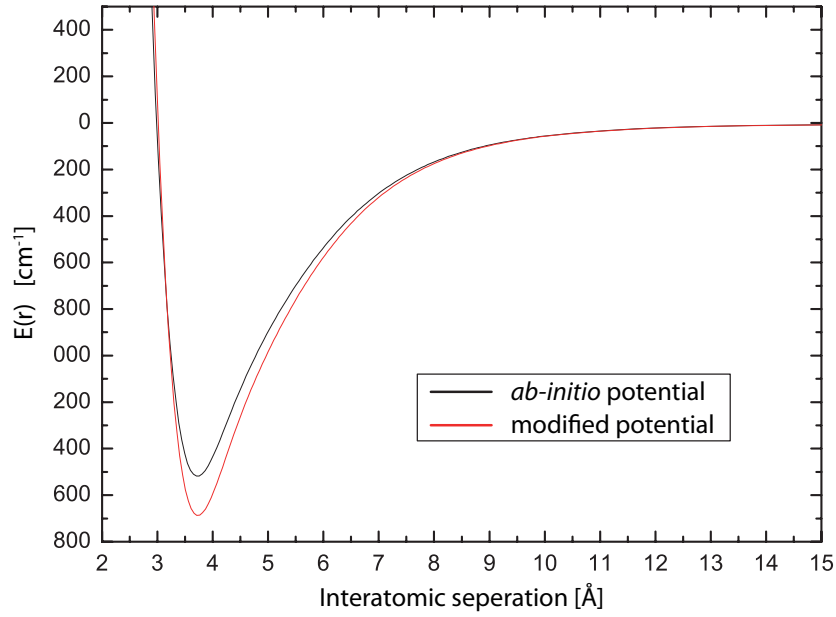
Fig. 2.6 shows the term energies of the $J = 1$ state for both isotopologues. The inset shows the difference between term energies caused by isotopic shift. Here, for ${}^6\text{Li}$ - ${}^{40}\text{K}$, the data presented in Tab. 2.2 is plotted. For the ${}^7\text{Li}$ - ${}^{39}\text{K}$ isotopologue, the data from the Dunham expansion is taken for term energies with $v=0, \dots, 18$. For the states with $v=19, \dots, 32$, the experimental data determined from the lowest rotational states available is taken and levels $v=33-34$ are taken to be the same for both isotopologues. It is to be noted that states of the ${}^7\text{Li}$ - ${}^{39}\text{K}$ isotopologue with higher excitations than $v=34, J = 1$, that might possibly exist in the case of ${}^7\text{Li}$ - ${}^{39}\text{K}$, are disregarded here. Thus, while the data shown for the $1^1\Pi$ potential of ${}^6\text{Li}$ - ${}^{40}\text{K}$ is complete, this might not be the case for ${}^7\text{Li}$ - ${}^{39}\text{K}$.

It is striking that while the deviation between the two isotopologues follows a rather smooth function up to vibrational level 18, it becomes less so for the vibrationally higher excited states. Because the vibrational energy levels 0-18 have been obtained from the Dunham expansions for both isotopologues, which do not include shifts of single levels due to perturbations, the data lies on a smooth curve here. This is however not the case for the levels 19-32 in which experimental data is compared to the data that has been constructed by the use of the fit function shown in Fig. 2.5.

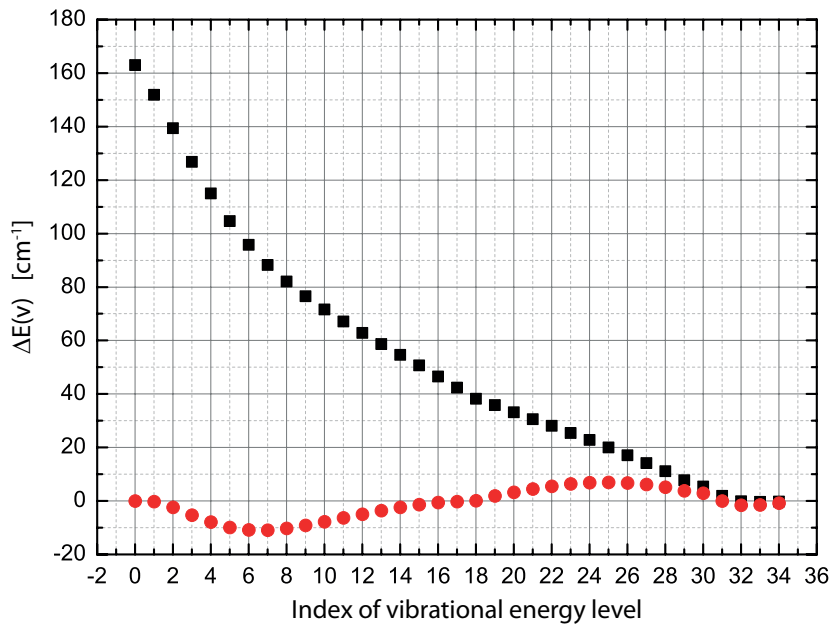
2.2.5 Relevant Franck - Condon factors

In order to determine wavefunctions of states in the electronically excited $1^1\Pi$ potential a modified version of the *ab-initio* potential function shown in Fig. 2.2 is constructed. A comparison with experimental data shows that the depth of the *ab-initio* potential [Allouche, 2011] is too shallow by approximately 10% or 168 cm^{-1} . In order to obtain a simple correction to the potential the *ab-initio* potential is scaled to the experimental depth of 1687.020 cm^{-1} [Pashov et al., 1998]. As this results in too many and still not quite matching vibrational energy levels, also the length is scaled slightly by a factor of 36/37. Further, the internuclear distance at the potential minimum is a little too small as compared to the RKR-potential derived from the Dunham expansion. Thus, the potential is shifted to the value given in [Jastrzebski et al., 2001, Pashov et al., 1998]. The scaled potential together with the original potential is shown in Fig. 2.7 (a). Fig. 2.7 (b) shows the deviation of calculated ${}^6\text{Li}$ - ${}^{40}\text{K}$ vibrational energy levels with

2. The ultracold Li - K mixture, bound and unbound states



(a)



(b)

Figure 2.7: (a): the $1^1\Pi$ potential, *ab-initio* (black) [Allouche, 2011] and modified (red). (b): energies of vibrational levels with $J = 1$ are compared to the experimental ones that are listed in Tab.2.2. The deviation between calculated vibrational energies and experimental ones is shown. The black squares represent data for which the *ab-initio* potential has been used to calculate vibrational $J = 1$ level energies, while for the red circles the modified potential has been used.

2.2 Li- K interaction potentials and bound states

Coupling of levels $1^1\Pi$: $\{v=0, \dots, 34; J=1\}$ to $X^1\Sigma^+$: $\{v=0, 47; J=0\}$			
$1^1\Pi$ v	F.-C. factor $X^1\Sigma^+$: $v=0$ $\leftrightarrow 1^1\Pi$: v	F.-C. factor $X^1\Sigma^+$: $v=47$ $\leftrightarrow 1^1\Pi$: v	Multiplied Franck-Condon factor
0	7.2×10^{-2}	$< 10^{-7}$	$< 10^{-10}$
1	1.4×10^{-1}	$< 10^{-7}$	$< 10^{-10}$
2	1.7×10^{-1}	$< 10^{-7}$	$< 10^{-10}$
3	1.5×10^{-1}	$< 10^{-7}$	$< 10^{-10}$
4	1.2×10^{-1}	$< 10^{-7}$	$< 10^{-10}$
5	9.2×10^{-2}	$< 10^{-7}$	$< 10^{-10}$
6	6.8×10^{-2}	$< 10^{-7}$	$< 10^{-10}$
7	4.9×10^{-2}	$< 10^{-7}$	$< 10^{-10}$
8	3.5×10^{-2}	$< 10^{-7}$	$< 10^{-10}$
9	2.4×10^{-2}	$< 10^{-7}$	$< 10^{-10}$
10	1.7×10^{-2}	$< 10^{-7}$	$< 10^{-10}$
11	1.2×10^{-2}	$< 10^{-7}$	$< 10^{-10}$
12	8.8×10^{-3}	$< 10^{-7}$	$< 10^{-10}$
13	6.3×10^{-3}	$< 10^{-7}$	$< 10^{-10}$
14	4.5×10^{-3}	$< 10^{-7}$	$< 10^{-10}$
15	3.3×10^{-3}	$< 10^{-7}$	$< 10^{-10}$
16	2.4×10^{-3}	$< 10^{-7}$	$< 10^{-10}$
17	1.8×10^{-3}	$< 10^{-7}$	$< 10^{-10}$
18	1.3×10^{-3}	2.0×10^{-6}	2.6×10^{-9}
19	1.0×10^{-3}	1.2×10^{-7}	1.2×10^{-10}
20	7.6×10^{-4}	7.3×10^{-5}	5.5×10^{-8}
21	5.8×10^{-4}	1.7×10^{-5}	9.7×10^{-9}
22	4.4×10^{-4}	7.5×10^{-4}	3.4×10^{-7}
23	3.4×10^{-4}	5.3×10^{-4}	1.8×10^{-7}
24	2.6×10^{-4}	2.1×10^{-3}	5.5×10^{-7}
25	2.0×10^{-4}	9.0×10^{-4}	1.8×10^{-7}
26	1.5×10^{-4}	3.5×10^{-3}	5.2×10^{-7}
27	1.1×10^{-4}	8.6×10^{-4}	9.5×10^{-8}
28	7.9×10^{-5}	6.0×10^{-3}	4.7×10^{-7}
29	5.1×10^{-5}	1.7×10^{-2}	8.7×10^{-7}
30	3.0×10^{-5}	4.4×10^{-5}	1.3×10^{-9}
31	2.1×10^{-5}	5.2×10^{-2}	1.0×10^{-6}
32	1.7×10^{-5}	1.1×10^{-1}	1.9×10^{-6}
33	1.3×10^{-5}	1.6×10^{-1}	2.1×10^{-6}
34	8.3×10^{-6}	2.3×10^{-1}	1.9×10^{-6}

Table 2.3: Columns 2 and 3: Franck-Condon factors for the relevant states ($v=0, J=0$ and $v=47, J=0$) in the ground state potential with states in the electronically excited $1^1\Pi$ potential. All electronically excited states are those with the lowest rotational excitation $J=1$. 4th column: multiplied values from columns 2 and 3. Because of the precision of the numerical calculations, Franck-Condon factors smaller than 10^{-7} and multiplied factors smaller than 10^{-10} are not given.

2. The ultracold Li - K mixture, bound and unbound states

$J = 1$ from the ones presented in Tab.2.2, for both the *ab-initio* and the modified potential.

As will be shown in Sec.2.4 of this chapter, the molecules that are produced at the Feshbach resonance at 155 G are created in a superposition state of highly vibrationally excited states in the $X^1\Sigma^+$ and $a^3\Sigma^+$ potentials. Here, the highest vibrationally excited state in the $X^1\Sigma^+$ potential with $v = 47$, $J = 0$, is used in order approximate the singlet part of the Feshbach molecules' wavefunction at zero magnetic field. The other relevant wavefunction in the $X^1\Sigma^+$ potential is naturally the target wavefunction of the absolute ro-vibrational ground state. For these two wavefunctions the Frank-Condon factors with the 35 electronically excited $J = 1$ wavefunctions in the $1^1\Pi$ potential are calculated, which was modified as explained. In the first two columns of Tab.2.3 the Franck-Condon factors for the states $X^1\Sigma^+ : v = 0, J = 0$ and $X^1\Sigma^+ : v = 47, J = 0$ and the electronically excited states $1^1\Pi : v = 0, \dots, 34, J = 1$ are listed. The third column gives the multiplied factors of columns 2 and 3.

As expected the largest overlap integral of the absolute ground state wavefunction with the electronically excited states' wavefunctions appear for states that carry low vibrational excitation, but not the ground state in the electronically excited potential. This is a consequence of the relative shift of the potentials' minima. It can be seen that the absolute ground state wavefunction has comparatively large overlap integrals with even the wavefunctions of the most excited states in the $1^1\Pi$ potential. This is however not true for the vibrationally excited state wavefunction with $v = 47$ in the ground state potential. Here, reasonably big factors occur only for levels with $v \geq 24$. This causes the largest multiplied Franck-Condon factors to be found for states very close to the asymptote of the $1^1\Pi$ potential.

In order to estimate the accuracy of the given numbers the change of the calculated Franck-Condon factors for possible variations of the $1^1\Pi$ potential function are investigated. On the base of a comparison of the different results, e.g. gained from the *ab-initio* $1^1\Pi$ potential shown in black in Fig.2.7, an error of not more than 50% is estimated for the factors specified in Tab.2.3. However, in special cases one or two factors may show a larger deviation.

With the calculation of some relevant Franck-Condon factors, this section about Li-K bound states is concluded. The next section gives an overview about scattering at ultracold temperatures. In respect to the coherent Raman transfer of Feshbach molecules the stability and lifetime of samples of ultracold Li-K atoms and dimers is most important. Questions in regard to these properties of the Li-K mixture are addressed.

2.3 Scattering in the ultracold Li-K mixture

In time-independent scattering theory, the wave function of a scattered wave at a large enough distance from a scattering potential can be approximated as [Sakurai, 1994, Pethick and Smith, 2002, Lukin, 2006]

$$\lim_{r \rightarrow \infty} \Psi_k(\mathbf{r}) = e^{ikz} + f_k(\Theta) \frac{e^{ikr}}{r} \quad (2.22)$$

for a spherical symmetric scattering potential. Here the total wavefunction Ψ_k contains an unchanged plane wave oriented in the $\hat{\mathbf{z}}$ direction and a scattered spherical wave the

2.3 Scattering in the ultracold Li-K mixture

amplitude of which is modulated dependent on a scattering angle Θ .

The differential scattering cross-section defined in terms of the wavefunction given in Eq. 2.22

$$\frac{d\sigma}{d\Omega} = |f_k(\Theta)|^2 \frac{v_{\text{final}}}{v_{\text{initial}}} \quad (2.23)$$

is dependent on the probability density of the function f_k that describes the angle dependency of the scattered wave. For elastic collisions, the initial v_{initial} and final v_{final} particle velocities are the same, while for inelastic collisions, the differential scattering cross-section is further changed by a factor proportional to the change in velocity of the particles.

To obtain the total scattering cross-section, Eq. 2.23 is integrated over all solid angles:

$$\sigma = 2\pi \frac{v_{\text{final}}}{v_{\text{initial}}} \int_0^\pi d\Theta |f_k(\Theta)|^2 \sin\Theta . \quad (2.24)$$

2.3.1 Elastic scattering

Useful for the treatment of low energy scattering processes is a partial wave expansion. Again assuming a spherical symmetric potential $V(r)$, a wavefunction can be expanded in terms of spherical harmonics [Sakurai, 1994, Landau and Lifshitz, 1981]:

$$\Psi = \sum_{l=0}^{\infty} A_l P_l(\cos(\Theta)) R_l(r) \quad (2.25)$$

where P_l is the l^{th} Legendre polynomial. The angular and radial dependencies P_l and R_l depend on the partial wave order l . It is customary to call the partial waves with $l = 0, 1, 2, \dots$ s- p- and d waves etc. In order to relate Eq. 2.25 to Eq. 2.22, the incoming plane wave e^{ikz} can be expressed in terms of spherical harmonics:

$$e^{ikz} = \sum_{l=0}^{\infty} i^l (2l+1) P_l(\cos(\Theta)) J_l(kr) . \quad (2.26)$$

Here $J_l(kr)$ is the spherical Bessel function of order l . When Eq. 2.25 is substituted into the Schrödinger equation for a particle of reduced mass μ , one arrives at a set of uncoupled equations for the radial dependency,

$$\left[\frac{\hbar^2}{2\mu} \left(\frac{2}{r} + \frac{d^2}{dr^2} - \frac{l(l+1)}{r^2} \right) - V(r) \right] R_l(r) = -\frac{\hbar^2 k^2}{2\mu} R_l(r) \quad (2.27)$$

one for each partial wave l . Here, the energy of the plane wave part of the wavefunction, $\hbar^2 k^2 / 2\mu$ can be seen on the right side of the equation. Not only the potential $V(r)$ matters for the scattering process, but also a centrifugal part. These together form the effective potential that the partial wave of order l is scattered from. In Fig. 2.8, the effective singlet ground state potentials for partial waves with $l = 1, \dots, 6$ are shown. It can be seen that particles with $l > 0$ have to pass a centrifugal barrier, that gets higher for each partial wave, in order to get into the region where $V(r)$ is dominant over the centrifugal part of the effective potential. In our experiment temperatures

2. The ultracold Li - K mixture, bound and unbound states

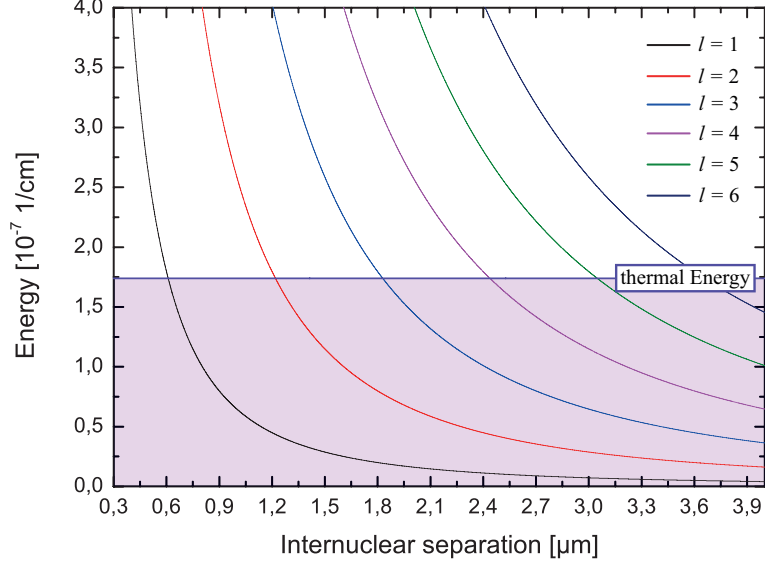


Figure 2.8: Effective ${}^6\text{Li}$ - ${}^{40}\text{K}$ singlet ground state potentials at large distance, for partial waves with $l = 1, \dots, 6$. The violet horizontal line marks the thermal energy of particles at 250 nK, a typical temperature for particles in our Li - K mixture. It can be seen that the centrifugal barrier hinders partial waves with $l > 0$ to be scattered off $V(r)$ as particles cannot approach each other closer than approximately 600 nm. At this distance the potential itself is negligible in comparison to the centrifugal part of the effective potential.

of approximately 250 nK are reached, which corresponds to $1.7 \times 10^{-5} \text{ cm}^{-1}$ [Taglieber et al., 2008, Taglieber, 2008]. In Fig. 2.8 this thermal energy is marked by a horizontal violet line. This allows partial waves $l > 0$ to only probe the slowly varying outer region of the effective potential, thus picking up little phase shift. The result is a suppression of all partial waves $l > 0$, while only s-wave scattering occurs.

Phenomenologically this means that particles in the zero energy scattering limit will always be scattered with the same amplitude in every direction, with f_k constant. As a consequence it becomes possible to describe scattering at sufficiently low temperatures with a single parameter, which is called the scattering length a .

Particle statistics plays a crucial role in low energy scattering. In the case of indistinguishable particles, correct symmetrization of the wavefunction needs to be taken care of. As the scattering of identical particles by an angle Θ produces the same result as scattering by an angle $\Theta + \pi$ the wavefunction is in this case a sum of both scattering events:

$$\Psi_k(r) = \frac{e^{ikz} \pm e^{-ikz}}{\sqrt{2}} + \frac{f_k(\Theta) \pm f_k(\pi + \Theta)}{\sqrt{2}} \frac{e^{ikr}}{r}. \quad (2.28)$$

Here the upper sign stands for bosons, while the lower is for fermions. The differential scattering cross-section for the case of the wavefunction in Eq. 2.28 is

$$\frac{d\sigma}{d\Omega} = \left| \frac{f_k(\Theta) \pm f_k(\pi + \Theta)}{\sqrt{2}} \right|^2 \quad (2.29)$$

with the signs as before. It can directly be seen that for the case of identical bosons only

2.3 Scattering in the ultracold Li-K mixture

even partial waves contribute, while for the case of fermions the amplitudes for even partial waves cancel and only odd ones contribute.

As a consequence, at low enough collision energies, when only the s-wave contributes to scattering, the scattering of bosons is enhanced, while fermions do not scatter. The total scattering cross-sections for the three possible types of colliding particles are

$$\lim_{k \rightarrow 0} \sigma_k = \begin{cases} 8\pi a^2 & \text{identical bosons} \\ 0 & \text{identical fermions} \\ 4\pi a^2 & \text{distinguishable particles} \end{cases} \quad (2.30)$$

where a is the scattering length.

It is to be emphasized again that the preceding equations are only valid for spherical symmetric interaction potentials. The scattering properties of colliding Li-K molecules, is more difficult to treat as it is not by all means spherical symmetric (see Chap. 1). Further, the interaction depends critically on the vibrational and rotational excitation states of the molecules. For vibrationally highly excited ${}^6\text{Li}$ - ${}^{40}\text{K}$ molecules the fermionic character of the molecules' constituents can greatly reduce s-wave scattering, even though the molecules are bosonic. Deeply bound molecules possess an electric dipole moment. The interaction in this case depends on the relative orientations of the two dipoles participating in the collision.

2.3.2 Inelastic scattering

Inelastic collisions are important for the description of scattering processes of atoms and molecules in the Li-K mixture. In these events the scattering cross-sections in Eqns. 2.23, 2.24 are scaled by the factor $v_{\text{final}}/v_{\text{initial}}$.

Typical trapping potential depths in our optical dipole trap (see Chap. 3) are on the order of $k_B \times 100 \mu\text{K}$, which corresponds to approximately $h \times 2 \text{ MHz}$. As this energy is small compared to most hyperfine splittings of the atoms in the Li-K mixture, it is clear that the kinetic energy that can be released by spin changing inelastic collisions is large compared to the trap depth. Thus, spin exchange collisions will lead to strong heating of the scattered particles and trap loss. In the Li-K mixture, exothermic two-particle collisions that preserve the total spin projection quantum number $M_F = m_{\text{Li}} + m_{\text{K}}$ lead to fast decay of the ultracold sample. A preparation of any of one species in the absolute ground state, with the other one in a low-lying state energetically stabilizes the mixture [Simoni et al., 2003, Wille et al., 2008]. Fewer states exist if Rb is added to the mixture [Taglieber, 2008] (see Chap. 3).

When three particles take part in a scattering event, dimer formation can occur while the third particle and the dimer carry away the liberated energy as kinetic energy. Usually, three body interactions are not limiting experiments under typical conditions with densities on the order of $10^{13}/\text{cm}^3$ to $10^{14}/\text{cm}^3$ and background scattering lengths on the order of one hundred Bohr radii. Approximately starting at densities on the order of $10^{15}/\text{cm}^3$ three body losses dominate [Ketterle and Zwierlein, 2006]. The situation changes in the vicinity of a Feshbach resonance, where the scattering length becomes large. Observing magnetic field dependent losses for magnetically induced Feshbach resonances is a widely used tool for finding and characterizing these resonances [Chin et al., 2010].

Scattering of vibrationally excited molecules

Vibrational relaxation in molecular samples is a process very similar to three body decay. In this case molecule - molecule or atom - molecule scattering can lead to the liberation of a large amount of internal molecular energy. The vibrationally highly excited molecule(s) participating in the scattering event can undergo a radiationless transition to a lower molecular state. The difference in energy is carried away by the particles as kinetic energy. These scattering events can severely limit the lifetime of ultracold molecular samples, especially in the case of bosonic dimers consisting of bosonic atoms [Petrov et al., 2005].

We measure lifetimes of our ultracold atom-molecule sample at a total particle density on the order of $10^{13}/\text{cm}^3$ that are strongly dependent on the magnetic field [Voigt et al., 2009, Voigt, 2009]. These measurements are described in detail in Sec. 4.6. On the atomic side and at magnetic field strengths lower than the Feshbach resonance lifetimes of several ms are recorded.

Very long molecular lifetimes up to seconds have previously been observed for molecules consisting of fermions in other groups [Regal et al., 2004b, Cubizolles et al., 2003, Jochim et al., 2003a, Strecker et al., 2003]. Two effects are thought to lead to the long lifetime of molecules consisting of fermions in the vicinity of a wide Feshbach resonance [Petrov et al., 2005]. Firstly, in the magnetic field strength range with large scattering length, the molecules are only very loosely bound and their wavefunction extends to large distances. This leads to very small Franck - Condon factors of Feshbach - and lower lying vibrational states, which can be seen in Fig. 2.3 for the case of Li - K molecules. The second mechanism depends on the quantum statistics of the fermionic constituents of the long-lived molecules together with the slow relative motion at ultracold temperatures. The physical picture of this effect [Petrov et al., 2005], which has been described for halo dimers [Ferlandino et al., 2008, Krems et al., 2009], is the following: For the occurrence of vibrational relaxation to a specific lower lying vibrational state, the molecule and its scattering partner must approach each other approximately to the length scale given by the extension of a wavefunction of the low lying vibrational state. This means that at least two of the fermionic particles must approach each other closely. Due to quantum statistics the manybody wavefunction must however vanish at the distance $r = 0$. As the momentum of the atoms in the bound molecular state is $k \sim 1/a$ and the wavefunction is therefore only slowly varying, the probability of the third particle involved in the scattering event advancing to short distances is suppressed. It needs to be pointed out that the mechanisms described above are limited to the case of wide Feshbach resonances, while the 155 G Li - K resonance has been classified as narrow. Thus, it is not clear how far this reasoning can be applied to the case of the Li - K molecules.

In [Voigt et al., 2009] the lifetime of an atom - molecule sample was measured, which is expected to be lower than the one of a pure molecular sample. However also for a pure molecular sample of vibrationally highly excited ${}^6\text{Li}$ - ${}^{40}\text{K}$ molecules at magnetic fields far from and on the atomic side of the Feshbach resonance, the lifetime is expected to be no longer than ten to several ten ms. For these deeper bound but highly vibrationally excited states, the molecular wavefunction is expected to extend to no distances farther than several ten Angstrom. The vibrationally most excited singlet and triplet wavefunctions in the ${}^6\text{Li}$ - ${}^{40}\text{K}$ ground state potential at zero magnetic field are shown

2.3 Scattering in the ultracold Li- K mixture

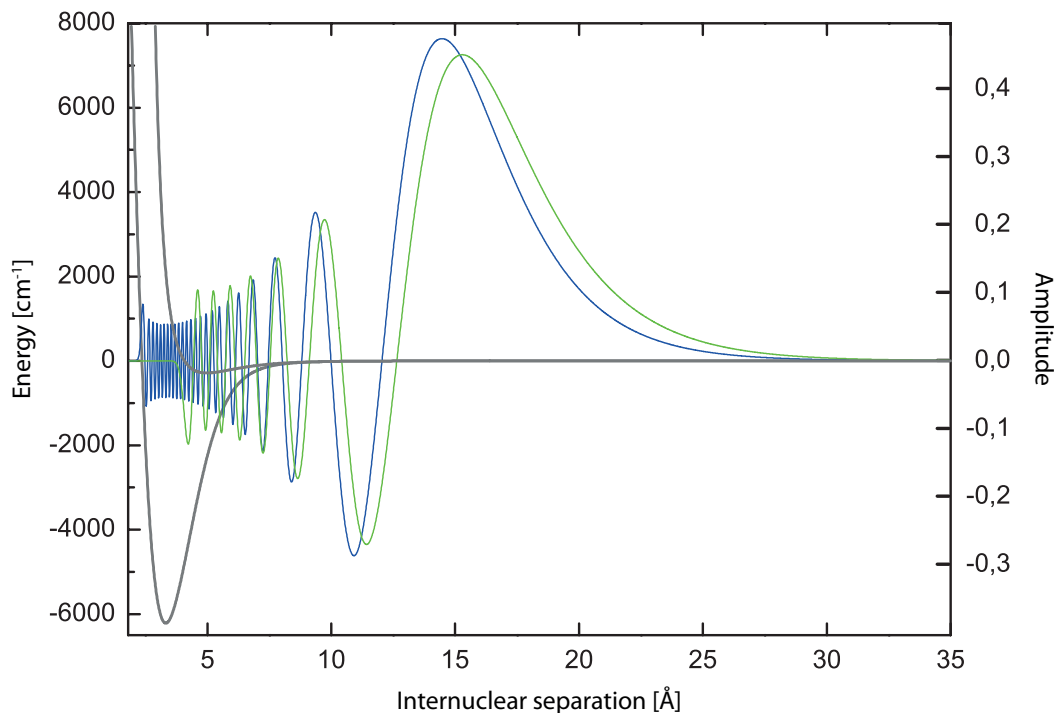
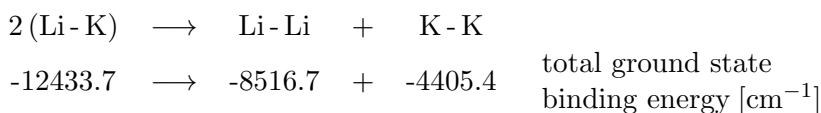


Figure 2.9: ${}^6\text{Li}$ - ${}^{40}\text{K}$ singlet and triplet ground state potentials taken from [Tiemann et al., 2009]. The wavefunctions of the uppermost bare molecular singlet (blue) and triplet (green) states are shown. At zero magnetic field they can be seen to extend no farther than several ten Å.

in Fig. 2.9. As explained in Sec. 2.4, for zero magnetic field, the state of the Feshbach molecules associated at the 155 G resonance is a superposition of the two shown states.

Scattering of ground state molecules

Even though vibrational relaxation can naturally not occur in the case of ground state molecules, energetically lower lying states of the Li- K mixture exist. The chemical reaction



is strongly exothermic with $\Delta E = -488.4 \text{ cm}^{-1}$ [Tiemann et al., 2009, Zavitsas, 2003, Falke et al., 2006]. Whenever a molecule takes part in a scattering event in which it is approached to short range (approximately 3-4 Å; see Fig. 2.3 for the extension of the ground state wavefunction), the probability of the occurrence of a chemical reaction is almost unity [Idziaszek and Julienne, 2010, Chin et al., 2010, Ospelkaus et al., 2010b]. Thus, even the lifetime of a pure sample of ground state molecules will be limited, if no additional measures to stabilize the samples are taken. Other than in the case of

2. The ultracold Li - K mixture, bound and unbound states

identical fermionic molecules [Ni et al., 2008, Ospelkaus et al., 2010b] no p-wave barrier keeps bosonic molecules from approaching each other closely at cold temperatures.

The scattering properties of polar and unpolar ground state molecules are expected to be different. Further, as previously mentioned in Chap. 1, versatile ways exist to tune the dipolar interaction, on which the scattering depends in addition to the molecular van der Waals interaction. No experimental data on the molecule - molecule scattering length of Li - K unpolarized ground state molecules exists. However a prediction of the lifetime of a molecular sample in a three dimensional bulk gas can be gained from a comparison to available experimental data. In [Ospelkaus et al., 2010b] a lifetime of roughly 19 ms is reported for a spin mixture of fermionic ^{40}K - ^{87}Rb molecules. The value should be roughly, up to a factor of 2 (see Eq. 2.30), the same as the one for identical bosonic molecules, as both interact via s-waves. In addition, the density of scattering partners in the spin mixture is expected to be lower than in the case of the bosonic ground state molecules. The theoretical prediction for ^6Li - ^{40}K ground state molecules with no dipole moment in the laboratory frame is that they should be the most chemically reactive of all, Li - Na ... Li - Cs, heteronuclear bosonic alkali metal dimers. A loss rate coefficient that is larger by a factor of 4.7 than the one for ^{40}K - ^{87}Rb is predicted [Quéméner et al., 2011]. As the densities that can be expected for a sample of ^6Li - ^{40}K ground state molecules in our experiment are similar to the ones achieved in the Boulder group [Ospelkaus et al., 2010b], lifetimes of around 4-5 ms are to be expected.

In order to reach the lowest absolute state the hyperfine degree of freedom will need to be considered [Ospelkaus et al., 2010a,b]. Control over the hyperfine state of the ground state molecules will be of importance.

In the case of polar ground state molecules, the scattering properties are more complicated than for unpolar molecules. The scattering of dipoles depends on their orientation. Furthermore, the long-range dipolar interaction causes stronger phase shifts of the scattered particles' wavefunctions at larger distances. This means identical molecules do not experience only s-wave scattering at the temperatures reached in experiment. In [Bohn et al., 2009] the scattering properties of dipolar molecules are investigated, while loss rates in a three dimensional bulk gas are predicted in [Quéméner et al., 2011].

Mainly two possibilities exist to stabilize samples of heteronuclear bosonic alkali metal ground state molecules, both of which keep molecules from approaching each other to short distances: Firstly, molecular samples can be loaded into sufficiently deep optical lattices. With one molecule per lattice site, the decay will be strongly suppressed. Second, as previously mentioned in Chap. 1, the dipolar interaction in a quasi two dimensional gas can be tuned to strong, purely repulsive values [Büchler et al., 2007a]. As ^6Li - ^{40}K ground state molecules possess large induced dipole moments in comparison to other heteronuclear alkali metal ground state molecules, the strength of the repulsive potential can be tuned to comparatively large values. This might allow a stabilization of the samples in a 2D trap geometry, even at temperatures of a few hundred nK. In Singapore, DC electrodes that will be used for a polarization of ground state molecules have been designed and implemented. The electrodes should allow to reach molecular dipole moments of up to 1.9D. Further, preparations for a 2D optical trap have been started.

With this, the section about the scattering properties of Li - K atoms and molecules at ultracold temperatures is concluded. The next section treats Feshbach resonances

2.4 Feshbach resonances

and the production of Li-K molecules by use of these scattering resonances. For the choice of electronically excited states the determination of the spin-singlet fraction of the state of the Feshbach molecules is most important. This is determined for the Feshbach molecules that have been produced in our group.

2.4 Feshbach resonances

Through the use of Feshbach resonances it is possible to control the interactions of particles in an ultracold sample. The basic underlying principle will briefly be described here. For a detailed description the reader is referred to the textbook [Krems et al., 2009] or review articles [Köhler et al., 2006, Chin et al., 2010, Gurarie and Radzihovsky, 2007].

Fig. 2.10 illustrates how a Feshbach resonance arises. Here, only two scattering channels [Pethick and Smith, 2002] are taken into account. At large atomic separations, particles in the sample possess a kinetic energy E . When they approach each other, the interatomic potential $V_{bg}(R)$ in the entrance channel becomes important. As $E > 0$ this scattering channel is open, which means particles in a quantum state corresponding to the entrance channel will separate again after the scattering event. However, there could exist another quantum state of the particles, for which the interatomic potential is $V_C(R)$. In this potential, bound states are to be found in the energy range around E . If there exists a mechanism that couples the entrance channel state to one of these bound, closed channel (in respect to scattering) states, a Feshbach resonance arises. In this case the coupling between the channels mixes the continuum state of the entrance channel with the bound state of the closed channel to a new eigenstate of the two channel system.

If the magnetic momenta of the closed channel states μ_{mol} and the open channel states μ_{atom} are different, the relative difference in energy $E - E_C$ can be controlled by

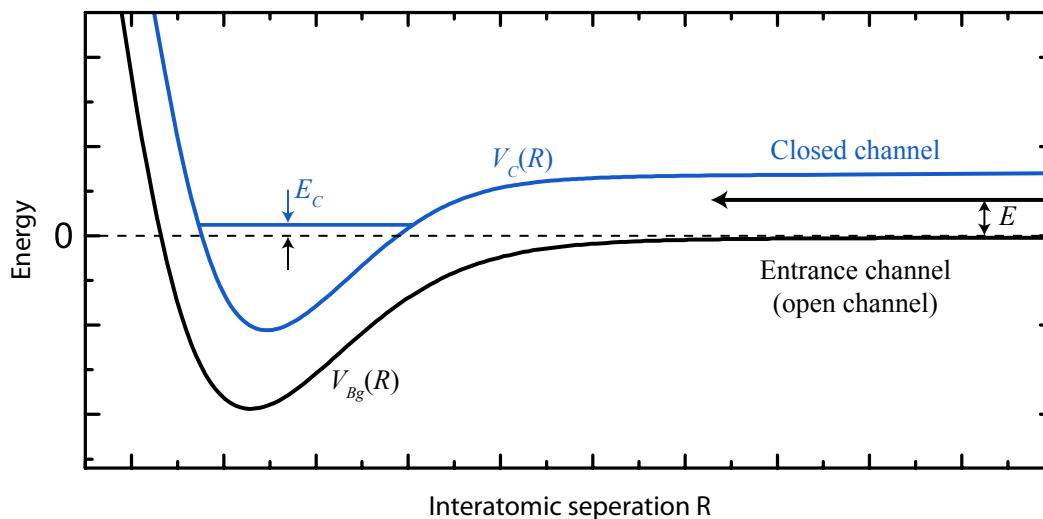


Figure 2.10: Principle of a Feshbach resonance. A coupling between the open channel at energy E and the closed channel at energy E_C mixes the two states.

2. The ultracold Li - K mixture, bound and unbound states

a magnetic field [Chin et al., 2010]:

$$E - E_C = (\mu_{\text{atom}} - \mu_{\text{mol}}) (B - B_{\text{res}}) = E_{\text{bind}} = \mu_{\text{res}} (B - B_{\text{res}}) \quad (2.31)$$

where B_{res} is the magnetic field at which the bare uncoupled state crosses the threshold energy (chosen zero in Fig. 2.10). Like this, the coupling, which is only relevant if the relative energy difference is small, can be controlled in a magnetically tunable Feshbach resonance. This tuneability allows to control the scattering length (see Eq. 2.30) via the strength of a magnetic field [Moerdijk et al., 1995]:

$$a(B) = a_{\text{bg}} \left(1 - \frac{\Delta}{B - B_0} \right) . \quad (2.32)$$

Here a_{bg} refers to the background scattering length due to $V_{\text{bg}}(R)$, Δ is the resonance width and B_0 is the resonance position. The resonance occurs at magnetic field strengths at which the molecular state energetically crosses with the open channel state at the threshold energy E .

Feshbach resonances are usually classified as entrance- or closed channel dominated [Köhler et al., 2006, Chin et al., 2010]. The relevant parameter used for the characterization is the dimensionless resonance strength parameter

$$s_{\text{res}} = \frac{a_{\text{bg}}}{\bar{a}} \frac{\Gamma_0}{\bar{E}} \simeq \frac{a_{\text{bg}}}{R_{\text{vdW}}} \frac{\Gamma_0}{E_{\text{vdW}}} \quad (2.33)$$

with $R_{\text{vdW}} = \frac{1}{2} \left(\frac{2\mu C_6}{\hbar^2} \right)^{1/4}$ and $E_{\text{vdW}} = \frac{\hbar^2}{2\mu R_{\text{vdW}}^2}$.

Here Γ_0 is the resonance strength parameter, which has the dimension of energy, and R_{vdW} is the van der Waals length, determined by the C_6 van der Waals coefficient and the reduced mass μ . For the exact definition of \bar{a} and \bar{E} the reader is referred to [Chin et al., 2010]. For $s_{\text{res}} \ll 1$, resonances are entrance channel dominated. This means that there exists a wide range of magnetic fields around the resonance in which the coupled state contains a negligible closed channel fraction. This regime is called “universal” as states only depend on the single parameter a and not on the specific interaction potentials between atoms. For closed channel dominated resonances $s_{\text{res}} \gg 1$. For these resonances the universal description is only possible for small magnetic field ranges around the Feshbach resonance position at B_0 . The reader is referred to the above mentioned review articles for a more thorough and detailed description of the classification of Feshbach resonances.

In [Wille et al., 2008] an experimental and theoretical survey of the interspecies Feshbach resonances in the ${}^6\text{Li}$ - ${}^{40}\text{K}$ system is presented. All resonances are found to be closed channel dominated. For a theoretical description the Asymptotic Bound State Model is used. The model is briefly described in the following section and applied to determine the magnetic field dependent spin state of the molecules produced at the 155 G ${}^6\text{Li}$ - ${}^{40}\text{K}$ Feshbach resonance.

Several schemes for the production of ultracold molecules by the use of Feshbach resonances have been applied [Chin et al., 2010]. Most common of all, it is possible to transfer the coupled state, which in principle contains a negligible closed channel fraction

2.4 Feshbach resonances

on resonance, into a purely bound state by a magnetic field sweep. In an ideal system, it is thought possible to convert the whole population of atoms to molecules by such a sweep [Köhler et al., 2006], whereas in a non-ideal system the conversion efficiency is limited due to finite time intervals of the magnetic field sweep and phase space density of the atomic cloud [Köhler et al., 2006]. However, even without a magnetic field sweep, molecules can be associated at magnetic field strengths in the range of the Feshbach resonance. This is due to the closed channel fraction that the coupled state can contain, dependent on the magnetic field strength and type of resonance (see Chap. 4).

After careful optimization of the magnetic field ramping speed an atom to ${}^6\text{Li}$ - ${}^{40}\text{K}$ molecule conversion efficiency of around 50% was reached with our experiment [Voigt et al., 2009] at the 155 G interspecies resonance. This achieved efficiency is high for the type of resonance, which is closed channel dominated and decaying [Naik et al., 2011].

2.4.1 Asymptotic Bound State Model

The Asymptotic Bound State Model [Moerdijk et al., 1995] and its application to Feshbach resonances is described in detail in [Tiecke et al., 2010]. Its advantage over coupled channels calculations is its relative simplicity and that it is computationally way less costly. This is due to the assumed knowledge of the bare molecular energies that are used in this model. These can be gained from accurately known molecular potentials or experimental data. The latter can for example be gained from molecular spectroscopy (e.g. of the type described in Chap. 6 or radio frequency spectroscopy) or inelastic loss spectroscopy with ultracold samples (see Sec. 2.3.2). Further, the set of bare molecular eigenenergies used in the calculation can be limited. Bare molecular states, which contribute only very little admixture to coupled molecular states, can be excluded from the calculations. This facilitates the treatment significantly, but still yields accurate results.

Here, only discrete states are included in the Asymptotic Bound State Model. In [Tiecke et al., 2010], the model is extended to include continuum states above threshold. This allows a theoretical determination of the resonance characteristics and a determination of the resonance width.

In the following, the Asymptotic Bound State Model is used to estimate the singlet fraction of the electronic state of the ${}^6\text{Li}$ - ${}^{40}\text{K}$ molecules produced at the 155 G interspecies Feshbach resonance. This value is most important for the coherent transfer of the vibrationally highly excited molecules produced at the Feshbach resonance to the absolute ro-vibrational singlet ground state by means of STIRAP. The transition selection rules, which are discussed in Chap. 5, prohibit electronic dipole transitions between molecular singlet and triplet manifolds.

The Asymptotic Bound State Model requires the diagonalization of the Hamiltonian:

$$\mathcal{H} = \underbrace{\mathcal{H}_{\text{rel}}}_{\mathbf{p}^2/2\mu+\mathcal{V}} + \underbrace{\mathcal{H}_{\text{int}}}_{\mathcal{H}_{\text{Z}}+\mathcal{H}_{\text{hf}}} . \quad (2.34)$$

This Hamiltonian contains two contributions: one, \mathcal{H}_{rel} , for the relative motion of two atoms described in a center of mass frame by the motion of a particle with reduced mass

2. The ultracold Li - K mixture, bound and unbound states

μ in the adiabatic Born - Oppenheimer potential \mathcal{V} . The other summand, \mathcal{H}_{int} , describes the internal energy of the particles. As in [Tiecke et al., 2010], the internal energy is described here by two contributions: the Zeeman interaction

$$\mathcal{H}_Z = (\gamma_e \mathbf{s} - \gamma_i \mathbf{i}) \cdot \mathbf{B} \quad (2.35)$$

depending on \mathbf{s} and \mathbf{i} which are the electron and nuclear spins of the two colliding atoms with the respective gyromagnetic ratios. \mathbf{B} is the magnetic field vector. The other contribution is the hyperfine interaction

$$\mathcal{H}_{hf} = \frac{a_{hf}}{\hbar^2} \mathbf{i} \cdot \mathbf{s} \quad (2.36)$$

with the hyperfine structure coefficient a_{hf} .

Basis sets

The Breit - Rabi formula [Breit and Rabi, 1931] describes the dependency of the eigenstates on the magnetic field for the atomic states with $L = 0$ and $S = 1/2$. The components of \mathcal{H}_{int} are diagonal in this pair basis set and eigenstates can be labeled $|f, m_f\rangle_\alpha \otimes |f, m_f\rangle_\beta$. Here f, m_f are quantum numbers specifying atomic hyperfine states of the atoms α and β . It is to be noted that f is only a good quantum number at zero magnetic field. The threshold energy, chosen as zero in Fig. 2.10 is determined by the use of this equation.

The molecular potential \mathcal{V} is diagonal in the basis of the total electron spin $\{|S\rangle\}$. For alkali atoms $S = \{0, 1\}$, corresponding to singlet and triplet potentials. Thus, the potential can be written in the form

$$\mathcal{V}(r) = \sum_S |S\rangle V_s(r) \langle S| \quad (2.37)$$

After a partial wave expansion, see Sec. 2.3.1, the eigenvalues and eigenstates of \mathcal{H}_{rel} can be found by solving Eq. 2.27. The binding energies of vibrational levels within the potentials V_S are labeled \mathcal{E}_ν^{Sl} and the eigenstates are $|\Psi_\nu^{Sl}\rangle |Y_{m_l}^l\rangle$. Here ν and l are the vibrational and rotational quantum numbers of the molecule, while $Y_{m_l}^l$ are spherical harmonics (see Eq. 2.25 for the case $m = 0$). The full bare molecular basis set including electron magnetic M_S and nuclear magnetic $i_m^{\alpha, \beta}$ quantum numbers is $|\Psi_\nu^{Sl}\rangle |S, M_S, i_m^\alpha, i_m^\beta\rangle$. As the sum of the magnetic quantum numbers $M_F = M_S + i_m^\alpha + i_m^\beta$ is conserved by \mathcal{H} , the number of spin states that need to be included in this basis set is reduced. The mixing of coupled states of this basis is found to originate from the \mathcal{H}_{hf} component of the Hamiltonian, as all other components are diagonal in this basis set.

Only bound state energies in the potential \mathcal{V} and no continuum states are included in the model as it is used here.

2.4 Feshbach resonances

Diagonalization of \mathcal{H}

In order to find the coupled eigenvalues and eigenstates of the Hamiltonian \mathcal{H} , the secular equation

$$\det \left[\langle \Psi_\nu^{S^l} | \langle S, M_S, i_m^\alpha, i_m^\beta | \mathcal{H} - \mathcal{E}_b | S', M'_S, i_m^{\alpha'}, i_m^{\beta'} \rangle | \Psi_{\nu'}^{S'^l} \rangle \right] = \det \left[\left(\mathcal{E}_\nu^{S^l} + \mathcal{E}_Z^{S M_S i_m^\alpha i_m^\beta} - \mathcal{E}_b \right) \delta_{\nu S M_S i_m^\alpha i_m^\beta, \nu' S' M'_S i_m^{\alpha'} i_m^{\beta'}} + \langle \Psi_\nu^{S^l} | \Psi_{\nu'}^{S'^l} \rangle \langle S, M_S, i_m^\alpha, i_m^\beta | \mathcal{H}_{hf} | S', M'_S, i_m^{\alpha'}, i_m^{\beta'} \rangle \right] = 0 \quad (2.38)$$

has to be solved. Here, $\mathcal{E}_Z^{S M_S i_m^\alpha i_m^\beta}$ are the Zeeman energies of the respective states, while the δ -distribution reflects the fact that for these contributions, the basis $|\Psi_\nu^{S^l}\rangle |S, M_S, i_m^\alpha, i_m^\beta\rangle$ is an eigenbasis. $\langle \Psi_\nu^{S^l} | \Psi_{\nu'}^{S'^l} \rangle$ are wavefunction overlap integrals of the respective bare molecular states.

Following the procedure described in [Tiecke et al., 2010] the secular Eq. 2.39 is solved numerically. The free parameters are the wavefunction overlap integrals and the energies of the relevant bare molecular states. For the calculations carried out here, the Franck-Condon factors are taken to be unity in good approximation. Qualitatively, the good wavefunction overlap integral, which results in a Franck-Condon factor of 0.979 [Tiecke et al., 2010], can be seen in Fig.2.9, where the uppermost bare molecular wavefunctions in the singlet and triplet potentials are shown. For simplicity only the two binding energies of the uppermost bare $J = 0$ molecular states in the singlet and triplet potentials are included in the calculation.

Results

Fig. 2.11 shows the eigenenergies of the $M_F = -2$ manifold's coupled states, which are eigenstates of \mathcal{H} , in the magnetic field range 0.. 200 G. Also the threshold energy, which is calculated by use of the Breit-Rabi formula, is shown. A Feshbach resonance arises, where the energy of a coupled molecular state crosses with the threshold energy. In this way, the coupled molecular state with the eigenenergy labeled ⑤ is found to cause the resonance at 155 G.

In order to determine the singlet fraction \mathcal{S} of the now identified coupled molecular state $|\textcircled{5}\rangle$, the latter is projected onto the bare molecular basis $|\Psi_\nu^{S^l}\rangle |S, M_S, i_m^\alpha, i_m^\beta\rangle$. An addition of all expectation values of the relevant singlet (triplet) states gives the respective fractions of these states in the coupled molecular state:

$$\mathcal{S}(B) = \sum_{\substack{i_m^\alpha, i_m^\beta \\ M_F = -2}} |\langle S, M_S, i_m^\alpha, i_m^\beta | \textcircled{5} \rangle|^2 . \quad (2.39)$$

Fig. 2.12, shows the singlet and triplet fractions of state $|\textcircled{5}\rangle$ and their dependence on the magnetic field. Feshbach molecules exist practically [Costa et al., 2010a] only below the resonance position, thus the result for the magnetic field strength range between 155 - 200 G is somewhat hypothetical. A singlet fraction of 41.8 % is found on resonance,

2. The ultracold Li - K mixture, bound and unbound states

decreasing to approximately 10% at zero magnetic field. Considering the motional degrees of freedom the molecule is thus found to be in a superposition state, which at zero magnetic field strength, consists of the two wavefunctions shown in Fig. 2.9. Their magnetic field dependent admixtures are shown in Fig. 2.12.

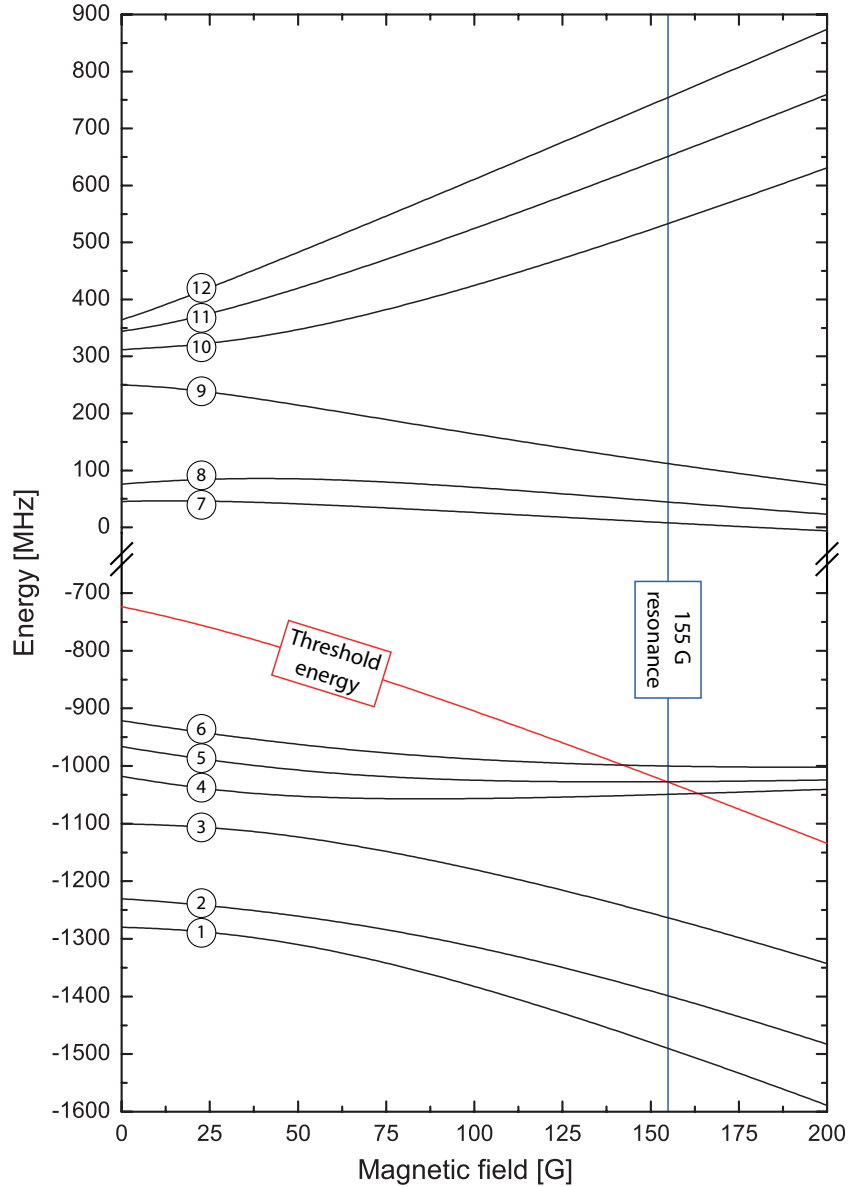


Figure 2.11: Eigenenergies of \mathcal{H} labeled ① - ⑫ and threshold energy (red). At 155 G the coupled molecular state with the eigenenergy specified by ⑤ crosses the threshold energy. This causes the Feshbach resonance at which the molecule production reported in [Voigt et al., 2009] takes place.

2.4 Feshbach resonances

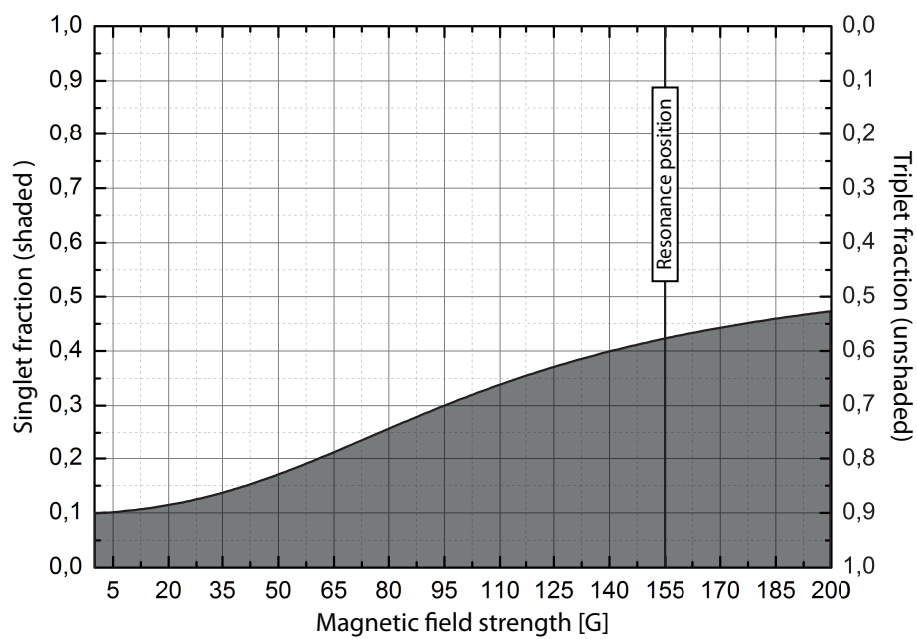


Figure 2.12: Magnetic field strength dependent singlet fraction (shaded area) of the coupled molecular state $|\textcircled{5}\rangle$. Singlet and triplet fractions naturally add up to 1, thus the triplet fraction is given as the unshaded area.

Chapter 3

Experimental apparatus

This chapter gives a brief overview over the experimental apparatus used to create a quantum degenerate mixture of the two fermionic, ${}^6\text{Li}$ and ${}^{40}\text{K}$, and the bosonic, ${}^{87}\text{Rb}$, alkali metal species. As the apparatus is described in detail in previous theses [Taglieber, 2008, Voigt, 2009, Costa, 2011], the aim of Sec. 3.1 is to give an overview over the most important aspects of the machine rather than a detailed description.

In Sec. 3.2, the optical trapping of particles by dipole forces is briefly described and applied to estimate the trapping potentials for ${}^6\text{Li}$ and ${}^{40}\text{K}$ atoms as well as ${}^6\text{Li}$ - ${}^{40}\text{K}$ molecules. The change in the trapping potential which the molecules experience when transferred from the highly excited Feshbach state to the absolute ro-vibrational ground state is calculated for typical trap parameters that have previously been used.

In Sec. 3.3 the imaging of particles in the Li-K mixture is described. While absorption imaging is easily possible for the atomic species, the former can only be applied to weakly bound Feshbach molecules in the present experimental apparatus. Some remarks on the direct imaging of ground state molecules are given.

3.1 The production of an ultracold mixture with up to three species

A drawing of the vacuum apparatus including magnetic field coils is shown in Fig. 3.1. Three compartments exist: one (Mot chamber) with a pressure optimized for magneto-optical trapping [Raab et al., 1987], a second one (UHV chamber) with a pressure below 10^{-11} mBar, and a third compartment that contains an oven and a Zeeman slower [Phillips and Metcalf, 1982, Taglieber, 2008] for ${}^6\text{Li}$. The slow ${}^6\text{Li}$ atoms entering the Mot chamber from the Zeeman slower are simultaneously captured together with ${}^{40}\text{K}$ and ${}^{87}\text{Rb}$ in a magneto-optical trap (Mot) [Taglieber et al., 2006]. The latter species are emitted from vapour dispensers installed in the Mot chamber. Following the loading of the Mot, two phases (dark Mot and compressed Mot, see [Taglieber, 2008]) and an optical molasses phase increase the phase space density of the three species mixture. Subsequently, the atoms in the mixture are optically pumped to the only combination of states that is stable against spin exchange collisional loss (see Chap. 2). In the ${}^6\text{Li}$ - ${}^{40}\text{K}$ - ${}^{87}\text{Rb}$ mixture, these states are ${}^{87}\text{Rb} : |F = 2, m_F = 2\rangle$, ${}^{40}\text{K} : |F = 9/2, m_F = 9/2\rangle$, ${}^6\text{Li} : |F = 3/2, m_F = 3/2\rangle$.

3.1 The production of an ultracold mixture with up to three species

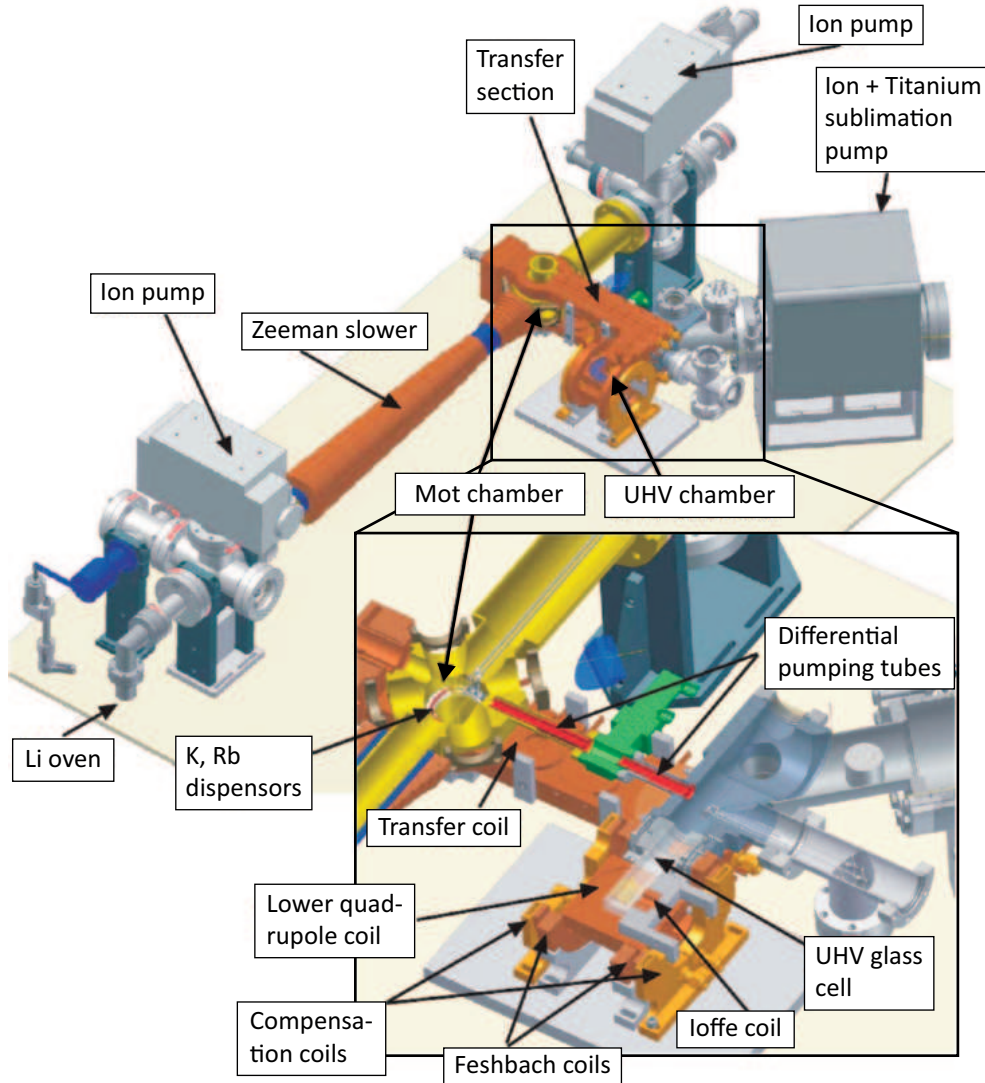


Figure 3.1: Vacuum apparatus with magnetic field coils. The main parts are labeled. The pressure in the Li oven and Mot chamber compartments is stabilized by ion pumps, while an integrated design that consists of a Titanium sublimation pump and an ion pump works on the side of the UHV chamber. A differential pumping tube consisting of 2 parts and vacuum valve (green) separates the UHV chamber from the Mot chamber. Transfer coils are used for the magnetic transport of particles from the Mot chamber to the glass cell, which is part of the UHV chamber. The final stages of an experimental cycle take place in the glass cell, where particles can be held in either a quadrupole trap, a quadrupole - Ioffe configuration (QUIC) trap, or an optical dipole trap. In the drawing the coils for magnetic trapping of the particles are labeled separately.

3. Experimental apparatus

In order to protect the sample of trapped atoms from collisions with the background gas and significantly increase the lifetime up to 70 s, it is transferred through a differential pumping tube to the second compartment denoted as ultra-high-vacuum (UHV) chamber in Fig. 3.1. This is achieved by means of a magnetic transport of the trapped atoms [Greiner et al., 2001].

On the UHV side, the cloud of trapped atoms is first compressed by an increase of the quadrupole coils' magnetic field gradient. Subsequently, the trap geometry is changed from a simple quadrupole to a quadrupole-Ioffe configuration trap in order to avoid zero magnetic field at the trap center. Now the mixture is ready for a long forced evaporation of ^{87}Rb [Davis et al., 1995b, Luiten et al., 1996, Ketterle and Druten, 1996]. In order to avoid unwanted transitions in the other particle species, the evaporation is achieved by means of a MW field which causes transitions between the $|F = 2, m_F = 2\rangle$ and $|F = 1, m_F\rangle$ manifolds of ^{87}Rb . As Rb is cooled further and further, the elastic interspecies collisions that occur lead to a sympathetic cooling [Myatt et al., 1997, DeMarco and Jin, 1999] of the fermionic species. Due to the small scattering cross-section of Li-Rb collisions, the cooling of K by Rb is far more efficient than the cooling of Li by Rb on the timescale of the forced evaporation. As, however, Li thermalizes with K on a faster timescale, the cooling of Li via K is the main mechanism to reach a quantum degeneracy of Li. In this manner, three species quantum degeneracy at temperatures of $T_K = 184 \text{ nK} = 0.35 T_F$, $T_{\text{Li}} = 313 \text{ nK} = 0.27 T_F$ and with particle numbers of $N_K = 1.3 \times 10^5$, $N_{\text{Li}} = 0.9 \times 10^5$ are reached [Taglieber et al., 2008]. The Rb cloud consists of a condensed fraction ($N_{\text{condensed}} = 4.5 \times 10^4$) and a thermal fraction at $T_{\text{Rb}} = 189 \text{ nK}$ ($N_{\text{thermal}} = 1.5 \times 10^5$). However, for most experiments so far only the fermionic species were kept, while Rb was evaporated through the trap bottom and possible remaining atoms were subsequently cleaned away with a resonant light pulse.

In order to be able to deploy homogeneous magnetic fields to a sample of ultracold atoms by the use of the Feshbach coils, the atoms can be loaded into an optical dipole trap [Grimm and Weidemüller, 1999]. The trap was realized with a 1064 nm Nd:YAG laser in the course of a diploma thesis, in which it is described [Wieser, 2006]. As more magnetic states are trappable in the dipole trap than in the magnetic trap, richer physics of particle scattering can be realized. Experiments at Feshbach resonances become possible only in this trap. Some details of optical dipole traps are discussed in the following section, while the reader is referred to [Voigt, 2009] for a detailed description of the Feshbach coils.

The utilized laser systems are described in detail in previous theses [Taglieber, 2008, Voigt, 2009, Costa, 2011] and will not be described here again. Due to the three species setup, many different light frequencies are needed. Detailed hyperfine level schemes for the atomic species are indicated in Fig. 3.2. Here Mot-, repumping-, imaging- and optical pumping transitions are shown. In addition there are detuned light fields for Zeeman slowing in the case of ^6Li . Further light fields that are not shown include the one for dipole trapping of the particles and one for imaging potassium at high magnetic fields.

3.2 Optical trapping of atoms and molecules

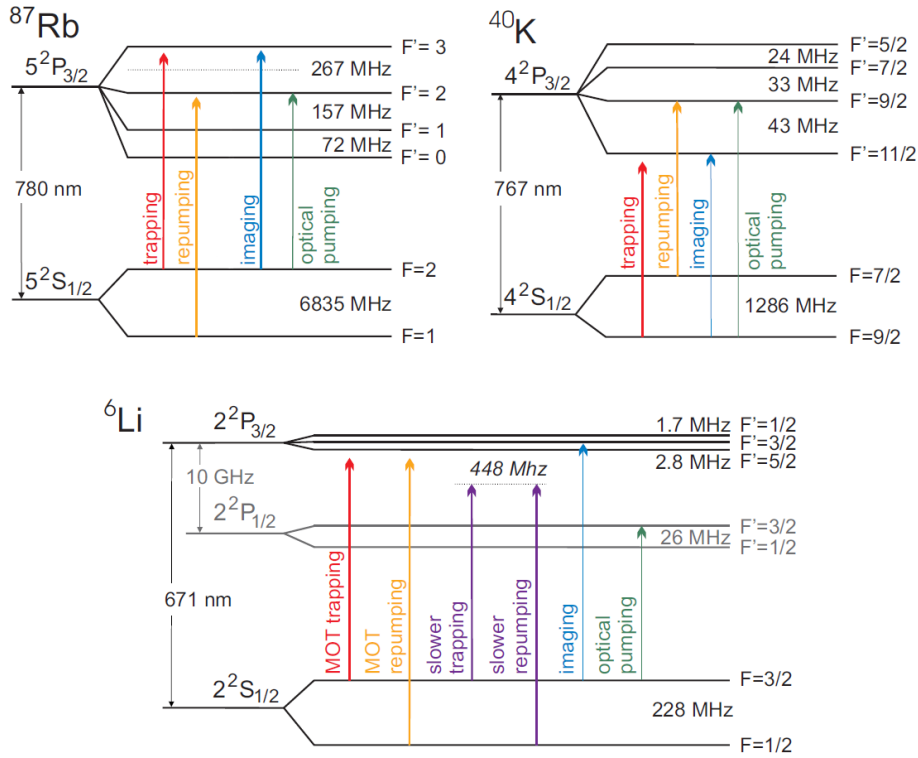


Figure 3.2: Atomic hyperfine energy level schemes for ^6Li , ^{40}K and ^{87}Rb . The transitions driven throughout the experimental cycle and their use are indicated.

3.2 Optical trapping of atoms and molecules

In the oscillator model for the mechanism of trapping by dipole forces, a particle is treated as an electric oscillator which is driven by a classical electric field. The latter is the electrical part of a light field in optical dipole traps [Grimm and Weidemüller, 1999]. The light field induces a dipole moment in the particle, which in turn interacts with the former. Driving forces oscillating at frequencies lower than the resonance frequency of the oscillator will cause an oscillation of the particle's dipole moment in phase with the driving light field. In this case the particle will experience a force towards locations in which the light intensity is strongest. If, on the other hand, the light field oscillates faster than the resonance frequency of the particle's oscillator, a phase shift of approximately π will occur between the polarization of the particle and the light field. In this case the particle is pushed away from locations of strong intensity. It is to be noted that this simple picture of the functional mechanism of a dipole trap, even though physically intuitive, will not yield exact quantitative results. However, in the case of the D lines of atomic alkali metals with their simple electron configuration, good agreement with experiment is found. Thus, the potential landscape created by a laser beam detuned in frequency from an electric dipole transition of a particle can be estimated by a quantitative application of the described theory.

The amplitude \tilde{p} of the dipole moment when a particle is polarized by a classical

3. Experimental apparatus

electric field with amplitude \tilde{E} is

$$\tilde{p} = \alpha \tilde{E} , \quad (3.1)$$

where α is the particle's polarizability. The interaction potential of the particle's dipole moment with the polarizing electric field is [Grimm and Weidemüller, 1999]

$$U_{\text{dip}}(r) = -\frac{1}{2\epsilon_0 c} \Re\epsilon(\alpha) I(r) . \quad (3.2)$$

Here $\Re\epsilon(\alpha)$ denotes the real part of α , the factor $1/2$ takes into account that the dipole moment is induced, ϵ_0 is the permittivity of vacuum and c the speed of light in vacuum. $I(r) = 2\epsilon_0 c |E|^2$ is the light field's intensity, which depends on the electric field strength E .

For the D lines of alkali metal atoms, the polarizability can in good approximation be obtained from a classical calculation based on Lorentz's model of a classical oscillator [Grimm and Weidemüller, 1999]:

$$\alpha_{\text{atom}} = 6\pi\epsilon_0 c^3 \frac{\Gamma}{\omega_0^2(\omega_0^2 - \omega^2 - i\Gamma\frac{\omega^3}{\omega_0^2})} . \quad (3.3)$$

Here ω is the trapping light frequency, ω_0 is the atom's transition frequency and Γ is the on resonance damping rate of the oscillator (linewidth of the atom's transition). With Eqns. 3.2 and 3.3, the dipole potential for the atomic alkali metal species becomes

$$U_{\text{dip}}(r) = -\frac{3\pi c^2}{2\omega_0^3} \left(\frac{\Gamma}{\omega_0 - \omega} + \frac{\Gamma}{\omega_0 + \omega} \right) I(r) . \quad (3.4)$$

In the case of molecules the polarizability is dependent on the ro-vibrational excitation. Theoretical data for the polarizability of Li-K molecular states in the $X^1\Sigma^+$ potential, dependent on their orientation and vibrational excitation, can be found in [Urban and Sadlej, 1995, Deiglmayr et al., 2008, Deiglmayr, 2009]. A selection of these data is shown on Tab. 3.1. The data is used here in order to obtain an estimate for the trapping potentials that are to be expected for Feshbach- and ground state molecules in the optical dipole trap of our experimental setup. It is to be noted that the published values are static polarizabilities. As previously mentioned, a static electric field *orients* molecules with a permanent dipole moment, and the main response of such a molecule to a static electric field is due to its orientation. This is however not the case in the

vibrational index	average polarizability [au]	vibrational index	parallel polarizability [au]	perpendicular polarizability [au]
0	318.7	0	489.7	236.2
47	450	38	955	340

Table 3.1: Li-K polarizabilities in atomic units [au] for selected states in dependence on the vibrational excitation and orientation [Deiglmayr et al., 2008]. These data are used to determine the optical trapping potentials presented in Fig. 3.3.

3.2 Optical trapping of atoms and molecules

light field of the dipole trap, which is oscillating at much higher frequencies than the rotational frequencies of molecular states. In this case the molecule interacts with the square of the electric field strength. For the case of a linearly polarized trapping light field this leads to the *alignment* of an induced dipole moment in the plane in which the light is polarized, but no *orientation* of the molecule [Friedrich and Herschbach, 1999]. If only a fast oscillating field is present, the polarizability averaged over all possible orientations of a molecule can be considered in order to estimate trap potentials. It is to be noted that the combination of a static electric field with a strong light field can however significantly facilitate the orientation of molecules [Friedrich and Herschbach, 1999]. This is due to the different polarizabilities along different molecular axes (see Tab. 3.1), which help to orient a molecule once the symmetry of the molecular state is broken by the static electric field. Depending on the parameters of static electric field strength and laser beam intensity, their relative orientations, as well as the rotational state of the molecule, the trapping potentials in these cases widely differ. Even untrapped, low field seeking states can be produced. The intensities of the light fields that typically have been used for trapping in our experiment are however too low for a useful exploitation of this effect.

Of special interest in the present case of ground state transfer are so called “magical wavelengths”. At these special wavelengths, the molecular polarizabilities, and thus the optical trapping potentials, are in good approximation the same for both the vibrationally highly excited state as well as the vibrational ground state. This allows to avoid a decreased phase space density of molecular samples following a STIRAP transfer. In order to calculate magical wavelengths, the coupling to electronically excited molecular states has to be determined. Thus, a precise knowledge of wavelengths and strengths of transitions to relevant electronically excited states have to be gained. In [Vexiau et al., 2011] magical wavelengths for the Cs_2 molecule are calculated. These effects cannot be described by the quasi static treatment deployed here.

In Fig. 3.3 (a) the trapping potentials of Li and K atoms and molecules in the ro-vibrational ground state and the vibrationally most excited state are compared. A dipole trap in horizontal-vertical configuration, as used in the current experimental setup, is assumed (see [Voigt, 2009] for details). A one-dimensional cut through the trap center in the direction perpendicular to both beams is shown. Both foci with Gaussian beam waists of $50\ \mu\text{m}$ are aligned to overlap in the center of the trap. The power in the horizontal beam is 2.44 W while the vertical beam power is 1.21 W. The wavelength of the trapping light is 1064 nm. Due to different polarizabilities, different particles experience different trap depths. For molecules, states with the highest vibrational excitations in the ground state singlet and triplet potentials show very similar polarizabilities. Thus, the shown potential (green) is a good approximation for the trapping potential that the Feshbach molecules experience (see Sec. 2.4.1). Further, molecules that are unpolarized in the laboratory frame are assumed. Averaged polarizabilities, given in Tab. 3.1, are used in Eq. 3.2 to determine the dipole potential functions. It is to be noted that the selection rules for ro-vibrational molecular transitions prohibit the trap laser field to excite molecules to continuum states. This transition rule is strict and only makes a trapping of molecules by use of a 1064 nm laser possible at all.

When molecules are oriented, the anisotropic molecular polarizability has to be considered. Thus, the trap potential experienced by molecules depends on the polarization

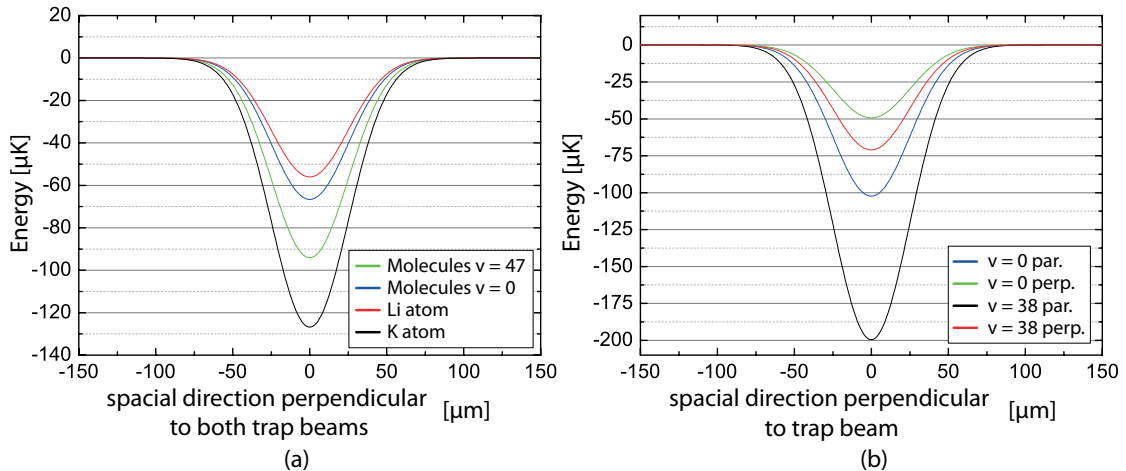


Figure 3.3: (a) dipole trap potentials for Li, K atoms and molecules in the $X^1\Sigma^+$ potential with vibrational quantum numbers $v = 0$ and $v = 47$. An averaged polarizability has been assumed for the molecules. The following trap depths are found: Li: $56.0 \mu\text{K}$, K: $126.8 \mu\text{K}$, ground state molecules: $66.6 \mu\text{K}$, molecules with vibrational excitation $v = 47$: $94.1 \mu\text{K}$. (b) Dependence of the trapping potential on the respective orientations of internuclear axis and electric field vector of the trapping light field. Trapping potentials for parallel as well as perpendicular orientations are shown for each the ro-vibrational ground state and the most polarizable state with $v = 38$ in the $X^1\Sigma^+$ potential. The following trap depths are found: ground state molecules parallel (perpendicular): $102.4 \mu\text{K}$ ($49.38 \mu\text{K}$), molecules with vibrational excitation $v = 38$ parallel (perpendicular): $199.7 \mu\text{K}$ ($55.4 \mu\text{K}$).

of the light field used for trapping. This is shown in Fig. 3.3 (b), where fully oriented molecules are assumed. It is to be noted that a complete orientation will however not be possible with the electrodes implemented in our experimental apparatus (see Sec. 2.3.2). Here, for simplicity a single linearly polarized 1064 nm trapping laser beam with a power of $2.44 + 1.21 \text{ W} = 3.65 \text{ W}$ and a focus of $50 \mu\text{m}$ is assumed. Again, the trap potential perpendicular to the beam in the plane of the beam focus is shown. The trap potentials of the $v = 0$ and $v = 38$ vibrational states in the molecular $X^1\Sigma^+$ potential depend on the relative orientations of the internuclear axis and the trapping light polarization. It can be seen that the trapping potentials for the ro-vibrational ground state differ by around 50% for parallel and perpendicular relative orientations of light field and internuclear axis. For the most polarizable state, with vibrational excitation $v = 38$, the anisotropy is still stronger.

The trap potentials for molecules are used in Sec. 5.4 to determine the decrease in phase space density of the molecular sample which is expected to follow the non-adiabatic change in trap potential caused by a fast STIRAP transfer. It is to be noted that the calculation refers to dipole trap settings that remain unchanged during transfer.

3.3 Imaging of particles in the Li- K mixture

3.3 Imaging of particles in the Li- K mixture

3.3.1 Absorption imaging of the atomic species and Feshbach molecules

If a cloud of atoms or molecules is illuminated by a light beam that is resonant or near resonant with a transition, the scattering that occurs casts a shadow in the light beam. The light can then be imaged on a camera making the density profile of the cloud $\tilde{n}(x, y)$ in the direction along the light beam visible. Thus, by measuring the optical density, the real column density profile and the approximate number of atoms in the cloud can be determined.

A light beam with an intensity profile $I_0(x, y)$ is attenuated by

$$I(x, y) = I_0(x, y)e^{-D(x, y)} \quad (3.5)$$

when passing through the cloud with optical density $D(x, y)$. The optical density depends on the particle column density $\tilde{n}(x, y)$

$$D(x, y) = 2\sigma_0 \frac{1}{1 + \frac{I}{I_{Sat}} + \frac{4\Delta^2}{\Gamma^2}} \tilde{n}(x, y) \quad (3.6)$$

where $\sigma_0 = \lambda^2/2\pi$ is the polarization averaged resonant scattering cross section of the atoms, I the beam intensity, which is taken to be constant in the region of the atoms, I_{Sat} the saturation intensity of the respective transition, Δ the detuning of the light from resonance, and Γ the decay rate of the excited state. $\tilde{n}(x, y)$ is found by a partial integration of the respective density profile given in Sec. 2.1.

The imaging of the different atomic species at low magnetic field is performed by employing the cycling optical transitions indicated in Fig. 3.2 and described in detail in [Taglieber, 2008, Voigt, 2009]. An additional laser is used to be able to image K at high magnetic fields as described in [Voigt, 2009, Costa, 2011].

The imaging of molecules is easily feasible only for highly excited molecules for which the binding energy is smaller than the linewidth of the imaging transition. In this case

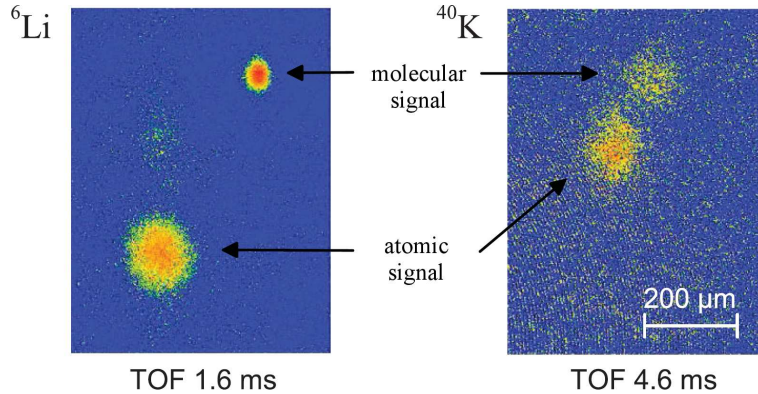


Figure 3.4: Absorption images of Li and K and molecular clouds after tof. Due to unfavorable Clebsch - Gordon coefficients the K image is recorded with not as good signal to noise ratio as the Li image.

the molecules can be excited to a continuum state of an electronically excited potential. The probability of spontaneous decay to lower lying states of the ground state potentials is small in this case as the Franck - Condon factors for these transitions are small. Thus the first scattered photon will with high probability dissociate the molecule. After this, normal atomic imaging on the mentioned cycling transition is possible.

Due to the different magnetic moments of the atomic species and the produced Feshbach molecules, it is possible to separate the clouds in an inhomogeneous magnetic field. Like this, it is possible to separately image molecules and atoms, as is described in [Voigt et al., 2009, Voigt, 2009]. Fig. 3.4 shows an absorption image obtained after time - of - flight (TOF) of the so separated clouds.

3.3.2 Imaging of deeply bound Li - K molecules

The direct imaging of deeply bound molecules is challenging as there exist no cycling transitions. Thus, a molecule, once excited to an electronically excited state, will, after spontaneous emission, with high probability end up in a state that is different from the state it was excited from. To good approximation, the transition matrix element R for a molecular transition factors into three contributions [Herzberg and Huber, 1950, Bernath, 2005]:

$$R = R_{\text{el}}^{n,m} \cdot R_{\text{vib}}^{v',v''} \cdot R_{\text{rot}}^{J',J''} . \quad (3.7)$$

Here, $R_{\text{el}}^{n,m}$ denotes the electronic part of the transition matrix element, which is of the order of a similar transition for an atom. $R_{\text{vib}}^{v',v''}$ is the vibrational transition matrix element, the modulus squared of which $|R_{\text{vib}}^{v',v''}|^2 = |\langle v' | v'' \rangle|^2$ is the Franck - Condon factor for the transition. $R_{\text{rot}}^{J',J''}$ is the rotational transition matrix element, the modulus squared of which is often called Hönl - London coefficient. This is a geometric factor which depends on the type of molecule. Within this thesis, the rotational factors for Zeeman transitions of a rigid symmetric top are used [Crawford, 1934]. Factors for other molecular geometries can e.g. be found in [Kovacs, 1969].

In order to estimate the number of photons that can be scattered from a Li - K molecular open cycle transition involving the ro - vibrational ground state and an electronically excited state in the $1^1\Pi$ potential (see Sec. 2.2.4), the Franck - Condon factors presented in Tab. 2.3 are used. For a transition from the absolute singlet ground state, the largest Franck - Condon factor of 0.17 is found for the transition to the state with $v = 2$ in the $1^1\Pi$ potential. By an application of the sum rule for vibrational transitions [Bernath, 2005], this means, that the probability of a spontaneous decay back to the vibrational ground state is 17%. Further, the rotational branching, described by the Hönl - London factors needs to be taken into account. For emission from the $1^1\Pi$, $v = 2$, $J = 1$, $M = 0$ state (strongest Zeeman transition), the latter are:

$$\begin{aligned} \sum \text{P - transitions:} & \quad 2 \\ \sum \text{Q - transitions:} & \quad \frac{3}{2} \\ \sum \text{R - transitions:} & \quad \frac{7}{10} . \end{aligned} \quad (3.8)$$

Only for the decay via a P - transition will the molecule end up in the same state from which it was excited. From an application of the sum rule for rotational branching

3.3 Imaging of particles in the Li-K mixture

[Bernath, 2005] follows that the probability for decay back to the rotational ground state is $\simeq 0.476$. Thus only $1/(1 - (0.17 \cdot 0.476)) \simeq 1.09$ photons can be scattered before a molecule falls back into a dark state after spontaneous emission. From this, it can be seen that a direct imaging of molecules needs rather high molecule numbers and a sensitive imaging system with a good signal to noise ratio. Direct imaging of ground state molecules has been achieved for the case of K-Rb [Wang et al., 2010]. It is to be noted that the Franck-Condon factor reported in [Wang et al., 2010] for the very similar transition in K-Rb is in very good agreement with the one for Li-K presented in Tab. 2.3.

A direct imaging of ground state molecules might be facilitated if they are confined in a tight optical lattice. In this case the extension of a highly excited molecular or a continuum state could be spatially restricted. This may lead to sufficient transition matrix elements of the ground state to a state slightly above the continuum of the electronically excited potential. In this case a short resonant light pulse could transfer the molecules into this electronically excited continuum state, followed by an imaging of atoms on the D2 line, much like in the case previously described for the molecules shown in Fig. 3.4. Like this, a cycling transition could be used for imaging.

Chapter 4

Experimental investigation of the Feshbach resonance at 155 G

This chapter describes how cross-dimensional relaxation is used to investigate the scattering properties of ${}^6\text{Li}$ - ${}^{40}\text{K}$ in the vicinity of the Feshbach resonance at 155 G. The results are published in [Costa et al., 2010a,b]. In Sec. 4.1 cross-dimensional relaxation is briefly described, while the technical details of the experimental sequence are presented in Sec. 4.2. The measurement allows a precise determination of the position and width of the Feshbach resonance (Sec. 4.4). The magnetic field dependent Li-K scattering cross sections, which are experimentally determined in Sec. 4.5, are observed to follow a Fano resonance function. Further, the dependence of the lifetime on the molecular binding energy is determined for Li-K Feshbach molecules, which are produced in the state that is determined in Sec. 2.4.1. The magnetic field dependent molecular lifetime is of importance for both the STIRAP (see Chap. 5) and even more so for the molecular spectroscopy (see Chap. 6). For the latter, the lifetime sets the rate at which frequency intervals can be probed for molecular transitions by direct use of the Feshbach molecules. Further, in the context of the choice of an optimal magnetic field strength for STIRAP, the precise knowledge of the width and position of the Feshbach resonance is beneficial.

4.1 Cross - dimensional relaxation

The method of cross-dimensional relaxation relies on observing the equilibration of a sample of particles which has previously been prepared in an out-of-equilibrium state. More specifically, the particles of a sample are prepared in a state in which their kinetic energy is anisotropically distributed. Thus, there exist perpendicular directions in which the mean particle kinetic energies are at a maximum in one direction while being minimal in the other. Yet, separately along each of these axes, the kinetic energies are in thermal equilibrium at all times, even though being time dependent. Thus, different temperatures can be assigned in different directions for the state of the sample at the beginning of the equilibration. The timescale on which these mean kinetic energies evolve to equilibrate to the same value allows to infer properties of the interaction between particles, like collisional cross sections.

The method of cross-dimensional relaxation has previously been used experimentally

4.1 Cross - dimensional relaxation

[Monroe et al., 1993, Regal et al., 2003, Goldwin et al., 2004] and treated theoretically [Roberts, 2001, Goldwin et al., 2005]. s- and p-wave collisions of particles of the same species as well as in Bose-Fermi mixtures have been characterized in this manner.

We observe cross - dimensional relaxation in a mixture of spin polarized ${}^6\text{Li}$ and ${}^{40}\text{K}$ atoms at temperatures at which only s-wave collisions need to be considered. Thus, particles of one species do not scatter among themselves and only interspecies interactions lead to cross - dimensional thermalization. Theoretically, this case is worked out in [Hahn, 2009, Costa, 2011] in a manner similar to the description given in [Goldwin et al., 2005]. The reader is referred to these references for a detailed quantitative description of cross - dimensional relaxation by a classical kinetic model.

In order to predict relaxation rates in the Li-K mixture, the normalized collision rates

$$\Gamma_{i,\text{coll}} = \langle n_{\text{Li,K}} \rangle_i \sigma_{\text{Li,K}} v_{\text{rel}} , \quad i \in \{\text{Li, K}\} , \quad (4.1)$$

where $\langle n_{\text{Li,K}} \rangle_i = \frac{1}{N_i} \int d^3r n_{\text{Li}}(\mathbf{r}) n_{\text{K}}(\mathbf{r})$

of a particle of species $i \in \{\text{Li, K}\}$ with particles of the other species are considered. Here, v_{rel} denotes the relative velocity of particles of both species and $\sigma_{\text{Li,K}}$ is the total s-wave scattering cross section for collisions of Li and K. $\langle n_{\text{Li,K}} \rangle_i$ is the overlap integral of the particle density functions n_{Li} and n_{K} , normalized by the total number of particles N_i of species i .

From the classical kinetic theory it is found that the decrease in energy anisotropy can be approximated to follow a single exponential decay, if the masses of the scattering partners in the mixture differ not too much. By introducing an additional mass dependent factor $\beta_{i,j}$, the relaxation rate

$$\Gamma_{i,j} = \frac{1}{\beta_{i,j}} \Gamma_{i,\text{coll}} , \quad i \in \{\text{Li, K}\} \quad (4.2)$$

of the energy anisotropy of a particle of species i within a cloud of particles of species j is obtained. $\beta_{i,j}$ can be interpreted as the mean of the number of collisions that are needed to reach a $1/e$ decay of an initially present energy anisotropy. For particles with unequal masses $\beta_{i,j} \neq \beta_{j,i}$, which means also the number of collisions needed for thermalization is different. In addition, experimentally, it is not always easily possible to set $N_i = N_j$, which can further lead to a discrepancy in the collision rate per particle.

Let us choose a coordinate system along the directions of maximum ($\hat{\mathbf{x}}$) and minimum ($\hat{\mathbf{z}}$) mean kinetic energies. For the case $\beta_{i,j} \simeq \beta_{j,i}$ the decay of the energy anisotropy during cross - dimensional relaxation can be approximated by

$$\Delta E(t) = (\langle E_x \rangle_{t=0} - \langle E_z \rangle_{t=0}) e^{-\Gamma_{i,j} t} . \quad (4.3)$$

Here, $\langle E_x \rangle_{t=0}$ denotes maximum mean kinetic energy, while $\langle E_z \rangle_{t=0}$ denotes the minimum mean kinetic energy in the sample at time $t = 0$, directly after the generation of the energy anisotropy.

It is to be emphasized that this description is based on a classical theory. Thus, for very cold samples far in the quantum degenerate regime, the theory will estimate larger $\Gamma_{i,j}$ than are experimentally observed. This is due to a decrease in scattering rates

caused by Pauli blocking [DeMarco et al., 2001]. The approximations mentioned above remain accurate for temperatures in the range of $T/T_F > 0.5$ (see Sec. 2.1) and in the regime where only s-wave scattering contributes.

4.2 Experimental generation of kinetic energy anisotropies

The generation of energy anisotropies that are large enough to experimentally observe cross-dimensional relaxation with a good signal to noise ratio can be challenging. In the experiment a mixture of two effects are used to generate the energy anisotropy. These are a change in the geometry and depth of our optical dipole trap (see Sec. 3.2) and the change in trap geometry resulting from the loading of particles from the QUIC trap into the optical dipole trap (see Chap. 3).

In Fig. 4.1 a sketch of the experimental sequence is shown. After the initial preparation of a mixture of ${}^6\text{Li}$, ${}^{40}\text{K}$ and ${}^{87}\text{Rb}$ in a cigar shaped QUIC trap (see [Taglieber et al., 2008, Taglieber, 2008]), Rb is completely evaporated and some particles that might remain are subsequently cleaned away by a resonant light pulse. The remaining fermionic species are in turn loaded into an optical dipole trap, for which the trapping frequencies are kept low in order to keep the particle densities low. This limits the collision rates during the rather long timespan needed for an adiabatic transfer between the traps and keeps the mixture from undergoing cross-dimensional relaxation at times when this is still unwanted. Due to the respective orientations of the magnetic and optical traps and the change in trapping frequencies, an anisotropy in the mean kinetic particle energies is generated in the course of changing from the magnetic to the optical trap. For the definition of a quantization axis, the Feshbach magnetic field strength is ramped to 3 G during the time the magnetic trap is switched off. Afterwards, the magnetic field strength is ramped to 20 G at which the atoms are transferred to the hyperfine states (${}^6\text{Li}$: $|1/2, 1/2\rangle$, ${}^{40}\text{K}$: $|9/2, -5/2\rangle$) for which the Feshbach resonance at 155 G occurs (see Sec. 2.4.1). Subsequently, the magnetic field strength is ramped to a value close to the one at which cross-dimensional relaxation is observed and the particle densities are increased. For this, the optical trapping power is increased, which is done in a way that also increases the already present energy anisotropy. With this last step, the final energy anisotropy between the \hat{x} and \hat{z} directions is generated. Now the magnetic field strength is changed to the final value at which the cross-dimensional relaxation takes place and the mixture is held in trap for a timespan t during which it undergoes cross-dimensional relaxation. The final trap frequencies in the optical trap are determined as

$$\begin{aligned}
 {}^6\text{Li} : |1/2, 1/2\rangle & \left\{ \begin{array}{l} \nu_x = 963 \text{ Hz} \\ \nu_y = 1076 \text{ Hz} \\ \nu_z = 479 \text{ Hz} \end{array} \right\} \pm 5\% \\
 {}^{40}\text{K} : |9/2, -5/2\rangle & \left\{ \begin{array}{l} \nu_x = 561 \text{ Hz} \\ \nu_y = 627 \text{ Hz} \\ \nu_z = 279 \text{ Hz} \end{array} \right\} \pm 5\%
 \end{aligned}$$

After the holding time t , the optical trap is switched off and the Li and K clouds are imaged at low magnetic field after time of flight (tof, see Chap. 2) durations of 2 ms for Li and 5 ms for K. Gaussian density functions instead of Fermi-Dirac profiles are fit

4.2 Experimental generation of kinetic energy anisotropies

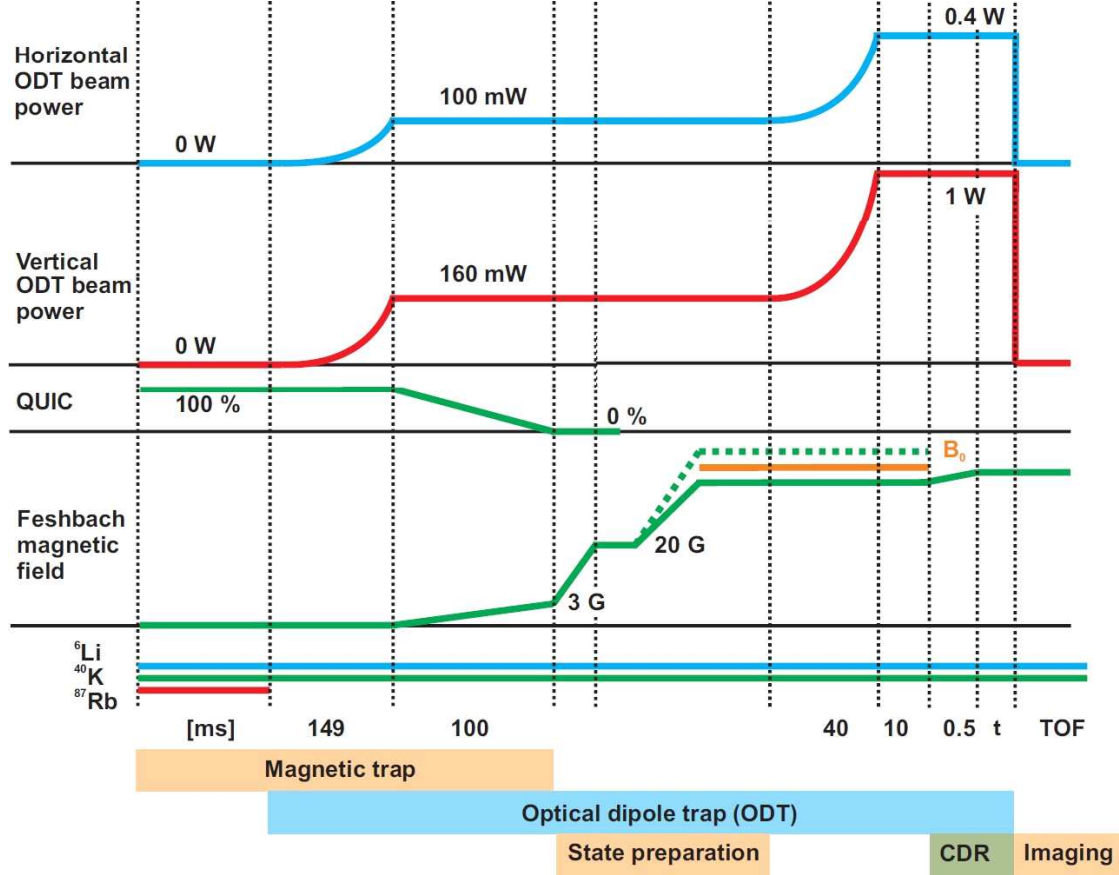


Figure 4.1: Sketch of the experimental sequence for the observation of cross-dimensional relaxation of ${}^6\text{Li}$ and ${}^{40}\text{K}$. B_0 marks the magnetic field strength at which the Feshbach resonance occurs. t denotes the variable holding time at which the parameters for cross-dimensional relaxation have been set. The time spans during which certain stages of the experimental sequence are passed, are given. The figure is taken from [Costa, 2011].

to the cloud images as a good approximation, since the mixture is not prepared in the deeply degenerate regime. For this, the classical intra trap density function Eq. 2.7, is scaled by the use of Eq. 2.13 with the known trapping frequencies and tof . This allows to determine the cloud temperatures in the directions \hat{x} and \hat{z} . When the clouds are fully thermalized, we observe atom numbers of $N_{\text{Li}} \simeq 50000$ and $N_{\text{K}} \simeq 70000$ at temperatures of $T_{\text{Li}} \simeq 0.5 T_F^{\text{Li}}$ and $T_{\text{K}} \simeq 0.6 T_F^{\text{K}}$ for magnetic field strengths not too close to resonance. An error in the determination of the mean energy per particle of not more than 6% is made by the use of Gaussian fits in this regime. Further, the observed temperatures allow a description of the physics of cross-dimensional relaxation by means of the classical model.

In order to be able to record thermalization curves of the mixture in dependence on the absolute magnetic field strength, the latter is precisely calibrated. This is achieved by driving the radio frequency (rf) transition $|9/2, -9/2\rangle \rightarrow |9/2, -7/2\rangle$ in ${}^{40}\text{K}$ and state selective imaging at high magnetic field. The dependency of the rf transition frequency

on the magnetic field is known from the Breit - Rabi formula [Breit and Rabi, 1931]. By optimization of the transferred population, the precise transition frequency is found.

4.3 Experimental observation of cross - dimensional relaxation

In order to measure the difference in the cross - dimensional relaxation rates for Li and K, a measurement of the energy anisotropy after a variable hold time t at a magnetic field strength of 152.4 G is carried out for both species. Here, a magnetic field strength is chosen for which losses for the long time spans t are not too large, but still the scattering length is larger than the background scattering length. Fig. 4.2 shows data on the thermalization of the energy differences $\langle E_x \rangle / \langle E_z \rangle$. Least square fits to the data for each species are obtained by use of the function

$$\frac{\langle E_x \rangle}{\langle E_z \rangle}(t) = \frac{1 + \varepsilon_x e^{-\Gamma_{i,j} t}}{1 + \varepsilon_z e^{-\Gamma_{i,j} t}}, \quad (4.4)$$

$$\text{where } \varepsilon_k = \frac{3 \langle E_k \rangle_{t=0}}{\langle E_x \rangle_{t=0} + \langle E_y \rangle_{t=0} + \langle E_z \rangle_{t=0}} - 1 \quad (k \in \{x, z\}).$$

In order to determine $\langle E_y \rangle_{t=0}$, the imaging direction in the experiment was changed. In this way, the cross - dimensional relaxation rates

$$\Gamma_{\text{Li,K}} = 63 \pm 8 \text{ ms}^{-1}$$

$$\Gamma_{\text{K,Li}} = 19 \pm 2 \text{ ms}^{-1}$$

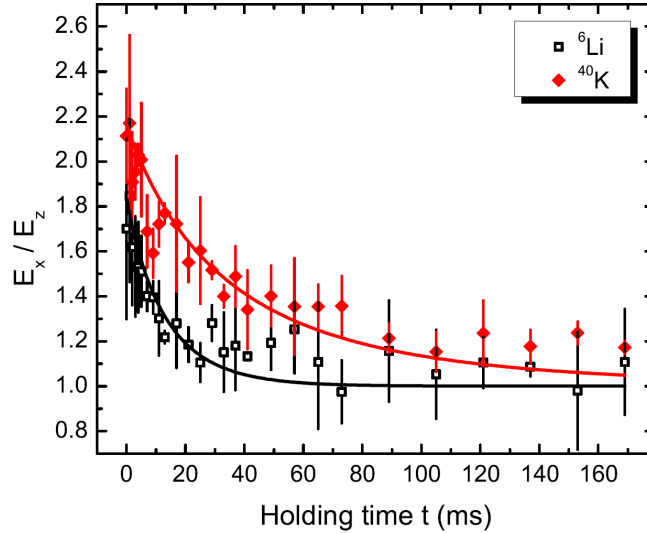


Figure 4.2: Cross - dimensional relaxation of ${}^6\text{Li}$ and ${}^{40}\text{K}$. Large energy anisotropies of $\langle E_x \rangle / \langle E_z \rangle = 2.2$ ($\langle E_x \rangle / \langle E_z \rangle = 1.8$) have been generated for Li (K). Particle numbers for this measurement are $N_{\text{Li}} = 35000$ and $N_{\text{K}} = 80000$. An uncertainty in overall atom numbers of 50% is assumed. The figure is taken from [Costa, 2011].

4.4 Experimental determination of the position and width of the 155 G resonance

are found. The $\beta_{i,j}$ -factors are found from additionally taking the particle number into account:

$$\frac{\beta_{\text{K,Li}}}{\beta_{\text{Li,K}}} = \frac{\Gamma_{\text{Li,K}} N_{\text{Li}}}{\Gamma_{\text{K,Li}} N_{\text{K}}} = 1.5 \pm 1.1 .$$

Due to the rather high uncertainty in the particle numbers the error is specified relatively large. It is however consistently found for different magnetic field strengths that the thermalization of Li occurs faster than that of K.

The kinetic model for thermalization [Hahn, 2009, Costa, 2011] predicts a ratio of the same $\beta_{i,j}$ -factors of 2.8. This prediction does however not take different temperatures of the species into account. An analysis shows that this can significantly change the ratio of $\beta_{i,j}$ -factors [Costa, 2011]. The different temperatures of the species are likely due to the different Fermi energies for both species in the trap. We estimate a difference of 23% in the Fermi energies between the species in our trap, which could be causing the difference between the predicted and measured $\beta_{i,j}$ -factors. However, for a concluding statement on the matter, a more precise determination of the atom numbers, which vary for each of the data points shown in Fig. 4.2, would need to be achieved.

4.4 Experimental determination of the position and width of the 155 G resonance

In order to use cross-dimensional relaxation to determine the position B_0 and width Δ of the 155 G resonance the magnetic field strength is varied while keeping the holding timespan t constant. For the determination of the maximum scattering cross section, t is chosen such, that the energy anisotropy $(\langle E_x \rangle / \langle E_z \rangle)(t)$ does not quite reach unity, even for the magnetic field strengths closest to the resonance. On the other hand, for the determination of the minimum scattering cross section it is advantageous to choose longer time spans. Taking the average of many such measurements, the values

$$\begin{aligned} B_0 &= 154.71 \pm 0.05 \text{ G} \\ \Delta &= 1.02 \pm 0.07 \text{ G} \end{aligned}$$

are determined experimentally. These averaged values include measurements at different trapping frequencies in order to lower the possible impact of density effects. The measured values are in agreement with other measurements that have been reported [Naik et al., 2011]. While the resonance position is well in agreement with theoretical values obtained from coupled channel calculations, the theoretical prediction for the resonance width is smaller ($\Delta_{\text{theo}} = 0.88 \text{ G}$). This can be attributed to the finite temperatures and fermi energies of the sample, which both cause particle threshold energies (see Fig. 2.10) to occupy a finite interval. In the present case of a narrow resonance, the latter can lead to the observed broadening as the energy range in which a coupling between open and closed scattering channels occurs can approach the order of the threshold energy range of the mixture.

4.5 Resonant ${}^6\text{Li}$ - ${}^{40}\text{K}$ scattering cross sections around 155 G

Cross-dimensional relaxation is used to map out the Li-K scattering cross sections in the magnetic field strength range where the 155 G resonance occurs. For this, the scattering rates $\Gamma_{\text{Li,K}}$ of Li have been determined from data of the kind shown in Fig. 4.2, for different values of the magnetic field strength around the Feshbach resonance. Analyzing Li data is advantageous, since, in our case the Clebsch-Gordan coefficients for imaging at high magnetic field strengths are more favorable and also the cross-dimensional equilibration occurs faster. This is of importance for a measurement very close to the Feshbach resonance, where three body losses limit the lifetime of the sample (see Sec. 2.3.2). From the $\Gamma_{\text{Li,K}}$, which are experimentally found, the magnetic field dependent total scattering cross section $\sigma_{\text{Li,K}}(B)$ is determined. According to Eq. 2.30, $\sigma_{\text{Li,K}}(B)$ is directly related to the scattering length $a(B)$ which can be tuned by the magnetic field in accordance with Eq. 2.32. Fig. 4.3 shows the data obtained in this manner. Also shown is a theoretical Fano resonance function for which the parameters B_0 and Δ , that have been experimentally determined as described above, and the off-resonant scattering length a_{bg} [Wille et al., 2008] are used. The Fano function for the resonance has been determined from the Asymptotic Bound State Model (see Sec. 2.4.1). In the data we observe a change in $\sigma_{\text{Li,K}}(B)$ of almost three orders of magnitude. Considering the errors due to the particle number determination, we find good agreement between theory and our

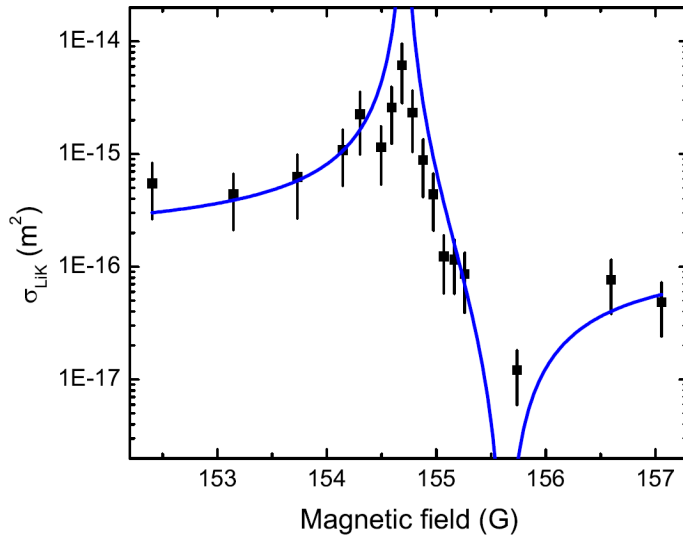


Figure 4.3: Experimental data of the scattering cross section measured with cross-dimensional relaxation in the magnetic field range around the 155 G ${}^6\text{Li}$ - ${}^{40}\text{K}$ Feshbach resonance. The solid line corresponds to a prediction gained from the asymptotic bound state model with the parameters $B_0 = 154.71$ G, $\Delta = 1.02$ G, $a_{\text{bg}} = 63.5 a_0$. Further, the particle wave number k is set equal to the Fermi wave number k_F and $\mu_{\text{res}} = 1.7\mu_B$ (see Eq. 2.31). Here μ_{res} is the difference in magnetic momenta between atoms and molecules, while μ_B is the Bohr magneton. The figure is taken from [Costa, 2011].

4.6 Magnetic field dependent lifetime of ${}^6\text{Li}$ - ${}^{40}\text{K}$ dimers

measurement of the off-resonant scattering cross sections.

The following effects, which could cause a deviation of the measured scattering cross sections, are estimated not to be significant: Firstly, the influence of Pauli blocking will change $\sigma_{\text{Li,K}}(B)$ by not more than 15%, at the temperatures we are working with [DeMarco et al., 2001, Gehm, 2003]. Secondly, except for the datapoint closest to resonance, the effect of hydrodynamic behavior [Ketterle and Zwiernik, 2006] is excluded.

4.6 Magnetic field dependent lifetime of ${}^6\text{Li}$ - ${}^{40}\text{K}$ dimers

In [Voigt et al., 2009, Voigt, 2009, Costa, 2011] a measurement of the magnetic field dependent lifetime of a mixture of atoms and molecules is presented. The precise parameters for the width and position of the 155 G Feshbach resonance are used here (see also [Costa, 2011]) to determine the lifetime in dependence on the magnetic field strength.

For the measurement, a sample of Li and K atoms is prepared at a magnetic field strength of 156.44 G in the states for which the Feshbach resonance occurs. The trapping frequencies in the optical dipole trap are lowered for these measurements to

$$\begin{aligned} {}^6\text{Li} : |1/2, 1/2\rangle & \begin{cases} \nu_x = 285 \text{ Hz} \\ \nu_y = 440 \text{ Hz} \\ \nu_z = 333 \text{ Hz} \end{cases} \\ {}^{40}\text{K} : |9/2, -5/2\rangle & \begin{cases} \nu_x = 168 \text{ Hz} \\ \nu_y = 256 \text{ Hz} \\ \nu_z = 194 \text{ Hz} \end{cases} . \end{aligned}$$

Atomic particle densities of $n_{\text{Li}} = 2.9 \times 10^{12} \text{ cm}^{-3}$ and $n_{\text{K}} = 2.2 \times 10^{13} \text{ cm}^{-3}$ at temperatures of $T_{\text{Li}} = 0.3 T_F^{\text{Li}}$ and $T_{\text{K}} = 0.4 T_F^{\text{K}}$ are measured. After both species are transferred to the respective magnetic states, the magnetic field strength is adiabatically lowered by use of a linear ramp until the value at which the measurement is carried out is reached. At this field strength the mixture is held for variable durations t before being released from the trap. Subsequently, the molecular and atomic clouds are separated and imaged as described in Sec. 3.3. $1/e$ lifetimes are determined from the decaying molecule number obtained from fits to the clouds. Further, the average cloud density of molecules is determined at $t = 0$. From these values, the density weighted lifetimes are determined. Fig. 4.4 shows the results of two types of measurements:

Firstly, the density weighted lifetimes, depending on the magnetic field strength and the approximate molecular binding energy, are shown. In order to estimate the binding energy, Eq. 2.31 and the value $\mu_{\text{res}} = 1.6 \mu_B$ from the coupled channels calculation in [Naik et al., 2011] are used. The lifetimes are obtained in the manner discussed above. The newly determined field strength B_0 at which the Feshbach resonance occurs is marked by an orange line, while the orange bar stands for the 50 mG uncertainty of the measurement.

Secondly, the results of an indirect measurement of molecule formation is shown (Li, K atom number measurement, see [Voigt et al., 2009, Voigt, 2009, Costa, 2011] for details). For these data, the atomic mixture is prepared at 156.90 G followed by a linear adiabatic change of the magnetic field strength towards 154.54 G. Here, the rate of

4. Experimental investigation of the Feshbach resonance at 155 G

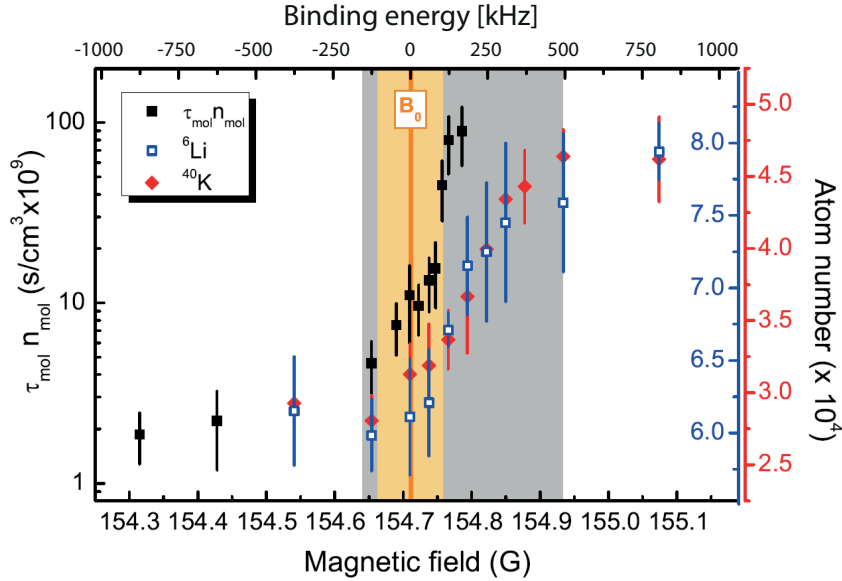


Figure 4.4: Density weighted lifetimes of molecules in atom - molecule mixtures in dependence on the magnetic field strength and the estimated molecular binding energy. It is to be emphasized that the binding energies are obtained from a calculation and not from an experimental determination. B_0 denotes the field strength at the Feshbach resonance. The orange bar represents the error of 50 mG in the determination of the resonance position. Note that molecules are seen also on the atomic side of the resonance. The gray bar marks the region in which atom numbers (molecule numbers) change significantly by around two orders of magnitude.

change in the magnetic field strength has been optimized to produce a maximum number of molecules. After molecule production the magnetic field is adiabatically ramped to the value B for the measurement and subsequently quickly reduced to low values for imaging. In this fashion, the losses in atom number, dependent on the final magnetic field strength B are observed. As for the data points at magnetic field strengths higher than the Feshbach resonance, a molecular associating and a dissociating field strength sweep have occurred and the losses are associated with molecule production.

As shown in Fig. 4.4, molecules are observed even at magnetic field values of 70 mG above the Feshbach resonance. For the BEC-BCS crossover at narrow Feshbach resonances, this has been theoretically predicted [Gurarie and Radzihovsky, 2007]. In [Costa, 2011], the underlying principles for molecule existence above the Feshbach resonance are discussed. Further, the obtained data is interpreted in the light of the predictions described in [Gurarie and Radzihovsky, 2007]. The interested reader is referred to these references. A similar measurement is reported in [Spiegelhalter et al., 2010]. In this publication the magnetic field dependent molecule fraction, however at the 168 G ^6Li - ^{40}K resonance, is investigated. The resonance is narrower, molecules are observed in a smaller magnetic field range and molecular lifetimes are shorter.

It is to be noted that the interpretation of the data for magnetic field strengths $B > B_0$ has not been concluded. While the observation of long-lived molecular Feshbach

4.6 Magnetic field dependent lifetime of ${}^6\text{Li}$ - ${}^{40}\text{K}$ dimers

states is in qualitative agreement with the theoretical predictions mentioned above, this theoretical treatment does not include a description of the dynamics occurring in the sample. Further investigation is needed for an interpretation of these data as molecular lifetimes. In this context the molecular lifetime in a pure molecular sample will be measured in Singapore. In order to purify the mixture of Li and K atoms and Li-K molecules, resonant light pulses will be used to clear out unbound atoms from the trap. The technical details to achieve this have already been solved in Singapore. Raman ground state transfer will be attempted only if a pure molecular sample is obtained, as in this case both the samples of Feshbach molecules and molecules in the ro-vibrational ground state will be more stable and detection will be easier.

Chapter 5

Raman transitions between molecular states of Li - K

In this chapter the details of the Stimulated Raman Adiabatic Passage (STIRAP) sequence, which is planned to be used to coherently transfer the Feshbach molecules into the absolute ro - vibrational ground state, are described. First, a brief review on STIRAP is given in Sec. 5.1. Then, Raman laser wavelengths are determined based on the ro - vibrational term energies, which are presented in Sec. 2.2.4. Further, the Franck - Condon factors presented in Sec. 2.2.5 are used to estimate the transition dipole moments of transitions between states in the $X^1\Sigma^+$ and $1^1\Pi$ potentials. These are used for an estimation of Rabi frequencies that can be expected, which in turn are used to estimate the duration of STIRAP transfer under realistic experimental conditions. Also, other considerations with respect to the optimization of the STIRAP sequence and the electronically excited levels that can be addressed are mentioned in Sec. 5.3. The photon recoil that is to be expected from the transfer, as well as the change in the phase space density is briefly estimated in Sec. 5.4.

From the Rabi frequencies and the duration of a proposed STIRAP sequence, the requirements for the Raman laser system, which is presented in Chap. 7, can be deduced. It is found that several mW of light power for each of the Raman light fields are sufficient. Further, 1 kHz of relative linewidth will be sufficient in order to ensure coherence over the duration of STIRAP transfer.

5.1 Intensity controlled Stimulated Raman Adiabatic Passage in a Λ - configuration three level system

This section gives a brief review on intensity controlled STIRAP. However, the general dynamics of a three level system in the presence of two light fields that cause a coupling of levels will not be described here. For detailed information on this subject the reader is referred to [Berman, 1997, Vitanov et al., 2001]. Intensity controlled STIRAP allows for much more efficient and stable population transfer as compared to transfer schemes in which a π - pulse condition [Berman, 1997] has to be satisfied. Thus, STIRAP is less sensitive to technical imperfections as compared to other schemes. This makes it well suitable for the coherent ground state transfer of Feshbach molecules.

5.1 Stimulated Raman Adiabatic Passage in a Λ -configuration three level system

Here, a semi-classical description for STIRAP in a Λ -configuration three level system is adopted, the details of which can be found in [Vitanov et al., 2001]. Fig. 5.1 schematically shows the energies of the so called diabatic states $|e\rangle$, $|i\rangle$ and $|g\rangle$. Both levels $|e\rangle$ and $|g\rangle$ are coupled to level $|i\rangle$ by two separate light fields. In the case of state transfer of the Li-K molecules, state $|e\rangle$ could denote the vibrationally excited Feshbach state, $|g\rangle$ could denote the ro-vibrational ground state in the singlet potential and $|i\rangle$ could denote an electrically and vibrationally excited state in the $^1\Pi$ potential (see Sec. 2.2.3, Fig. 2.3).

In the description given here only electric dipole transitions and no decay from any of the states is taken into account and the rotating wave approximation (RWA) [Berman, 1997] is adapted. With this, the single photon Rabi frequencies

$$\Omega_{g,i}(t) = -\frac{\langle i|\mathbf{d}\cdot\mathbf{E}_{g,i}(t)|g\rangle}{\hbar} \quad (5.1)$$

$$\Omega_{e,i}(t) = -\frac{\langle i|\mathbf{d}\cdot\mathbf{E}_{e,i}(t)|e\rangle}{\hbar} \quad (5.2)$$

are a measure of the coupling of the levels by the light fields. Here, \mathbf{d} denotes the transition dipole moment and $\mathbf{E}(t)$ is electric field amplitude of the light field in RWA which has a slow time dependence and does not oscillate with the rest frame light frequency. The common detuning of both light fields is denoted Δ , while δ names a respective detuning of both light fields from two photon resonance (in angular frequency units). In the RWA the Hamiltonian of the three level system is of the form

$$\mathcal{H}(t) = \hbar \begin{pmatrix} 0 & \frac{1}{2}\Omega_{e,i}(t) & 0 \\ \frac{1}{2}\Omega_{e,i}(t) & \Delta & \frac{1}{2}\Omega_{g,i}(t) \\ 0 & \frac{1}{2}\Omega_{g,i}(t) & \delta \end{pmatrix}. \quad (5.3)$$

For efficient STIRAP it is essential that two photon resonance between the states $|e\rangle$ and $|g\rangle$ is fulfilled, that is to say $\delta = 0$, which will be assumed in the following. By a diagonalization of \mathcal{H} the adiabatic eigenenergies

$$\epsilon_+(t) = \frac{1}{2}(\Delta + \sqrt{\Delta^2 + \Omega^2(t)}) \quad (5.4)$$

$$\epsilon_0(t) = 0 \quad (5.5)$$

$$\epsilon_-(t) = \frac{1}{2}(\Delta - \sqrt{\Delta^2 + \Omega^2(t)}) \quad , \quad (5.6)$$

with

$$\Omega(t) = \sqrt{\Omega_{g,i}^2(t) + \Omega_{e,i}^2(t)} \quad (5.7)$$

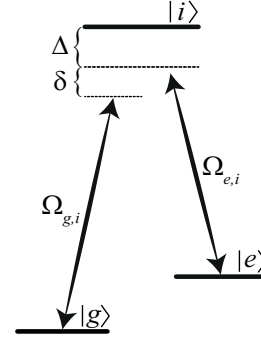


Figure 5.1: Three level system in Λ -configuration. States are coupled by the electric dipole operator $-\mathbf{d}\cdot\mathbf{E}(t)$ with the single photon Rabi frequencies $\Omega_{g,i}(t)$, $\Omega_{e,i}(t)$.

5. Raman transitions between molecular states of Li - K

and eigenstates

$$\Phi_+(t) = \sin(\vartheta(t)) \sin(\varphi(t))|g\rangle + \cos(\varphi(t))|i\rangle + \cos(\vartheta(t)) \sin(\varphi(t))|e\rangle \quad (5.8)$$

$$\Phi_0(t) = \cos(\vartheta(t))|g\rangle - \sin(\vartheta(t))|e\rangle \quad (5.9)$$

$$\Phi_-(t) = \sin(\vartheta(t)) \cos(\varphi(t))|g\rangle - \sin(\varphi(t))|i\rangle + \cos(\vartheta(t)) \cos(\varphi(t))|e\rangle \quad (5.10)$$

in the presence of the classical electrical fields are found. The adiabatic eigenstates are given in the basis of the diabatic states that are eigenstates of the system when no light fields are present. The mixing angles

$$\tan(\vartheta(t)) = \frac{\Omega_{e,i}(t)}{\Omega_{g,i}(t)} \quad \text{and} \quad \tan(2\varphi(t)) = \frac{\Omega(t)}{\Delta} \quad (5.11)$$

are found.

In intensity controlled STIRAP $\Phi_0(t)$ is adiabatically rotated from an angle $\vartheta = 0$, for which it coincides with state $|e\rangle$, to $\vartheta = \pi/2$ for which it coincides with $|g\rangle$. This is accomplished by a relative change in the power of the two light fields, which changes the Rabi frequencies $\Omega_{e,i}(t)$ and $\Omega_{g,i}(t)$ and thus the mixing angle $\vartheta(t)$. The state vector $|\Psi(t)\rangle$ follows the rotation of $|\Phi_0(t)\rangle$ as is schematically shown in Fig. 5.2. It is important to note that $|\Phi_0(t)\rangle$ does not contain any admixture of the decaying electronically excited state $|i\rangle$. This is most important for the coherence of the transfer process.

Fig. 5.2 corresponds to the so called counterintuitive STIRAP pulse sequence, which is schematically shown in Fig. 5.3. Here a Gaussian envelope of the light pulses with time is assumed, as it is planned to be used for a transfer of Feshbach molecules. In the case of a STIRAP transfer of Feshbach molecules, the originally populated state $|\Psi(t=0)\rangle$ corresponds to state $|e\rangle$. In the first part of the sequence, $\Omega_{e,i}(t)$ is negligible, while $\Omega_{g,i}(t)$ is present. This serves to align the adiabatic state $|\Phi_0(t)\rangle$ with $|e\rangle$ and adiabatically leads to an Autler - Townes splitting of levels [Vitanov et al., 2001]. Due to the Autler - Townes splitting the process is coherent even if both light fields are kept on single photon resonance $\Delta = 0$ and $|i\rangle$ is a decaying state. The rotation of $|\Psi(t)\rangle$ and $|\Phi_0(t)\rangle$ take place when both light fields are present. In the end of the symmetric sequence, when $|\Psi(t)\rangle$ and $|\Phi_0(t)\rangle$ coincide with $|g\rangle$, the Autler - Townes splitting, this time caused by $\Omega_{g,i}(t)$, is adiabatically reduced to zero. Thus, by applying the pulse sequence shown in Fig. 5.3, the two-photon transition is made without any decay from state $|i\rangle$.

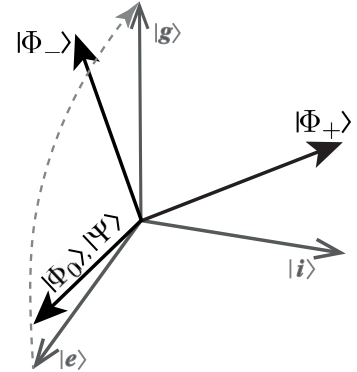


Figure 5.2: Adiabatic transfer of the population from state $|e\rangle$ to $|g\rangle$ by adiabatic following of $|\Psi(t)\rangle$ and rotation of the adiabatic state $|\Phi_0\rangle$. For $t = 0$, $|\Phi_0\rangle$ and $|\Psi(t)\rangle$ coincide with $|e\rangle$, while for $t \gg 2T$ they coincide with $|g\rangle$.

5.2 Wavelengths and dipole moments of transitions between molecular states in the $X^1\Sigma^+$ and $1^1\Pi$ potentials

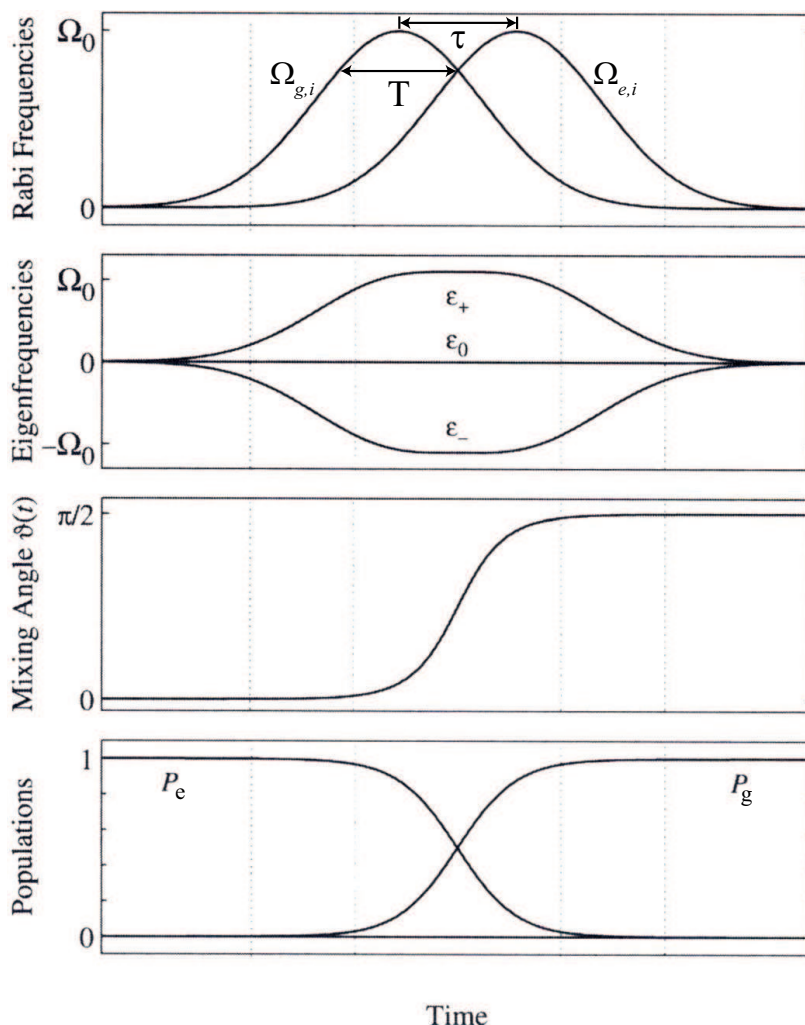


Figure 5.3: Rabi frequencies, eigenenergies, mixing angle and fractional populations during the so called counterintuitive STIRAP pulse sequence. Ω_0 denotes the maximum Rabi frequencies occurring during the pulse sequence, which are adjusted to be the same. T is the width of the Gaussian pulses and τ is the pulse delay, which is chosen $\tau = T$. This figure is a modified version of the figure in [Vitanov et al., 2001].

5.2 Wavelengths and dipole moments of transitions between molecular states in the $X^1\Sigma^+$ and $1^1\Pi$ potentials

In this section the wavelengths of transitions between molecular states and an estimation for the respective transition strengths, that can be expected, are presented. Based on the ro-vibrational term energies of molecular states presented in Chap.2, Tabs.2.1 and 2.2, the transition wavelengths are calculated. Further, the Franck-Condon factors presented in Tab.2.3 are used for an estimation of the dipole matrix elements that can be expected. These are in turn used for a rough estimation of the Rabi frequencies $\Omega_{e,i}$ and $\Omega_{g,i}$ that are to be expected. The presented Rabi frequencies are useful for an

5. Raman transitions between molecular states of Li - K

estimation of the powers of the light fields and coherence times that are needed for the Raman lasers. The results for the transition wavelengths and transition dipole moments, that are to be expected, are given in Tab. 5.1. No values $< 4 \times 10^{-4}$ are given as the Franck - Condon factors are not known with sufficient accuracies for these transitions.

The transition dipole moments are calculated following Eq. 3.7. However, in addition, the singlet fraction in the Feshbach state $|5\rangle$ (see Sec. 2.4.1) has been taken into account on the $|e\rangle \leftrightarrow |i\rangle$ transition. Thus, the total transition dipole moments are

$$R_{\text{tot}}^{\text{Fb} \leftrightarrow i} = \sqrt{\mathcal{S}} R_{\text{rot}}^{01} R_{\text{vib}}^{v'v''} R_{\text{el}} \quad (\text{Feshbach state to } |i\rangle) \quad (5.12)$$

$$R_{\text{tot}}^{g \leftrightarrow i} = R_{\text{rot}}^{01} R_{\text{vib}}^{v'v''} R_{\text{el}} \quad (|i\rangle \text{ to } |g\rangle) \quad (5.13)$$

where:

Singlet fraction $\mathcal{S}(B=0)$. Due to the transition selection rules only the singlet part of the spin state (see Eq. 2.39) contributes to the transition dipole moment. At small magnetic fields $\sqrt{\mathcal{S}(B=0)} \simeq \sqrt{0.1}$. It is to be noted that this does not mean that only a fraction of the population can be transferred. The fact that the Feshbach state is not a pure singlet state leads only to a decrease in transition strength.

Rotational matrix element R_{rot}^{01} . It is assumed that a small magnetic field is applied during the electric dipole transition, which serves as a quantization axis. Hönl-London factors for transitions between magnetic rotational states of a rigid symmetric top molecule are used for an estimation of the electric transition dipole moment [Crawford, 1934]. Linearly polarized electric field vectors in the direction of the magnetic field are assumed. The fields drive the P - transitions:

$$\begin{aligned} X^1\Sigma^+, v=47, J=0, M=0 & \xrightarrow{\Delta J=1, \Delta M=0} 1^1\Pi, v=0, \dots, 34, J=1, M=0 \\ 1^1\Pi, v=0, \dots, 34, J=1, M=0 & \xrightarrow{\Delta J=-1, \Delta M=0} X^1\Sigma^+, v=0, J=0, M=0 \end{aligned}$$

where the Hönl-London factors are defined with respect to emission. As usual, M refers to the magnetic quantum number. While the magnetic splitting of states in the $X^1\Sigma^+$ potential is neglected here, the Zeeman splitting of states in the $1^1\Pi$ potential is considered. It is to be noted that the $J=1, 1^1\Pi$ state carries the angular momentum in the electron cloud and $N=0$, just as in the $X^1\Sigma^+$ states (see Sec. 2.2.1). As for both, Feshbach state and ro-vibrational ground state, the angular momenta are the same, the rotational factors for both the upward and downward transitions are $R_{\text{rot}}^{01} = \sqrt{2}$. The assumed transitions are the strongest transitions between magnetic states of the molecule.

Vibrational matrix elements $R_{\text{vib}}^{v'v''} = |\langle v'|v''\rangle|$. The Franck-Condon factors $|\langle v'|v''\rangle|^2$ are given in Tab. 2.3.

Electronic transition dipole moment R_{el} . For the rough estimation presented here the atomic ^{40}K D2 transition dipole moment of 5.8 ea_0 is used (see [Tiecke, 2010, LeBlanc, 2006]). As the sum of all allowed ro-vibrational transitions in a molecule are on the order of the associated atomic transition [Herzberg and Huber, 1950], this approximation

5.2 Wavelengths and dipole moments of transitions between molecular states in the $X^1\Sigma^+$ and $1^1\Pi$ potentials

Wavelengths and transition dipole moments for transitions between levels $1^1\Pi$: $\{v=0, \dots, 34; J=1\}$ and $X^1\Sigma^+$: $\{v=0, 47; J=0\}$				
$1^1\Pi$ v	$X^1\Sigma^+$: $v=0$ $\rightarrow 1^1\Pi$ [nm]	d [e·a ₀]	$X^1\Sigma^+$: $ \textcircled{5}\rangle$ $\rightarrow 1^1\Pi$ [nm]	d [e·a ₀]
0	570.38	1.1	875.03	$< 4 \times 10^{-4}$
1	565.89	1.5	864.51	$< 4 \times 10^{-4}$
2	561.76	1.6	854.90	$< 4 \times 10^{-4}$
3	558.01	1.5	846.25	$< 4 \times 10^{-4}$
4	554.63	1.4	838.50	$< 4 \times 10^{-4}$
5	551.59	1.2	831.57	$< 4 \times 10^{-4}$
6	548.84	1.0	825.34	$< 4 \times 10^{-4}$
7	546.34	0.88	819.70	$< 4 \times 10^{-4}$
8	544.05	0.75	814.55	$< 4 \times 10^{-4}$
9	541.94	0.62	809.83	$< 4 \times 10^{-4}$
10	539.98	0.52	805.47	$< 4 \times 10^{-4}$
11	538.16	0.44	801.43	$< 4 \times 10^{-4}$
12	536.47	0.37	797.68	$< 4 \times 10^{-4}$
13	534.89	0.32	794.20	$< 4 \times 10^{-4}$
14	533.43	0.27	790.97	$< 4 \times 10^{-4}$
15	532.07	0.23	787.98	$< 4 \times 10^{-4}$
16	530.80	0.20	785.21	$< 4 \times 10^{-4}$
17	529.63	0.17	782.66	$< 4 \times 10^{-4}$
18	528.56	0.14	780.32	0.0018
19	527.6	0.13	778.3	$< 4 \times 10^{-4}$
20	526.8	0.11	776.4	0.011
21	526.0	0.10	774.8	0.0052
22	525.3	0.084	773.3	0.035
23	524.8	0.074	772.1	0.029
24	524.2	0.064	771.0	0.058
25	523.8	0.057	770.0	0.038
26	523.4	0.049	769.2	0.075
27	523.1	0.042	768.6	0.037
28	522.9	0.036	768.0	0.098
29	522.7	0.029	767.6	0.16
30	522.5620	0.022	767.3143	0.0084
31	522.4201	0.018	767.0083	0.29
32	522.3265	0.016	766.8065	0.42
33	522.2899	0.014	766.7278	0.51
34	522.2781	0.011	766.7022	0.61

Table 5.1: Wavelengths and transition dipole moments d for transitions between Feshbach state $|\textcircled{5}\rangle$ and ro-vibrational ground state ($v = 0$) in the $X^1\Sigma^+$ potential and vibrational states with $J = 1$ in the $1^1\Pi$ potential. The accuracies given in Tabs. 2.1 and 2.2 expressed in wavelengths instead of wavenumbers are: levels 0 – 18: ± 0.05 nm; levels 19 – 29: ± 0.3 nm; levels 30 – 34: ± 0.0002 nm. All values are calculated for small magnetic field strengths.

5. Raman transitions between molecular states of Li - K

is justified. This approximation is likely to slightly underestimate the transition dipole moment by approximately a factor of 4 [Wang et al., 2010]. The definition of R_{rot}^{01} however includes a rotational branching factor for the respective Zeeman P - transition [Crawford, 1934], which is $1/4.2$. Thus, the electronic transition dipole moment $R_{\text{el}} = 1/\sqrt{4.2} \cdot 5.8 \text{ ea}_0 \simeq 1/2.0 \cdot 5.8 \text{ ea}_0$ is obtained.

The transition dipole moments presented in Tab. 5.1 are in good agreement with the dipole moments for other alkali metal dimers that are published [Ni et al., 2008, Aymar and Dulieu, 2007]. In the following the former are used to estimate Rabi frequencies for transitions between molecular states. Fig. 5.4 shows the single photon Rabi frequencies of four selected transitions. The uppermost diagrams show Rabi frequencies between the Feshbach state and the energy level with $v = 33$ in the $1^1\Pi$ potential, $\Omega_{e,i}$, and the coupling between the ro-vibrational ground state in the $X^1\Sigma^+$ potential and the same $1^1\Pi$ state, $\Omega_{g,i}$. The state with $v = 33$ in the $1^1\Pi$ potential is predicted to offer the strongest two photon transition of all states in the excited potential. The light intensities needed to achieve equal Rabi frequencies $\Omega_{e,i} = \Omega_{g,i}$ are however very different for this energy level. The most similar transition strengths are predicted to occur when level $v = 27$ in the $1^1\Pi$ potential is addressed. The Rabi frequencies for this energy level are shown in the second line of graphs.

In order to convey more intuitively how large these Rabi frequencies are, the times needed to reach a π -pulse condition are given in the lowest graph. It can be seen that even though the intensities needed are far larger than in the atomic case, they are nevertheless still experimentally manageable. Further, if rectangular Raman pulses are applied to fulfill a π -pulse condition, the multiplied Rabi frequencies are relevant. In this case the electronically excited $1^1\Pi$, $v = 33$ vibrational state is best addressed.

It has to be emphasized here again that the values for transition dipole moments and Rabi frequencies given in this section refer to the case of small magnetic field strength. During the experimental optimization of STIRAP transfer an optimum magnetic field at which to drive the transitions will need to be found experimentally. A magnetic field in the range $0 < B < 154.7 \text{ G}$ mostly has two effects with respect to the transition strengths: Firstly, as mentioned in Chap. 2, the Franck-Condon factors depend on the magnetic field strength. The magnetic field changes the molecular binding energy and the extension of the wavefunction. Thus, the molecular wavefunction on the atomic side close to the Feshbach resonance will extend to distances much farther than the wavefunctions shown in Fig. 2.9. This leads to a decrease of wavefunction overlap with increasing magnetic field and thus a decrease in transition strength. Secondly, as shown in Fig. 2.12, the singlet fraction of the wavefunction increases with increasing magnetic field. This leads to an increase in the transition strength.

It needs to be pointed out here again that the perturbation of the electronically excited states are not known. As the perturbation can change the character of electronically excited states, e.g. by an admixture of states with other multiplicity, this can also change the transition dipole moments significantly. If electronically excited states are perturbed to contain fractions of states with other multiplicity, the selection rules for electric dipole transitions will lead to a decrease of transition strengths. This happens in the same manner as shown for the case of the Feshbach state $|\textcircled{5}\rangle$. A spectroscopic de-

5.2 Wavelengths and dipole moments of transitions between molecular states in the $X^1\Sigma^+$ and $1^1\Pi$ potentials

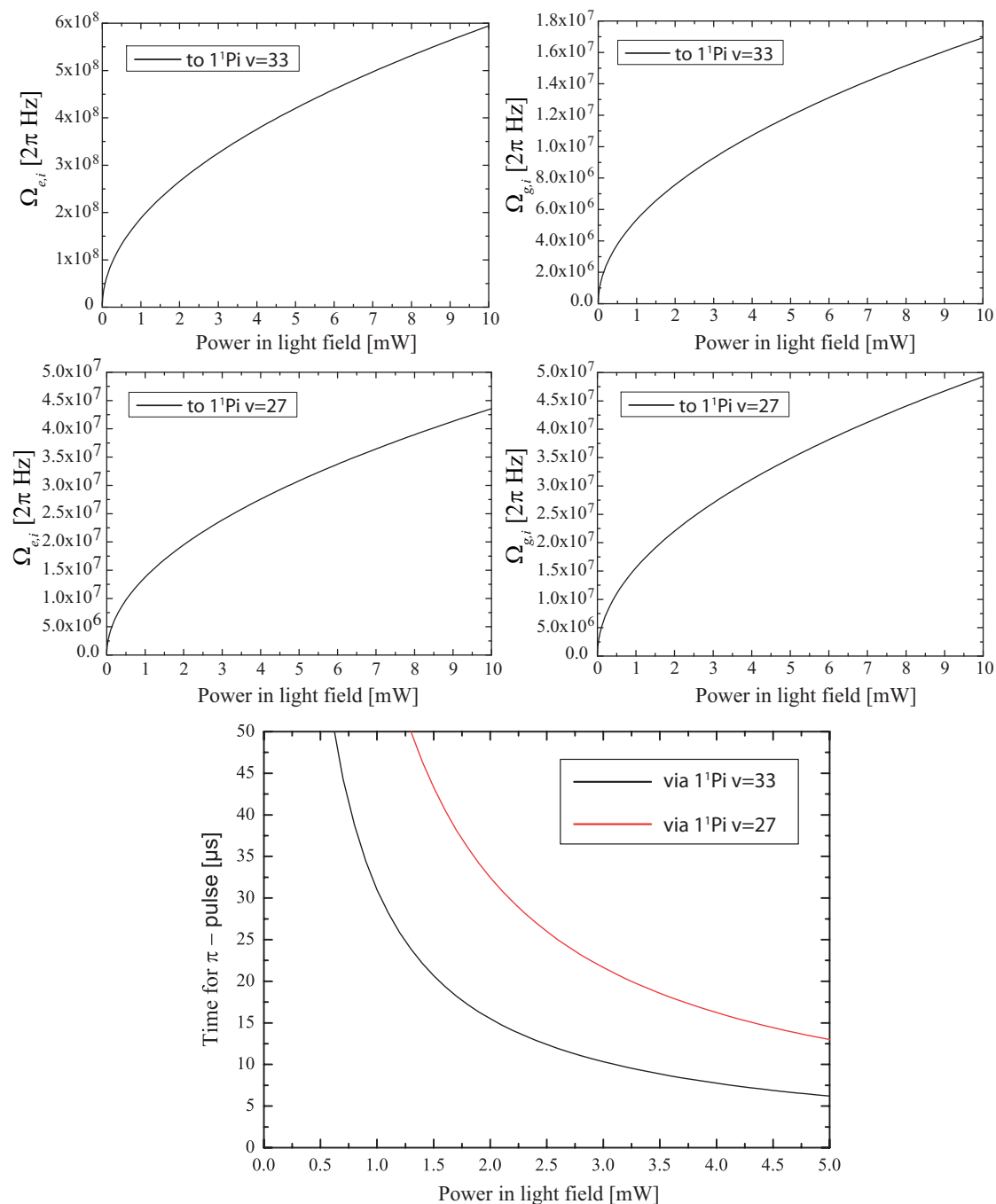


Figure 5.4: Top graphs: Single photon Rabi frequencies for transitions to the electronically excited states $1^1\Pi$, $v = 33$ and $v = 27$. $1^1\Pi$ level $v = 33$ offers the strongest two photon transition while $v = 27$ offers the most equal transition strengths. Bottom graph: time needed for a π -pulse. For this estimation, Gaussian light beams with $1/e^2$ waists of $75 \mu\text{m}$ and single photon detunings of 500 MHz are assumed.

termination of the transition strengths will help to understand the mutual perturbations of electronically excited states.

5.3 Optimization of the STIRAP pulse sequence

In this section the most important aspects for driving STIRAP between the previously discussed energy levels are described.

5.3.1 Selection rules

Most importantly, of course, one should only attempt to drive allowed transitions, even though in molecules the term “forbidden” is not as strict as in atomic transitions. Selection rules for molecular transitions depend on the coupling case. Sets of selection rules for the different coupling cases can be found in [Herzberg and Huber, 1950, Bernath, 2005]. For the transitions in Li - K that are planned to be driven here Hund’s case (a) is appropriate. All the $X^1\Sigma^+ \leftrightarrow 1^1\Pi$ transitions presented in Tab. 5.1 are allowed. Further, relevant transitions between states $X^1\Sigma^+ \leftrightarrow 2^1\Sigma^+$ are allowed (see Sec. 5.3.5).

5.3.2 Adiabaticity criterion

In order to minimize spontaneous emission from the electronically excited state $|i\rangle$, it is important that the state $|\Psi\rangle$ follows the adiabatic state $|\Phi_0\rangle$ during the transfer. Non-adiabatic transfer will lead to an admixture of the states $|\Phi_+\rangle, |\Phi_-\rangle$ to $|\Psi\rangle$, which contain an admixture of the decaying state $|i\rangle$. Practically, a pulse area of 10 is sufficient for efficient population transfer [Vitanov et al., 2001]:

$$\Omega_0 T > 10 \quad , \quad (5.14)$$

where the maximum Rabi frequencies Ω_0 are assumed to be the same. T is the single photon pulse width, which is assumed to be the same for both pulses (see Fig. 5.3).

In addition to the pulse area, the pulse envelope functions, each of the single photon Rabi frequencies $\Omega_{e,i}$ and $\Omega_{g,i}$ and the pulse delay τ have to be chosen. Smooth Gaussian intensity envelopes of the pulses are favorable and experimentally easily feasible to generate in our laboratory. It is favorable to adjust the intensities such that the Rabi frequencies are approximately the same. If this is the case, a pulse delay equal to the pulse width T is optimal in good approximation. If the Rabi frequencies differ, but by not too much, a good starting point for optimization is to make the pulse areas the same and choose the delay $(T_{e,i} + T_{g,i})/2$. Interestingly, when the Rabi frequencies are very different but still the pulse widths are chosen to be the same, no spontaneous scattering will occur, but an adiabatic return of $|\Psi\rangle$ to the original state [Vitanov et al., 2001]. Thus it is important to experimentally control the Rabi frequencies well. Further, more light power will only increase the adiabaticity and make the transfer more stable against differences in the Rabi frequencies and unmatched two photon detunings δ .

In Sec. 2.3.2, it is estimated that the lifetime of the ground state molecules will be on the order of a few ms. Thus, it is important that the transfer be faster than around $500 \mu\text{s}$. This timespan is also on an order on which the coherence of the Raman lasers is experimentally still well manageable.

5.3 Optimization of the STIRAP pulse sequence

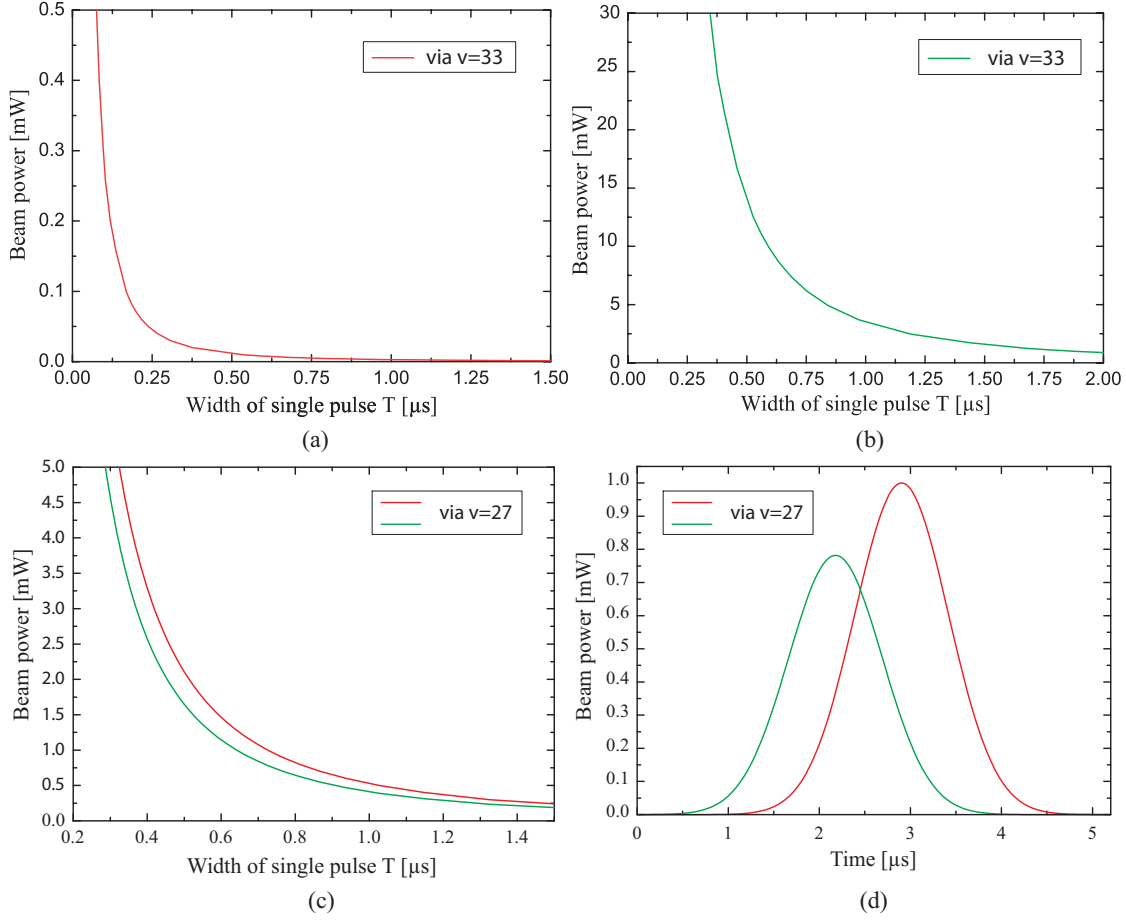


Figure 5.5: (a) - (c): optical powers needed for target pulse widths that are determined from adiabaticity criterion, Eq. 5.14, for transitions via $1^1\Pi v = 33$, $v = 27$. (d): a possible pulse sequence for a two-transition via $1^1\Pi$, $v = 27$. Gaussian beams with $1/e^2$ waists of $75 \mu\text{m}$ are assumed. (a) pulse widths for the light field coupling $|e\rangle \leftrightarrow |1^1\Pi v = 33\rangle$. (b) pulse widths for the light field coupling $|1^1\Pi v = 33\rangle \leftrightarrow |g\rangle$. (c) pulse widths for the light field coupling $|e\rangle \leftrightarrow |1^1\Pi v = 27\rangle$ (red) and $|1^1\Pi v = 27\rangle \leftrightarrow |g\rangle$ (green). (d) pulse sequence for an adiabatic transition $|e\rangle \leftrightarrow |g\rangle$ with both light fields resonant with $1^1\Pi$, $v = 27$.

Fig. 5.5 (a) - (c) show an estimation of the intensity needed for single photon widths of Gaussian pulses determined from the adiabaticity criterion Eq. 5.14. The intensities are adjusted such that the peak Rabi frequencies are the same. Due to the different strengths of the transitions, the intensities needed to do so are different. As before, all values refer to small magnetic field strengths. In the following and in Fig. 5.5, in accordance with Fig. 5.1, the vibrationally excited Feshbach state will be denoted $|e\rangle$ while the ro-vibrational ground state will be labeled $|g\rangle$.

Fig. 5.5 (a) and Fig. 5.5 (b) show that due to the very different transition strengths that occur for transitions when both light fields are resonant to level $1^1\Pi$, $v = 33$, the intensities needed differ by more than two orders of magnitude. Experimentally this

5. Raman transitions between molecular states of Li - K

means that much power in the green light field at 522.29 nm is needed in order to keep the pulse lengths short but still ensure adiabaticity in the beginning of the pulse sequence. Thus, even though the multiplied strengths for transitions via levels in the $1^1\Pi$ potential are the largest for the vibrational energy level $v = 33$, this might not be the optimal level for a STIRAP transfer. Other than when the transfer is achieved by a single π -pulse, where the detuning and the effective Rabi frequency [Berman, 1997] matter, the power of each light field separately matter for the adiabaticity of STIRAP (see Eq. 5.11).

The most similar transition strengths are predicted for vibrational level $v = 27$. For this electronically excited state, the intensities in dependence of pulse widths are shown in Fig. 5.5(c). The powers that are needed in both light fields are experimentally well manageable and very similar. The total timespan of the pulse sequence can even be chosen shorter as when the vibrational energy level $v = 33$ is addressed, as adiabaticity is ensured for far lower beam powers in the beginning of the sequence. A possible STIRAP sequence with Gaussian pulses that addresses the vibrational energy level $v = 27$ is shown in Fig. 5.5(d). Peak beam powers of $781 \mu\text{W}$ for the first pulse with the wavelength 523.1 nm and 1 mW for the second pulse with the wavelength 768.6 nm have been chosen. This results in the same peak single photon Rabi frequencies of 13.7 MHz (angular frequency units) for both pulses that are spaced by the same pulse width of $0.73 \mu\text{s}$. It can be seen that the whole transfer sequence has a duration of around $5 \mu\text{s}$. This duration is on the order of what is reported for the ground state transfer of K - Rb [Ni et al., 2008]. Due to the rather short duration it is possible to choose even somewhat larger waists of the Gaussian beams than are assumed in the calculation of the Rabi frequencies. This makes the beams easier to align, more stable for longer time spans and gives a larger volume of close to constant Rabi frequencies. It is to be noted that the given values are the lowest values that still fulfill Eq. 5.14. These values might however not be large enough to ensure adiabaticity since the electronically excited state decays fast. In practice it might be beneficial to use somewhat higher Rabi frequencies and/or pulse widths.

Depending on the green laser that is to be used another vibrational energy level might be optimal. This is to be determined when the Raman laser system, which is described in Chap. 7, is fully characterized.

5.3.3 Cloud temperature and sensitivity the detunings Δ and δ

As the produced Feshbach molecules possess a finite temperature, different velocity classes of molecules interact with different light frequencies in their rest frame during the STIRAP sequence. As the two-photon linewidth is narrow in Raman transitions, it is interesting to estimate the effect of a two-photon detuning δ on STIRAP with respect to the transfer efficiency that one might expect. On average the Feshbach molecules that are produced possess a slightly higher temperature than the atoms had of which they are created. In the case of the Feshbach molecules produced in our experiment a rough estimation for the temperature is around 500 nK. Together with both Raman laser frequencies that resonantly address the vibrational energy level $v = 27$ in the $1^1\Pi$ potential a Doppler shift of 43.2 kHz is found.

In addition to the two-photon detuning, the transfer efficiency of the process in dependence of the common single photon detuning Δ is interesting with respect to the

5.3 Optimization of the STIRAP pulse sequence

accuracy with which the electronically excited state has to be addressed.

Linewidths of STIRAP transitions can be defined with respect to the transfer efficiency. Δ_{FWHM} and δ_{FWHM} denote the full-width-half-maximum (FWHM) detuning values of the common detuning from single photon resonance and the relative detuning from two-photon resonance of the two light fields. For each Δ_{FWHM} and δ_{FWHM} , 50% of the population is still transferred. STIRAP has the following scaling properties of Δ_{FWHM} and δ_{FWHM} in dependence on the maximum Rabi frequency Ω_0 [Vitanov et al., 2001]:

$$\Delta_{\text{FWHM}} = c(\tau) \Omega_0^2 \quad (5.15)$$

$$\text{with } c(\tau) \simeq 0.13 \quad \text{for } \frac{\tau}{T} = 1 \quad [\text{Vitanov and Stenholm, 1997a}]$$

$$\delta_{\text{FWHM}} = d(\tau) \Omega_0 \quad (5.16)$$

Here, Gaussian intensity pulses and equal maximum Rabi frequencies for each of the pulses have been assumed. It can be seen that the two-photon linewidth is much narrower than the single photon linewidth, due to its linear scaling with Ω_0 . Further, again, as in the previous section, large as possible Rabi frequencies are beneficial to the transfer process. Very roughly, the proportionality constants $c(\tau)$ and $d(\tau)$ are on the same order of magnitude [Vitanov et al., 2001].

The peak Rabi frequencies of 13.7 MHz presented in the previous section together with $d(\tau) = 0.1$ will lead to a two-photon linewidth of approximately 1.3 MHz. This is on the same order as the Fourier limit for the light pulses with a duration of $0.73 \mu\text{s}$. Thus, for the pulse sequence presented in Fig. 5.5 (d), the finite temperature of the Feshbach molecules is not expected to limit the transfer efficiency in practice.

5.3.4 Decay from the electronically excited state

As mentioned, higher intensities of the light fields will increase the coherence. Further, other than when square pulses are switched on that fulfill a π -pulse condition for state transfer, a larger detuning Δ does not increase the coherence of the transfer process, but deteriorates it. The higher the decay rate of the excited state is, the higher the intensities of the laser fields, which need to be kept of single photon resonance, are needed. This makes the state $|\Psi\rangle$ follow $|\Phi_0\rangle$ more accurately throughout the transfer, thereby reducing spontaneous emission from the decaying energy level $|i\rangle$. An estimation on the transfer efficiency in dependence on the decay rate of the excited state can be found in [Vitanov and Stenholm, 1997b]. It is to be noted that the electronically excited states are decaying fast, which deteriorates adiabaticity. This effect can be counteracted by the use of larger pulse areas.

5.3.5 STIRAP via multiple excited states

The idealized three level system shown in Fig. 5.1 neglects the fact that in Li-K molecules more than two energy levels are coupled by each of the two light fields present during STIRAP. Even though the Feshbach molecules are produced in a single coupled quantum state with $M_F = -2$, labeled $|\textcircled{5}\rangle$ in Sec. 2.4.1, the STIRAP light fields in general couple this state to several molecular hyperfine states in each the intermediate state $|i\rangle$ and

5. Raman transitions between molecular states of Li - K

the ro-vibrational ground state $|g\rangle$. This wealth of molecular hyperfine states has been neglected in Sec. 2.2.

In [Vitanov et al., 1999] the effect of multiple unevenly distributed intermediate states, each of which are coupled unequally to $|e\rangle$ and $|g\rangle$, is studied. It is found that only if all the ratios $\Omega_{e,i}^k/\Omega_{g,i}^k$ are the same for all intermediate states k , there exists an adiabatic dark state with no admixture of the electronically excited states. This system behaves as a Λ -system. If this is not fulfilled, the transfer state acquires an admixture of the decaying electronically excited states. Still, adiabatic following from the initial to the target state is possible, however there can be a strong dependence on the single-photon detunings, which depend on the relative strengths of the couplings to the excited states. Further, it has been shown that generally, when the two light fields are tuned across a manifold of N intermediate states while keeping two-photon resonance, N detuning ranges with high transfer efficiency and $N - 1$ with low transfer efficiency occur. Practically in this case it is best to choose a single-photon detunings slightly above or below all intermediate states. Experimentally, multiple intermediate states are thought to have prohibited successful ground state transfer in one case [Nägerl, 2012a]. It was necessary to address a different intermediate molecular state in this case.

While in the $^1\Sigma$ potentials a splitting of levels at zero magnetic field occurs only due to the interaction of both nuclear spins, the latter also couple to the orbital angular momentum present in the case of the $^1\Pi$ potentials. With $I_{\text{Li}} = 1$ and $I_{\text{K}} = 4$, $(2I_{\text{Li}} + 1)(2I_{\text{K}} + 1) = 27$ hyperfine energies exist in the case of the $^1\Sigma$ potentials. In the case of the $^1\Pi$ potentials, this number is again multiplied by $(2L + 1) = 3$, and the splitting due to the coupling of the nuclear spins to the orbital angular momentum of the electron cloud is far larger. For magnetic field strengths > 20 G the coupling of the nuclear spins to the magnetic field is expected to be stronger than the spin-spin coupling. The coupling of the nuclear spins to a possible rotational excitation N (see Fig. 2.1) is neglected here as all molecular states treated in this thesis are of the case $N = 0$. Further, no λ -doubling is taken into account, as only one of the levels in the doublet is addressed by electric dipole transitions. This is due to the parity selection rules. The single photon linewidth Δ_{FWHM} (see Eq. 5.15) is much larger than the energy spacing of vibrational levels and it needs to be ensured that the lasers are set resonantly with one vibrational level. In this case it is to be expected that the coupling to the other vibrational levels can be neglected.

As with atoms, it depends on the polarization of the Raman light fields which hyperfine levels are addressed. For example, in the case of σ^+ transitions of both light fields $\Delta M_F = +1$ for the single photon transition, where M_F is the hyperfine magnetic quantum number. Thus, in the case of the intermediate states in the $1^1\Pi$ potential the Feshbach state is coupled to 9 intermediate states. The two-photon transition in turn will populate three hyperfine states with $M_F = 0$ in the ro-vibrational ground state.

With regard of the number and splitting of the energy levels in the $1^1\Pi$ potential, it could be advantageous to drive transitions via a state in the $2^1\Sigma^+$ potential. In Sec. 2.2, the $1^1\Pi$ potential has been chosen since comparatively large Franck-Condon factors are to be expected for states in this potential. Further, the accuracy and abundance of experimental data allows for a rather precise determination of ro-vibrational energy levels and Franck-Condon factors. Due to the precise data presented in Sec. 2.2 and Tab. 5.1 it will be relatively fast possible to try a ground state transfer via an intermediate

5.4 Photon recoil and non - adiabatic change of the dipole trapping potential

state in the $1^1\Pi$ potential. In the case of a state in the $2^1\Sigma^+$ potential, a spectroscopy over a larger wavelength range is likely to be needed. It is to be emphasized however that the states in the potentials dissociating to the $K(4p)$ - $Li(2s)$ perturb each other. As a result, the different states contain admixtures of states of other potentials. Thus, it is not obvious that addressing a state in the $2^1\Sigma^+$ potential will reduce the number and splitting of intermediate states in all cases. Further, the perturbation may alter the transition strengths.

5.4 Photon recoil and non - adiabatic change of the dipole trapping potential

Due to the widely different wavelengths needed for a Raman ground state transfer, there exists a comparatively large momentum transfer from the photons to the molecules due to the photon recoil, even for copropagating Raman beams. The transferred kinetic energy is estimated to correspond to $0.4 \mu\text{K}$. In comparison to the trap depths achieved by use of the trap configuration described in Sec. 3.2, this is small and no loss of molecules is to be expected. However, a heating of the molecular sample of $0.4 \mu\text{K}$ poses a constraint on the temperature that can be reached with ground state molecules without further efforts. As the transfer process is coherent, additional coherent manipulation can however be used to again remove the deposited kinetic energy. Another possibility is to move the optical trap after Raman transfer with a velocity of about 12 mm/s , corresponding to the velocity of the molecules after transfer. In this moving frame, the trapped cloud's center of gravity will have no momentum.

In addition to the photon recoil, the dipole trapping potential is different for molecules in the Feshbach state and the ro - vibrational ground state. For a wavelength of 1064 nm and the trap parameters previously used for molecule production, the change in trapping potential is shown in Fig. 3.3. As the transfer duration is of much shorter duration than the trap oscillation period, this non - adiabatic change will decrease the phase space density. If the change in trapping potential is assumed as instantaneous, the same trap configuration as described for Fig. 3.3 is used and a sample temperature of $500 \mu\text{K}$ is assumed, a 68% increase in occupied phase space is determined. As mentioned, by the choice of a magic wavelength for an optical trap this increase in phase space density can be avoided.

Chapter 6

Molecular spectroscopy

Even though the frequencies of transitions between states in the $X^1\Sigma^+$ and $1^1\Pi$ potentials are known with comparatively high precision, spectroscopic investigations are still needed. Exact transition frequencies and transition strengths will need to be experimentally determined in order to be able to start optimizing STIRAP with parameters that already allow for transfer. In this way, optimization can quickly be achieved. Further, it might prove advantageous to address states in electronically excited potentials other than the $1^1\Pi$ or states that are mixed by mutual perturbation. For these, a spectroscopy over a larger wavelength range might need to be carried out. A precise two-photon spectroscopy further allows the determination of the ro-vibrational ground state Stark shift. From this, the molecular dipole moment induced in the laboratory frame in dependency on an applied DC electric field can be determined.

This chapter describes how the single photon spectroscopy of electronically excited states (Sec. 6.1) as well as the two-photon spectroscopy of low lying states in the $X^1\Sigma^+$ potential (Sec. 6.3) can be carried out efficiently. For the use of molecular spectroscopy, the precision of a commercial interferometric laser frequency stabilization has been increased to MHz precision. The results of this work, which was done in collaboration with the device's manufacturer¹, is described in Sec. 6.2, while a detailed description of the calibration methods and other technical details can be found in App. A. Also, the work is published in [Brachmann et al., 2012].

6.1 Spectroscopy of the electronically excited states

There are several different possible approaches for the single photon spectroscopy of the electronically excited states. Which type of spectroscopy is best used is mostly determined by the accuracy with which the respective energy levels are known. For the rather precisely known states in the $X^1\Sigma^+$ and $1^1\Pi$ potentials presented in Sec. 2.2.4 the transition frequencies can directly be found by use of the Feshbach molecules. The direct use of the molecules, which are in a single quantum state, allows for easier and faster interpretation of recorded spectra in comparison to alternative methods like e.g. photoassociation spectroscopy [Ridinger et al., 2011]. Thus, once spectra are recorded, it is to be expected that the association of states to potentials can be achieved quickly.

¹TEM Messtechnik GmbH, Großer Hillen 38, 30559 Hannover, Germany

6.1 Spectroscopy of the electronically excited states

When the molecules are electronically excited by resonant light, spontaneous emission occurs after a timespan on the order of the lifetime of the excited state. As has been mentioned before (see Sec. 3.3), the decay is most likely to a different energy level than the one that had been populated before the excitation. Thus, when light resonant with a transition to an electronically excited state irradiates the molecules, a loss of detected molecules can be seen on fast timescales. By observing loss features in dependence on the frequency of the spectroscopy laser, the electronically excited states can be found.

In Chap. 5 it is found that energy levels in the $1^1\Pi$ potential in the range of the vibrational index from $v=23$ to $v=34$ are of most interest for STIRAP transfer. In order to spectroscopically investigate energy levels in this range, the operating range needed for a spectroscopy laser is 766.6-772.1 nm, and thus 5.5 nm (see Tab 5.1). Further, an as large as possible tuning range of the spectroscopy laser as well as a high maximum sweep rate is beneficial to efficiently carry out the spectroscopy.

A possible approach for spectroscopy could involve two steps: In the first step the spectroscopy laser is quickly swept over comparatively large wavelength intervals with a comparatively high intensity of the light field. In this manner large frequency intervals can be examined for transitions. However, the transition frequencies will be known with little accuracy, as an observed loss of molecules after sweeping the spectroscopy laser only means that there is a transition somewhere in wavelength range over which the sweep was carried out. In a second step the intensity of the spectroscopy laser is reduced, which also reduces power broadening of the transitions. The wavelength range in which a transition has been found in the first step is then investigated at higher resolution.

In order to estimate how fast it is possible to sweep the spectroscopy laser in the first step and still cause significant trap loss, the scattering rates of the molecules are estimated for transitions between the Feshbach state and states in the $1^1\Pi$ potential. With the condition for saturation of an optical transition

$$\frac{I}{I_{\text{sat}}} = 2 \frac{\Omega_{e,i}^2}{\Gamma^2} \quad (6.1)$$

the saturation intensity I_{sat} can be determined from the predicted intensity dependent Rabi frequencies (see Fig. 5.4) for each transition strength. Here Γ is the linewidth of the molecular transition that is addressed and I the intensity of the radiation field. The time it takes for a molecule to scatter one photon can be estimated from the well known formula for the steady state resonance fluorescence of a two-level system [Metcalf and van der Straten, 1999]:

$$T_{\text{scatt}} = \frac{1}{R_{\text{scatt}}} = \frac{2}{\Gamma} \frac{1 + 4(\Delta/\Gamma)^2 + I/I_{\text{sat}}}{I/I_{\text{sat}}}, \quad (6.2)$$

where Δ is the detuning from single photon resonance. As one scattered photon per molecule is enough for the spectroscopic investigations, T_{scatt} directly sets the maximum rate at which the laser used for excitation can be swept in order to find transitions. To get an estimate what maximum tuning rate is possible for the relevant transitions from the Feshbach state to states with $v > 22$ in the $1^1\Pi$ potential, 20 mW of optical power are assumed here. A transition dipole moment of $> 0.0015 ea_0$ is assumed here for all transitions to levels with $v > 22$ (see Tab. 5.1) and the molecular linewidths are

roughly estimated as 20 MHz [Wang et al., 2010]. With these values the time it takes a molecule to scatter one photon, in the case of a detuning of the light field of $\Delta = \Gamma$, is approximately $T_{\text{scatt}} = 5 \mu\text{s}$. For a very rough estimation the scattering rate is taken to be constant in the whole detuning range $-\Gamma < \Delta < +\Gamma$, which is an underestimation. Thus the maximum tuning rate is very conservatively estimated $2\Gamma/T_{\text{scatt}} = 8 \text{ GHz/ms}$. This is based on the assumption that the molecule will scatter one photon during the time the laser detuning is in the frequency range $-\Gamma < \Delta < +\Gamma$. The high intensity will lead to power broadening, which is however not an issue when large frequency intervals are first searched for transitions.

The transition wavelengths presented in Tab. 5.1 are estimated to be known with an accuracy of better than 150 GHz. Further, the lifetime of a pure sample of molecules is likely to be on the order of 10 ms, however dependent on the magnetic field. The lifetime of a pure molecular sample will be measured as soon as it is produced. Conservatively, it can be estimated that the sample of pure molecules will be available for spectroscopy for a duration of at least 1-2 ms. Even for these very conservative estimates it will thus be possible to find all transitions to the $1^1\Pi$ potential, that might be relevant for ground state transfer, very quickly. Even for the less well known transitions with $v=22-29$ a rough localization will not take more than 15 experimental cycles (2 min./cycle).

As has been mentioned, it could turn out that ground state transfer via a level in the $2^1\Sigma^+$ potential might be attempted. The relevant vibrational energy levels computed from the *ab-initio* potential shown in Fig. 2.2 will be accurate on a level of around $100 \text{ cm}^{-1} \simeq 3 \text{ THz}$. Thus, a spectroscopy on basis of these data will be more cumbersome.

As has been mentioned, states in the different potentials dissociating to the $\text{K}(4P) - \text{Li}(2s)$ asymptote perturb each other and have similar energies. Thus, states, once found, will need to be characterized with respect to their singlet or triplet character and also an assignment to a potential will be useful. Further, transition strengths should be measured experimentally.

The estimated maximum tuning speeds of a laser used for spectroscopy of the electronically excited states are comparatively high. Thus, in order to test large frequency ranges for the presence of transitions, it is advantageous to use a laser that can be tuned fast. It is planned to use a grating stabilized diode laser (see Chap. 7) for Raman transfer, single- and two-photon spectroscopy. A tuning speed on the order of 10 GHz/ms can be achieved with this laser and also mode-jump free tuning of up to 50 GHz is possible. In order to achieve the high sweep rates over wide frequency intervals, working with a laser that is not frequency stabilized is the simplest possibility. As the temperature in the new laboratory in Singapore is very stable, laser drift rates are expected to be low. Thus it will be sufficient to only monitor the laser's frequency drift, which can be accomplished by means of the available frequency comb (see Sec. 7.1). The laser can be tuned by feeding a suitably fast triangular waveform, triggered on the experimental cycle, to the piezoelectric control input.

After a frequency interval that contains a transition has been found in the manner described above, the higher resolution spectroscopy can be carried out in a second step. In order to perform this task conveniently, efficiently and with high precision, a commercial interferometric laser frequency stabilization has been calibrated by use of a frequency comb in order to increase its precision to the MHz level. A brief overview over this work is presented in the following Sec. 6.2, while details are given in App. A.

6.2 A tool for molecular spectroscopy

In collaboration with TEM Messtechnik a calibration scheme for their patented interferometer based laser frequency stabilization [Müller-Wirts, 2001] has been worked out. Several calibration steps are implemented, which are shown to improve the absolute precision of the device to the MHz level. The device allows for almost arbitrarily wide tuning of a continuously stabilized laser in the wavelength range of interest. Here, only a brief overview of the work is given, while details are described in App. A.

6.2.1 Functional principle

The central optical part of the laser frequency stabilization is a plane-parallel BK7 etalon of low finesse (see Fig. A.1), which is passed by two test beams of the laser that is to be stabilized. From its geometrical thickness of 50 mm follows a free spectral range (FSR) of around 2 GHz. Two quadrature signals (see Fig. 6.1) are derived from the wavelength dependent fringe pattern, which are recorded by two pairs of photo diodes. For laser frequency stabilization, the recorded quadrature signal values are compared to electronically generated ones and the laser is tuned until the mismatch between the values vanishes. It is to be noted, that the interferometer includes no moving parts, but the laser is stabilized such that the intensity recorded by the photo diodes is kept constant to match the digitally generated set values. This allows for high bandwidth feedback and fast tuning of stabilized lasers. In the current design frequency steps of 1 MHz to around 800 MHz can be electronically generated with a rate of 1 kHz and a feedback bandwidth of around 75 kHz is achieved. However, now there exists a new electronic design of the interferometer control unit which can electronically generate quadrature signals at the much higher rate of 2.5 MHz. If the new control unit is used the first spectroscopy step described in the previous section can be omitted.

In order to stabilize a laser to an absolute target frequency, two measurement values are needed in addition to the quadrature signals: Firstly, the interferometer signals are periodic. Thus, the signals are ambiguous and a laser has to be preset to a target wavelength with an accuracy of better than one half of an FSR prior to closing the feedback loop. This can be achieved with a commercial wavemeter of comparatively low precision. Secondly, the interferometer phase offset at an arbitrary but precisely known laser wavelength has to be determined. Any laser of precisely known wavelength will suffice for this, e.g. a mode of a frequency comb or a single mode laser stabilized to a saturation spectroscopy.

6.2.2 Calibration steps

Four calibration steps are implemented in order to reach MHz precision:

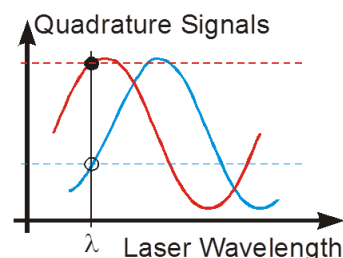


Figure 6.1: Wavelength dependent quadrature signals to which a laser is stabilized.

First, an automated sequence is carried out which electronically normalizes the interferometer signals and adjusts the relative phase of the recorded fringe pattern to $\pi/2$ (see Fig. 6.1). This is part of the commercial patented design and will not be described in detail in this thesis. For technical details of this calibration step the interested reader is referred to [Müller-Wirts, 2001].

Second, the interferometer phase offset, which is subject to slow drift due to temperature fluctuations, needs to be determined. In the measurements presented in Sec. A.3, the offset phase is determined by the use of a continuous wave (cw) reference laser locked to a saturation spectroscopy of ^{87}Rb .

Third, a periodic frequency deviation of up to 40 MHz occurs due to the deviation of the interferometer fringe pattern from true sine and cosine functions. The equidistant fringe pattern of an etalon with a small FSR of 60 MHz is used as a marker for the frequency intervals that are covered when a stabilized laser is tuned (see Sec. A.3.3). This etalon is realized with an optical single mode fiber. From the frequency deviations measured in this way, a look-up-table (LUT) is generated. The LUT is used to compensate the deviations occurring within one FSR of the etalon to which the laser is stabilized.

Fourth, in order to be able to tune stabilized lasers with high precision over frequency intervals corresponding to many etalon FSRs, the latter has to be determined with high precision. The etalon's FSR is wavelength dependent due to the dispersion occurring in the BK7 medium. When predicting interferometer angles for target laser frequencies, dispersion is taken into account by use of the Sellmeier formula (see Sec. A.2.1). However, the Sellmeier coefficients of BK7 are not known with an accuracy that allows MHz precision. Thus, the remaining effect of a wavelength dependency of the etalon's optical path length needs to be compensated. As described in detail in Sec. A.3.4, a frequency comb is used to calibrate the etalon's optical path length and characterize the systematic deviations occurring over a wide wavelength range. Using the experimental data, the precise calibration of the etalon's FSR in the wavelength range 750-795 nm is achieved.

6.2.3 Accuracy of the calibrated interferometer setup

Fig. 6.2 shows data taken with the fully calibrated interferometer setup. Here, f_{dev} denotes the absolute frequency deviation of a laser that is stabilized by the interferometric laser frequency stabilization. For the data shown in Fig. 6.2(a), the calibration in the wide wavelength range 750-795 nm is achieved by using the data represented as red circles, which are shown in Fig. A.4 of the appendix, for the fourth calibration step. The data shown in Fig. 6.2(a) are then generated from the dataset shown as black squares in Fig. A.4. It is to be pointed out that the data used for calibration and the data used to generate Fig. 6.2(a) are taken on consecutive days, which shows that the interferometer setup is very stable. The slight remaining systematic deviation in the data is most likely due to the mechanical stability of the interferometer setup. However this has not been investigated further and no conclusive remark can be given on the matter.

Fig. 6.2(b) and Fig. 6.2(c) show three datasets in a smaller frequency interval of one etalon FSR at 396 THz and two datasets in a 450 GHz wide frequency interval around the reference laser frequency. It can be seen that also on these scales no large frequency deviations occur. The offset between the datasets shown in Fig. 6.2(b) is due to comparatively large linewidth of the (DFB-) reference laser.

6.2 A tool for molecular spectroscopy

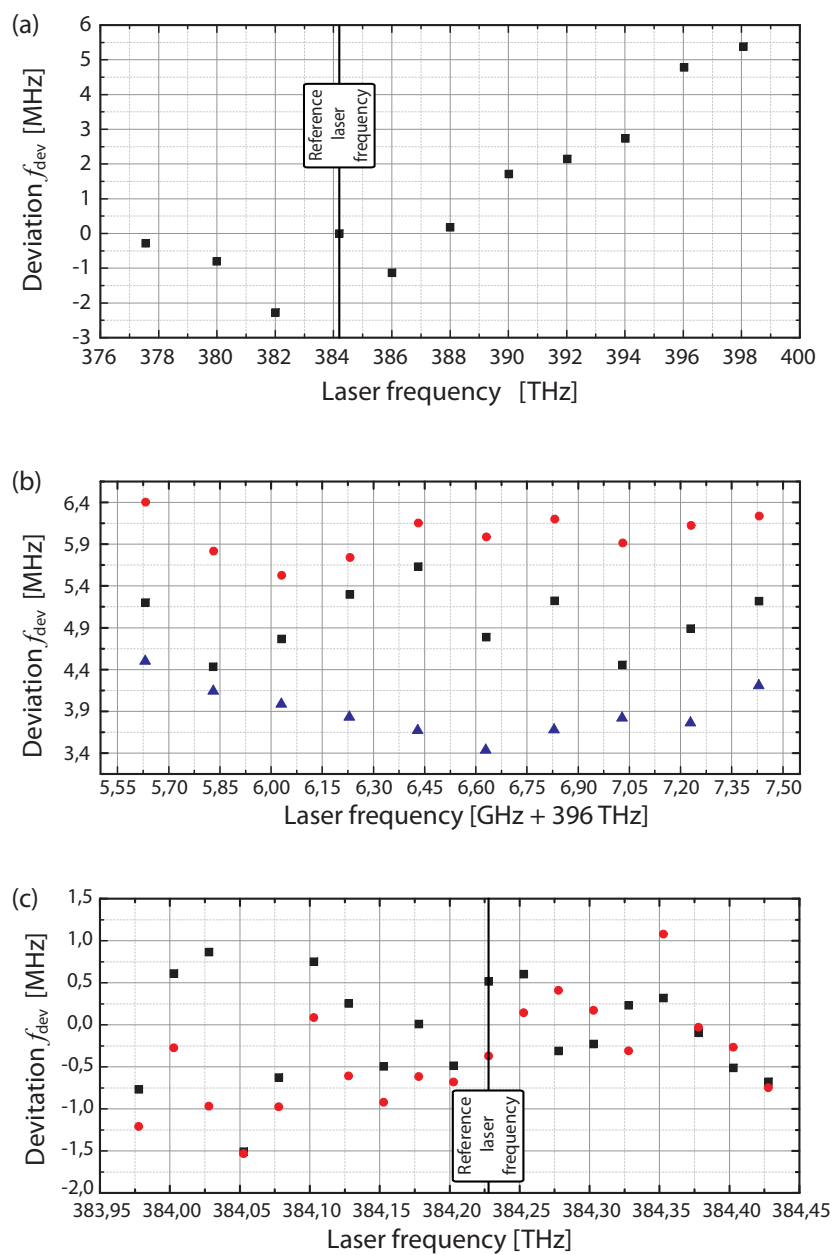


Figure 6.2: Datasets taken with the fully calibrated interferometer setup. (a) large wavelength interval 750 - 795 nm. (b) 3 datasets taken within one etalon FSR. (c) 2 datasets taken in a frequency interval of 450 GHz around the reference laser frequency.

6.2.4 Molecular spectroscopy with the calibrated interferometer setup

In the new laboratory in Singapore, a frequency comb is available for highest precision molecular spectroscopy. As an extension to the frequency comb system the interfero-

metric laser stabilization is very convenient for spectroscopy. It allows to tune a laser independently of the frequencies of the comb modes and over frequency ranges large compared to the comb repetition frequency. In order to achieve this, a spectroscopy laser is stabilized to the interferometer setup and the frequency comb is used as the reference for the described offset phase measurement. As the frequency comb provides reference frequencies in the whole wavelength range of interest for the spectroscopy, the calibration step that includes the described dispersion correction beyond the Sellmeier equation can be omitted. In this way, an accuracy as the one shown in Fig. 6.2 (c) is to be expected in the whole wavelength range of interest, while the spectroscopy laser can be tuned in a fast and convenient manner. This allows to cover large frequency intervals in the limited lifetime of the Feshbach molecules.

6.3 Two-photon spectroscopy of low lying states in the $X^1\Sigma^+$ potential

With precise knowledge about the excited molecular states the two-photon spectroscopy for the resonant two-photon transition into the absolute ro-vibrational ground state can be approached. While it is more than sufficient to determine the single-photon transition frequency to an accuracy of around 10 MHz, the two-photon transition frequency needs to be determined with an accuracy $\simeq 10$ kHz. Depending on which transition is chosen to be addressed, the second Raman laser needs to have a wavelength in the range 522.2-524.8 nm (see Tab. 5.1). Thus an operating range of 2.6 nm is needed if one wants the freedom to be able to address all relevant vibrational energy levels in the $1^1\Pi$ potential. Further, the vibrational energy levels in the $X^1\Sigma^+$ potential are known with a precision of better than 600 MHz. This sets the scale on which the laser should be tunable.

Instead of directly trying to optimize STIRAP transfer, two-photon dark resonance spectroscopy [Vitanov et al., 2001] is a good way to find two-photon resonance [Ni et al., 2008]. For this, the two light fields are adjusted to very different Rabi frequencies. The weak test light field ($\Omega_{e,i}$) stays tuned to the previously found single photon resonance frequency, which causes loss of all molecules if no other light field is resonant. The much stronger pump light field ($\Omega_{g,i}$) causes an Autler-Townes splitting in the case of two-photon resonance. It is tuned stepwise with each experimental cycle in order to find two photon resonance. When the two photon resonance is found, no molecules are lost from the trap, as the decay processes from the Autler-Townes splitted excited states interfere destructively and no photons from the test light field are scattered any more. The step size Δ_{cycle} with which the pump light frequency can be tuned from one experimental cycle to the next depends on the Rabi frequency of the pump light field, which causes the Autler-Townes splitting $\hbar\Omega_{g,i}$. Each of the splitted line profiles are approximately Lorentzian and $\Delta_{\text{cycle}} \approx \Omega_{g,i}/2$ is a good choice. Thus, for this type of spectroscopy, a high intensity of the pump light field $\Omega_{g,i}$ is favorable, in order to be able to choose a larger Δ_{cycle} and to faster find two-photon resonance. Further, it needs to be kept in mind that the decaying state $|i\rangle$ has a comparatively large linewidth. For the two-photon spectroscopy, an Autler-Townes splitting that is larger than the molecular linewidth, which is expected to be on the order of 20 MHz [Wang et al., 2010], is needed.

An estimation of the intensity dependent Rabi frequencies $\Omega_{g,i}$ for transitions

6.3 Two-photon spectroscopy of low lying states in the $X^1\Sigma^+$ potential

$X^1\Sigma^+$, $v = 0 \leftrightarrow 1^1\Pi, v = \{27, 33\}$ is shown in Fig. 5.4. It can be seen that for 10 mW of optical power in a Gaussian beam with a $1/e^2$ waist of $75 \mu\text{m}$, the expected Autler-Townes splitting is around 17 MHz for the weakest of the four transitions. This is roughly on the order of the molecular linewidth and two-photon spectroscopy is still feasible. However for the measurement a somewhat smaller beam focus on the order of $30\text{-}40 \mu\text{m}$ might be beneficial, for increased intensity. For the probe light field $\Omega_{e,i}$, something on the order of $50 \mu\text{W}$ is sufficient. Due to the comparatively precisely known states in the $X^1\Sigma^+$ potential, it is to be expected that two-photon resonance should not take too long to be found.

When two-photon resonance is found, the transition strengths should be experimentally determined, which can be inferred from the observed Autler-Townes splitting for the pump laser. With this, the optimization of STIRAP transfer can begin, the details of which are described in Sec. 5.3. As it will presently in our experiment not be possible to directly image molecules in the ro-vibrational ground state (see Sec. 3.3), two STIRAP sequences can be used. These transfer population back and forth between the ground state and the vibrationally excited state from which the molecules can be imaged at magnetic fields close to the Feshbach resonance (see [Ni et al., 2008] for details).

By use of the two-photon spectroscopy, the molecular dipole moment induced in the laboratory frame can be determined. As molecules in the Feshbach state do not possess such a dipole moment, only the ground state energy will show a Stark shift if a DC electric field is applied. By determination of the Stark shift the dipole moment of ground state molecules can be inferred.

Chapter 7

Raman laser system

Due to the two very different wavelengths of the Raman lasers needed for ground state transfer, the technical realization of a laser system is challenging. Phase coherence of one (red) Raman laser, in the wavelength range 767-772.1 nm, with another (green) Raman laser, in the wavelength range 522-524.8 nm, has to be ensured during Raman transfer. In Chap. 5 it is derived that the transfer duration can conservatively be estimated $< 100 \mu\text{s}$. Further requirements on the tuneability of the Raman lasers are posed by the need to perform molecular two-photon spectroscopy (see Chap. 6). Based on these requirements, the design of the Raman laser system is part of this thesis. Two design possibilities are worked out, which are described in Sec. 7.1.

The Raman laser system designs include five main components, three of which are commercial while the remaining two are custom built. Commercial devices are: a fiber laser based frequency comb (Menlo Systems GmbH) to provide a coherent link between the two Raman lasers, a Rb-GPS time standard (Precision Test Systems, GPS10RBN) that provides the long term frequency stability over time intervals longer than several ten seconds and the red Raman laser (Toptica DLPro). Custom made are: the green Raman laser and a Fabry-Pérot resonator (FPR), which provides the short time frequency stability over time spans shorter than several ten seconds. While the work on the green Raman laser is performed in Singapore and is not part of this thesis, the construction of a stable Zerodur FPR and laser frequency stabilization to the FPR is demonstrated here. These latter two components of the laser system are the main experimental contributions to the Raman laser system.

In Sec. 7.2, the construction of the FPR, frequency stabilization of the red Raman laser to the FPR and characterization data is presented. A linewidth of the stabilized Raman laser of approximately 500 Hz and an Allan deviation below 2.5×10^{-12} for a duration of > 40 s is demonstrated. This Allan deviation corresponds 1 kHz rms frequency change at a Raman laser wavelength of 768 nm.

7.1 Design of the Raman laser system

In the following the design of the Raman laser system and two possible alternatives are presented.

7.1 Design of the Raman laser system

7.1.1 The laser system

In Fig. 7.1 a schematic of the Raman laser system design is shown. As a central unit a fiber laser based frequency comb (Menlo Systems GmbH) [Holzwarth et al., 2000, Udem et al., 2002] is used to bridge the frequency difference of 182 THz between the Raman lasers while ensuring phase coherence. A commercial rubidium clock combined with GPS (Precision Test Systems, GPS10RBN) serves as a time standard for stabilizing the comb's repetition- ($f_{rep} = 250$ MHz) and carrier envelope (freely selectable $0 < f_{ceo} < 250$ MHz) frequency. However, in short time intervals, which are relevant for the Raman transition, the time standard is not stable enough. Thus, two lasers cannot simply be frequency stabilized (locked) to the comb if they are to be used as Raman lasers. Further stabilization is required.

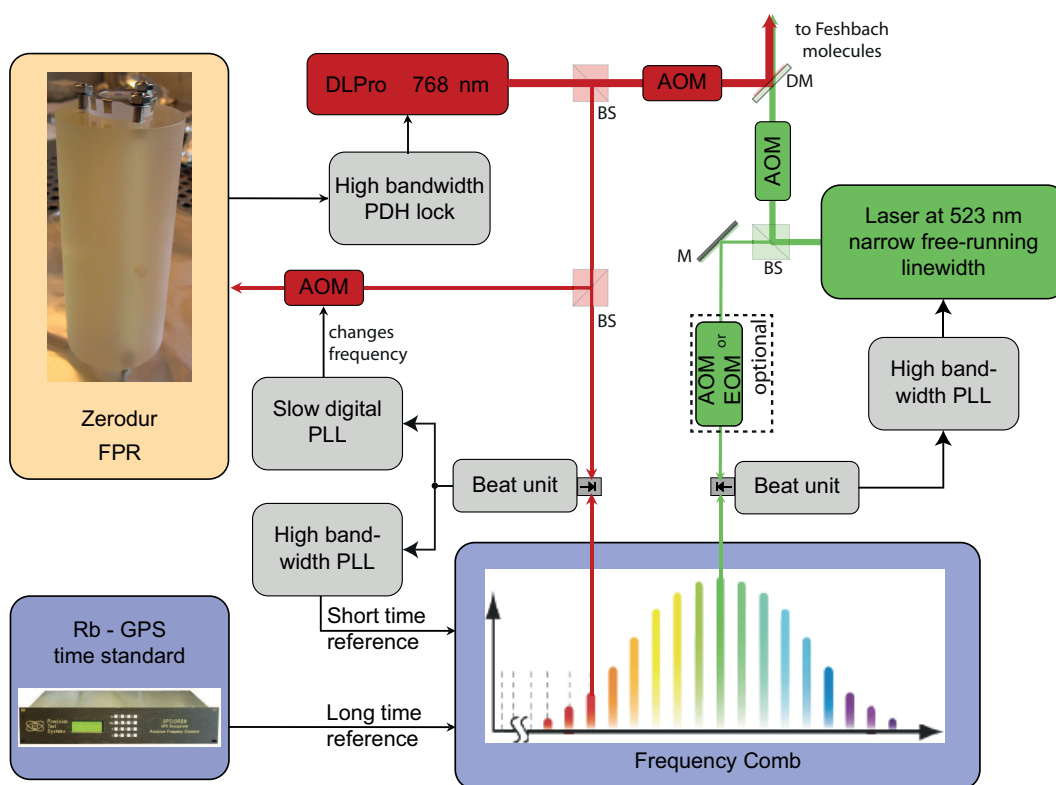


Figure 7.1: Schematic of the primary design for the Raman laser system. A total of six frequency stabilizations are used in the system: the combs' f_{ceo} , f_{rep} are stabilized by the Rb-GPS time standard, at high feedback frequencies f_{rep} is in addition stabilized to the laser at 768 nm, while the laser at 768 nm is stabilized to the Fabry-Pérot resonator (FPR), at low feedback frequencies the light for PDH locking is stabilized to the comb and the laser at 523 nm is stabilized to the comb. The FPR has a free spectral range (FSR) of 1.3 GHz. Laser at 523 nm: Diode Pumped Solid State Laser (DPSSL) or directly emitting diode laser, Laser at 768 nm: Toptica DLPro, DM: dichroic mirror, BS: beam splitter, AOM: acousto-optical modulator, EOM: electro-optical modulator, PLL: Phase-locked-loop.

As a time standard for short times, a Zerodur reference FPR was built in the course of this thesis' work. It is described and characterized in detail in Sec. 7.2. A grating stabilized diode laser (Toptica DLPro) is stabilized to an FPR resonance at 768 nm using high bandwidth Pound-Drever-Hall (PDH) frequency stabilization, which reduces its linewidth to below 500 Hz. The frequency difference between this laser and a comb mode at 768 nm is measured with a beat note. It is known that the FPR will be more stable than the Rb-GPS time standard for time intervals up to at least 40 s (see Sec. 7.2.3), while for longer times the latter is better used. Thus, it makes sense to use the obtained beat signal in two ways:

Firstly, the FPR's drift is compensated by using the frequency comb that is stabilized to the Rb-GPS time standard as a reference. This is achieved by a slow digital phase lock that only on average cancels the phase mismatch recorded over time periods of several ten seconds [Cacciapuoti et al., 2005]. The error signal, which is obtained from the beat signal, is used to shift the light frequency used for PDH locking via an acousto-optical modulator (AOM). As the laser is stabilized to an FPR resonance it will follow when the light frequency is changed by means of the AOM. Like this, the laser at 768 nm can be tuned by tuning the modulation frequency of the AOM.

Secondly, the narrow linewidth laser at 768 nm is used as a reference for short times for the frequency comb. This is advantageous, since an error in frequency can directly be measured at optical frequencies. Thus, the multiplication of radio- to optical frequencies, which also multiplies the noise of the signals, is avoided. Around 768 nm the comb modes are expected to have a linewidth of about 500 kHz, if the comb's repetition frequency is only stabilized at radio frequencies. Here, a hard phase lock between a radio frequency (RF) standard and the beat signal obtained from laser and comb is established and the comb modes' linewidths are expected to be reduced to approximately 500 Hz. The feedback bandwidth for repetition frequency stabilization that can be achieved by use of a Piezoelectric actuator is too limited for a hard phase lock between laser and comb mode at 768 nm without many cycle slips. Thus, for a high bandwidth feedback an electro-optical modulator is built into the resonator of the femtosecond fiber laser generating the fundamental spectrum for the comb. This enables fast changes of its optical path length with a specified bandwidth of around 1 MHz. A stable fast feedback lock of the comb to the laser at 768 nm has been demonstrated. A relative linewidth of several ten millihertz, which is resolution limited by the used spectrum analyzer, is measured between the comb mode and the laser at 768 nm.

The work on the green Raman laser is carried out in Singapore and not part of the work for this thesis. It is realized as a Diode Pumped Solid State Laser (DPSSL). Continuous-wave frequency doubling of the wavelength 1046 nm in a single pass waveguide has been demonstrated. The light at 1046 nm is directly emitted from a laser diode and subsequently amplified by the use of a tapered amplifier (TA). In this way, a light power of 10 mW at 523 nm is achieved. Crucial for this laser subsystem is a narrow free-running linewidth and a high modulation bandwidth, which allows for the implementation of a hard phase lock to a comb mode at 523 nm. As, due to the stabilization to the laser at 768 nm, we expect the frequency comb modes to have narrow linewidths, both light fields at 523- and 768 nm are thus made phase coherent in a time interval long enough for STIRAP transfer. It is to be noted that a green laser diode directly emitting at

7.1 Design of the Raman laser system

523 nm has recently become commercially available¹. The laser diode could potentially simplify the green laser subsystem.

AOMs in both beam paths to the molecules are used for the intensity regulation that is needed for STIRAP. In addition they allow the optical frequencies to be tuned by several MHz independently of the lasers.

In order to be able to tune the laser without the beat frequency with the comb mode at 523 nm changing, a high frequency AOM² or EOM³ can be used. The use of a high frequency EOM for optical serrodyne [Johnson et al., 2010, Kohlhaas et al., 2012] can be more efficient as compared to a high frequency AOM.

It remains to be investigated how successful a stabilization of the whole comb via the stabilization of a single comb mode at 768 nm is. As the coating of the FPR mirrors is optimized for both Raman wavelengths, it is possible to stabilize both Raman lasers to the FPR with a narrow resulting linewidth. Thus, a direct measurement of the linewidth of a comb mode at 523 nm will be possible as soon as a laser is available. For this, a beat signal between the green laser stabilized to the FPR and a comb line at 523 nm will need to be recorded.

It is to be noted that no frequency comb is needed at all if the both lasers are locked to the FPR. As shown in Sec. 5.3.3, STIRAP is very stable against common mode detunings of both Raman light fields. Thus, the precision of a standard wavemeter is high enough for FPR drift compensation. Further, the energy spacing of vibrational levels is large enough that a common mode drift on the order of 100-300 MHz does not affect STIRAP transfer efficiency. As the frequency comb facility is however available in Singapore, it can be used as a means of drift compensation.

7.1.2 Alternative laser system designs

If sufficiently long coherence times are not achieved with the laser system as it is presented in Fig. 7.1 or the technical realization of the system turns out not to be reliable enough for experiment, two other possible solutions have been worked out. These are described in the following.

Both Raman lasers stabilized to the Fabry-Pérot resonator

As mentioned before, the coating of the FPR mirrors is optimized for both Raman wavelengths. A design scheme in which both Raman lasers are individually stabilized to the same FPR is shown in Fig. 7.2. It is very similar to the design shown in Fig. 7.1 and only the differences to the design previously presented will be described here. The main differences are: Firstly, both lasers are stabilized to the FPR and the comb in the same way as already described for the laser at 768 nm in the previous section. Secondly, the hard phase lock of the comb to the laser at 768 nm is optional, as the feedback via the AOMs is slow enough to average the comb modes' frequency noise. A stabilization of both lasers to the same FPR has the advantage that most of the noise on the lasers, which is due to the mechanical stability of the FPR, is common mode. This means that the

¹Osram AG

²Brimrose Corporation

³Jenoptik AG

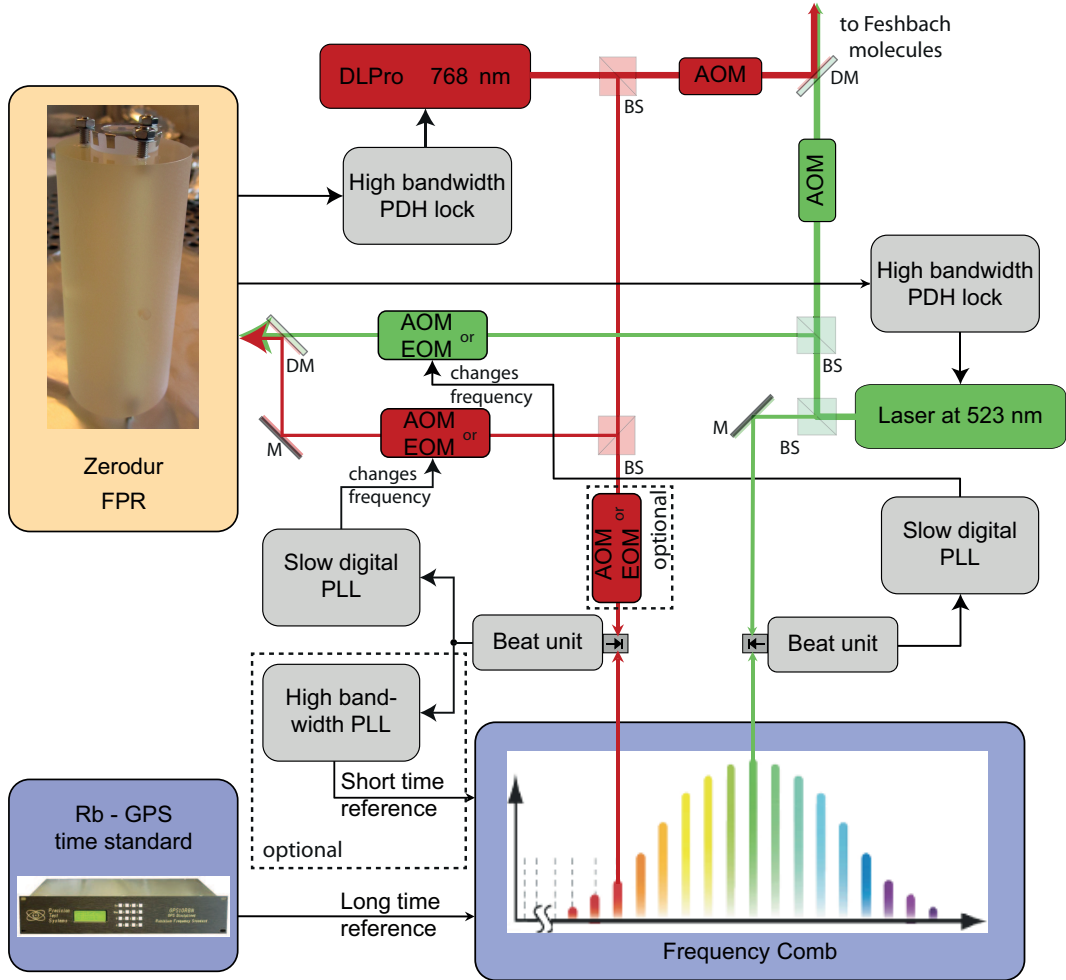


Figure 7.2: Schematic of an alternative design for the Raman laser system. Here, also a total of six locks are used in the system: the combs' f_{ceo} , f_{rep} are stabilized by the Rb-GPS time standard, both Raman lasers are stabilized to the FPR and light for the locks to the FPR modes is tuned to follow their drifts. In this design no narrow linewidths of the comb's modes are needed, thus the respective high bandwidth PLL is optional. Laser at 523 nm: Diode Pumped Solid State Laser (DPSSL) or directly emitting diode laser, Laser at 768 nm: Toptica DLPro, DM: dichroic mirror, BS: beam splitter, AOM: acousto-optical modulator, EOM: electro-optical modulator, PLL: Phase-locked-loop.

FPR mode at 523 nm changes frequency in a way correlated to the mode at 768 nm, only the change in frequency for a given length change of the FPR will be larger by a factor of $768/523$. Thus, for the laser at 523 nm, a linewidth below $768/523 \cdot 500 \text{ Hz} = 735 \text{ Hz}$ is expected if locked to the FPR. This means a relative linewidth below 235 Hz, ensuring long enough coherence times for the STIRAP durations that are expected.

A high bandwidth AOM (multi pass configuration) or EOM is used to achieve tuning of the laser at 523 nm up to one free spectral range (1.3 GHz) of the FPR. This is needed for the two photon spectroscopy (see Sec.6.3). In addition, although not inherently

7.1 Design of the Raman laser system

necessary, it might be comfortable to control the frequency used for the PDH lock at 768 nm and the light used in a beat with the comb mode at 768 nm by the same means.

This design has the advantage that both the lock of the comb to the laser at 768 nm and the high bandwidth PLL of the laser at 523 nm, which might be technically most difficult to realize, can be omitted. However, a disadvantage is that a high frequency AOM (inefficient) or EOM (further technical complication, however allows widest tuning range) is needed.

If no frequency comb is used in the laser system, a wavemeter can be used to track FPR drifts. A wavemeter with the option to directly achieve drift compensation is commercially available⁴.

Transfer beat method

Another possibility is the implementation of the transfer beat technique demonstrated at Physikalisch-Technische Bundesanstalt, Germany. For a description of the method, the interested reader is referred to [Telle et al., 2002]. The technique allows a comb with wide mode linewidths to be used to link two lasers at widely different frequencies via a “virtual beat” signal. Even though the comb modes’ linewidths are not narrow, the technique allows to still use one of the lasers as a reference of high precision in short time intervals for the other, via the comb. With this, a narrow relative linewidth of both lasers can be obtained. The transfer beat exploits the fact that just as for the case of the FPR, the comb modes’ frequencies change in a correlated way in response to a perturbation. At optical frequencies in roughly the same wavelength range, relative linewidths of several tens of Hertz have been demonstrated using the transfer beat technique [Telle et al., 2002].

7.1.3 Tuneability of the Raman lasers

As described in Chap. 6, only the two - photon spectroscopy of the ro - vibrational energies in the singlet ground state potential will be carried out with the Raman laser system. These levels are known with an accuracy of approximately 600 MHz (see Sec. 2.2.4). Thus, a tuneability of the laser at 523 nm of less than one free spectral range (FSR) of the FPR is needed for this task. Further, a tuneability that is large enough to compensate the drift of the FPR is needed. In addition, the resonance modes of the Zerodur FPR can be seen as quasi fixed in frequency. Because of this, the frequency difference between the molecular resonance frequencies and the closest FPR mode frequency needs to be bridged.

In the design shown in Fig. 7.1 the laser at 523 nm can be tuned by changing the frequency of the beat note with the comb. The AOM in the beam path to the experiment allows to change the frequency by several ten MHz. This allows to always obtain beat frequencies different from zero, which technically facilitates the lock electronics. Here, simultaneous adjustment of the RF filters, which select a beat signal with a specific comb mode, is needed when tuning the laser. As indicated in Fig. 7.1, an optional AOM or

⁴High Finesse GmbH, Auf der Morgenstelle 14D, 72076 Tübingen, Germany

EOM can be used to tune the laser while keeping the beat frequency constant. The cost for this is that more light power at 523 nm is needed.

An AOM can be used to tune the laser at 768 nm. However, in the present laser setup this AOM is replaced by an EOM used for serrodyning. In Singapore, it has been demonstrated that equally good results of laser stabilization are achieved with this technique as by use of an AOM. 1.3 GHz tuning range are needed in order to be able to tune the laser to any frequency within one FSR of the FPR to which the Raman laser at 768 nm is stabilized. As described in Chap. 6, the red Raman laser will however not be tuned during the two-photon spectroscopy that involves a single electronically excited molecular state. Thus, for any chosen electronically excited molecular state the beat frequency with the comb mode does not change. Only FPR drift compensation and a bridging between the molecular single-photon resonance frequency and the FPR resonance frequency needs to be accomplished. The bridging can be accomplished by use of an AOM with an especially selected frequency. Then, also an AOM with a comparatively low modulation frequency and good diffraction efficiency can be used, as the tuning range needed for FPR drift compensation is comparatively small. In a multi pass configuration, an AOM modulation frequency of 200-400 MHz is a good compromise between tuning range and diffraction efficiency.

When both Raman lasers are locked to the FPR as shown in Fig. 7.2, a tuning of up to 1.3 GHz (1 FSR) of both light fields used for stabilization to the FPR is needed. This can be achieved by the previously mentioned methods using high bandwidth AOM and/or multi pass configuration or by serrodyning with an EOM.

7.2 Zerodur Fabry - Pérot reference resonator

As a part of the Raman laser system, the Zerodur FPR is the reference which provides the required short term stability. Lasers at both Raman wavelengths, 523- and 768 nm, can be locked to the resonator using Pound-Drever-Hall (PDH) frequency stabilization. A linewidth of the locked laser of 500 Hz is demonstrated for a grating stabilized diode laser at 768 nm. The laser's Allan deviation is measured to stay below 2.5×10^{-12} for time intervals up to 40 s, which corresponds to 1 kHz rms frequency change at 768 nm.

7.2.1 Fabry - Pérot resonator design

High mechanical stability and low drift rates are requirements for the reference FPR. To achieve low drift rates a Zerodur spacer is used in the FPR design. Zerodur (Schott AG) is a material similar to Ultra Low Expansion Glass (Corning Incorporated). These glasses have very small thermal expansion coefficients. Furthermore there exists a temperature, close to room temperature, at which the materials dimensions are contracted to a minimum. At this temperature, there is no first order thermal expansion of the material.



Figure 7.3: Mirror attached to spacer.

7.2 Zerodur Fabry - Pérot reference resonator

Mechanical stability and isolation against vibration is of utmost importance for low frequency jitter of FPR modes. Thus, special attention has been paid to the mechanical stability of the design. The resonator spacer is mounted vertically, resting on 3 nylon screws. The soft screws, which damp out high frequency vibrations are effectively a mechanical low pass filter. The mechanical resonances of the spacer occur at much higher frequencies than the low frequencies transmitted by the screws. Further, the excitation of the lowest longitudinal resonance mode is avoided due to mid plane mounting. Like this, the resonator is largely decoupled from mechanical perturbations.

The FPR spacer with an attached mirror is shown in Fig. 7.3. In order to prevent the metal mirror holder, which has a large thermal expansion coefficient, from deforming the mirror, it is made of very thin stainless steel. The nuts, see Fig. 7.3, are only loosely closed, while the edges of the mirror holder are bent up to press the mirror down to the spacer. Thus, the holder acts like a soft spring and forces on the mirror are small.

In order to further decouple the FPR from acoustics, changes in air pressure and

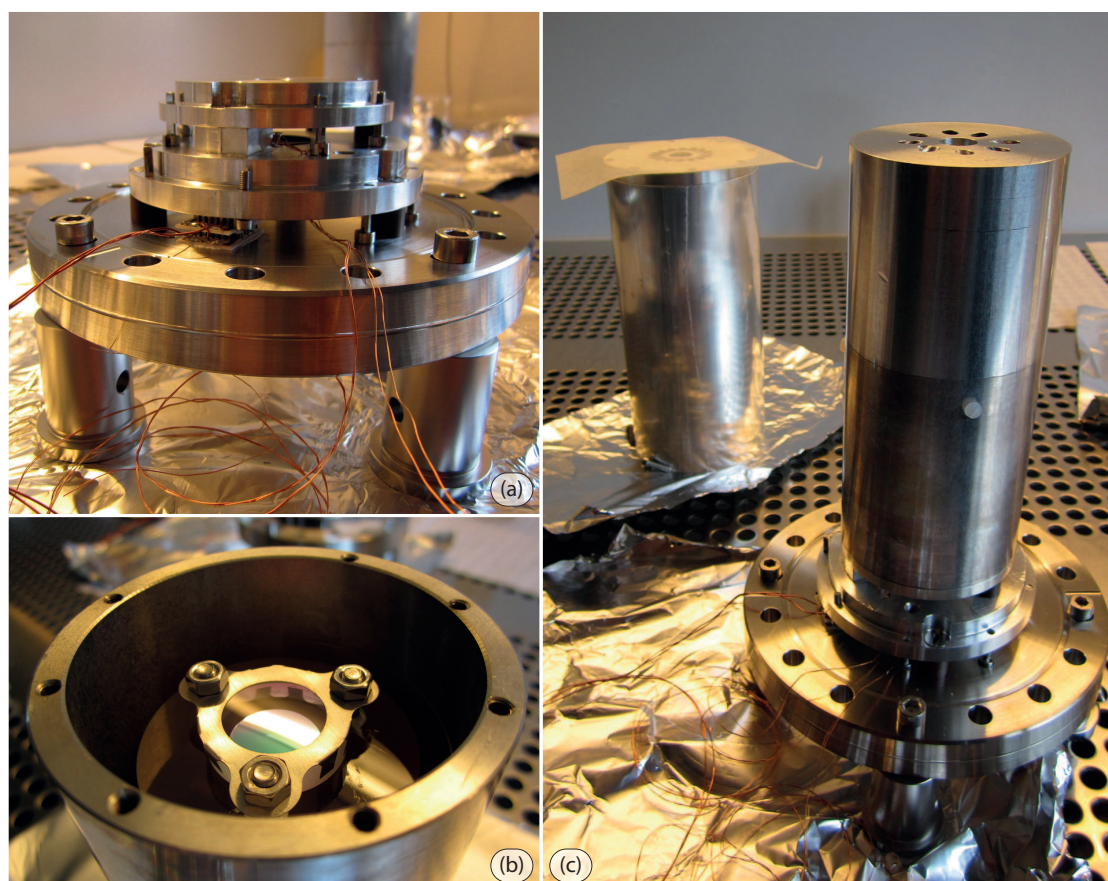


Figure 7.4: (a) heat shield bottom parts mounted to bottom plate of the vacuum chamber. Peltier elements and the thermistor are glued in place. (b) spacer with mirrors attached mounted in inner heat shield. The spacers dimensions are (diameter \times length) 50×115 mm. (c) inner heat shield containing the Zerodur spacer is mounted. Outer heat shield in the background awaits mounting.

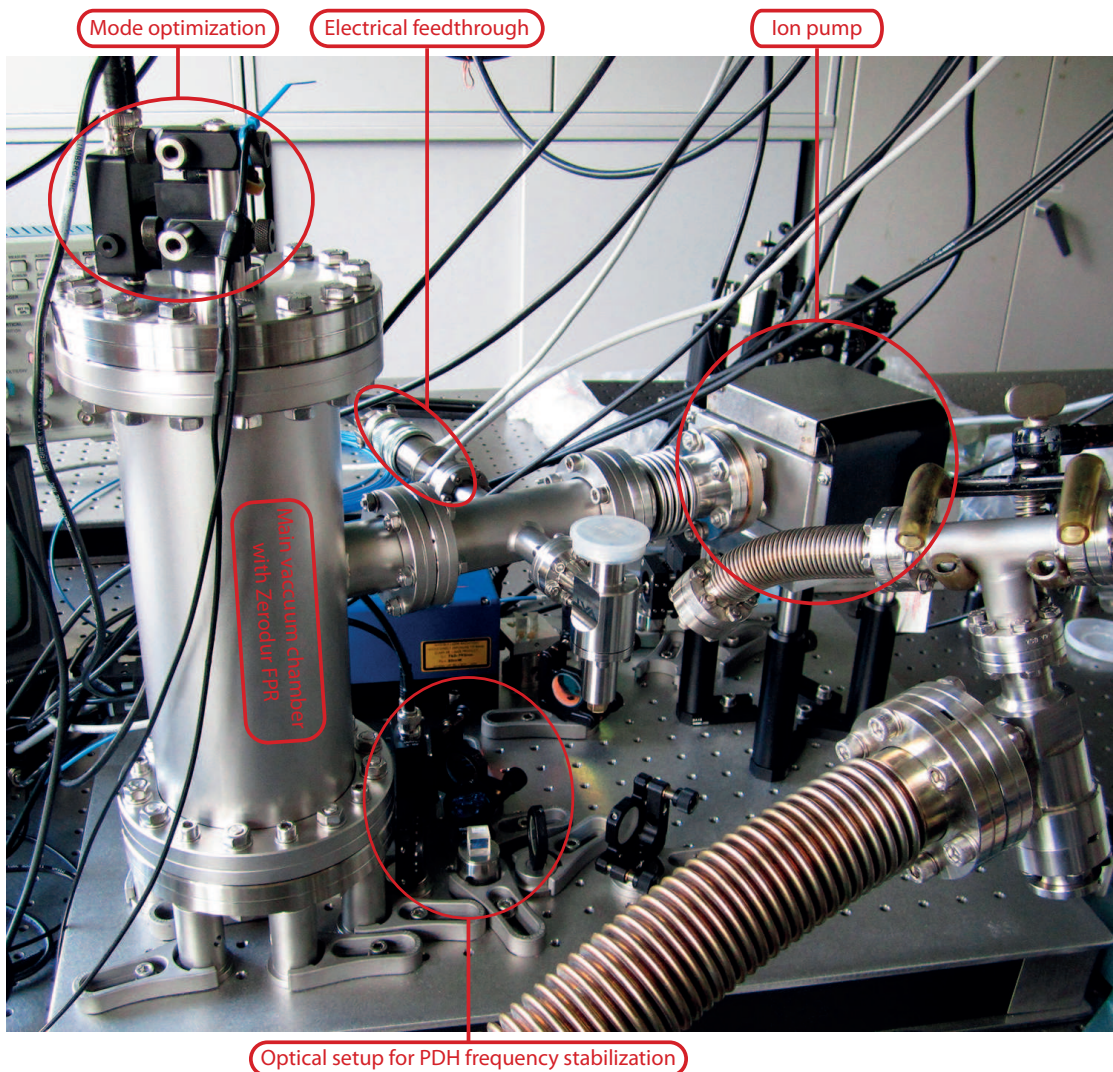


Figure 7.5: Completed setup with FPR mounted inside vacuum apparatus and ion pump ready for evacuation. A camera and photodiode are being used for mode optimization. The optical components for PDH frequency stabilization are set up directly in front of the main vacuum chamber (see paragraph about PDH frequency stabilization).

air temperature in the laboratory, it is placed in vacuum. Two heat shields inside a small vacuum chamber ensure temperature stability of the spacer. For an offset with respect to the laboratory temperature, which is needed to reach Zerodur's zero expansion temperature, the temperature inside the inner heat shield is stabilized. In addition, this provides even more stable conditions in temperature for the FPR. The design of the heat shields and vacuum chamber are shown in Figs. 7.4 and 7.5.

Fig. 7.4(a) shows the bottom of the vacuum chamber to which the bottom plates of the outer and inner heat shields are mounted. The temperature between both heat shields is measured by two temperature sensors, an AD590 and a thermistor, while the regulation is achieved by a stack of 2 Peltier elements. The latter are glued between outer

7.2 Zerodur Fabry - Pérot reference resonator

heat shield and the bottom of the vacuum chamber. Fig. 7.4(b) shows the FPR mounted inside the inner heat shield. Fig. 7.4(c) shows the inner heat shield that contains the FPR, mounted. The heads of two nylon screws can be seen on the heat shield cylinder's outside. Holes for evacuation can be seen on both, the top parts of the outer heat shield, which can be seen in the background in Fig. 7.4(c) and the inner heat shield. These do not allow a straight line of sight from outside the heat shields to the resonator spacer. This limits the impact of black body radiation. Furthermore the outer heat shields contain wedged windows at the entry aperture for the laser beams. The windows are anti-reflection coated for 523- and 768 nm and partially reflect far infrared.

Fig. 7.5 shows the completed setup before initial evacuation. A cross junction is mounted to the main vacuum chamber containing the FPR inside the heat shields. Connected are an electrical feed through for temperature sensors and Peltier elements inside the vacuum, a valve to which the pumps for initial evacuation can be connected and an ion pump. After 4 days of bake out, a pressure of 2×10^{-7} Torr was reached, enough to operate the ion pump and shield against air pressure and temperature fluctuations.

To achieve further acoustical isolation of the vacuum chamber itself, the whole honeycomb breadboard on which the setup is built will in future be placed inside a box constructed as a multiplex-wood-quartz-sand-multiplex-wood sandwich. The sand layer inside the box's walls provides very good acoustical damping of the box itself. Also, in the inside of this box, convoluted foam is placed to achieve an as quiet as possible surrounding for the FPR.

Optical design

In order to reach a linewidth of below 1 kHz of a laser stabilized to the resonator, a mirror reflectivity of approximately 99.92% corresponding to a resonator finesse of roughly 4000 is chosen. From the resonator length of 115 mm, a free spectral range of 1.3 GHz and a resonator mode linewidth of about 320 kHz (Full-Width-Half-Maximum) is expected.

For laser frequency stabilization to a FPR mode, a symmetric line shape is beneficial. As the resonator's TEM_{00} is chosen for stabilization, care needs to be taken to avoid higher order Hermite-Gaussian resonator modes close in frequency to the TEM_{00} modes. This is achieved by carefully choosing the curvature of the FPR mirrors. The resonance frequencies are calculated as [Saleh and Teich, 1991]

$$f_{q,l,m} = q \frac{c_0}{2d} + (l + m + 1) \frac{\Delta\zeta c_0}{2\pi d} \quad (7.1)$$

with the Gouy phase $\zeta(z) = \text{ArcTan}\left(\frac{z}{z_0}\right)$
and $\Delta\zeta = \zeta(z|_{\text{mirror } 2}) - \zeta(z|_{\text{mirror } 1})$.

Here, q specifies the longitudinal and l, m the transversal resonance mode order, d the mirror spacing on the optical axes and c_0 the speed of light in vacuum. The Guoy phase at a location z on the optical axes depends on the Rayleigh range z_0 , which is determined by the condition that wavefront and mirror curvatures must be the same at the location of the mirrors. Fig. 7.6 shows the resonance frequencies for the used mirror spacing of 115 mm and curvature 250 mm calculated from Eq. 7.1. It can be seen that no low order modes appear close in frequency to the TEM_{00} mode. Very good mode matching for the

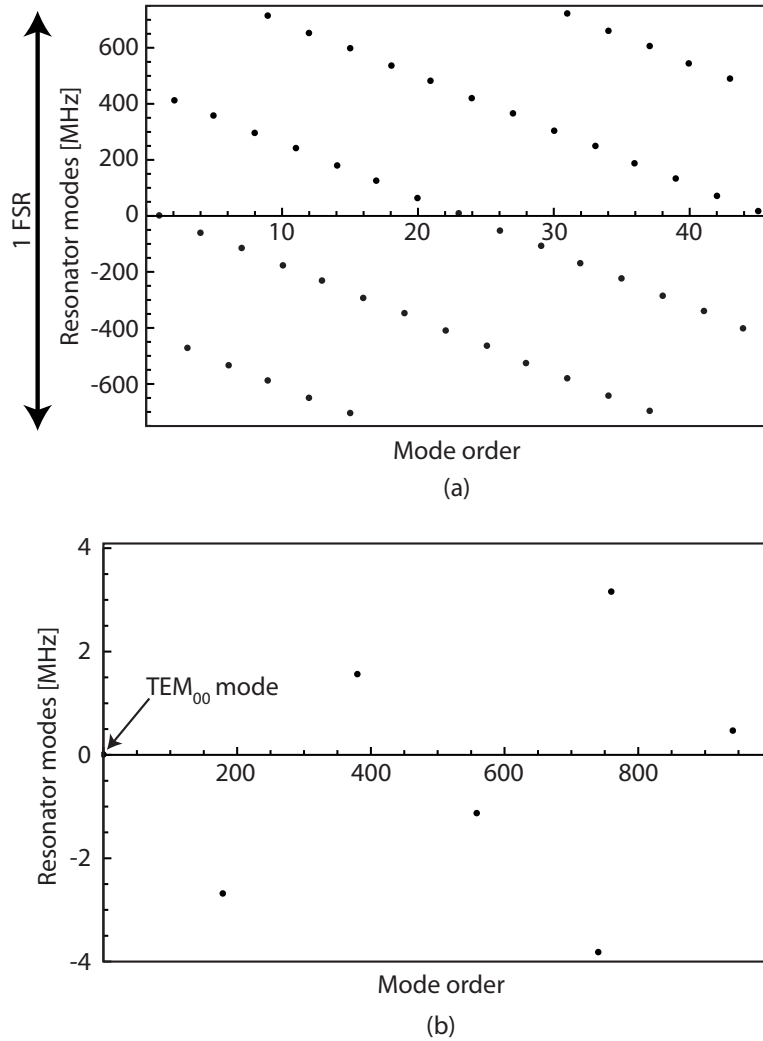


Figure 7.6: Calculated resonator modes for a mirror curvature of 250 mm and spacing of 115 mm. (a) resonator modes with a total mode order of $1 \leq q + l + m \leq 50$ that are within the same frequency interval of one free spectral range. (b) resonator modes up to a total mode order $1 \leq q + l + m \leq 1000$ that are closer in frequency than 4 MHz to the TEM_{00} mode. The first mode up to ~ 1 MHz close in frequency to the TEM_{00} mode has $q \sim 560$ longitudinal and $l + m \sim 400$ transversal mode order.

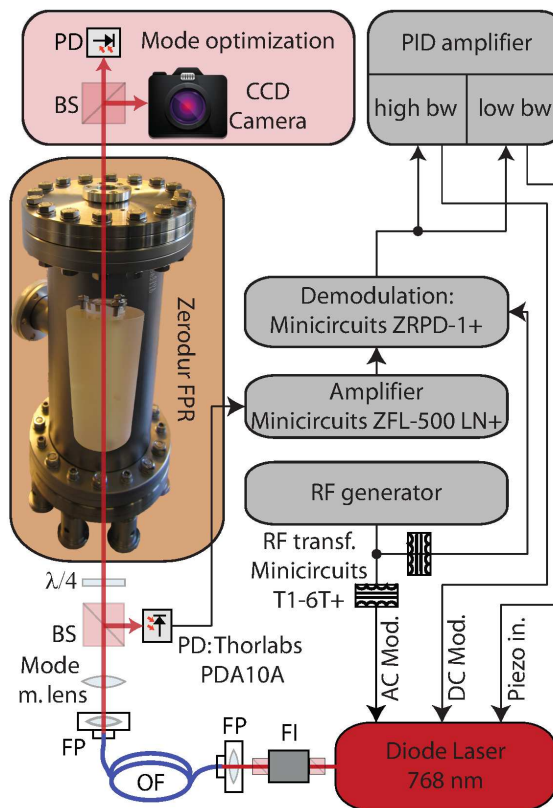
TEM_{00} is achieved with a 300 mm lens. With this the excitation of higher transversal modes is strongly suppressed.

7.2.2 Pound - Drever - Hall frequency stabilization

Pound - Drever - Hall technique is used for stabilization of lasers to the described FPR. As the technique is commonly used, no description is given here. For detailed treatments of the subject the reader is referred to [Drever et al., 1983, Black, 2001]. Key to a narrow linewidth of a laser stabilized to the reference FPR is a low noise, high bandwidth

7.2 Zerodur Fabry - Pérot reference resonator

Figure 7.7: Optic and electronic components for PDH frequency stabilization to the reference FPR. Approximately $100\ \mu\text{W}$ of optical power emitted by the stabilized laser are coupled into the FPR. For error signal generation, the current through the laser diode is modulated with 7.4 MHz. The bandwidths of the fast and slow PID amplifiers are: 0-1.5 MHz and 0-20 kHz. The high bandwidth PID amplifier settings for frequency stabilization are ($f_{-3\text{dB}}$ values): Low bandwidth integrator (fast PID amplifier) 30 kHz, high bandwidth integrator 420 kHz, differentiator 1.3 MHz. Ground separation is achieved by means of RF transformers where it is beneficial. bw: bandwidth, Mode matching lens: 300 mm, BS: polarizing Beam Splitter cube, FP: Fiber Port, OF: Optical Fiber, $\lambda/4$: $\lambda/4$ waveplate, PD: Photo Diode, FI: Faraday Isolator.



feedback loop.

In the Raman laser system, a Topptica DLPro grating stabilized diode laser at 768 nm, stabilized to the presented FPR is used. The technical details of the used PDH stabilization are described in this section.

Fig. 7.7 shows a block diagram of the optical and RF components for laser frequency stabilization to the FPR. After the diode laser, a short optical fiber is used to obtain a clean TEM_{00} mode as well as making the FPR alignment independent of the alignment of the used grating stabilized diode laser. By passing the $\lambda/4$ waveplate two times, the light reflected from the FPR is turned in polarization by 90° . This causes it to be reflected off the polarizing beam splitter cube (BS) and to be detected by the commercial high bandwidth photodiode. From the obtained RF signal, the error signal is obtained as described in [Black, 2001], split up and fed to a commercial PID amplifier⁵. This device consists of two completely separated PID amplifiers, which have different bandwidths. The low bandwidth PID branch acts on the piezoelectric transducer controlling the grating of the diode laser. This mostly compensates thermal drifts of the laser. The high bandwidth PID branch acts onto the laser diode current. For this PID amplifier, the gain setting of the proportional branch, as well as the cutoff frequencies and gain settings of 2 integrators and a differentiator are carefully optimized for the specific loop delay of the stabilized laser. When all settings are correctly adjusted, the feedback circuits are able to reduce the laser linewidth to approximately 1/1000 of the FPR

⁵Optilas LTD, Latvia

linewidth, which is roughly 300 Hz for the design presented here.

In FPR transmission, the light is detected by a photodiode and a CCD camera. These are used for selection and optimization of the coupling into the TEM_{00} mode, which is used for laser stabilization.

7.2.3 Characterization of the Fabry - Pérot resonator and the stabilized Raman laser

In this section the characterization data recorded with the laser setup shown in Fig. 7.7 is presented. For these measurements, the diode laser is stabilized to a FPR resonance at 768.23 nm.

Resonator ring-down

In order to confirm the resonator's finesse after assembly of the apparatus, its photon lifetime was determined by recording the ring-down behavior. For that, the grating stabilized laser is quickly tuned over a FP-resonance line at 768 nm, which is achieved by ramping the current through the laser diode. Fig. 7.8 shows the optical power reflected from the resonator during ramping. Here, "time" is proportional to the laser's frequency. When the laser is tuned over the FPR resonance line, the reflected optical power oscillates. This is due to the time and frequency dependent interference of the

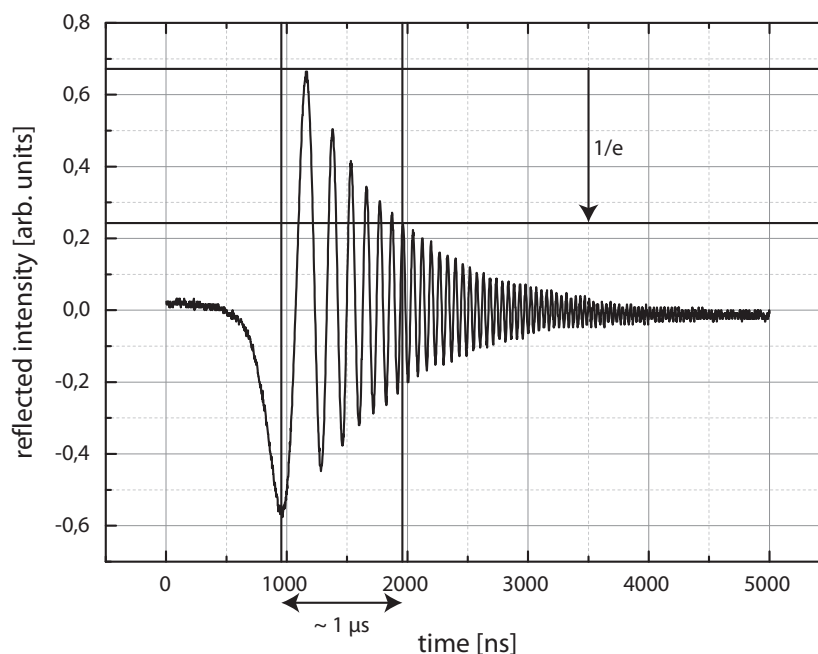


Figure 7.8: FPR ring-down. Approximately after $\tau = 1 \mu\text{s}$ the amplitude of the oscillation has dropped by $1/e$. Using equation 7.2, a resonator linewidth of 318 kHz is estimated. With the resonator's dimensions a finesse of 4000 is found, well in agreement with the mirrors' specification.

7.2 Zerodur Fabry - Pérot reference resonator

light stored in and leaking out of the FPR with the light reflected off the FPR. The light stored inside the FPR has a fixed frequency, while the laser is tuned. Thus, the beat frequency between the light leaking out of the FPR and the light of the laser depends on time, which leads to the oscillations.

From the recorded reflected optical power, the photon lifetime can be estimated as indicated in Fig. 7.8. The Full-Width-Half-Maximum (FWHM) FPR resonance linewidth is related to this value by [Saleh and Teich, 1991]

$$\Delta f_{\text{FWHM}} = \frac{1}{\pi\tau} , \quad (7.2)$$

which together with the known FPR's dimensions can be used to estimate the resonator's finesse. The value of 4000, found in this manner, agrees very well with the mirrors' specification.

Measurement of the resulting laser linewidth

Fortunately another FPR, which can be used at the same wavelength and which is already characterized, is available at Max-Planck-Institute of Quantum Optics (MPQ). It is constructed similarly. Thus, it was possible to confirm the narrow linewidth of the Raman laser at 768.23 nm, when locked to the presented reference FPR, by setting up a beat note with another laser locked to the second FPR.

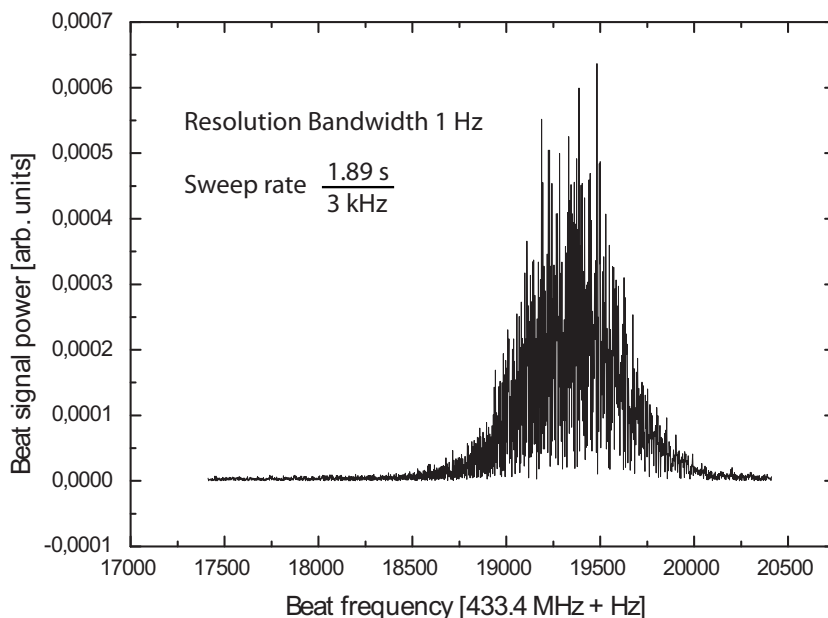


Figure 7.9: Beat note at 768.23 nm of the Raman laser with a laser of similar linewidth at MPQ which was set up for this purpose. A signal recorded with the indicated resolution bandwidth and sweep rate of the spectrum analyzer that is used are shown. The beat note's FWHM is about 700 Hz. For both PDH locks of the lasers to the FPRs approximately 200 μW of optical power are used. Each of the beams for the beat note carries about 900 μW of optical power.

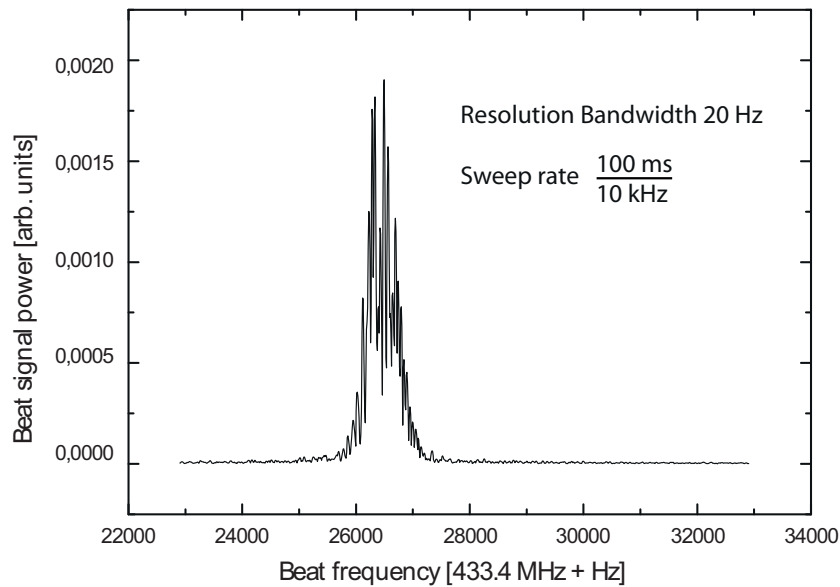


Figure 7.10: Beat note at 768.23 nm of the Raman laser with a laser of similar linewidth at MPQ which was set up for this purpose. To record this data set, the resolution bandwidth and sweep rate of the spectrum analyzer was changed, while all other parameters were the same as in the dataset shown in Fig. 7.9.

Beat notes between the lasers are shown in Figs. 7.9 and 7.10. These have been recorded by use of a spectrum analyzer. Widths of approximately 700 Hz FWHM are found. As both laser systems are independent and the lasers have approximately the same linewidth, it can be estimated that the linewidth of the Raman laser locked to the presented reference FPR is $700/\sqrt{2}$ Hz \approx 500 Hz. This is well below the goal of 1 kHz which was planned to be achieved for the Raman laser at 768 nm. As the FPR drift rates are very low (see following paragraph), the width of the beat signal stays well below 1 kHz, even for observation periods of several seconds. Thus, the beat linewidth of 700 Hz is measured even for the spectrum analyzer’s maximum resolution bandwidth of 1 Hz, for which a sweep time of 1.89 s is required for a frequency interval of 3 kHz.

At lower resolution bandwidth (Fig. 7.10) and faster data acquisition rates, the beat signal is observed to contain mostly acoustical noise at frequencies below 1 kHz. As expected, the mechanical stability of the design is limiting the linewidth. Thus, it is important to shield the vacuum apparatus against acoustics and vibrations transmitted by cables. It is to be noted that the setup was not placed inside the mentioned wooden box for acoustical shielding during the recording of the measurement data presented in this section. Thus, the data presented here needs to be understood as a “worst case” in respect to perturbations due to acoustics. Transmission of vibrations via the cables connected to the setup have been observed, especially via the rather stiff high voltage cable for connection of the ion pump. It is important to conduct the wires in a way that minimizes these influences.

As shown in Sec. 5.3.2, estimated Raman pulse durations are on the order of ten to several tens of μ s. As previously mentioned, the relative phase stability of both Raman

7.2 Zerodur Fabry - Pérot reference resonator

lasers during STIRAP transfer is most relevant, which corresponds to perturbations at frequencies higher than approximately 100 kHz. It is to be emphasized that while the knowledge of the phase noise spectral density allows to infer the linewidth of a signal, the opposite is not true. Thus, further data on the stabilized laser's noise is needed for a conclusive characterization. A possible measurement setup for the high frequency noise contributions could include a second FPR of medium finesse. For this, light of the stabilized laser is coupled into the second FPR and is tuned to a frequency which lies on the side of a resonance of the second FPR. The observation of the amplitude noise on a high bandwidth photodiode can be used to infer the phase noise spectral density, if the amplitude noise is also recorded and taken into account. Like this, frequency dependent phase noise contributions in the high frequency range could be found by a Fourier transformation of the data taken by use of the second FPR.

While the measurement described above is a rigorous test of the high frequency phase noise contributions, the PDH error signal itself can to some extent be used to estimate these contributions. From other characterization measurements carried out at MPQ, the typical noise levels on the error signals of other narrow stabilized lasers are known. From a comparison of the noise levels and the previously determined width of the FPR resonance, it can be inferred that noise contributions at these high frequencies are at an negligible level for our experiment. Thus, the relative phase stability will be more than sufficient to achieve stable STIRAP transfer when sequence durations do not exceed 100 μ s.

Fabry-Pérot resonator drift

In addition to a narrow linewidth of a laser stabilized to the FPR, low drift rates are wanted. Approximately 36 hours after finishing the bakeout procedure of the resonator's vacuum apparatus, the previously described beat note between the two lasers was set up and a three day recording of the relative laser frequency was started. This data is shown in Fig. 7.11. The relative drift rate is seen to be slowly decreasing, because the temperature is still equilibrating after bake out of the vacuum chamber. Thus lower drift rates are still to be expected. When fully equilibrated, the beat is expected to stay within a 5 – 10 MHz frequency interval. An average drift rate of 22 Hz/s is found, while the rates in the beginning and the end of the measurement period are 36 Hz/s and 15 Hz/s.

It is to be emphasized that a common mode drift of both lasers individually stabilized to the two FPRs cannot be completely excluded. During the measurement, both laser systems were in the same room and were experiencing a common room temperature drift. Further, both FPRs have Zerodur mirror spacers with similar lengths. Thus, even though the FPRs were of course individually temperature stabilized, the laser frequencies could have changed in a correlated way. This means that the total drift cannot be inferred from the data shown in Fig. 7.11 alone. However, the drift rate of the MPQ FPR had been measured before against an absolute reference and is known to be less than 35 Hz/s. Hence, the absolute drift rate of the Raman laser FPR is not higher than 50 Hz/s at the end of the shown measurement period.

About half a year later, the FPR drift was again measured against the frequency comb system presented in Sec. 7.1. As the laser system is stabilized to GPS, common

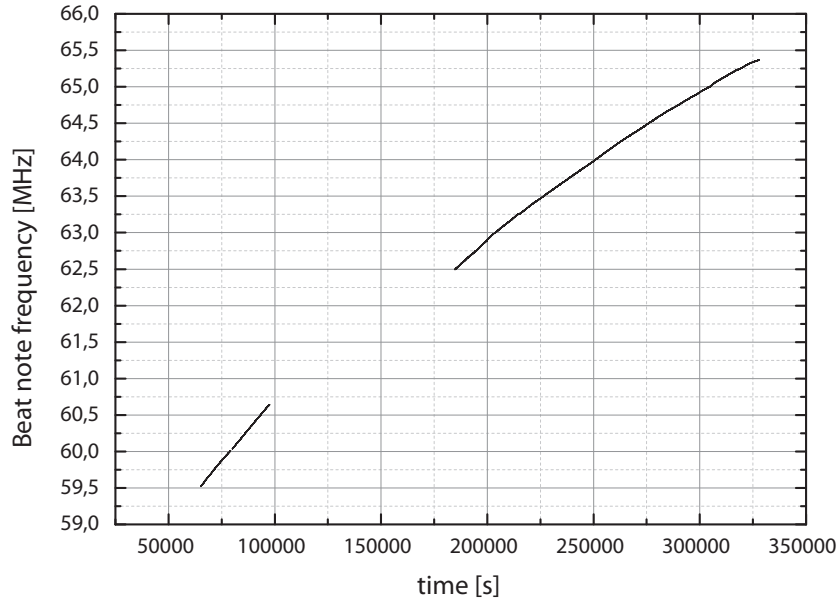


Figure 7.11: Beat frequency over a period of approximately 3 days. One period during which one of the lasers fell out of stabilization is missing.

mode frequency drifts can be ruled out in this case. The measured drift rate after this long equilibration time is < 5.2 Hz/s. It is to be noted that this corresponds to a relative drift rate of < 2.4 Hz/s if both Raman lasers are directly and only stabilized to the FPR. With a two-photon linewidth of 500 kHz (see Sec. 5.3.3), this means, that even without drift compensation no decrease in STIRAP transfer efficiency is to be expected on a timescale of two days.

Allan deviation

A standard measure for frequency stability in the time domain is the Allan variance [Allan, 1966, Riley, 2008]

$$\sigma_y^2(\tau) = \frac{1}{2(M-1)} \sum_{i=1}^{M-1} (\bar{y}_{i+1} - \bar{y}_i)^2 . \quad (7.3)$$

Here τ denotes a time interval during which an average frequency \bar{y} is measured. M frequency deviations are averaged. σ_y , the square root of the Allan variance, is called Allan deviation. For a measurement of the true standard Allan variance, a dead time free π -type frequency counter is needed [Riley, 2008, Dawkins et al., 2007].

In order to obtain time dependent characterization data for the frequency stability of the presented reference FPR, the Allan deviation of data recorded with the previously described beat note is calculated here. For counting the beat signal a Kramer frequency counter [Kramer and Klische, 2001, Szplet et al.] is used. The determination of the relative Allan deviation of both FPRs allows a comparison to the one specified for the commercial Rubidium-GPS time standard, which provides the long-term time reference

7.2 Zerodur Fabry - Pérot reference resonator

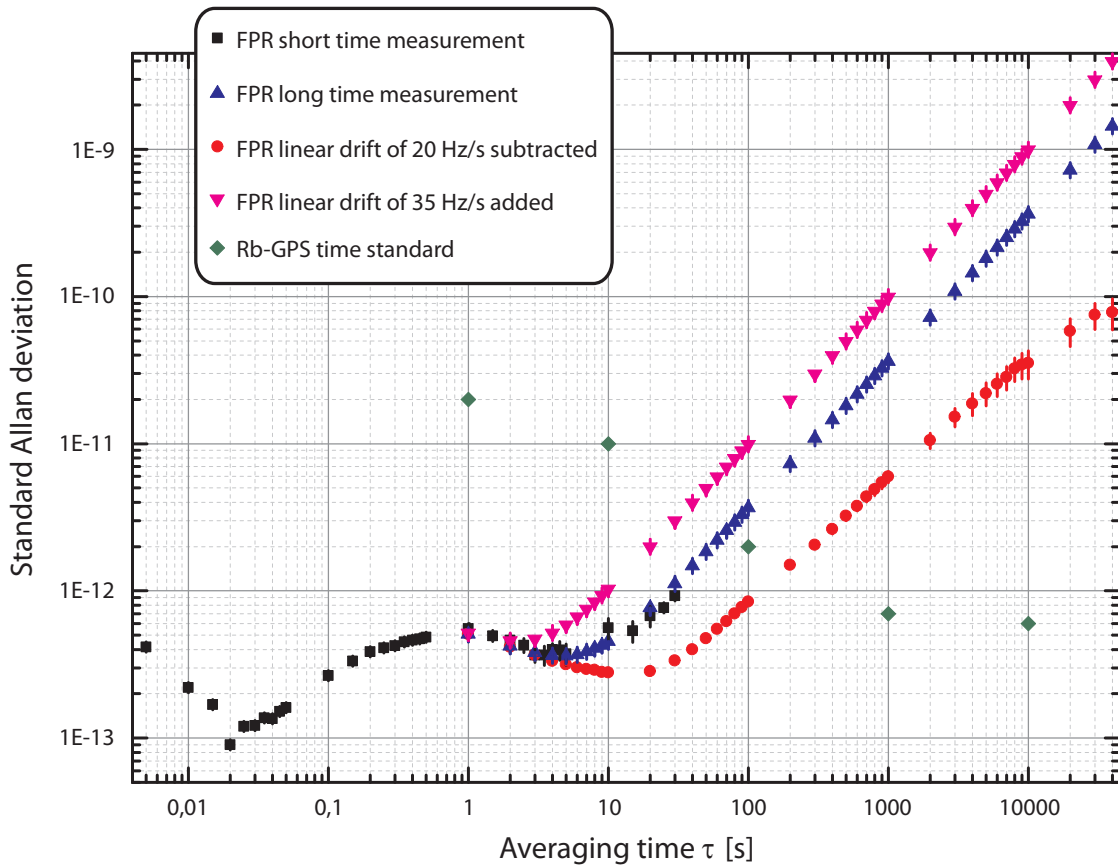


Figure 7.12: Allan deviation, determined from a measured beat signal between both lasers stabilized to the respective FPRs, compared to the Rb-GPS time standard. Black squares and blue triangles represent data for the two FPRs, which was measured on two consecutive days, without modification. For the red circles, a linear drift of 20 Hz/s has been subtracted from the beat signal data which was used to determine the blue triangles. For the pink triangles a linear drift of 35 Hz/s was added to the same data. Green rhombuses represent the specification of the Rb-GPS time standard. The lowest Allan deviation of the combined references in the time intervals of measurement, approximately 1×10^{-13} , is reached for a time interval τ of roughly 20 ms. The highest value of the combined references is approximately 3×10^{-12} , for a time interval of roughly 40 s. For the FPR data, error bars are included, while the Rb-GPS's Allan deviation is specified to be smaller than the values represented by the green rhombuses.

in the Raman laser system. By comparing these data sets it is possible to determine a crossover frequency for switching from one to the other time standard.

Fig. 7.12 shows the Allan deviations of the two lasers stabilized to their respective FPRs, as well as the specification for the Rubidium-GPS time standard. Mostly phase noise of the lasers leads to increased Allan deviations for short time intervals below 20 ms, where the minimum deviation of 1×10^{-13} is found. At 768 nm, this corresponds to a relative rms frequency change of 39 Hz. It is interesting to note that the two data

points for the shortest time intervals correspond to rms frequency changes below the Fourier limit, which is 200 Hz for the first data point at 5 ms, while the measured Allan deviation of 4×10^{-13} corresponds to an rms frequency change of 160 Hz at 768 nm. This is due to the very good signal to noise ratio of the used frequency counter and the fact that many photons contribute to the signal. As the precision to which a frequency can be determined by the counter is far better than the measured values, the two points represent data that is limited by laser noise rather than the Fourier limit. In the data a local maximum is observed at 1 s. This appears due to a drifting interferometer between the fiber coupling and the first FPR mirror. Due to the angle polished fiber used, this effect is of small importance. However, it has been demonstrated that it can be avoided by placing an optical isolator after the fiber coupling [Alnis, 2011]. For time intervals longer than several seconds, the drift of the FPRs is limiting.

The same beat signal data (blue triangles) was modified to obtain the Allan deviations shown as red circles and pink triangles. For the red circles, a linear drift of 20 Hz/s was subtracted. In this data set, the increasing Allan deviation for long times is due to the curvature of the relative FPR drift. The dataset was taken directly following the drift data acquisition shown in Fig. 7.11 in which a curvature can also be seen very well. Thus it is not surprising that the FPR drift is not exactly compensated. As described in the previous paragraph, there could have been a common change in laser frequency of both lasers due to a correlated FPR drift. In worst case, a total FPR drift rate of 50 Hz/s, which is 35 Hz/s higher than the measured relative drift, could occur. This is taken into account by adding 35 Hz/s drift to the measured beat signal, which is shown in the data set represented by pink triangles. Thus, the true Allan deviation for long time intervals is probably somewhere between the pink and blue triangles.

From Fig. 7.12, it can be estimated that for time intervals shorter than 40 s it is advantageous to use the presented FPR as a reference for the Raman laser system, while for longer time intervals the Rb-GPS time standard is better used. This is helpful when choosing crossover frequencies for the feedback circuits stabilizing the frequency comb and Raman lasers to the respective FPR and Rb-GPS time standards.

At 768 nm (390 THz), an Allan deviation of 2.5×10^{-12} corresponds to an rms frequency change of 1 kHz, which is planned to be reached in the Raman laser system. From Fig. 7.12, it can be seen that this target value is reached for the Raman laser at 768 nm in almost all time intervals > 2 ms if both time standards, FPR and Rb-GPS are being used. The highest Allan deviation of the combined time standards is 3×10^{-12} at 40 s corresponding to 1170 Hz rms frequency change.

It is to be noted that decoherence of the Raman light fields can arise due to noise sources present in the beam paths on which the light is transported to the sample of molecules. A Michelson interferometer can be used to characterize the noise pick-up of the individual light fields on their beam paths. As the noise spectrum will however mostly include acoustical frequencies, it is not expected to be relevant on the timescale of the STIRAP sequence.

From the characterization data presented in this section, it is found that the FPR provides the stability needed for an efficient and stable Raman transfer.

Chapter 8

Conclusion and outlook

The realization of a quantum gas with strong dipolar long-range interaction has been a long standing goal in the atomic physics community. One way to pursue this goal is to exploit the permanent electric dipole moment of heteronuclear alkali metal dimers in their absolute ro-vibrational ground state. ${}^6\text{Li}-{}^{40}\text{K}$ is a bosonic dimer consisting of fermionic atoms which possesses a large dipole moment of 3.56 Debye. The production of vibrationally highly excited ${}^6\text{Li}-{}^{40}\text{K}$ Feshbach molecules at ultracold temperatures has been demonstrated in our group [Voigt et al., 2009]. In order to be able to exploit the large dipole moment, preparations for coherent state transfer to the absolute ro-vibrational ground state have been started.

In this thesis the detailed experimental and theoretical preparations to achieve coherent state transfer by means of Stimulated Raman Adiabatic Passage (STIRAP) are presented. The preparations will allow to approach the project in a straightforward and efficient manner after the rebuilding of the experimental apparatus in Singapore is finished.

The experimental work includes detailed investigations of the s-wave scattering of atomic ${}^6\text{Li}$ and ${}^{40}\text{K}$ in the vicinity of the 155 G Feshbach resonance. This work is published in [Costa et al., 2010a]. Precise experimental data on the width and magnetic field strength at which the resonance occurs is gained from observing cross-dimensional relaxation of ${}^6\text{Li}$ and ${}^{40}\text{K}$. This reveals the production of molecules on the atomic side of the resonance, thereby establishing the first observation of a many body effect in the crossover regime of a narrow Feshbach resonance. Further, these data can be used to relate the previously measured lifetime of Feshbach molecules [Voigt et al., 2009], produced at the 155 G resonance, to magnetic field strengths. The decay of the energy anisotropy that is generated for cross-dimensional relaxation is quantitatively investigated and compared to theoretical predictions of a classical kinetic model.

The planning of the Raman laser system used for ground state transfer is one of the main topics of this thesis. As a reference for short time intervals up to several tens of seconds, the Fabry-Pérot resonator, which has been manufactured in the course of the work done for this thesis, is a main part of the Raman laser system. Laser frequency stabilization of the Raman laser at around 768 nm with a linewidth of approximately 500 Hz is demonstrated. Other characterization data include the resonator's Allan deviation and data on resonator drift. Further, frequency stabilization of a frequency comb,

which is another main part of the Raman laser system, to the reference Fabry-Pérot resonator is demonstrated.

In order to be able to carry out the spectroscopy of electronically excited molecular states efficiently, the precision of a commercial interferometric laser frequency stabilization has been enhanced to the MHz level. The calibration procedure and results are published in [Brachmann et al., 2012]. The details of this technical work are presented in App. A.

The planning of the Raman laser system is based on the theoretical work presented in Chaps. 2, 5 and 6. Detailed information on the ${}^6\text{Li}$ - ${}^{40}\text{K}$ ground state and electronically excited potentials is given. Existing experimental as well as theoretical data on the molecular potentials and term energies of ${}^7\text{Li}$ - ${}^{39}\text{K}$ as well as ${}^6\text{Li}$ - ${}^{40}\text{K}$ are analyzed. The determination of isotopologue energy shifts allows to gain complete sets of high precision data on the relevant term energies of vibrational states in the $X^1\Sigma^+$ and $1^1\Pi$ potentials. Further, the data on the vibrational states in the $1^1\Pi$ potential is used to increase the precision of an existing *ab-initio* potential function. Molecular states of the ${}^6\text{Li}$ - ${}^{40}\text{K}$ isotopologue are numerically calculated and the Franck-Condon factors for the relevant electronic transitions are determined. In this manner electronically excited molecular states that promise suitable candidates for a STIRAP transfer are found. From the molecular term energies the transition wavelengths needed for STIRAP transfer are determined.

The Asymptotic Bound State Model [Moerdijk et al., 1995, Tiecke et al., 2010] is applied to the ${}^6\text{Li}$ - ${}^{40}\text{K}$ 155 G Feshbach resonance. In this context, the spin state in which the molecules are produced is determined. This allows the calculation of the magnetic field dependent fraction of the spin singlet part of the molecular state. Together with the Franck-Condon factors calculated in Chap. 2, the spin singlet fraction is the most relevant factor for an estimation of the transition strength. The transfer duration predicted in Chap. 5 is on the order of $5\ \mu\text{s}$ for Raman beam powers of around 1 mW. This suggests that the STIRAP transfer with the laser system described in Chap. 7 is very well possible.

Molecular single- and two-photon spectroscopy will need to be carried out. For this purpose, samples of Feshbach molecules can directly be used. However, in order to do so the atoms remaining after the association of Feshbach molecules need to be removed from the sample. The technical details to achieve this by the use of resonant light pulses have been worked out in Singapore. However, as no Feshbach molecules have been generated after the movement to Singapore, pure molecular samples have not yet been produced. When this is the case, one of the most interesting questions with respect to the production of ground state molecules will be the experimental determination of the lifetimes of pure samples of molecules in the Feshbach state.

Due to the comparatively high precision with which the wavelengths of transitions between vibrational states in the $X^1\Sigma^+$ and $1^1\Pi$ potentials are determined here, the molecular spectroscopy of these energy levels will be quickly realizable. Once transitions are found, their strengths will need to be experimentally determined and the association of molecular states to molecular potentials will need to be found. Further, possible mutual perturbations among the electronically excited states will need to be characterized.

After this, STIRAP can be attempted. As mentioned in Chaps. 5 and 6, the presence of multiple electronically excited states, that are simultaneously addressed by the

STIRAP lasers, might reduce transfer efficiency or even make it impossible. States in the $1^1\Pi$ potential carry one quantum of orbital angular momentum in the electron cloud and exhibit a Zeeman splitting of magnetic states. Thus, even though comparatively large transition strengths are estimated for vibrational states in the $1^1\Pi$ potential, these might not be the optimal choice for STIRAP transfer. Due to the high precision with which the molecular term energies in the $X^1\Sigma^+$ and $1^1\Pi$ potentials are determined here, it will however be possible to experimentally investigate this quickly and efficiently. If it is found that transfer via a state in the $1^1\Pi$ potential is not possible with high efficiency, a good option is to try states in the $2^1\Sigma^+$ potential. These exhibit only a negligible Zeeman splitting of energy levels. Through the use of the calibrated interferometric laser frequency stabilization, the molecular spectroscopy, that in this case will need to be carried out over the larger wavelength intervals, will be experimentally realizable in a convenient and efficient manner.

One parameter that needs to be experimentally optimized for efficient STIRAP transfer is the choice of a magnetic field value. Here, it is to be pointed out that all the term energies, transition wavelengths and Franck-Condon factors presented in Chaps. 2 and 5, are calculated for zero magnetic field. In [Ni et al., 2008], magnetic field strengths close to the Feshbach resonance are successfully used for STIRAP transfer. From this it is possible to infer that the extension of the molecular wavefunctions at these high magnetic field strengths is not significantly larger than in the zero magnetic field case and that the Franck-Condon factors are expected to differ not widely from the zero field ones. Thus, the optimal magnetic field strength might be just one to very few Gauss below resonance. As the 155 G ^6Li - ^{40}K resonance is narrow, the open channel admixture decreases rapidly for magnetic field strengths below the resonance. This causes the wavefunction of the Feshbach state to be constrained to smaller internuclear distances below resonance than in the case of a broad resonance.

In our present experimental setup, no direct detection of ground state molecules is possible. However, the indirect proof of transfer by a loss of detected molecules can be gained. This is a common technique. The lost, or more accurate, “hidden” particles can be recovered by a reverse transfer back to the original Feshbach state, where imaging is possible at magnetic field values close to the Feshbach resonance.

In order to be able to induce an electric dipole moment of the ground state molecules in the laboratory frame, DC high voltage electrodes have been designed in Singapore. These are used to be able to generate high voltage DC fields at the location of the trapped particles, which are in very good approximation homogeneous. The electrodes are placed inside the vacuum chamber in order to achieve as high as possible electric field strengths. In their final position the electrodes have been tested up to voltages of 15 kV, corresponding to a field strength of approximately 8.5 kV/cm. From this, a laboratory dipole moment of 1.9 D is expected to be achievable for ^6Li - ^{40}K absolute ground state molecules. In the design, much attention has been paid to the distortion of the field at the position where the ultracold samples are trapped. These occur due to the surrounding electrically conductant parts at ground potential. Other groups have encountered charge up of parts of the vacuum apparatus once high voltage DC fields are applied close to the location where ultracold samples are trapped [Morsch, 2010]. Especially the charge up of the glass cell itself can pose a significant difficulty, since the particles’ trapping potentials can be significantly distorted in this way. It will need to

be experimentally determined how significant these effects are. Electrically conductant anti-reflective glass coatings¹ or charge mobilization by UV light might pose solutions in case such problems occur. Possibly, Iralin coated surfaces of glass cells could also directly be used as electrodes for the polarization of molecules.

Once transfer has successfully been achieved at high efficiency the first measurements will include a lifetime measurement of ground state molecules in the three dimensional trap. Further, it will be very interesting to find out what molecular dipole moments in dependency on the DC electric field strengths can be achieved. The direct measurement of molecular dipole moments can be achieved by two photon Stark spectroscopy [Ni et al., 2008]. This spectroscopy is much the same as the two-photon spectroscopy described in Chap. 6, with the only addition being the DC electric field. As the vibrationally highly excited Feshbach state possesses a negligible dipole moment, a measured Stark shift can be attributed to the ground state. The dipole moment induced in the laboratory frame is directly determined from the measured Stark shift. Further, a measurement of the molecular lifetime in dependency on the dipole moment will be interesting.

As estimated in Chap. 2, the theoretically expected lifetimes of ⁶Li - ⁴⁰K ground state molecules in a three dimensional bulk gas are rather short. The reason is the occurrence of the ultracold chemical reaction $2 \text{Li} - \text{K} \rightarrow \text{Li} - \text{Li} + \text{K} - \text{K}$. When dipole moments are induced in the laboratory frame, and in addition to the van-der-Waals interaction the dipolar interaction is of a relevant strength, an even further increase of the reactive constants are predicted [Quéméner et al., 2011]. While an experimental determination of the chemical rate constants in dependence on the strength and dominant type of interaction is an interesting subject by itself, the limited lifetime poses constraints for other investigations. However, a stabilization against chemical reactions is predicted in systems with strong dipolar interaction in reduced dimensionality [Micheli et al., 2010]. In this trap configuration and molecules with dipole moments oriented in the direction of tight confinement, the dipolar interaction is purely repulsive [Pupillo et al., 2008]. This stabilizes molecular samples against decay due to chemical reactions as it prevents molecules to enter into the short length scales needed for chemical reactions to occur. When a two dimensional trap is available in Singapore, it will be interesting to measure how well this stabilization mechanism will be functional at the temperatures of a few hundred nK that are expected for ground state molecules produced in our present experimental apparatus. Further, it will be interesting to measure the lifetimes of samples of polar molecules in dependence on the orientation of the dipole moment relative to the direction of tight confinement. In this manner the anisotropy of the dipolar interaction can be observed as interactions are switched from purely repulsive to attractive in one direction of the two dimensional trap geometry. This attractive interaction should lead to a fast decay of molecular samples. A further possibility to suppress chemical reactions is to load the particles into a sufficiently deep optical lattice. Preparations for one to three dimensional optical lattice configurations, in which ground state molecules can be trapped, are underway in Singapore.

In order to enter into regimes relevant for the simulation of most effects in condensed matter systems, a further cooling of molecules will need to be achieved. Laser cooling on the narrow Rb line at 420 nm might be an option for reaching lower temperatures. By

¹e.g. Iralin coating, Optics Balzers AG, Neugrüt 35, 9496 Balzers, Liechtenstein

8. Conclusion and outlook

starting out with colder atomic particles, lower temperatures of the molecular samples are achieved. In this manner it might be possible to enter a molecular superfluid phase with repulsive dipolar interactions in two dimensions, or produce short lived Bose-Einstein condensates with anisotropic long range interaction in three dimensions.

Appendix A

Calibration of an interferometric laser frequency stabilization to megahertz precision

In this appendix the details of the work carried out in collaboration with TEM Messtechnik¹ are presented. At first, in Sec. A.1, the functional principle of the commercial interferometric laser frequency stabilization is briefly reviewed. The main focus of this appendix is however the calibration procedure that allows to reach frequency deviations as low as 5.7 MHz (rms 1.6 MHz) in the whole wavelength interval 750 – 795 nm. Careful analysis of the calibration data, some of which are gained by means of a frequency comb, and calibration results are presented. This allows to implement several calibration steps that compensate different systematic errors. Parts of this work have been published in [Brachmann et al., 2012].

The calibrated laser frequency stabilization is a convenient tool for spectroscopy in the wavelength range of transitions from the Feshbach state to the relevant rovibrational energy levels of molecular potentials dissociating to the K(4p)-Li(2s) asymptote (see Sec. 2.2.2). The main advantages are the exceptionally wide in-lock tuning capability, allowing to use the full in-lock tuning range of any laser design available in the wavelength range today, together with a high bandwidth frequency stabilization that allows for a fast tuning of lasers.

A.1 Functional principle

The locking scheme of TEM Messtechnik's laser frequency stabilization is based on one quadrature interferometer, which provides continuous frequency dependent voltage signals with high resolution over a large wavelength range. Similar devices used as high precision wavemeters contain several interferometers with etalons of different thicknesses [Kobtsev et al., 2007]. By means of an additional feedback, stabilization and tuning of the laser wavelength can be accomplished with these devices. However, due to the comparatively long exposure times, the feedback bandwidth of these wavemeter based

¹TEM Messtechnik GmbH, Großer Hillen 38, 30559 Hannover, Germany

A.1 Functional principle

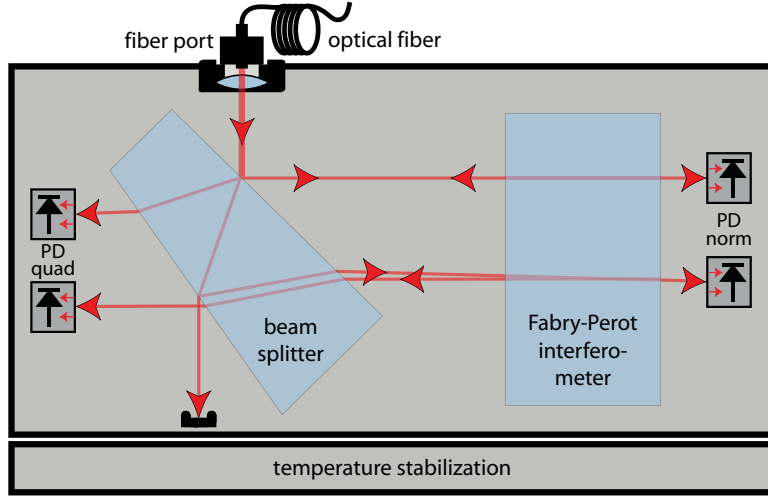


Figure A.1: Patented interferometer setup with a Fabry-Perot interferometer realized as a BK7 etalon of a geometrical thickness of 50 mm. PD: photo detector, quad: quadrature, norm: normalization. See [Müller-Wirts, 2001] for details.

laser frequency stabilizations is low and limiting the use for laser frequency stabilization. Only a brief outline of the interferometer's functional principle will be given here, as it is explained in detail elsewhere [Müller-Wirts, 2001].

As an interferometer a low finesse etalon of BK7 glass with plane parallel surfaces, mounted in a Fizeau type setup (see Fig. A.1) is used. A test beam entering the device through an optical fiber is split into two. Both beams pass the interferometer, however under a slight relative angle resulting in a 90° relative phase shift between the interference fringes. Two pairs of photodiodes record the fringe pattern in transmission and reflection of the etalon and are used to electronically construct two normalized periodic interferometer signals U_x and U_y , which depend on the frequency ν of the test laser beam. Due to the etalon's low finesse, their frequency dependence can be approximated by sine and cosine functions:

$$\begin{pmatrix} U_x(\nu) \\ U_y(\nu) \end{pmatrix} \simeq \begin{pmatrix} \cos(\varphi(\nu)) \\ \sin(\varphi(\nu)) \end{pmatrix}. \quad (\text{A.1})$$

Hence, U_x and U_y can be used as quadrature signals describing a circular path in the x-y plane, which depend on the total interferometer phase $\varphi(\nu)$. In order to obtain an error signal for frequency stabilization of a laser, the quadrature signals are compared with electronically generated set signals

$$\begin{pmatrix} U_{\text{set},x} \\ U_{\text{set},y} \end{pmatrix} = \begin{pmatrix} \cos(\varphi_{\text{set}}) \\ \sin(\varphi_{\text{set}}) \end{pmatrix} \quad (\text{A.2})$$

that depend on a single chosen set phase φ_{set} . The difference between φ and φ_{set} is used as a frequency error signal that varies with constant slope throughout one period of the quadrature signals. This allows to use the etalon for frequency stabilization of a laser at any frequency within one period of U_x and U_y by means of a feedback loop.

A. Calibration of an interferometric laser frequency stabilization

Further, in-lock tuning can be accomplished over a large wavelength range including many periods of U_x and U_y by alteration of the generated φ_{set} .

As the quadrature signals are periodic functions of the optical frequency, they are ambiguous. Hence, for stabilization to a specific target frequency one has to preset the laser's frequency to an accuracy better than one half of the quadrature signal period before closing the feedback loop. This corresponds to approximately 1 GHz and can be achieved by means of a standard wavemeter. With the help of this additional measure, each frequency is unambiguously assigned a phase, and lasers can continuously be tuned over an almost arbitrary amount of FSRs.

A.2 Phase - frequency relation

In order to use the interferometer for precision laser stabilization to arbitrary target frequencies in the wavelength range of operation the relation between interferometer phase φ and the laser frequency ν has to be known with very high accuracy.

The interferometer phase φ depends on the laser frequency ν and, if multiple interferences are neglected, the time τ the light needs to pass the etalon twice:

$$\varphi(\nu) = 4\pi\nu \frac{n(\nu)L}{c_0} \simeq 2\pi\nu\tau . \quad (\text{A.3})$$

The value τ is a device constant, determined by the geometrical length L and the refractive index n , which together constitute the etalon's frequency dependent optical pathlength $n(\nu) \cdot L$. c_0 is the speed of light in vacuum. Thus, for a precise prediction of interferometer phases, the optical pathlength, which is a frequency and time dependent quantity, needs to be determined with high precision. The following paragraph describes how the calculation of target interferometer phases is implemented and what quantities need to be determined. Sec. A.3 describes how these quantities are experimentally obtained and how the effect of multiple reflections within the etalon can be compensated for.

A.2.1 Prediction of an interferometer phase

This section briefly describes how interferometer phases for target frequencies are calculated in practice. Technically, the calculation is implemented as a subroutine in the computer control program of the device. The wavelength dependent calibration of the etalon's FSR, which is obtained by use of the subroutine, allows to tune lasers conveniently to absolute frequencies instead of interferometer phases. A flowchart of the computer program is shown in Fig. A.2. The program includes the implementation of the calibrations described in the later Secs. A.3.2 and A.3.4. By reference to Fig. A.2 the calculation of interferometer phases is explained. It is to be noted that only 3 experimentally determined measurement values are used in combination with Eqns. A.4, A.3 and A.5 in order to compute all main values.

The wavelength dependent index of refraction of the BK7 medium can be described by the Sellmeier equation [Born and Wolf, 1999]

$$n^2(\lambda) = 1 + \frac{B_1\lambda^2}{\lambda^2 - C_1} + \frac{B_2\lambda^2}{\lambda^2 - C_2} + \frac{B_3\lambda^2}{\lambda^2 - C_3} , \quad (\text{A.4})$$

A.2 Phase - frequency relation

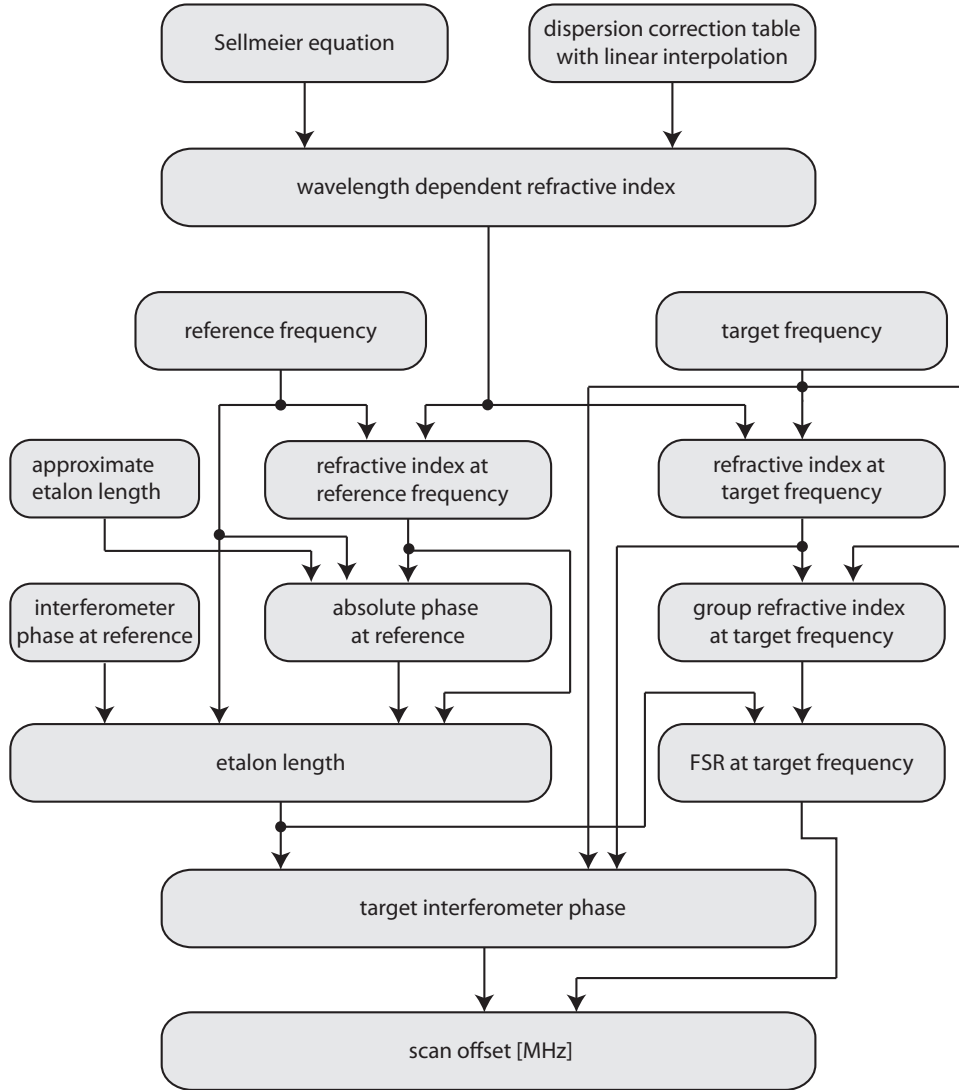


Figure A.2: Schematic describing how interferometer phase and etalon FSR are calculated for an optical target frequency. Arrows show which quantities are calculated by use of which other ones. For a precise calculation of the interferometer phase at a target frequency by use of this scheme the following three quantities need to be experimentally determined: An approximate etalon length, interferometer phase at a known reference frequency and a correction table for the refractive index. Using these the following main quantities are calculated: Refractive indices are calculated based on Eq. A.4, etalon lengths and interferometer phases are calculated by use of Eq. A.3 and the group refractive index is calculated from Eq. A.5.

A. Calibration of an interferometric laser frequency stabilization

which is the starting point in the calculation. According to the etalon's manufacturer² the coefficients

$$\begin{aligned}
 B_1 &= 1.03961212 & C_1 &= 6.00069867 \times 10^{-3} \mu\text{m}^2 \\
 B_2 &= 2.31792344 \times 10^{-1} & C_2 &= 2.00179144 \times 10^{-2} \mu\text{m}^2 \\
 B_3 &= 1.01046945 & C_3 &= 1.03560653 \times 10^2 \mu\text{m}^2
 \end{aligned}$$

describe the true index of refraction up to an accuracy of $\sim 5 \times 10^{-6}$. This is on the order of the homogeneity of the glass. As the accuracy is not high enough to reach a precision on the MHz level, the refractive index is corrected by a dispersion correction table that needs to be obtained. It is emphasized here that the table obtained in Sec. A.3 only changes the refractive index, but does not claim to determine it more precisely. It corrects for systematic error sources of physical as well as technical origin leading to a deviation of the calculated from the real interferometer phases for a given target frequency.

The etalon length L , which is a second quantity determining the optical pathlength, is only known on the precision level of several μm corresponding to several interferometer orders in the wavelength range around 770 nm. In order to keep the correction obtained from the dispersion correction table small, an approximate etalon length needs to be determined that results in an optical pathlength, which is precise on the level of an interferometer order (see Sec. A.3.4). The precision with which the approximate length is known is further improved by a measurement of the interferometer phase at a precisely known reference frequency. The left side, mid-section of Fig. A.2 shows how this is implemented: First Eq. A.3 is used with the approximate etalon length which yields an absolute interferometer phase expected at the reference frequency. The fractional digits of this interferometer phase is corrected using the measured phase at the same laser frequency. As the total interferometer phase cannot simply be measured, the obtained correction will always be on a level smaller than a wavelength at the reference frequency. Now Eq. A.3 is again used to compute a corrected etalon length. With this, all quantities in Eq. A.3 are known and an interferometer phase for a target frequency can be computed. This is shown on the right upper-mid section of Fig. A.2.

In order to be able to perform in-lock tuning of the laser in units of frequency, it needs to be known how much frequency difference one interferometer order corresponds to. Then, the interferometer phase can be scaled by use of the FSR and stabilized lasers can be tuned in units of frequency. In other words, a wavelength dependent calibration of the etalon's free spectral range (FSR) needs to be accomplished. The reciprocal $1/\tau$ in Eq. A.3 is often defined as the FSR. To account for the medium's dispersion throughout an FSR, it is however defined here in a slightly different manner by replacing the refractive index n with the group refractive index

$$n_{\text{gr}}(\nu) = n + \nu \frac{dn(\nu)}{d\nu} \quad (\text{A.5})$$

in Eq. A.3. The length of the BK7 etalon of about 50 mm corresponds to an FSR of approximately 2 GHz. The calibration of the FSR is shown in the lower midsection

²Schott AG

A.3 Calibrations

of Fig. A.2. Here, the frequency difference to the frequency, which is a multiple of 2π interferometer orders away from the reference laser frequency, is denoted “scan offset”.

A.3 Calibrations

After the description of two basic calibration steps, this section describes how the optical pathlength of the interferometer’s etalon is determined with high precision. Further it is described how the effect of multiple reflection within the etalon, which leads to a deviation from the sinusoidal dependence assumed in Eq. A.1, can be compensated for. For an absolute frequency precision on the MHz level, a relative uncertainty in calibration of $\sim 10^{-9}$ needs to be reached.

A.3.1 Signal correction

In practice, the voltage values (U_x, U_y) , which are obtained from the photodiode signals, rather form an ellipse than a circle in an x - y plane. The size of the ellipse might even vary and it might be shifted with respect to the origin. In order to adjust the signals with respect to their offsets, amplitudes and the quadrature phase difference, a fit algorithm for second order curves is applied to a set of samples obtained while tuning the laser over one FSR [Birch, 1990, Heydemann, 1981]. The fit parameters bring out the correction factors wanted. Like this the phase and amplitudes of the recorded quadrature signals can be changed to match the description as given in Eq. A.1.

A.3.2 Etalon drift

The measured quadrature signal is subject to a drift of $n \cdot L$, e.g. due to length changes of the etalon caused by temperature fluctuations. We use a reference laser of precisely known frequency to keep track of and correct for small optical path length changes, that result in an offset of the measured phase at a given frequency. The measured phase is used for two purposes: Firstly, it is one of three experimentally determined quantities used in the calculation scheme shown in Fig. A.2. Secondly, it is used for resetting the control programs “zero scan offset” phase. Hence, when tuning a laser within a certain wavelength range, frequency offsets are measured with respect to a frequency in the scan range that is shifted by exactly $k \cdot 2\pi$ interferometer orders from the reference frequency. Here, the integer k denotes the phase difference between the total phase at the reference frequency and the frequency corresponding to “zero scan offset”.

In the measurements presented here the reference laser is stabilized by means of a saturation spectroscopy to the D2 optical transition line of ^{87}Rb at 384.227981 THz. The temperature stabilization is found to provide conditions stable enough that the interferometer phase is not drifting more than $\pi/4$ if the room temperature fluctuates by about 5 – 6°C. This corresponds to a drift of approximately 250 MHz which is small enough that the correction of the etalon length described in Sec. A.2 leads to correct results. Thus, only length changes smaller than the reference wavelength need to be corrected for.

In practice, as typical interferometer drift rates are on the order of 100–200 kHz/min, this measurement has to be carried out about every 10 minutes, which can be done

A. Calibration of an interferometric laser frequency stabilization

automatically within approximately one to two seconds.

A.3.3 Compensation for the effect of multiple interference

A systematic deviation due to the approximation of the exact Airy function describing the interferometer signal as a sinusoidal function of the laser frequency in Eq. (A.3) has to be considered. In practice this can be accomplished by calibrating the set phase for a given target wavelength throughout one FSR. The calibration is achieved by comparing the frequency response of the interferometer with that of an etalon made of an optical fiber. With a fiber length of 2.5 m the resulting FSR of 60 MHz is much smaller than the FSR of the interferometer. Therefore, the fiber etalon's fringe pattern varies much faster when the laser frequency is tuned as compared to the interferometer signals U_x and U_y . This allows to use the fringes of the fiber etalon as equidistant markers for frequency intervals. In this way the deviations from the linear frequency dependence of the interferometer phase φ can be measured.

The maximum nonlinearity found for the quadrature interferometer is on the order of 2% of one FSR, corresponding to a maximum of 40 MHz deviation in target frequencies within one etalon FSR of 2 GHz. In order to compensate this systematic deviation in practice, the recorded data are electronically represented in a look-up-table (LUT). The LUT is used to modify the set phase φ_{set} for frequency tuning of the stabilized laser. With a set phase corrected by use of the LUT a remaining nonlinearity of 0.05% is found using the same method. This corresponds to an accuracy of better than 1 MHz within one FSR. It is important to note that this procedure is easily repeated and an exact LUT can be created when the interferometer is used in a different wavelength range at a different refractive index of the etalon. However, it was found in repeated measurements that one LUT remained valid when changing the frequency of the laser by several hundred FSR.

A.3.4 Calibration of the etalon's optical pathlength

This section describes how a calibration of the optical pathlength over a wide wavelength range is achieved. Further, the approximate etalon length is determined on the level of the precision of the Sellmeier equation. The dispersion correction table described in Sec. A.2 is created.

Approximative determination of the geometrical etalon length

The etalon's length L can be measured to the precision with which the refractive index is known using a measurement procedure often referred to as absolute length interferometry [Thiel et al., 1995]. For this, Eq. A.3 is differentiated:

$$\begin{aligned} \frac{d\varphi}{d\nu} &= 2\pi \frac{d}{d\nu}(\nu\tau) \\ &= 4\pi \frac{L}{c_0} \left(n + \nu \frac{dn(\nu)}{d\nu} \right) = 4\pi \frac{n_{\text{gr}}(\nu)L}{c_0} . \end{aligned} \quad (\text{A.6})$$

Here, n_{gr} denotes the group refractive index used in the definition of the etalon's free spectral range. n_{gr} is determined by use of Eqns. A.4 and A.5. The geometrical etalon

A.3 Calibrations

length is found to be proportional to the slope of the interferometer phase change:

$$L = \frac{c_0}{4\pi n_{gr}} \frac{d\varphi}{d\nu} . \quad (\text{A.7})$$

For an experimental determination of the slope $d\varphi/d\nu$, a widely tunable distributed feedback diode laser (DFB) is used as a light source. While tuning the diode laser over an interval of 875 GHz, the light frequency change is measured by means of a wavemeter (High Finesse WS-7). Simultaneously, the interferometer signals are recorded and the phase change is determined from this. A linear fit to the data pairs is made. Tuning the laser to higher frequencies one time and towards lower ones another time, two slightly different values are found:

$$\begin{aligned} L_{\text{up}} &= 50048.99 \mu\text{m} \\ L_{\text{down}} &= 50047.38 \mu\text{m} . \end{aligned}$$

The difference in the values found may be due to a thermal drift of the etalon as no correction using the reference laser was made when sampling values. In addition, due to the relative uncertainty of n_{gr} of $\sim 5 \times 10^{-6}$, an error of about 100 nm for these geometrical length values has to be considered.

In a second step, a saturation spectroscopy of Rubidium D1 and D2 lines is used and the respective interferometer phase values φ_1 , φ_2 at the frequencies of the two known hyperfine transitions are measured. As the measurements need to be taken without continuous tuning, it is however unknown how many full interferometer orders are covered by the frequency interval $\nu_2 - \nu_1$. Still, the following relation must hold:

$$\begin{aligned} (\varphi_2 \bmod 2\pi) &- (\varphi_1 \bmod 2\pi) + 2\pi k \\ &= 4\pi \frac{L}{c_0} (\nu_2 n(\nu_2) - \nu_1 n(\nu_1)) \\ &= 4\pi \frac{L}{c_0} \bar{n} \Delta\nu + \bar{\nu} \Delta n , \end{aligned} \quad (\text{A.8})$$

where k is an integer and $n(\nu_1)$, $n(\nu_2)$ are the refractive indices at the respective frequencies.

With

$$\begin{aligned} \nu_1 &= 377105911 \text{ MHz} \\ \nu_2 &= 384229319 \text{ MHz} \\ \varphi_1 \bmod 2\pi &= 2\pi \cdot 0.3505 \\ \varphi_2 \bmod 2\pi &= 2\pi \cdot 0.7045 \\ n(\nu_1) &= 1.510878 \\ n(\nu_2) &= 1.511179 \end{aligned}$$

it is found that the assumption of $k = 3640$ comes closest to the values L_{up} , L_{down} obtained in the first calibration step. Solving Eq. A.8 for L yields the result for the second calibration step: $L_{\text{2nd step}} = 50052.22 \mu\text{m}$.

A. Calibration of an interferometric laser frequency stabilization

If the two interferometer phases obtained by use of the spectroscopy are used and a total calculated interferometer order is added, two even more precise length values are found:

$$\varphi_2 = 2\pi \cdot 1218201.7045 \quad \text{yields} \quad L_{3\text{rd step}} = 50052.217 \mu\text{m}$$

and

$$\varphi_1 = 2\pi \cdot 190250.3505 \quad \text{yields} \quad L_{3\text{rd step}} = 50052.228 \mu\text{m}$$

which are in very good agreement. An average of the two latter values is used for a starting point in a further, more precise, determination of the approximate etalon length. How L can be determined more precisely is described in the following section.

Characterization and calibration over a large wavelength range

Using a grating stabilized diode laser (Toptica DLPro), a frequency comb and a reference laser locked to a D2 transition in Rubidium, a precise calibration of the interferometer is performed in the wavelength range 750–795 nm. In Fig. A.3 a sketch of the measurement setup is shown. For data acquisition with this setup, the following steps are repeated:

1. Choose an approximate application laser frequency.
2. Lock application laser to the interferometer.

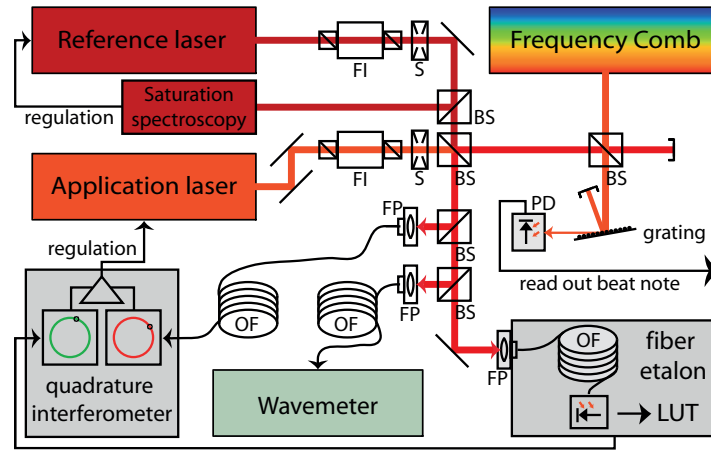


Figure A.3: Setup for calibration and characterization of the interferometer. The frequency comb is a self referenced femto-second fiber laser based design (Menlo Systems). A Hydrogen maser and GPS are utilized as time standards. The fiber etalon is used to record the data used in the Look-Up-Table (LUT). A beat note with a frequency comb is recorded using a spectrum analyzer. Application laser: Toptica DLPro, Reference laser frequency 384.227981 THz (DFB diode laser, TEM Messtechnik), Saturation spectroscopy (Cosy, TEM Messtechnik), Wavemeter: High Finesse WS/7, FI: Faraday isolator, S: Shutter, BS: Beam Splitter, PD: Photo Diode, OF: polarization maintaining Optical Fiber, FP: Fiber Port.

A.3 Calibrations

3. Perform signal correction (see Sec. A.3.1).
4. Generate LUT (see Sec. A.3.3) for the specific application laser frequency range using the fiber etalon.
5. Switch shutters and use the reference laser locked to the ^{87}Rb D2 transition at 384.227981 THz to perform an offset phase measurement of the interferometer (see Sec. A.3.2).
6. Switch shutters back, lock application laser to the interferometer and tune in-lock to the interferometer phase for the measurement.
7. Read out beat note and wavemeter data and record the interferometer phase for this frequency.

From the beat note and wavemeter data, the frequency of the application laser, which is stabilized to the interferometer, is calculated. Now, the scheme for calculating interferometer phases presented in Sec. A.2.1 is carried out for the measured frequencies. Starting with the previously determined approximate etalon length and the refractive index as described by the Sellmeier equation, an expected interferometer phase and scan offset is calculated. Like this, the deviation of the calculated scan offset from the true one is found. Repeating this procedure, data points in the wavelength range 750 – 795 nm are obtained. By small adjustments of the approximate etalon length in units of half a reference wavelength a dataset for which the deviations are minimal is found.

The remaining frequency deviation after this procedure is shown in Figs. A.4 and A.5. Fig. A.4(a) shows systematic deviations of the calculated interferometer phases corresponding to several ten MHz over a wavelength range of 45 nm. This corresponds to a relative error on the order of 10^{-7} . In order to further characterize the performance of the interferometer, data within the two frequency intervals indicated in Fig. A.4(a) is taken. This is shown in Fig. A.5.

Fig. A.5(a) shows the frequency deviation occurring within one FSR. This gives a measure on how well the relation between interferometer phase and frequency is calibrated by means of the LUT. For a single scan small rms deviations are found. However, for repeated calibrations and subsequent scans over one FSR the precision of the device is limited by the reproducibility to an rms value of 0.9 MHz. This can be attributed to frequency offsets consistent with the linewidth of the reference laser.

Fig. A.5(b) demonstrates the capability of precise frequency tuning over a range corresponding to 225 FSRs. For this measurement a distributed feedback diode was used as an application laser, which was continuously stabilized throughout the scan.

The characterization obtained from the data shown in Fig. A.4(a) can be used to obtain the dispersion correction table which changes the refractive index in the calculation scheme presented in Sec. A.2.1. For practical purposes, a best fit to the data by a second order polynomial that serves as a calibration curve is used. The fit function is shown in Fig. A.4(a). The dispersion correction table effectively changes the etalon's wavelength dependent optical path length, which is used in the calculation of the interferometer phase for a target frequency. However no zeroth order correction is contained in the table. This means that the refractive index is not changed at the reference laser frequency.

A. Calibration of an interferometric laser frequency stabilization

Only a slope and a curvature is added to the refractive index originally described by the Sellmeier equation.

To demonstrate the effectiveness of this calibration the polynomial fit function obtained from the datasets shown in Fig. A.4(a) is used. The fit residuals are shown in Fig. A.4(b). A maximum frequency deviation of 5.7 MHz (rms 1.6 MHz) is found for the fully calibrated interferometer. Further, the data which is represented by black squares in Fig. A.5 can be used for calibration in a smaller wavelength range. In this manner, an rms deviation of 0.7 MHz for the dataset represented by red circles is found. Thus, the calibration described in Sec. A.3.1 proves valid for the complete wavelength range of approximately 1 nm.

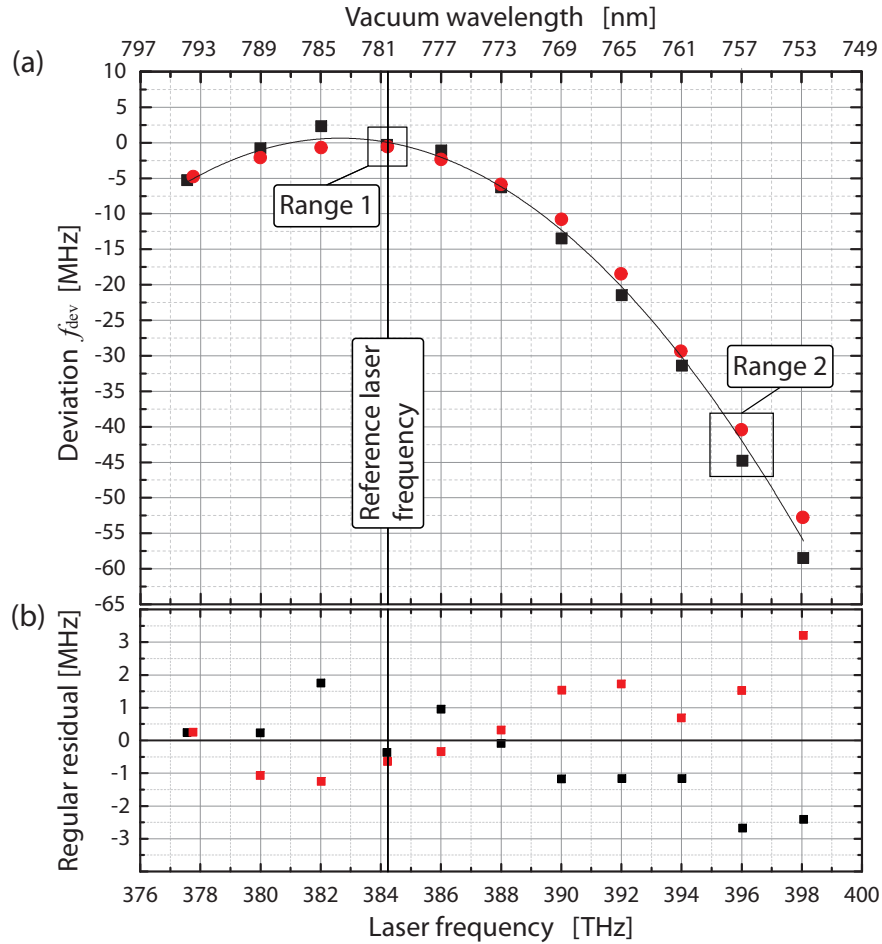


Figure A.4: (a) measured frequency deviation f_{dev} over the whole accessible wavelength range. Red circles and black squares are separate datasets taken on two consecutive days. One second order polynomial fit to both data sets is shown. The measurements for the frequency ranges 1 and 2 are shown enlarged in Fig. A.5. (b) residual of a fit to both datasets shown in (a). A vertical line marks the reference laser frequency in both graphs.

A.4 Discussion

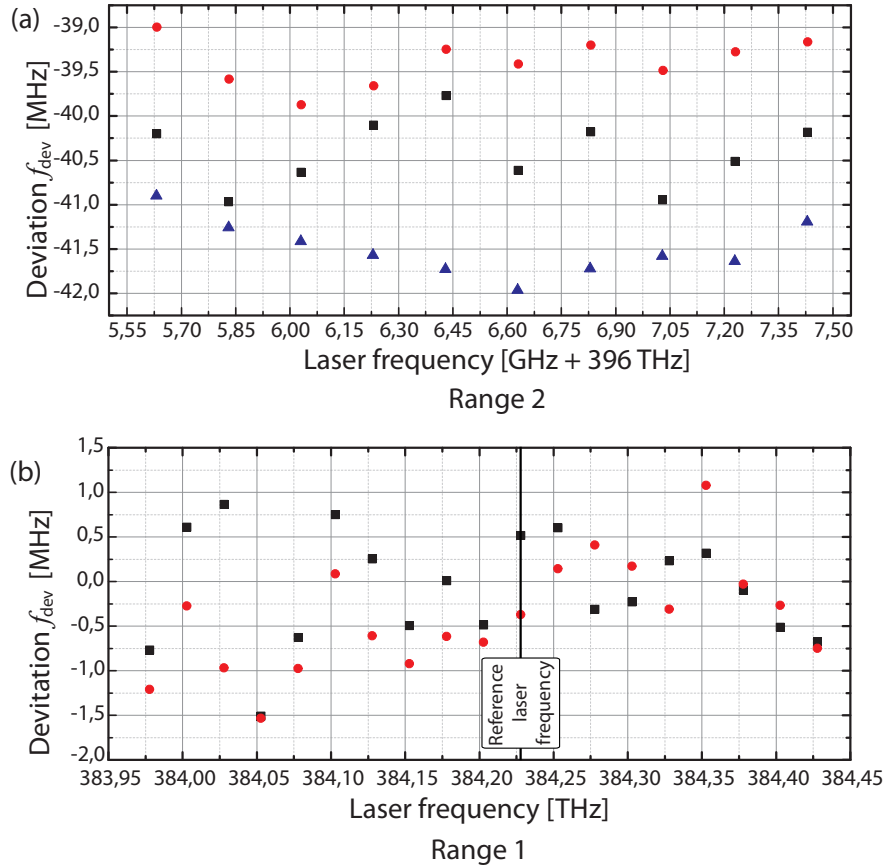


Figure A.5: Frequency ranges 1 and 2 shown with higher resolution. (a): Frequency range 2. Three sets of data points at the absolute frequency 396 THz within one FSR of the etalon are shown. Red circles and black squares are taken using different offset phase measurements but the same LUT. For the blue triangles a new LUT was generated and the offset phase was newly measured. A linear drift of 130 kHz/min obtained from repetitive measurements at the reference wavelength has been subtracted from all datasets for clearer visibility of the frequency-dependent error. (b): Frequency range 1. Two datasets close to the reference laser frequency (vertical line) are shown. To record this data, the reference laser (DFB diode laser) was controlled by the quadrature interferometer and interchanged with the application laser (Toptica DLPro).

A.4 Discussion

A.4.1 Etalon length calibration

Even though the interferometric length measurement carried out to determine the etalon's geometric thickness only reaches a limited precision of around $1 \mu\text{m}$, the calibration of the optical path length achieved is far more precise and on a level below 10 nm. Thus, the calculation of the interferometer phases schematically shown in Fig. A.2 might include a false geometric length, however this length compensates for an error in the refractive index. If we assume the refractive index described by the Sellmeier equation to deviate

A. Calibration of an interferometric laser frequency stabilization

from the true one,

$$n_{\text{Sellmeier}} = n_{\text{true}}(1 + \delta n), \text{ a length } L' = \frac{L}{(1 + \delta n)} \quad (\text{A.9})$$

compensates this error.

For the calculation scheme presented in Sec. A.2.1, the approximate etalon length used has to be known to better than half a wavelength of the reference laser frequency. Otherwise a wrong interferometer order is used for a determination of the etalon length. Fig. A.6 shows the same data set, however different approximate etalon lengths have been used for the calculation of the interferometer phases. A large first order deviation is seen in the data if the wrong interferometer order is used, while the deviation at the reference frequency stays close to zero in all cases. As can be seen, the value $L = 50.0510$ mm minimizes the deviation in the wavelength range 750 – 795 nm. Thus, it is also used to generate Figs. A.4 and A.5. The value differs from $L = 50.052251$ mm determined in the above paragraph. This could be due to a parasitic etalon that existed in the interferometer when the measurement using the wavemeter was carried out. This parasitic etalon was identified and removed later. Another possibility is a length change of the optical beam path if the alignment of the interferometer setup changed (see following paragraph).

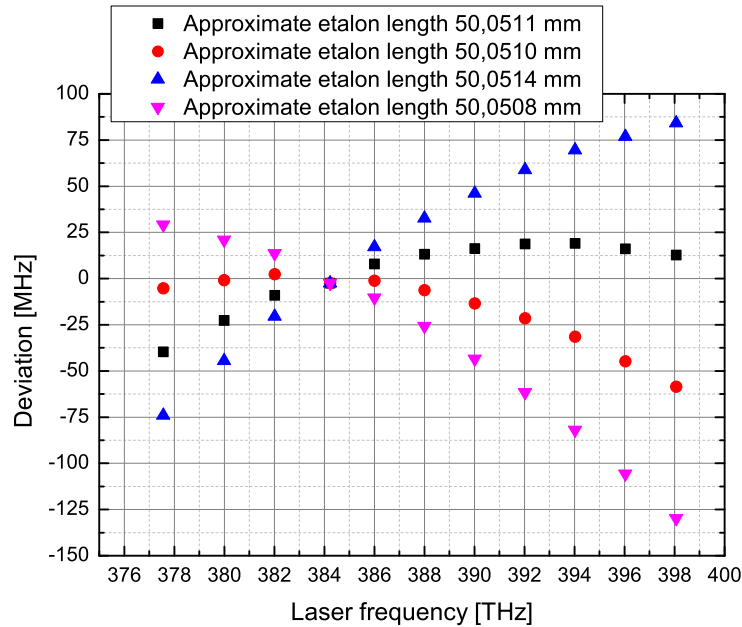


Figure A.6: The same data set is evaluated with four different approximate etalon lengths, corresponding to adjacent interferometer orders. Due to the sub-wavelength correction obtained by the use of the reference laser, the result for the final etalon length changes abruptly after a length change corresponding to one half of an FSR.

A.4 Discussion

A.4.2 Possible causes for systematic frequency deviations

Mainly two effects could be considered as reasons for the deviation observed in Fig. A.4:

- The real frequency dependent index of refraction $n(\nu)$ could deviate from the one described by the Sellmeier equation A.4.
- The geometrical beam path could have a frequency dependency $L = L(\nu)$.

Both effects are analyzed in the following.

Error in the description of the refractive index

The effect of errors in the refractive index described by the Sellmeier equation A.4 up to second polynomial order are estimated here. For this, the optical path length change resulting from a refractive index

$$\begin{aligned}
 n'(\nu) &= n_{\text{Sellmeier}}(\nu) + 2.4 \cdot 10^{-10} n_{\text{Sellmeier}} \Big|_{\text{ref}} \\
 &+ 4.4 \cdot 10^{-5} \frac{dn_{\text{Sellmeier}}}{d\nu} \Big|_{\text{ref}} (\text{ref} - \nu) \\
 &+ 8.0 \cdot 10^{-2} \frac{d^2 n_{\text{Sellmeier}}}{d\nu^2} \Big|_{\text{ref}} (\text{ref} - \nu)^2 , \tag{A.10}
 \end{aligned}$$

which contains changes up to the second order, is calculated. The reference frequency of 384.227981 THz is denoted here by “ref”. If it is assumed for now that the Sellmeier equation A.4 is exact and the etalon length is exactly known, then using the optical path length $n_{\text{Sellmeier}}L$ leads to zero deviation. If, on the other hand, $n'L$ was used instead, first and second order deviations which are proportional to $\Delta n(\nu)L = (n_{\text{Sellmeier}}(\nu) - n'(\nu)) \cdot L$ would be expected:

$$\Delta\varphi(\nu) = \frac{4\pi\Delta n(\nu)L}{\lambda_{\text{medium}}}, \text{ or expressed as frequency } \Delta f_{\text{dev}}(\nu) = \frac{2\Delta n(\nu)L}{\lambda_{\text{medium}}} \cdot \nu_{\text{F}} . \tag{A.11}$$

Here, $\Delta\varphi$ is the deviation of interferometer phase while Δf_{dev} expresses the same as frequencies (see Eq. A.3), ν_{F} denotes the etalon’s frequency dependent free spectral range and λ_{medium} is the wavelength inside the etalon. Fig. A.7 shows the deviation resulting when the refractive index Eq. A.10 is used, together with the fit function that was obtained from a fit to the data shown in Fig. A.4.

With the etalon length determined from the condition that the overall frequency deviation be minimized and the offset at the reference laser frequency be zero, the zeroth order error is only due to statistics. As expected it is found to be very small. However, it is possible to obtain corrections in higher orders to the wavelength dependence of the refractive index described by the specified Sellmeier coefficients. Relative errors of $4.4 \times 10^{-5} \pm 1.6 \times 10^{-6}$ in the first order and $8.0 \times 10^{-2} \pm 2.9 \times 10^{-3}$ in the second order are found. These deviations are consistent with a relative uncertainty of the refractive index described by the Sellmeier parameters of 2×10^{-7} . This relative uncertainty is approximately on the order of magnitude that is specified for the accuracy of the refractive index (see Sec. A.2), if described by Eq. A.4. Further, the refractive index throughout the etalon’s BK7 glass is expected to vary on a similar order of magnitude due to the inhomogeneity of the glass. Thus, it is likely that the observed frequency deviation is indeed caused by a slightly deviating refractive index.

A. Calibration of an interferometric laser frequency stabilization

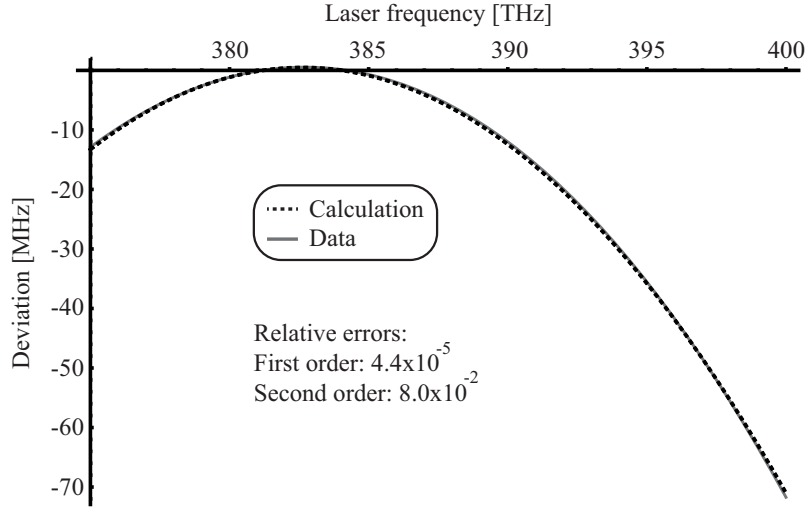


Figure A.7: Deviation resulting from the use of a slightly wrong refractive index. The solid gray line shows the result from the calculation described, while the dashed black line is the second order fit function to the data shown in Fig. A.4.

Wavelength dependency of the optical beam path

Another cause for deviation are test beams that are not aligned perfectly normal to the etalon's surface planes. This could be caused if the etalon's surfaces are not plane parallel or for misaligned test beams. In these cases, the dispersion of the glass will result in a wavelength dependent angle of refraction inside the etalon, thus causing a wavelength dependency of the beam path. The deviation arising due to an angle under which the etalon is passed is estimated here by use of the Sellmeier equation A.4 and Snell's law [Hecht, 2002]:

$$\Delta f_{\text{dev}}(\nu) = \frac{\nu_{\text{F}}}{\lambda_{\text{medium}}(\nu)} \left(2n(\nu) \left(\frac{L}{\sqrt{1 - \frac{n_{\text{air}}^2}{n^2(\nu)} \sin^2(\Theta_i)}}} - \frac{L}{\sqrt{1 - \frac{n_{\text{air}}^2}{n^2(\nu_{\text{ref}})} \sin^2(\Theta_i)}}} \right) + \right. \\ \left. + n_{\text{air}} \left(\frac{2 n_{\text{air}}^2 L \sin^2(\Theta_i)}{n(\nu) \sqrt{1 - \frac{n_{\text{air}}^2}{n^2(\nu)} \sin^2(\Theta_i)}}} - \frac{2 n_{\text{air}}^2 L \sin^2(\Theta_i)}{n(\nu_{\text{ref}}) \sqrt{1 - \frac{n_{\text{air}}^2}{n^2(\nu_{\text{ref}})} \sin^2(\Theta_i)}}} \right) \right). \quad (\text{A.12})$$

Here Θ_i is the angular deviation from normal incidence of a test beam in the plane of the first etalon surface ($\Theta_i = 0$: normal incidence). Further, n_{air} is the index of refraction of air, ν_{F} is the etalon's FSR and $\lambda_{\text{medium}}(\nu)$ is the wavelength in the etalon's medium. In Eq. A.12, two contributions to a change in the optical pathlength inside (first parenthesis) and outside (second parenthesis) of the medium are taken into account. According to the etalon's manufacturer no wedge bigger than several arc seconds is to be expected, which is much smaller than the probable incident angle. Thus the incident angle dominates the beam path change. Fig. A.8 shows the dependence of the expected deviation Δf_{dev} on the test beams' incident angle and laser frequency.

A.4 Discussion

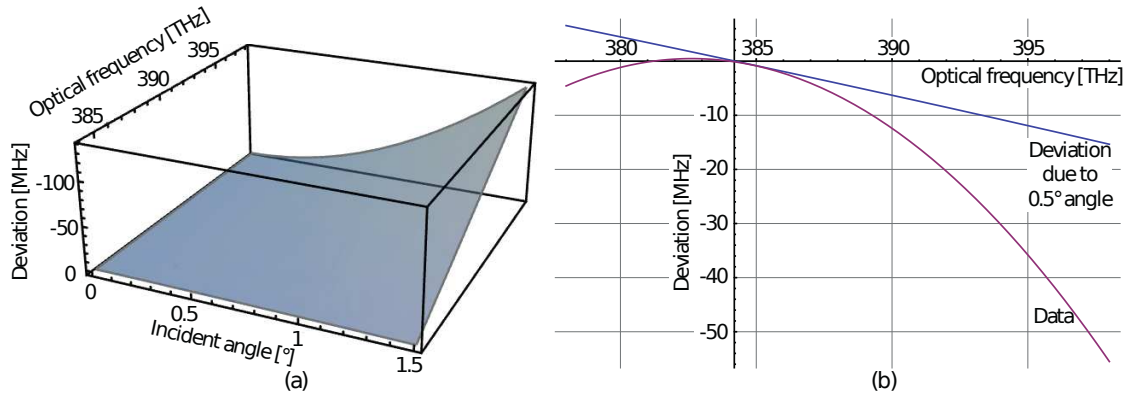


Figure A.8: Deviation if the etalon is passed under an angle. (a) the dependency onto the incident angle at a given frequency is roughly parabolic while the frequency at a given incident angle has a dependence which is very close to linear. (b) the blue line shows the expected deviation at an incident angle of 0.5° as a function of the frequency. The magenta curve is the fit function found in A.4(a).

The refractive index of BK7 has a positive slope in the considered frequency range. For test beams with $\Theta_i > 0$, the beam path for frequencies higher than the reference laser frequency always is shorter in comparison to when no refraction occurs. Thus, Δf_{dev} will always have a negative slope. If a linear deviation with a negative slope is added to the second order deviation found in the data A.4, the vertex of the parabola will be shifted towards lower frequencies. This means that the linear deviation caused by an incident angle of the test beams can only shift the parabola towards lower frequencies, whereas it is unknown if the first order error in the Sellmeier equation will cause a shift towards higher or lower frequencies.

Other than the refractive index, the angle under which the etalon is passed is likely to drift with time. Thus, it is a reasonable assumption to expect the vertex of the parabola to shift with time. For a 0.5° incident angle and an angular drift of $\pm 0.1^\circ$ a change in deviation of roughly ± 10 MHz is to be expected for an absolute laser frequency of $384.227981 + 14$ THz. Here again a reference laser frequency of 384.227981 THz is assumed.

Other causes

As previously stated, the error in the Sellmeier equation is on the order of the homogeneity of the glass. Thus, if the beam path changes, the effect of the limited homogeneity of the glass could have a larger impact on the resulting deviation and also change its frequency dependence. Also, in the estimations presented here, it is always assumed, that the beams are perfectly collimated. However, over such a wide wavelength interval the collimation of the beams is expected not always to be absolutely perfect. This additionally leads to frequency deviations.

The two datasets shown in Fig. A.4(a) can be seen to contain a slight systematic deviation. This effect, which occurred after one day is very likely due to a change in the optical beam path through the etalon.

A. Calibration of an interferometric laser frequency stabilization

For the data shown in Fig. A.4(a) only one LUT, recorded for the target frequency, was used. Thus, a slight frequency deviation is expected due to the differences in the LUTs. This deviation is time dependent as it depends on the respective phase associated with the reference frequency, which is drifting. The scatter seen in the data could be partially due to this effect. It could be avoided by working with two LUTs, one for each frequency range the interferometer is currently used with.

A.5 Stability of the calibration

In the course of device optimization, measurements were carried out over a period of half a year. Fig. A.9 shows a comparison of data taken in January and May 2011. As the interferometer with which the data was acquired was not optimized as well as the one with which the data shown in Fig. A.4 was taken, the residuals show larger values. However, the data acquired in the respective months agree very well with each other and are used here for an estimation of the interferometer's long term stability.

Fig. A.9(a) shows the vertex of all parabola fits shifted towards frequencies higher than the reference laser frequency, with an evident respective shift between the datasets taken in January as compared to the ones from May. A $\sim 50\%$ decrease of the first order fit parameter (A) between the data from January and the data from May is found, when

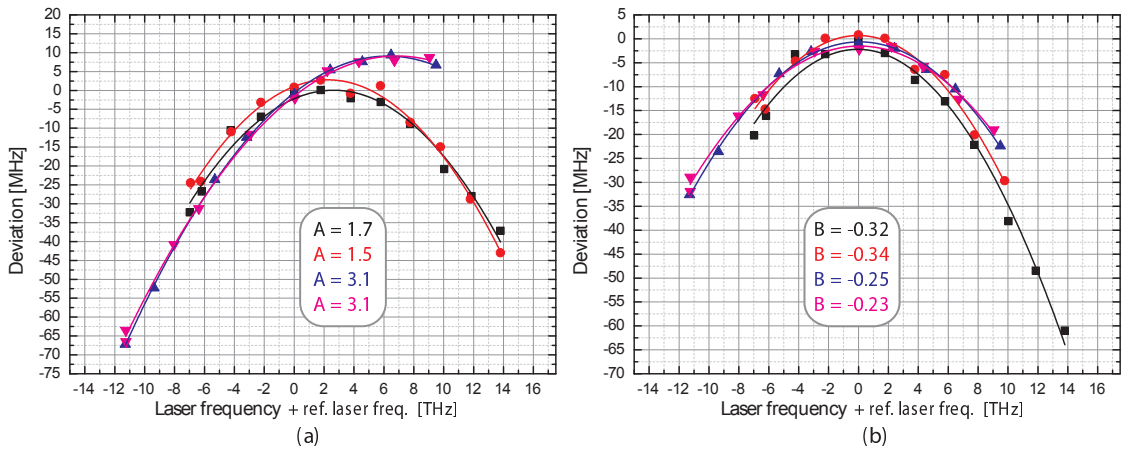


Figure A.9: Comparison of data taken with the same interferometer setup. Red circles: 18.05.2011, Black squares: 19.05.2011, Blue triangles pointing upwards: 17-25.01.2011, Magenta triangles pointing downwards: 26.-28.01.2011. For the data taken in January, a Coherent 899 Ti:Sa (application laser) and a grating stabilized diode laser (reference laser) was used, whereas the data taken in May was acquired using the setup shown in Fig. A.3. Two different reference laser frequencies are used: May 384.227981 THz, January 384.227988 THz (a) shows data taken and analyzed by the same procedure as described in Sec. A.3.4. The same approximate etalon length was used in the calculation of the interferometer phases in all datasets. (b) shifted data: Red circles, black squares: change in offset phase -120° ; Blue triangles pointing upwards, Magenta triangles pointing downwards: change in offset phase -214° . The first (A) and second (B) order polynomial fit coefficients are shown as inlets in (a) and (b).

A.6 Comparison of two interferometer setups

the same approximate etalon length is used. As described in Sec. A.4.2 a shift of the deviation parabola's vertex towards higher frequencies does not occur due to an angle $\Theta_i > 0$ in a perfectly homogeneous etalon. However, the observed change in deviation can be explained as a combined effect of a change in angle and an inhomogeneity of the etalon's refractive index (Sec. A.4).

In order to make a difference in parabola curvature better visible, the data was modified to shift the interferometer offset phase $\Delta\varphi$, measured at the reference laser frequency. As described in Sec. A.2.1, this changes the etalon length with which the interferometer phases are calculated. Like this, the parabolas' vertices are aligned at the reference laser frequency which is shown in Fig. A.9(b). A $\sim 35\%$ increase in curvature of the parabola fits between the data from January and the data from May is found. This higher order systematic change in the measured deviation agrees with the assumption that a different angle Θ_i will cause the deviation to change mostly due to the inhomogeneity of the etalon's BK7 glass.

The data shown in Fig. A.9 is insufficient to conclusively describe the stability of the calibration obtained in Sec. A.3.4. A more systematic study is necessary to specify an amount of time after which the calibration needs to be repeated. As is shown in Fig. A.1, the setup is a fiber coupled design. Since the removal and reconnection of the fiber could induce a change in angle under which the etalon is passed, this could limit the setup's precision. Thus, the six month time interval between the recording of the datasets shown in Fig. A.9 might not be as important for a change in calibration as the removal and reconnection of the fiber during that time. The data shown in Fig. A.9 can be seen as a "worst case" since the fiber directing the test beam light to the setup was removed, the temperature stabilization was switched off and the whole device was moved and taken off the optical table several times between the measurement data taken in January and May.

A.6 Comparison of two interferometer setups

During the course of the interferometer setup's optimization, two different devices were characterized in the wavelength range 750 – 795 nm. Different interferometers could in principle have different refractive indices of the BK7 etalons, leading to different measured deviations.

In Fig. A.10, two datasets, one for each interferometer, are compared. It can be seen in Fig. A.10(a) that the second order polynomial fits to the data points have different coefficients. As was argued in Sec. A.4, the difference between the first order fit coefficients could be due to a different angle under which the etalon is passed. As also the second order fit coefficients differ by approximately the same magnitude as the measurements shown in Fig. A.9, no essential difference between the interferometers is found.

A.7 Conclusive remarks

As it is shown that a correction of the refractive index up to second order serves very well to calibrate the setup, it will from now on only be necessary to measure the deviation at three roughly equally spaced frequencies within the wavelength range. The calibration is

A. Calibration of an interferometric laser frequency stabilization

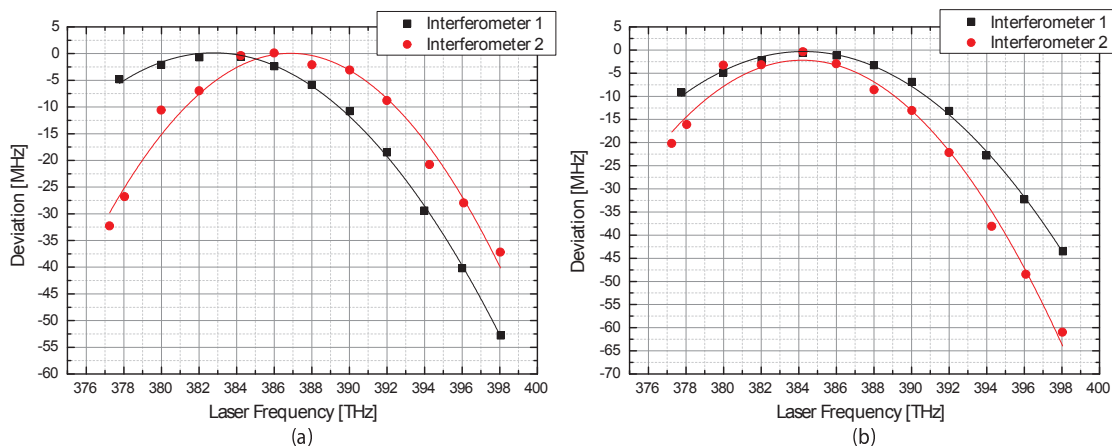


Figure A.10: Comparison of two interferometer setups. (a) measured data. The data points of interferometer 2 show a larger deviation from the fit, as this device has not been optimized equally well. A parasitic etalon was later found to be the cause. (b) The data shown in (a) has been modified in the same way as described in Sec. A.5 in order to place both vertices of the parabolas at the reference laser frequency. Black squares: change in offset phase $+50^\circ$, parabola curvature: -0.24 ; red circles: change in offset phase -120° , parabola curvature: -0.32 .

obtained by using a second order polynomial fit to these data points in the same way as described in Sec. A.3.4. In the examined wavelength interval, Doppler-free spectroscopies of optical transitions in rubidium and potassium are readily available and can serve as absolute frequency references. This eliminates the need for a frequency comb to carry out the last calibration step. In addition employing data at just three wavelengths allows for efficient recalibration in order to compensate possible slow systematic drifts on the time scale of days.

Together with the frequency comb newly available in our laboratory, the calibrated interferometer setup will be a very useful tool for the spectroscopy of Feshbach molecules. Frequency comb modes, available in the whole spectral region of interest, can be used as references for the automated interferometer offset phase measurement (see Sec. A.3.2), while a spectroscopy laser can easily be scanned over its whole tuning range. This makes it possible to easily scan a spectroscopy laser independently of, but referenced to, the frequency comb. As the interferometer is in this case always used close to a reference line its accuracy will be similar to the one shown in Fig. A.5(b). In this case the precise determination of the optical pathlength presented in Sec. A.3.4 can be omitted. Thus, all calibration steps can be carried out in an automated way within the experimental cycle that produce Feshbach molecules and without causing a delay. If not moved and with the temperature stabilization kept switched on, we expect the calibration curve obtained for the optical path length not to change significantly within several weeks.

In the device design described here, set phases can be generated at a rate of 1 kHz. This limits the sweep rate of a stabilized laser. A new electronic design of the control unit is able to generate set phases at the much higher rate of 2.5 MHz. This allows for fast in-lock tuning of a stabilized laser over large frequency intervals. The first spectroscopy

A.7 Conclusive remarks

step with a free-running laser that is described in Sec. 6.1 can be omitted using the new design.

Bibliography

- K. Aikawa, A. Frisch, M. Mark, S. Baier, A. Rietzler, R. Grimm, and F. Ferlaino. Bose-Einstein Condensation of Erbium. *Phys. Rev. Lett.*, 108:210401, May 2012. doi: 10.1103/PhysRevLett.108.210401.
- D. W. Allan. Statistics of atomic frequency standards. *Proceedings of the IEEE*, 54: 221–230, 1966.
- A.-R. Allouche. Web: <http://sites.google.com/site/allouchear/Home/diatomic>, 2011.
- J. Alnis. Private communication, 2011.
- M. H. Anderson, J. R. Ensher, and E. A. Cornell. Observation of Bose-Einstein Condensation in a dilute atomic vapor. *Science*, 1995.
- M. Aymar and O. Dulieu. Calculation of accurate permanent dipole moments of the lowest $^1,^3\Sigma^+$ states of heteronuclear alkali dimers using extended basis sets. *The Journal of Chemical Physics*, 122(20):204302, 2005. doi: 10.1063/1.1903944. URL <http://link.aip.org/link/?JCP/122/204302/1>.
- M. Aymar and O. Dulieu. Calculations of transition and permanent dipole moments of heteronuclear alkali dimers NaK, NaRb and NaCs. *Molecular Physics*, 105(11-12): 1733–1742, 2007. doi: 10.1080/00268970701494016.
- W. S. Bakr, J. I. Gillen, A. Peng, S. Fölling, and M. Greiner. A quantum gas microscope for detecting single atoms in a hubbard-regime optical lattice. *Nature*, 462:74–77, 2009.
- W. S. Bakr, A. Peng, M. E. Tai, R. Ma, J. Simon, J. I. Gillen, S. Fölling, L. Pollet, and M. Greiner. Probing the Superfluid-to-Mott insulator transition at the single-atom level. *Science*, 329(5991):547–550, 2010. doi: 10.1126/science.1192368. URL <http://www.sciencemag.org/content/329/5991/547.abstract>.
- V. Bednarska, I. Jackowska, V. Jastrzębski, and P. Kowalczyk. The molecular constants and potential energy curve of the ground state $X^1\Sigma^+$ in KLi. *J. of Molecular Spectroscopy*, 189(2):244–248, 1998. ISSN 0022-2852. doi: 10.1006/jmsp.1998.7543.
- P. Berman, editor. *Atom Interferometry*. Academic Press, 1997.
- P. F. Bernath, editor. *Spectra of Atoms and Molecules*. Oxford University Press, second edition, 2005.

BIBLIOGRAPHY

- K. P. Birch. Optical fringe subdivision with nanometric accuracy. *Precision Engineering*, 12(4):195–198, Oct. 1990.
- E. D. Black. An introduction to pound–drever–hall laser frequency stabilization. *American Journal of Physics*, 69(1):79–87, 2001. doi: 10.1119/1.1286663.
- J. L. Bohn. Electric dipoles at ultralow temperatures. 2009.
- J. L. Bohn, M. Cavagnero, and C. Ticknor. Quasi-universal dipolar scattering in cold and ultracold gases. *New Journal of Physics*, 11(5):055039, 2009.
- M. Born and E. Wolf. *Principles of Optics*. Cambridge University Press, 1999.
- T. Bourdel, J. Cubizolles, L. Khaykovich, K. M. F. Magalhaes, S. J. J. M. F. Kokkelmans, V. Shlyapnikov, G. and C. Salomon. Measurement of the interaction energy near a feshbach resonance in a ${}^6\text{Li}$ fermi gas. *Phys. Rev. Lett.*, 91:020402, Jul 2003. doi: 10.1103/PhysRevLett.91.020402.
- E. Braaten, D. Kang, and L. Platter. Universal relations for identical bosons from three-body physics. *Phys. Rev. Lett.*, 106:153005, Apr 2011. doi: 10.1103/PhysRevLett.106.153005.
- J. F. S. Brachmann, T. Kinder, and K. Dieckmann. Calibrating an interferometric laser frequency stabilization to megahertz precision. *Appl. Opt.*, 51(22):5517–5521, Aug 2012. doi: 10.1364/AO.51.005517.
- C. C. Bradley, C. A. Sackett, J. J. Tollett, and R. G. Hulet. Evidence of bose-einstein condensation in an atomic gas with attractive interactions. *Phys. Rev. Lett.*, 1995.
- G. Breit and I. I. Rabi. Measurement of nuclear spin. *Phys. Rev.*, 38:2082–2083, Dec 1931. doi: 10.1103/PhysRev.38.2082.2.
- H. P. Büchler, E. Demler, M. Lukin, A. Micheli, N. Prokof'ev, G. Pupillo, and P. Zoller. Strongly correlated 2d quantum phases with cold polar molecules: Controlling the shape of the interaction potential. *Phys. Rev. Lett.*, 98:060404, Feb 2007a. doi: 10.1103/PhysRevLett.98.060404.
- H. P. Büchler, A. Micheli, and P. Zoller. Three-body interactions with cold polar molecules. *Nature Physics*, 3:726–731, Feb 2007b. doi: 10.1038/nphys678.
- B. Bussery, Y. Achkar, and M. Aubert-Frécon. Long-range molecular states dissociating to the three or four lowest asymptotes for the ten heteronuclear diatomic alkali molecules. *Chemical Physics*, 116(3):319 – 338, 1987. ISSN 0301-0104. doi: 10.1016/0301-0104(87)80202-1.
- L. Cacciapuoti, M. de Angelis, M. Fattori, G. Lamporesi, T. Petelski, M. Prevedelli, J. Stuhler, and G. M. Tino. Analog + digital phase and frequency detector for phase locking of diode lasers. *Review of Scientific Instruments*, 76(5):053111, 2005. doi: 10.1063/1.1914785. URL <http://link.aip.org/link/?RSI/76/053111/1>.

- L. D. Carr, D. DeMille, R. V. Krems, and J. Ye. Cold and ultracold molecules: science, technology and applications. *New Journal of Physics*, 11(5):055049, 2009. URL <http://stacks.iop.org/1367-2630/11/i=5/a=055049>.
- C. Chin, M. Bartenstein, A. Altmeyer, S. Riedl, S. Jochim, J. H. Denschlag, and R. Grimm. Observation of the pairing gap in a strongly interacting fermi gas. *Science*, 305(5687):1128–1130, 2004. doi: 10.1126/science.1100818. URL <http://www.sciencemag.org/content/305/5687/1128.abstract>.
- C. Chin, R. Grimm, P. Julienne, and E. Tiesinga. Feshbach resonances in ultracold gases. *Rev. Mod. Phys.*, 82:1225–1286, Apr 2010. doi: 10.1103/RevModPhys.82.1225. URL <http://link.aps.org/doi/10.1103/RevModPhys.82.1225>.
- L. Costa. *An interacting Fermi-Fermi mixture at the crossover of a narrow Feshbach resonance*. PhD thesis, Ludwig-Maximilians-Universität München, 2011.
- L. Costa, J. Brachmann, A.-C. Voigt, C. Hahn, M. Taglieber, T. W. Hänsch, and K. Dieckmann. *s*-wave interaction in a two-species fermi-fermi mixture at a narrow feshbach resonance. *Phys. Rev. Lett.*, 105:123201, Sep 2010a. doi: 10.1103/PhysRevLett.105.123201.
- L. Costa, J. Brachmann, A.-C. Voigt, C. Hahn, M. Taglieber, T. W. Hänsch, and K. Dieckmann. Erratum: *s*-wave interaction in a two-species fermi-fermi mixture at a narrow feshbach resonance [phys. rev. lett. 105, 123201 (2010)]. *Phys. Rev. Lett.*, 105:269903, Dec 2010b. doi: 10.1103/PhysRevLett.105.269903. URL <http://link.aps.org/doi/10.1103/PhysRevLett.105.269903>.
- F. H. Crawford. Zeeman effect in diatomic molecular spectra. *Rev. Mod. Phys.*, 6:90–117, Apr 1934. doi: 10.1103/RevModPhys.6.90.
- J. Cubizolles, T. Bourdel, S. J. J. M. F. Kokkelmans, G. V. Shlyapnikov, and C. Salomon. Production of long-lived ultracold Li₂ molecules from a fermi gas. *Phys. Rev. Lett.*, 91:240401, Dec 2003. doi: 10.1103/PhysRevLett.91.240401.
- J. G. Danzl, E. Haller, M. Gustavsson, M. J. Mark, R. Hart, N. Bouloufa, O. Dulieu, H. Ritsch, and H.-C. Nägerl. Quantum gas of deeply bound ground state molecules. *Science*, 321(5892):1062–1066, 2008. doi: 10.1126/science.1159909.
- J. G. Danzl, M. J. Mark, E. Haller, M. Gustavsson, R. Hart, J. Aldegunde, J. M. Hutson, and N. H.-C. An ultracold high-density sample of rovibronic ground-state molecules in an optical lattice. *Nature Physics*, 6, Apr 2010.
- K. B. Davis, M. O. Mewes, M. R. Andrews, N. J. van Druten, D. S. Durfee, D. M. Kurn, and W. Ketterle. Bose-Einstein Condensation in a Gas of Sodium Atoms. *Phys. Rev. Lett.*, 1995a.
- K. B. Davis, M. O. Mewes, and W. Ketterle. An analytical model for evaporative cooling of atoms. *Applied Physics B: Lasers and Optics*, 60:155–159, 1995b. ISSN 0946-2171. URL <http://dx.doi.org/10.1007/BF01135857>. 10.1007/BF01135857.

BIBLIOGRAPHY

- S. Dawkins, J. McFerran, and A. Luiten. Considerations on the measurement of the stability of oscillators with frequency counters. *IEEE Transactions on Ultrasonics, Ferroelectrics and Frequency Control*, 54:918–925, 2007.
- J. Deiglmayr. *Structure, formation, and interactions of ultracold polar molecules*. PhD thesis, Albert-Ludwigs-Universität Freiburg, 2009.
- J. Deiglmayr, M. Aymar, R. Wester, M. Weidemüller, and O. Dulieu. Calculations of static dipole polarizabilities of alkali dimers: Prospects for alignment of ultracold molecules. *The Journal of Chemical Physics*, 129(6):064309, 2008. doi: 10.1063/1.2960624. URL <http://link.aip.org/link/?JCP/129/064309/1>.
- B. DeMarco and D. S. Jin. Onset of fermi degeneracy in a trapped atomic gas. *Science*, 285(5434):1703–1706, 1999. doi: 10.1126/science.285.5434.1703. URL <http://www.sciencemag.org/content/285/5434/1703.abstract>.
- B. DeMarco, S. B. Papp, and D. S. Jin. Pauli blocking of collisions in a quantum degenerate atomic fermi gas. *Phys. Rev. Lett.*, 86:5409–5412, Jun 2001. doi: 10.1103/PhysRevLett.86.5409. URL <http://link.aps.org/doi/10.1103/PhysRevLett.86.5409>.
- A. Derevianko, W. R. Johnson, M. S. Safronova, and J. F. Babb. High-precision calculations of dispersion coefficients, static dipole polarizabilities, and atom-wall interaction constants for alkali-metal atoms. *Phys. Rev. Lett.*, 82:3589–3592, May 1999. doi: 10.1103/PhysRevLett.82.3589.
- K. Dieckmann, C. A. Stan, S. Gupta, Z. Hadzibabic, C. H. Schunck, and W. Ketterle. Decay of an ultracold fermionic lithium gas near a feshbach resonance. *Phys. Rev. Lett.*, 89:203201, Oct 2002. doi: 10.1103/PhysRevLett.89.203201. URL <http://link.aps.org/doi/10.1103/PhysRevLett.89.203201>.
- E. A. Donley, S. L. N. R. Clausen, J. L. Cornish, E. Roberts, A. Cornell, and C. E. Wieman. Dynamics of collapsing and exploding bose-einstein condensates. *Nature*, 412:295–299, 2001.
- R. W. P. Drever, J. L. Hall, F. V. Kowalski, J. Hough, G. M. Ford, A. J. Munley, and H. Ward. Laser phase and frequency stabilization using an optical resonator. *Applied Physics B: Lasers and Optics*, 31(2):97–105, June 1983.
- S. Dürr, T. Volz, A. Marte, and G. Rempe. Observation of molecules produced from a bose-einstein condensate. *Phys. Rev. Lett.*, 92:020406, Jan 2004. doi: 10.1103/PhysRevLett.92.020406.
- S. Falke, I. Sherstov, E. Tiemann, and C. Lisdat. The $a^1\Sigma_u^+$ state of K_2 up to the dissociation limit. *The Journal of Chemical Physics*, 125(22):224303, 2006. doi: 10.1063/1.2375120. URL <http://link.aip.org/link/?JCP/125/224303/1>.
- F. Ferlaino, S. Knoop, M. Mark, M. Berninger, H. Schöbel, H.-C. Nägerl, and R. Grimm. Collisions between tunable halo dimers: Exploring an elementary four-body process with identical bosons. *Phys. Rev. Lett.*, 101:023201, Jul 2008. doi: 10.1103/PhysRevLett.101.023201.

- R. C. Forrey, N. Balakrishnan, V. Kharchenko, and A. Dalgarno. Feshbach resonances in ultracold atom-diatom scattering. *Phys. Rev. A*, 58:R2645–R2647, Oct 1998. doi: 10.1103/PhysRevA.58.R2645.
- B. Friedrich and D. Herschbach. Enhanced orientation of polar molecules by combined electrostatic and nonresonant induced dipole forces. *The Journal of Chemical Physics*, 111(14):6157–6160, 1999. doi: 10.1063/1.479917.
- E. Gehm. PhD thesis, Duke University, 2003.
- T. Gericke, P. Würtz, D. Reitz, T. Langen, and H. Ott. High-resolution scanning electron microscopy of an ultracold quantum gas. *Nature Physics*, 4:949–953, October 2008.
- S. Giorgini, L. P. Pitaevskii, and S. Stringari. Theory of ultracold atomic fermi gases. *Rev. Mod. Phys.*, 80:1215–1274, Oct 2008. doi: 10.1103/RevModPhys.80.1215. URL <http://link.aps.org/doi/10.1103/RevModPhys.80.1215>.
- J. Goldwin, S. Inouye, M. L. Olsen, B. Newman, B. D. DePaola, and D. S. Jin. Measurement of the interaction strength in a bose-fermi mixture with ^{87}Rb and ^{40}K . *Phys. Rev. A*, 70:021601, Aug 2004. doi: 10.1103/PhysRevA.70.021601. URL <http://link.aps.org/doi/10.1103/PhysRevA.70.021601>.
- J. Goldwin, S. Inouye, M. L. Olsen, and D. S. Jin. Cross-dimensional relaxation in bose-fermi mixtures. *Phys. Rev. A*, 71:043408, Apr 2005. doi: 10.1103/PhysRevA.71.043408. URL <http://link.aps.org/doi/10.1103/PhysRevA.71.043408>.
- M. Greiner, I. Bloch, T. W. Hänsch, and T. Esslinger. Magnetic transport of trapped cold atoms over a large distance. *Phys. Rev. A*, 63, 2001.
- M. Greiner, O. Mandel, T. Esslinger, T. W. Hänsch, and I. Bloch. Quantum phase transition from a superfluid to a mott insulator in a gas of ultracold atoms. *Nature*, 415, 2002.
- M. Greiner, C. A. Regal, and D. S. Jin. Emergence of a molecular Bose-Einstein condensate from a fermi gas. *Nature*, 426:537–540, 2003.
- A. Griesmaier, J. Werner, S. Hensler, J. Stuhler, and T. Pfau. Bose-einstein condensation of chromium. *Phys. Rev. Lett.*, 94:160401, Apr 2005. doi: 10.1103/PhysRevLett.94.160401.
- R. Grimm and M. Weidemüller. Optical dipole traps for neutral atoms. *Advances in Atomic, Molecular and Optical Physics*, 1999.
- A. Grochola, P. Kowalczyk, W. Jastrzebski, P. Crozet, and A. Ross. The $C^1\Sigma^+$ state of KLi studied by polarisation labelling spectroscopy technique. *ACTA PHYSICA POLONICA A*, 102(6):729, 2002.
- A. Grochola, W. Jastrzebski, P. Kowalczyk, P. Crozet, and A. Ross. The molecular constants and potential energy curve of the $D^1\Pi$ state in KLi. *Chemical Physics Letters*, 372(1&2):173 – 178, 2003. ISSN 0009-2614. doi: 10.1016/S0009-2614(03)00396-8.

BIBLIOGRAPHY

- V. Gurarie and L. Radzihovsky. Resonantly paired fermionic superfluids. *Annals of Physics*, 322(1):2 – 119, 2007. ISSN 0003-4916. doi: 10.1016/j.aop.2006.10.009. URL <http://www.sciencedirect.com/science/article/pii/S0003491606002399>.
- C. Hahn. *Cross-dimensional Relaxation in Fermi-Fermi Mixtures*. PhD thesis, Ludwig-Maximilians Universität München, 2009.
- E. Hecht. *Optics*. Addison Wesley, fourth edition, 2002.
- G. Herzberg and K. Huber. *Molecular spectra and molecular structure. I. Spectra of diatomic molecules*. Molecular Spectra and Molecular Structure. Van Nostrand Reinhold, 1950. ISBN 9780442033859.
- P. L. M. Heydemann. Determination and correction of quadrature fringe measurement errors in interferometers. *Applied Optics*, 20(19):3382–3384, Oct. 1981.
- R. Holzwarth, T. Udem, T. W. Hänsch, J. C. Knight, W. J. Wadsworth, and P. S. J. Russell. Optical frequency synthesizer for precision spectroscopy. *Phys. Rev. Lett.*, 85:2264–2267, Sep 2000. doi: 10.1103/PhysRevLett.85.2264. URL <http://link.aps.org/doi/10.1103/PhysRevLett.85.2264>.
- K. Huang. *Statistical Mechanics*. Wiley, second edition, 1987.
- F. Hund. Zur Deutung einiger Erscheinungen in den Molekülspektren. *Zeitschrift für Physik A Hadrons and Nuclei*, 36:657–674, 1926. ISSN 0939-7922. URL <http://dx.doi.org/10.1007/BF01400155>. 10.1007/BF01400155.
- Z. Idziaszek and P. S. Julienne. Universal rate constants for reactive collisions of ultracold molecules. *Phys. Rev. Lett.*, 104:113202, Mar 2010. doi: 10.1103/PhysRevLett.104.113202.
- S. Inouye, J. Goldwin, M. L. Olsen, C. Ticknor, J. L. Bohn, and D. S. Jin. Observation of heteronuclear feshbach resonances in a mixture of bosons and fermions. *Phys. Rev. Lett.*, 93:183201, Oct 2004. doi: 10.1103/PhysRevLett.93.183201. URL <http://link.aps.org/doi/10.1103/PhysRevLett.93.183201>.
- D. Jaksch, C. Bruder, J. I. Cirac, C. W. Gardiner, and P. Zoller. Cold bosonic atoms in optical lattices. *Phys. Rev. Lett.*, 81:3108–3111, Oct 1998. doi: 10.1103/PhysRevLett.81.3108. URL <http://link.aps.org/doi/10.1103/PhysRevLett.81.3108>.
- W. Jastrzebski, P. Kowalczyk, and A. Pashov. The perturbation of the $B^1\Pi+$ and $C^1\Sigma+$ states in KLi. *Journal of Molecular Spectroscopy*, 209(1):50 – 56, 2001. ISSN 0022-2852. doi: 10.1006/jmsp.2001.8389.
- S. Jochim, M. Bartenstein, A. Altmeyer, G. Hendl, C. Chin, J. H. Denschlag, and R. Grimm. Pure gas of optically trapped molecules created from fermionic atoms. *Phys. Rev. Lett.*, 91:240402, Dec 2003a. doi: 10.1103/PhysRevLett.91.240402.
- S. Jochim, M. Bartenstein, A. Altmeyer, G. Hendl, S. Riedl, C. Chin, J. Hecker Denschlag, and R. Grimm. Bose-einstein condensation of molecules.

BIBLIOGRAPHY

- Science*, 302(5653):2101–2103, 2003b. doi: 10.1126/science.1093280. URL <http://www.sciencemag.org/content/302/5653/2101.abstract>.
- D. M. S. Johnson, J. M. Hogan, S. w. Chiow, and M. A. Kasevich. Broadband optical serrodyne frequency shifting. *Opt. Lett.*, 35(5):745–747, Mar 2010. doi: 10.1364/OL.35.000745. URL <http://ol.osa.org/abstract.cfm?URI=ol-35-5-745>.
- R. Jördens, N. Strohmaier, K. Günter, H. Moritz, and T. Esslinger. A mott insulator of fermionic atoms in an optical lattice. *Nature*, 455:204–207, 2008.
- W. Ketterle and N. V. Druten. Evaporative cooling of trapped atoms. volume 37 of *Advances In Atomic, Molecular, and Optical Physics*, pages 181 – 236. Academic Press, 1996. doi: 10.1016/S1049-250X(08)60101-9.
- W. Ketterle and M. W. Zwiernik. Making, probing and understanding ultracold fermi gases. In *Proceedings of the International School of physics “Enrico Fermi”*, Jun 2006.
- W. Ketterle, D. Durfee, and D. Stamper-Kurn. Making, probing and understanding bose-einstein condensates. Apr 1999.
- S. Kobtsev, S. Kandrushin, and A. Potekhin. Long-term frequency stabilization of a continuous-wave tunable laser with the help of a precision wavelengthmeter. *Appl. Opt.*, 46(23):5840–5843, Aug 2007. doi: 10.1364/AO.46.005840. URL <http://ao.osa.org/abstract.cfm?URI=ao-46-23-5840>.
- T. Köhler, K. Góral, and P. S. Julienne. Production of cold molecules via magnetically tunable feshbach resonances. *Rev. Mod. Phys.*, 78:1311–1361, Dec 2006. doi: 10.1103/RevModPhys.78.1311.
- R. Kohlhaas, T. Vanderbruggen, S. Bernon, A. Bertoldi, A. Landragin, and P. Bouyer. Robust laser frequency stabilization by serrodyne modulation. *Opt. Lett.*, 37(6):1005–1007, Mar 2012. doi: 10.1364/OL.37.001005.
- I. Kovacs. *Rotational structure in the spectra of diatomic molecules*. Adam Hilger, 1969. ISBN 0852741421.
- P. Kowalczyk. : I thank P. Kowalczyk for generously giving out his data., 2012.
- G. Kramer and W. Klische. Multi-channel synchronous digital phase recorder. In *Frequency Control Symposium and PDA Exhibition, Proceedings of the 2001 IEEE International*, Jun 2001.
- R. Krems, W. Stwalley, and B. Friedrich. *Cold Molecules: Theory, Experiment, Applications*. CRC Press, 2009. ISBN 9781420059038.
- E. D. Kuhnle, H. Hu, X.-J. Liu, P. Dyke, M. Mark, P. D. Drummond, P. Hannaford, and C. J. Vale. Universal behavior of pair correlations in a strongly interacting fermi gas. *Phys. Rev. Lett.*, 105:070402, Aug 2010. doi: 10.1103/PhysRevLett.105.070402. URL <http://link.aps.org/doi/10.1103/PhysRevLett.105.070402>.

BIBLIOGRAPHY

- L. D. Landau and E. M. Lifshitz. *Quantum Mechanics, Non-relativistic Theory*. Butterworth Heinemann, 1981.
- F. Lang, K. Winkler, C. Strauss, R. Grimm, and J. H. Denschlag. Ultracold triplet molecules in the rovibrational ground state. *Phys. Rev. Lett.*, 101:133005, Sep 2008. doi: 10.1103/PhysRevLett.101.133005.
- L. J. LeBlanc. The hyperfine structure of potassium-40. Technical report, University of Toronto, Canada, 2006.
- R. J. LeRoy. Level 8.0: A computer program for solving the radial schrödinger equation for bound and quasibound levels. Technical report, University of Waterloo Chemical Physics Research Report CP-663, 2007. see <http://leroy.uwaterloo.ca/programs>.
- Z. Li, S. V. Alyabyshev, and R. V. Krems. Ultracold inelastic collisions in two dimensions. *Phys. Rev. Lett.*, 100:073202, Feb 2008. doi: 10.1103/PhysRevLett.100.073202. URL <http://link.aps.org/doi/10.1103/PhysRevLett.100.073202>.
- O. J. Luiten, M. W. Reynolds, and J. T. M. Walraven. Kinetic theory of the evaporative cooling of a trapped gas. *Phys. Rev. A*, 53:381–389, Jan 1996. doi: 10.1103/PhysRevA.53.381. URL <http://link.aps.org/doi/10.1103/PhysRevA.53.381>.
- M. Lukin. Atomic molecular optics 2. Lecture Notes, 2006.
- F. Martin, P. Crozet, A. J. Ross, M. Aubert-Frecon, P. Kowalczyk, W. Jastrzebski, and A. Pashov. On the $X^1\Sigma^+$ state of KLi. *The Journal of Chemical Physics*, 115(9): 4118–4124, 2001. doi: 10.1063/1.1388555.
- H. J. Metcalf and P. van der Straten. *Laser Cooling and Trapping*. Springer, 1999.
- A. Micheli, Z. Idziaszek, G. Pupillo, M. A. Baranov, P. Zoller, and P. S. Julienne. Universal rates for reactive ultracold polar molecules in reduced dimensions. *Phys. Rev. Lett.*, 105:073202, Aug 2010. doi: 10.1103/PhysRevLett.105.073202.
- A. J. Moerdijk, B. J. Verhaar, and A. Axelsson. Resonances in ultracold collisions of ^6Li , ^7Li , and ^{23}Na . *Phys. Rev. A*, 51:4852–4861, Jun 1995. doi: 10.1103/PhysRevA.51.4852. URL <http://link.aps.org/doi/10.1103/PhysRevA.51.4852>.
- C. R. Monroe, E. A. Cornell, C. A. Sackett, C. J. Myatt, and C. E. Wieman. Measurement of cs-cs elastic scattering at $T=30\ \mu\text{K}$. *Phys. Rev. Lett.*, 70:414–417, Jan 1993. doi: 10.1103/PhysRevLett.70.414.
- O. Morsch. Private communication, 2010.
- M. Movre and R. Beuc. van der waals interaction in excited alkali-metal dimers. *Phys. Rev. A*, 31:2957–2967, May 1985. doi: 10.1103/PhysRevA.31.2957. URL <http://link.aps.org/doi/10.1103/PhysRevA.31.2957>.
- T. Müller-Wirts. Patents: US 6,178,002 DE 197 43 493 A 1, 2001.

- C. J. Myatt, E. A. Burt, R. W. Ghrist, E. A. Cornell, and C. E. Wieman. Production of two overlapping bose-einstein condensates by sympathetic cooling. *Phys. Rev. Lett.*, 78:586–589, Jan 1997. doi: 10.1103/PhysRevLett.78.586. URL <http://link.aps.org/doi/10.1103/PhysRevLett.78.586>.
- H.-C. Nägerl. Private communication., 2012a.
- H.-C. Nägerl. Rb-Cs ground state molecules. Private communication., 2012b.
- D. Naik, A. Trenkwalder, C. Kohstall, F. Spiegelhalder, M. Zaccanti, G. Hendl, F. Schreck, R. Grimm, T. Hanna, and P. Julienne. Feshbach resonances in the ${}^6\text{Li}$ - ${}^{40}\text{K}$ fermi-fermi mixture: elastic versus inelastic interactions. *The European Physical Journal D - Atomic, Molecular, Optical and Plasma Physics*, 65:55–65, 2011. ISSN 1434-6060. 10.1140/epjd/e2010-10591-2.
- K. D. Nelson, X. Li, and D. S. Weiss. Imaging single atoms in a three-dimensional array. *Nature Physics*, 3:556–560, June 2007. doi: 10.1038/nphys645.
- K.-K. Ni, S. Ospelkaus, M. H. G. de Miranda, A. Pe’er, B. Neyenhuis, J. J. Zirbel, S. Kotochigova, P. S. Julienne, D. S. Jin, and J. Ye. A high phase-space-density gas of polar molecules. 322(5899):231–235, 2008. doi: 10.1126/science.1163861.
- K. M. O’Hara, S. L. Hemmer, S. R. Granade, M. E. Gehm, J. E. Thomas, V. Venturi, E. Tiesinga, and C. J. Williams. Measurement of the zero crossing in a feshbach resonance of fermionic ${}^6\text{Li}$. *Phys. Rev. A*, 66:041401, Oct 2002. doi: 10.1103/PhysRevA.66.041401. URL <http://link.aps.org/doi/10.1103/PhysRevA.66.041401>.
- C. Ospelkaus, S. Ospelkaus, L. Humbert, P. Ernst, K. Sengstock, and K. Bongs. Ultracold heteronuclear molecules in a 3d optical lattice. *Phys. Rev. Lett.*, 97:120402, Sep 2006. doi: 10.1103/PhysRevLett.97.120402.
- S. Ospelkaus, K.-K. Ni, G. Quéméner, B. Neyenhuis, D. Wang, M. H. G. de Miranda, J. L. Bohn, J. Ye, and D. S. Jin. Controlling the hyperfine state of rovibronic ground-state polar molecules. *Phys. Rev. Lett.*, 104:030402, Jan 2010a. doi: 10.1103/PhysRevLett.104.030402.
- S. Ospelkaus, K.-K. Ni, D. Wang, M. H. G. de Miranda, B. Neyenhuis, G. Quéméner, P. S. Julienne, J. L. Bohn, D. S. Jin, and J. Ye. Quantum-state controlled chemical reactions of ultracold potassium-rubidium molecules. *Science*, 327(5967):853–857, 2010b. doi: 10.1126/science.1184121.
- A. Pashov, W. Jastrzębski, and P. Kowalczyk. The $B^1\Pi+$ and $C^1\Sigma+$ states of KLi. *Chemical Physics Letters*, 292(4-6):615–620, 1998. ISSN 0009-2614. doi: 10.1016/S0009-2614(98)00702-7.
- C. J. Pethick and H. Smith. *Bose-Einstein Condensation in Dilute Gases*. Cambridge University Press, 2002.
- D. S. Petrov, C. Salomon, and G. V. Shlyapnikov. Diatomic molecules in ultracold fermi gases - novel composite bosons. *Journal of Physics B: Atomic, Molecular and Optical Physics*, 38(9):S645, 2005. URL <http://stacks.iop.org/0953-4075/38/i=9/a=014>.

BIBLIOGRAPHY

- D. S. Petrov, G. E. Astrakharchik, D. J. Papoular, C. Salomon, and G. V. Shlyapnikov. Crystalline phase of strongly interacting fermi mixtures. *Phys. Rev. Lett.*, 99:130407, Sep 2007. doi: 10.1103/PhysRevLett.99.130407. URL <http://link.aps.org/doi/10.1103/PhysRevLett.99.130407>.
- W. D. Phillips and H. Metcalf. Laser deceleration of an atomic beam. *Phys. Rev. Lett.*, 48:596–599, Mar 1982. doi: 10.1103/PhysRevLett.48.596. URL <http://link.aps.org/doi/10.1103/PhysRevLett.48.596>.
- G. Pupillo, A. Micheli, H. Büchler, and P. Zoller. Condensed matter physics with cold polar molecules. 2008.
- G. Quéméner, J. L. Bohn, A. Petrov, and S. Kotochigova. Universalities in ultracold reactions of alkali-metal polar molecules. *Phys. Rev. A*, 84:062703, Dec 2011. doi: 10.1103/PhysRevA.84.062703.
- E. L. Raab, M. Prentiss, A. Cable, S. Chu, and D. E. Pritchard. Trapping of neutral sodium atoms with radiation pressure. *Phys. Rev. Lett.*, 59(23):2631–2634, Dec 1987. doi: 10.1103/PhysRevLett.59.2631.
- C. A. Regal, C. Ticknor, J. L. Bohn, and D. S. Jin. Tuning p -wave interactions in an ultracold fermi gas of atoms. *Phys. Rev. Lett.*, 90:053201, Feb 2003. doi: 10.1103/PhysRevLett.90.053201.
- C. A. Regal, M. Greiner, and D. S. Jin. Observation of resonance condensation of fermionic atom pairs. *Phys. Rev. Lett.*, 92:040403, Jan 2004a. doi: 10.1103/PhysRevLett.92.040403.
- C. A. Regal, M. Greiner, and D. S. Jin. Lifetime of molecule-atom mixtures near a feshbach resonance in ^{40}K . *Phys. Rev. Lett.*, 92:083201, Feb 2004b. doi: 10.1103/PhysRevLett.92.083201.
- A. Ridinger, S. Chaudhuri, T. Salez, D. R. Fernandes, N. Bouloufa, O. Dulieu, C. Salomon, and F. Chevy. Photoassociative creation of ultracold heteronuclear ^6Li - $^{40}\text{K}^*$ molecules. *EPL (Europhysics Letters)*, 96(3):33001, 2011.
- W. J. Riley. *Handbook of frequency stability analysis*. U.S. Dept. of Commerce, National Institute of Standards and Technology, 2008.
- J. L. Roberts. PhD thesis, University of Colorado, 2001.
- J. M. Rost, J. C. Griffin, B. Friedrich, and D. R. Herschbach. Pendular states and spectra of oriented linear molecules. *Phys. Rev. Lett.*, 68:1299–1302, Mar 1992. doi: 10.1103/PhysRevLett.68.1299. URL <http://link.aps.org/doi/10.1103/PhysRevLett.68.1299>.
- S. Rousseau, A. Allouche, M. Aubert-Frécon, S. Magnier, P. Kowalczyk, and W. Jastrzebski. Theoretical study of the electronic structure of KLi and comparison with experiments. *Chemical Physics*, 247(2):193 – 199, 1999. ISSN 0301-0104. doi: 10.1016/S0301-0104(99)00206-2.

- J. J. Sakurai. *Modern Quantum Mechanics*. Addison Wesley Longman, revised edition, 1994.
- B. E. A. Saleh and M. Teich. *Fundamentals of Photonics*. Wiley, 1991.
- P. Schauß, M. Cheneau, M. Endres, T. Fukuhara, S. Hild, A. Omran, T. Pohl, C. Gross, S. Kuhr, and I. Bloch. Observation of spatially ordered structures in a two-dimensional rydberg gas. *Nature*, 491:87–91, 2012.
- F. Schreck, G. Ferrari, K. L. Corwin, J. Cubizolles, L. Khaykovich, M.-O. Mewes, and C. Salomon. Sympathetic cooling of bosonic and fermionic lithium gases towards quantum degeneracy. *Phys. Rev. A*, 64:011402, Jun 2001a. doi: 10.1103/PhysRevA.64.011402. URL <http://link.aps.org/doi/10.1103/PhysRevA.64.011402>.
- F. Schreck, L. Khaykovich, K. L. Corwin, G. Ferrari, T. Bourdel, J. Cubizolles, and C. Salomon. Quasipure bose-einstein condensate immersed in a fermi sea. *Phys. Rev. Lett.*, 87:080403, Aug 2001b. doi: 10.1103/PhysRevLett.87.080403.
- J. F. Sherson, C. Weitenberg, M. Endres, M. Cheneau, I. Bloch, and S. Kuhr. Single-atom-resolved fluorescence imaging of an atomic mott insulator. *Nature*, 467:68–72, 2010.
- A. Simoni, F. Ferlaino, G. Roati, G. Modugno, and M. Inguscio. Magnetic control of the interaction in ultracold K-Rb mixtures. *Phys. Rev. Lett.*, 90:163202, Apr 2003. doi: 10.1103/PhysRevLett.90.163202. URL <http://link.aps.org/doi/10.1103/PhysRevLett.90.163202>.
- F. M. Spiegelhalter, A. Trenkwalder, D. Naik, G. Kerner, E. Wille, G. Hendl, F. Schreck, and R. Grimm. All-optical production of a degenerate mixture of ${}^6\text{Li}$ and ${}^{40}\text{K}$ and creation of heteronuclear molecules. *Phys. Rev. A*, 81:043637, Apr 2010. doi: 10.1103/PhysRevA.81.043637.
- J. T. Stewart, J. P. Gaebler, T. E. Drake, and D. S. Jin. Verification of universal relations in a strongly interacting fermi gas. *Phys. Rev. Lett.*, 104:235301, Jun 2010. doi: 10.1103/PhysRevLett.104.235301.
- K. E. Strecker, G. B. Partridge, and R. G. Hulet. Conversion of an atomic fermi gas to a long-lived molecular bose gas. *Phys. Rev. Lett.*, 91:080406, Aug 2003. doi: 10.1103/PhysRevLett.91.080406.
- J. Stuhler, A. Griesmaier, T. Koch, M. Fattori, T. Pfau, S. Giovanazzi, P. Pedri, and L. Santos. Observation of dipole-dipole interaction in a degenerate quantum gas. *Phys. Rev. Lett.*, 95:150406, Oct 2005. doi: 10.1103/PhysRevLett.95.150406. URL <http://link.aps.org/doi/10.1103/PhysRevLett.95.150406>.
- R. Szplet, J. Kalisz, and R. Szymanowski. Interpolating time counter with 100 ps resolution on a single fpga device. *IEEE Transactions on Instrumentation and Measurement*, 49.
- M. Taglieber. *Quantum Degeneracy in an Atomic Fermi-Fermi-Bose Mixture*. PhD thesis, Ludwig-Maximilians-Universität München, 2008.

BIBLIOGRAPHY

- M. Taglieber, A.-C. Voigt, F. Henkel, S. Fray, T. W. Hänsch, and K. Dieckmann. Simultaneous magneto-optical trapping of three atomic species. *Phys. Rev. A*, 73:011402, Jan 2006. doi: 10.1103/PhysRevA.73.011402.
- M. Taglieber, A.-C. Voigt, T. Aoki, T. W. Hänsch, and K. Dieckmann. Quantum degenerate two-species fermi-fermi mixture coexisting with a bose-einstein condensate. *Phys. Rev. Lett.*, 100:010401, Jan 2008. doi: 10.1103/PhysRevLett.100.010401. URL <http://link.aps.org/doi/10.1103/PhysRevLett.100.010401>.
- S. Tan. Large momentum part of a strongly correlated fermi gas. *Annals of Physics*, 323(12):2971 – 2986, 2008. ISSN 0003-4916. doi: 10.1016/j.aop.2008.03.005. URL <http://www.sciencedirect.com/science/article/pii/S0003491608000432>.
- K. T. Tang, J. M. Norbeck, and P. R. Certain. Upper and lower bounds of two- and three-body dipole, quadrupole, and octupole van der waals coefficients for hydrogen, noble gas, and alkali atom interactions. *The Journal of Chemical Physics*, 64(7):3063–3074, 1976. doi: 10.1063/1.432569. URL <http://link.aip.org/link/?JCP/64/3063/1>.
- H. Telle, B. Lipphardt, and J. Stenger. Kerr-lens, mode-locked lasers as transfer oscillators for optical frequency measurements. *Applied Physics B: Lasers and Optics*, 74:1–6, 2002. ISSN 0946-2171. URL <http://dx.doi.org/10.1007/s003400100735>. 10.1007/s003400100735.
- J. Thiel, T. Pfeifer, and M. Hartmann. Interferometric measurement of absolute distances of up to 40m. *Measurement*, 16:1–6, 1995.
- T. G. Tiecke. Properties of potassium. Technical report, van der Waals-Zeeman Institute, The Netherlands, 2010.
- T. G. Tiecke, M. R. Goosen, J. T. M. Walraven, and S. J. J. M. F. Kokkelmans. Asymptotic-bound-state model for feshbach resonances. *Phys. Rev. A*, 82:042712, Oct 2010.
- E. Tiemann, H. Knöckel, P. Kowalczyk, W. Jastrzebski, A. Pashov, H. Salami, and A. J. Ross. Coupled system $a^3\Sigma^+$ and $X^1\Sigma^+$ of KLi: Feshbach resonances and corrections to the born-oppenheimer approximation. *Phys. Rev. A*, 79:042716, Apr 2009. doi: 10.1103/PhysRevA.79.042716.
- A. G. Truscott, K. E. Strecker, W. I. McAlexander, G. B. Partridge, and R. G. Hulet. Observation of fermi pressure in a gas of trapped atoms. *Science*, 291(5513):2570–2572, 2001. doi: 10.1126/science.1059318.
- T. Udem, R. Holzwarth, and T. W. Hänsch. Optical frequency metrology. *Nature*, 416, March 2002.
- M. Urban and A. J. Sadlej. Electronic structure and electric properties of the alkali metal dimers. *The Journal of Chemical Physics*, 103(22):9692–9704, 1995. doi: 10.1063/1.469984. URL <http://link.aip.org/link/?JCP/103/9692/1>.

BIBLIOGRAPHY

- R. Vexiau, N. Bouloufa, M. Aymar, J. Danzl, M. Mark, H. Nägerl, and O. Dulieu. Optimal trapping wavelengths of Cs₂ molecules in an optical lattice. *The European Physical Journal D - Atomic, Molecular, Optical and Plasma Physics*, 65:243–250, 2011. ISSN 1434-6060. doi: 10.1140/epjd/e2011-20085-4.
- N. Vitanov and S. Stenholm. Properties of stimulated raman adiabatic passage with intermediate-level detuning. *Optics Communications*, 135(4â6):394 – 405, 1997a. ISSN 0030-4018. doi: 10.1016/S0030-4018(96)00635-9. URL <http://www.sciencedirect.com/science/article/pii/S0030401896006359>.
- N. Vitanov, M. Fleischhauer, B. Shore, and K. Bergmann. Coherent manipulation of atoms and molecules by sequential laser pulses. volume 46 of *Advances In Atomic, Molecular, and Optical Physics*, pages 55 – 190. Academic Press, 2001. doi: 10.1016/S1049-250X(01)80063-X. URL <http://www.sciencedirect.com/science/article/pii/S1049250X0180063X>.
- N. V. Vitanov and S. Stenholm. Population transfer via a decaying state. *Phys. Rev. A*, 56:1463–1471, Aug 1997b. doi: 10.1103/PhysRevA.56.1463. URL <http://link.aps.org/doi/10.1103/PhysRevA.56.1463>.
- N. V. Vitanov, K.-A. Suominen, and B. W. Shore. Creation of coherent atomic superpositions by fractional stimulated raman adiabatic passage. *Journal of Physics B: Atomic, Molecular and Optical Physics*, 32(18):4535, 1999. URL <http://stacks.iop.org/0953-4075/32/i=18/a=312>.
- M. Viteau, M. G. Bason, J. Radogostowicz, N. Malossi, D. Ciampini, O. Morsch, and E. Arimondo. Rydberg excitations in bose-einstein condensates in quasi-one-dimensional potentials and optical lattices. *Phys. Rev. Lett.*, 107:060402, Aug 2011. doi: 10.1103/PhysRevLett.107.060402. URL <http://link.aps.org/doi/10.1103/PhysRevLett.107.060402>.
- A.-C. Voigt. *Heteronuclear Molecules from a Quantum Degenerate Fermi-Fermi Mixture*. PhD thesis, Ludwig-Maximilians-Universität München, 2009.
- A.-C. Voigt, M. Taglieber, L. Costa, T. Aoki, W. Wieser, T. W. Hänsch, and K. Dieckmann. Ultracold heteronuclear fermi-fermi molecules. *Phys. Rev. Lett.*, 102:020405, Jan 2009. doi: 10.1103/PhysRevLett.102.020405.
- J. Walraven. Elements of quantum gases: Thermodynamic and collisional properties of trapped atomic gases. Lecture Notes, 2009-2010.
- D. Wang, B. Neyenhuis, M. H. G. de Miranda, K.-K. Ni, S. Ospelkaus, D. S. Jin, and J. Ye. Direct absorption imaging of ultracold polar molecules. *Phys. Rev. A*, 81:061404, Jun 2010. doi: 10.1103/PhysRevA.81.061404.
- H. Wang and W. C. Stwalley. Ultracold photoassociative spectroscopy of heteronuclear alkali-metal diatomic molecules. *The Journal of Chemical Physics*, 108(14):5767–5771, 1998. doi: 10.1063/1.475987. URL <http://link.aip.org/link/?JCP/108/5767/1>.

BIBLIOGRAPHY

- T. Weber, J. Herbig, M. Mark, H.-C. Nägerl, and R. Grimm. Bose-einstein condensation of cesium. *Science*, 299(5604):232–235, 2003. doi: 10.1126/science.1079699. URL <http://www.sciencemag.org/content/299/5604/232.abstract>.
- W. Wieser. *An Optical Dipole Trap for Ultracold Bosons and Fermions*. PhD thesis, Ludwig-Maximilians-Universität München, 2006.
- R. J. Wild, P. Makotyn, J. M. Pino, E. A. Cornell, and D. S. Jin. Measurements of tan’s contact in an atomic bose-einstein condensate. *Phys. Rev. Lett.*, 108:145305, Apr 2012. doi: 10.1103/PhysRevLett.108.145305.
- E. Wille, F. M. Spiegelhalder, G. Kerner, D. Naik, A. Trenkwalder, G. Hendl, F. Schreck, R. Grimm, T. G. Tiecke, J. T. M. Walraven, S. J. J. M. F. Kokkelmans, E. Tiesinga, and P. S. Julienne. Exploring an ultracold fermi-fermi mixture: Interspecies feshbach resonances and scattering properties of ^6Li and ^{40}K . *Phys. Rev. Lett.*, 100:053201, Feb 2008. doi: 10.1103/PhysRevLett.100.053201.
- A. A. Zavitsas. The potential energy curve of the ground state of lithium, $X^1\Sigma_g^+ \text{Li}_2$. *Journal of Molecular Spectroscopy*, 221(1):67 – 71, 2003. ISSN 0022-2852. doi: 10.1016/S0022-2852(03)00202-9.
- W. T. Zemke and W. C. Stwalley. Analysis of exchange energy at long range for states of alkali diatomic molecules correlating to two ground state atoms. *The Journal of Chemical Physics*, 111(11):4962–4965, 1999. doi: 10.1063/1.479755. URL <http://link.aip.org/link/?JCP/111/4962/1>.
- B. Zimmermann, T. Müller, J. Meineke, T. Esslinger, and H. Moritz. High-resolution imaging of ultracold fermions in microscopically tailored optical potentials. *New Journal of Physics*, 13(4):043007, 2011. URL <http://stacks.iop.org/1367-2630/13/i=4/a=043007>.
- M. Zwierlein, J. Abo-Shaeer, A. Schirotzek, C. Schunck, and W. Ketterle. Vortices and superfluidity in a strongly interacting fermi gas. *Nature*, 453:1047–1051, 2005.
- M. W. Zwierlein, C. A. Stan, C. H. Schunck, S. M. F. Raupach, S. Gupta, Z. Hadzibabic, and W. Ketterle. Observation of bose-einstein condensation of molecules. *Phys. Rev. Lett.*, 91:250401, Dec 2003. doi: 10.1103/PhysRevLett.91.250401. URL <http://link.aps.org/doi/10.1103/PhysRevLett.91.250401>.

Danksagung

Hiermit möchte ich mich bei allen, die zum Gelingen dieser Arbeit beigetragen haben, bedanken.

Vor allem möchte ich Prof. T. W. Hänsch dafür danken mich in seine Arbeitsgruppe aufgenommen zu haben und besonders auch dafür, daß er mir so viel Freiraum gelassen und so lange so viel Unterstützung gewährt hat - auch nach dem Umzug der Gruppe nach Singapur. Das war wesentlich für die schwierige persönliche Entscheidung nicht mit nach Singapur umzuziehen.

Mein grosser Dank gilt auch Prof. Kai Dieckmann, der mich, trotz der Entscheidung in München zu bleiben, weiter unterstützt hat. Die zahlreichen Telefonate waren sehr hilfreich und ich bin sehr dankbar für das Korrekturlesen der Arbeit und des Papers und für die wertvollen Verbesserungsvorschläge. Auch wenn ich jetzt leider nicht direkt daran beteiligt sein kann die Li-K Grundzustandsmoleküle zu erzeugen, finde ich das Projekt weiterhin sehr interessant und hochaktuell. Ich wünsche ihm und allen in Singapur, dass das bald klappt.

Insbesondere möchte ich mich auch bei Dr. habil. Markus Weber für die Begutachtung dieser Arbeit bedanken.

Dank gilt meinem Kollegen Louis Costa, mit dem ich zum Anfang meiner Zeit in der Hänsch Gruppe viel im Labor zusammen gearbeitet habe. Auch wenn wir sehr unterschiedlich sind und die Zeiten im Labor nicht immer einfach waren, blieb der Ton doch immer freundlich.

Besonderer Dank gilt auch Janis Alnis. Sein großes Wissen über Laserresonatoren und Laserstabilisierung teilt er gerne und ist immer sehr nett und hilfsbereit. Ich danke ihm für die vielen fruchtbaren Diskussionen und habe viel vom ihm gelernt.

Thomas Kinders freundliche Art hat es sehr angenehm gemacht mit ihm zusammen zu arbeiten. Ich danke ihm für die vielen Diskussionen und dafür, dass er aus Hannover angereist ist. Ausserdem danke ich TEM für die Leihgabe einiger Komponenten.

Ich möchte mich bei allen bedanken mit denen ich in meiner Zeit als "Gast" am MPQ zu tun hatte. Vor allem bei Elisabeth Peters und Sascha Reinhardt, die sehr nette Menschen sind und denen ich sehr dafür danke mich so lange in ihrem Labor geduldet zu haben. Ausserdem bin ich Tobias Wilken dankbar für die Hilfe damit, geeignetes Frequenzkamm Licht für meine Anwendung zu erzeugen. Danke auch an alle Leute im

Wasserstoff labor, daß ich den Kamm benutzen durfte.

Desweiteren habe ich mich gefreut die Diplomanden Carolin Hahn und Mathias Mang kennen zu lernen. Es war sehr angenehm mit ihnen zusammen zu arbeiten. Master Mang, ich hoffe das wird was mit dem Kilimanjaro!

Toni Scheich, Nicole Schmid und Gabriele Gschwendtner möchte ich herzlich für die Unterstützung bei technischem und organisatorischen Dingen danken. Insbesondere Toni Scheichs besonnene Art macht die Zusammenarbeit mit ihm sehr angenehm.

Die gemeinsamen Mittagessen/-pausen mit den Angehörigen der Gruppen Treutlein/Hunger genieße ich immer sehr und sie werden mir in guter Erinnerung bleiben. Das war immer sehr unterhaltend - ich freue mich immer auf Menschen mit einer genügend großen Portion Humor zu treffen. Besonders freue ich mich David Hunger, Stephan Camerer, Max Riedel, Hanno Kaupp, Mathias Mader, Thomas Hümmer und Maria Korppi kennengelernt zu haben. Auch die Leute in der Weinfurter Gruppe haben dazu beigetragen, dass die Atmosphäre auf dem Flur angenehm war. Besonders Daniel Schlenk, Micheal Krug und Markus Weber haben dazu beigetragen.

Meinen Eltern Barbara und Axel möchte ich danken, dass sie mich, so wie im Studium, auch in der Promotion bei dem unterstützt haben, was ich machen wollte.

Natalia hat mich auch in den Tiefphasen der Doktorandenzeit ertragen. Vielen Dank für deine Geduld!